Airborne remote sensing of Grímsvötn subglacial volcano, Vatnajökull, Iceland

A thesis presented in fulfilment of the requirements for the degree of Doctor of Philosophy by

Sukina Stewart

BSc (Cardiff) 1998
PGCE (Keele) 1999

Environmental Science Department
Lancaster University

Geography Department
Lancaster University

February 2006

ProQuest Number: 11003689

ProQuest 11003689

Grímsvötn caldera lake, in the area of the 1998 eruption crater, June 2004.
(Photograph by S. Stewart)

Acknowledgments

Abstract

Grímsvötn, a subglacial volcano in Iceland, has a partially exposed geothermal system, that has, until recently, been used to make estimates of heat flux using calorimetry. Increased melting in Grímsvötn in the aftermath of the 1998 eruption has changed the ice conditions considerably, resulting in major leakage of the ice dam that used to seal Grímsvötn caldera lake. This makes calorimetric estimates of melting more difficult.

An aerial survey of Grímsvötn was carried out in June 2001. Thermal images of the Grímsvötn subglacial caldera show distinct areas of geothermal activity. Ground survey studies of the same area carried out by the Science Institute, University of Iceland, show that protruding ground above the ice, along with areas of open water, have high geothermal heat flux all year round. In these areas, heat is lost by radiation and geothermal steam emission. This component of heat flux cannot be detected by calorimetric estimates based on ice melting. Therefore an alternative method of calculating heat flux is adopted in this research based on a combination of remote sensing and meteorological information.

Aerial photographs collected for Grímsvötn have been used to map the main features along the caldera walls, such as crevasses and slumps that cannot be accurately mapped from the ground because of inaccessibility. A high resolution DEM of the case study sites has been generated from the aerial photographic coverage using a stereoscope and parallax bar. The combined data sets have been analysed both visually and quantitatively using a combination of ERDAS Imagine and ARCGIS environments. Together, these data establish that remote sensing can be used to map

and monitor an inaccessible volcano such as Grímsvötn, as well as aid in the understanding of the processes at work within one of the most powerful geothermal systems in the world.

Contents

List of Tables

List of Figures

Chapter 2

Chapter 3

Chapter 4

Chapter 5

Chapter 1 – Introduction

1.1. Introduction

During June 2001, the Natural Environment Research Council (NERC) Airborne Remote Sensing Facility (ARSF) carried out an aerial survey of the Grímsvötn subglacial volcano, Iceland. A selection of multispectral imagery and aerial photographs of the Grímsfjall Ridge section of the caldera was collected. As the region is reasonably inaccessible, being located within Vatnajökull, Europe's largest temperate ice sheet, remote sensing offered a potential alternative to traditional field techniques for studying this partially exposed caldera. The research undertaken in the study combines remote sensing with geographical information systems (GIS) to study the volcanological processes at work at Grímsvötn, along with evaluating the usefulness of using remotely sensed data for such an inaccessible and hazardous environment. This chapter provides an introduction, focusing on the reasons for studying subglacial volcanoes, and the aims of the research.

1.2.   Importance of Study

Traditional field-based methods for monitoring active volcanoes are difficult to use on subglacial volcanoes, because of problems of access and hazards associated with rapid melting of ice and snow during an eruption. Many strato-volcanoes with small summit ice caps are often near populated regions, and although not completely subglacial, have similar accessibility problems. However, even remote ice-covered strato-volcanoes are hazardous because of the rapid formation of melt water, which

can travel large distances from the volcano. Consequently, an improved understanding of processes and alternative methodologies for monitoring subglacial volcanoes, and improving hazard mitigation, is crucial.

Other hazards associated with subglacial volcanoes are similar to those of subaerial eruptions, such as ash and tephra injected into the atmosphere. Gronvold et al. (1995) related tephra layers in ice from subglacial eruptions to glacier fluctuations through time, which they related to climate change. By using subglacial volcanic remnants now exposed, Bourgeois et al. (1998) has been able to compare glacial and interglacial climatic fluctuations with tephra layers. Magma generation associated with pressure release following reductions in ice thickness (Björnsson 2002; Smellie & Hole 1997; Smellie 1999; 2002), along with increases in melt water availability, fragmentation rates and geothermal output are also important in understanding subglacial processes.

Unlike subaerial volcanoes, their subglacial counterparts can cause massive flooding because elevated heat flow can melt ice. Temperate glaciers are at their pressure melting temperature throughout their thickness and so water can migrate beneath the glacier allowing meltwater to flow from the eruption site to the edges of the glacier where it is released as a sudden flood called a jökulhlaup (Smellie 1999). An example is the 1996 Gjálp jökulhlaup in Iceland (Björnsson 2002).

Grímsvötn is Iceland's most active volcano (Guðmundsson 1989). This subglacial volcano, which erupted in 1998 and again in 2004, has a partially exposed geothermal system, and ground-based measurements have been used to make calorimetric estimates of the relationship between volcanic eruption rate and heat flux (Björnsson

1983, Björnsson & Guðmundsson 1993, Guðmundsson 2003). However, increased melting at Grímsvötn in the aftermath of the 1998 eruption changed the ice conditions considerably (Guðmundsson 2003). Increased melting at the ice dam that used to seal Grímsvötn in the periods between drainage in glacier floods (jökulhlaups) has resulted in major leakage of the dam (Guðmundsson 2003). This makes calorimetric estimates of melting more difficult. Thermal images of the Grímsvötn caldera show distinct areas of geothermal activity. The component of heat flow lost to the atmosphere cannot be measured using calorimetric techniques based on ice melting (Guðmundsson et al. 2004). Therefore an alternative method for calculating heat flux is now required. Furthermore, inflation changes prior to eruptions could be indicative of magma input into the system and a method for monitoring the topographic features such as slope change could be indicative of an eruption (Decker & Decker 1996).

1.3.   Aims of the PhD

The Natural Environmental Research Council (NERC) Airborne Remote Sensing Facility (ARSF) undertook an aerial survey of the Grímsvötn caldera, Iceland, in 2001. Some of the multispectral and aerial photographic data collected during this survey has been analysed during the last three years, and its usefulness for studying a subglacial volcano such as Grímsvötn has been assessed. At the same time as the aerial survey, a ground-based expedition from the Science Institute, University of Iceland, was undertaken to collect, temperature and topographic data. That data, along with some field-based measurements collected in 2004, has been used in evaluating the airborne remote sensing data sets.

The intention of this research was to establish whether it is possible to extract useful information from airborne remote sensing data about the thermal regime, morphological changes and volcanic processes of the Grímsvötn volcanic system. This was achieved by focusing on the following aims:

a.   to analyse remotely sensing data provided by the NERC ARSF, and comparing it to ground-based data collected by Icelandic collaborators, such as temperature and topographic data. This would evaluate the confidence in the temperature data extracted from the aerial imagery.

b.   to build on ground-based calorimetric research, by using the thermal imagery collected by the ARSF to calculate heat flux for an inaccessible and remote environment where *in situ* data are limited. Previous heat flux research has taken place from the Grímsvötn caldera lake, but leakage since 1998 has meant that alternative methods must be found.

c.   to map features such as crevasses and ice caves from the aerial photographs with the intention of monitoring morphological variations. Ice caves and crevasses can be indicative of instabilities within the ice, possibly due to heat at depth.

d.   to adopt a methodology for the production of high-resolution digital elevation models to monitor topographical changes. The methodology will be adapted for a subglacial environment and assessed. As above, variations in the ice surface could provide the first indication of increased heat beneath the ice.

It is hoped that this methodology could provide a new and precise method for observing and recording changes in other volcanological situations that are also poorly accessible.

1.4.   Structure of Thesis

Chapter two contains a review of subglacial volcanism, including the mechanisms and processes involved, and provides a wider introduction to subglacial basaltic volcanism. Chapter three reviews remote sensing and its techniques and applications for monitoring volcanoes: from thermal imaging by satellites, to geomorphological terrain analysis using photogrammetry and digital elevation models. In chapter four an in-depth look at Iceland, the study area, and in particular the geographical and geological setting of Grímsvötn is provided. Chapter five discusses the remote sensing data used in this study, and the preprocessing methodology used to geometrically correct the imagery along with enhancement techniques used in the preparation of the imagery for further analysis. Chapter six firstly establishes the confidence that we can have in the ARSF thermal imagery by comparing it to ground-based temperature data collected in 2001, at the time of the aerial survey, and further data collected during a field excursion in 2004. Then a methodology for calculating heat flux is tested on the remotely sensed temperature data to determine whether it is possible to calculate heat flux for the Grímsvötn crater lake. The results are then discussed and interpreted. Chapter 7 utilizes the aerial photographs to map the geomorphology of the Grímsfjall ridge, before leading on to the creation of a high resolution DEM of the 1998 eruption site and caldera lake. A series of 3D visualisations demonstrates the advantages in producing a DEM for the Grímsvötn caldera. Chapter 8 concludes the study by synthesising the findings and discussing a number of worthwhile areas for further study. A glossary of terms, abbreviations used within the thesis, and equations and physical symbols can be found in Appendix A.

Chapter 2 – Volcanological Aspects of Subglacial Eruptions

2.1.   Introduction

Subglacial volcanoes are found both beneath cold-based ice sheets in the polar-regions and beneath temperate glaciers, such as in Iceland (Smellie 1999). They vary in chemistry and explosivity but always involve the generation of large volumes of melt water (Björnsson 1974; Björnsson 2002). Due to the interaction with water from melted ice emergent subglacial eruptions are usually explosive or phreatic (Björnsson et al. 1982). The largest areas of continuous ice sheets are in the polar regions, such as Antarctica where a number of subglacial volcanoes are located, for example, Mount Erebus, Brown Bluff and Deception Island (Smellie and Skilling 1994). However other subglacial volcanoes occur beneath temperate glaciers. These glaciers are at their pressure melting temperature throughout their thickness meaning that overlying ice allows water to migrate through the glacier (Einarsson 1999), thus allowing melt water to flow from an eruption site to the edge of the glacier, released suddenly as a devastating flood known by the Icelandic term, jökulhlaups (Björnsson 1974).

This chapter provides a literature review of subglacial volcanism in both thin and thick ice environments, in order to more fully understand the processes occurring at Grímsvötn. The chapter begins with an examination of eruption processes for a number of case studies, before looking in more detail at subglacial eruption mechanisms occurring beneath subglacial basaltic volcanoes in Iceland.

2.2.   Subglacial Eruption Processes

The type of eruptive activity on a subglacial volcano depends on a number of factors including glacier type, ice thickness and magma chemistry (Björnsson 2002; Bourgeois et al. 1998; Einarsson 1999; Guðmundsson et al. 1997; Guðmundsson et al. 2002; Höskuldsson & Sparks 1997; Smellie 1999; 2002; Tuffen et al. 2002a, b). Most published work on subglacial volcanoes has concentrated on basaltic volcanism. Research by Höskuldsson & Sparks (1997) and Tuffen et al. (2002b) has shown that basaltic and rhyolitic morphologies are similar, in that fragmental deposits are overlain by near horizontal subaerial lava flows. When magma reaches the base of the glacier it starts to melt the ice (Smellie 2002). On the surface a depression known as an ice cauldron (Björnsson 1974) is formed due to subsidence, with large crevasses forming in a circular pattern in response to ice flowing towards the eruption site caused by the melting of ice and the subsequent release of water at the glacier base. Melt water accumulation is only likely at large basaltic eruptions due to the high temperature of basaltic magma (<1200°C) which is capable of melting up to 14 times its own volume (Allen 1980; Allen et al. 1982).

During basaltic tuya-forming subglacial eruptions, melt water accumulates until it reaches a level where the ice floats on the water and it escapes (Jones 1968, 1969; Björnsson 1988, 2002). The decrease in ice volume following melting to water, leads to a pressure reduction encouraging melt water to accumulate (Jones 1968). If pressure above the volcano is sufficient to inhibit explosive eruptions, pillow lavas will accumulate (fig. 2.1).
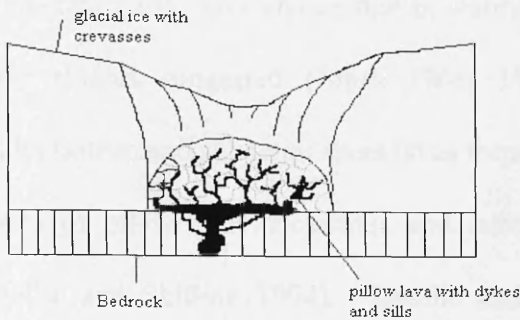
Fig. 2.1 Diagram of effusive phase of a subglacial eruption, showing formation of pillow lavas and cauldron on surface of ice (Jones 1969; Einarsson, 1999).

As the eruption continues, the ice roof collapses leading to the formation of a melt water lake (Jones 1968). Along with an increase in volcanic gases and steam, the eruption would become explosive in a similar way to a shallow submarine eruption (Decker & Decker 1996). An increase in volcanic material will cause the eruption to occur at shallower depths (Einarsson 1999). Jones (1968) interpreted field examples in Iceland, and showed that hyaloclastites would be formed within the melt water lake covering the pillow lavas (fig. 2.2).
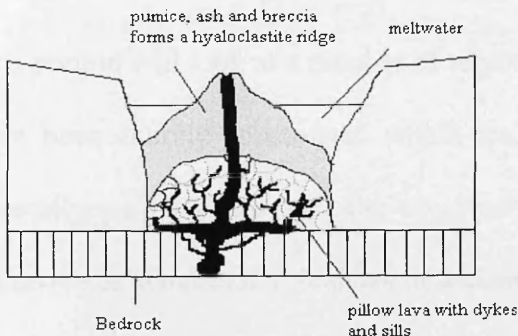
Fig. 2.2 Diagram of a subglacial eruption that has emerged from the ice to produce a hyaloclastites, covering a pillow lava pile. (Jones 1969; Einarsson, 1999).

Hyaloclastite ridges have been known to form from fissure eruptions within ice sheets (Guðmundsson et al. 2002, Einarsson 1999). The 1996 Gjálp eruption allowed important data to be collected on the production of a hyaloclastite ridge (Guðmundsson et al. 2002). Jones (1968) interpreted the field studies to show that as the hyaloclastite pile emerges, subaerial lava flows would be confined by the ice walls (Jones 1968). Models developed from fieldwork looking at preserved ridges composed of cores of pillows topped by hyaloclastite successions of ash and

8

fragmental lavas, have shown that in reality tuya formation is not as simplistic as the early studies suggested (Jones 1968, 1970; Einarsson 1999). In reality, the hyaloclastites and subaerial sheet lavas form a deltaic sequence, composed of multiple layers of pillows, hyaloclastites and subaerial lavas (Jones 1970; Skilling 1994; Smellie and Skilling 1994). Smellie and Hole (1997) and Smellie (1999, 2002) concluded that basaltic tuya production typically begins with the effusion of pillows, which, as the edifice grows and confining pressure decreases, becomes increasingly explosive. Finally, once the ice surface is breached, melt water flooding the vault interacts explosively with rising magma, triggering an eruption of ash and steam (Smellie and Hole 1997).

2.3. Global Subglacial Studies

This section will look at a number of regions which contain subglacial volcanoes that have been entirely constructed within ice. Although the subglacial volcanoes are generally partially exposed, the objective is to show that many of the processes occurring at subglacial volcanoes in Iceland also occur in other regions of the globe. Fig. 2.3 is a map of the world showing the global distribution of volcanoes where ice–magma interaction has been observed (Wood and Kienle 1990, Cronin et al. 1996, Hoblitt et al. 1998, Smellie 1999).
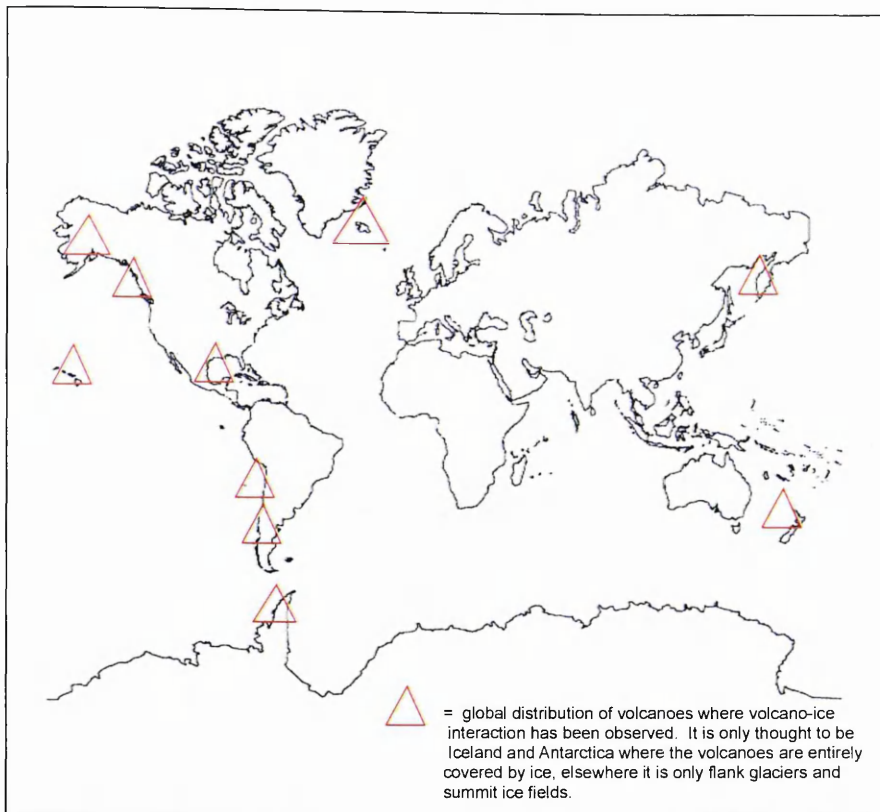
Fig. 2.3 Map of the global distribution of volcanoes where ice-volcano interaction has been studied (Wood and Kienle 1990, Cronin et al. 1996, Hoblitt et al. 1998, Smellie 1999).

2.3.1. Antarctica

Antarctica has been glaciated for much of the Cenozoic period (66.4 Ma to present); however the precise time at which continent-wide ice sheets spread is unknown. The Antarctic ice sheet is a dynamic system as shown by a series of glacial and intra glacial periods (Smellie et al. 1993).

The West Antarctic Ice Sheet (WAIS) sits above the West Antarctic Rift system, which is similar in dimensions to the East African Rift (Behrendt et al. 1992). The rift is characterised by exposures of alkaline volcanic rocks in isolated sequences associated with episodic extension from Late Mesozoic to the present. The separation of the southern hemisphere continents (179 – 162 Ma) left the East Antarctic craton surrounded by a series of extensional rifts (Behrendt et al. 1992). The western area of

Antarctica is characterised by the Ross Sea, and Marie Byrd Land volcanic province, a broad structural dome block faulted above sea level (Le Masurier 2002). Behrendt et al. (1992) suggested that the source of the extensive volcanism was a mantle plume or hot spot. This was based on results from geophysical measurements (magnetics, radar and gravity surveys) and field observations of exposed sections of volcanic edifices.

The studies show volcanic sources at the base of the ice throughout large areas of the West Antarctic ice sheet. Behrendt et al. (1992) suggested that the West Antarctic Rift System is a continuation of a propagating rift from the break up of Gondwanaland and, although stresses associated with asthenospheric doming by a suggested plume may not have been sufficient to cause rifting, it could have led to the reorganization of the rift. In turn this led to a weakened lithosphere and initiation of a new spreading ridge propagating to the Antarctic Peninsula (Behrendt et al. 1992).

Volcanism in Antarctica has been studied at individual centres such as Brown Bluff, a subglacial volcano, consisting of a subglacial sequence of pillow lavas, hyaloclastites and final subaerial stage lavas (Skilling 1994). Evidence for subglacial activity in the Brown Bluff subglacial formation can be seen in the interbedded volcaniclastic sediments (Skilling 1994). These reveal evidence of rapid changes in water level consistent with catastrophic drainage and high melt rates (Björnsson 2002). Skilling (1994) suggested that Brown Bluff is now a subaqueous to emergent volcano but was initially subglacial and its products were ponded within an englacial lake. Northern Alexander Island on the Antarctic Peninsula has also been studied, but unlike Brown Bluff, it had no ponded lake (Smellie et al. 1993). This has led to recognition of the importance of ice thickness and hydrological state i.e. snow, firn or ice (Smellie et al.

1993) on the hydrodynamic situation during a subglacial eruption. The 1969 Deception Island basalt-andesite eruption occurred beneath thin (100 m) ice along a 5 km fissure and shows some similarities with subglacial fissure eruptions in Iceland (Smellie 2002).

2.3.2. Canada

Hoodoo Mountain in British Columbia, Canada, is a Quaternary volcano resulting from extensional forces within the lithosphere (Edwards et al. 2002). It features a circular flat summit, capped by a 120 -150 m thick ice cap and is flanked by two valley glaciers. Throughout its history, Hoodoo has displayed different forms of glaciovolcanism. Edwards and Russell (2002) interpreted early lava flows from 80 thousand years ago as subaerial ice dammed flows, rather than those produced completely subglacially. However there are some distinct sequences, featuring breccias believed to have formed from eruptions beneath thin ice (Edwards et al. 2002).

2.3.3. Alaska

A number of volcanic centres can be found in Alaska and the Aleutian Islands, many of which have confining valley glaciers or summit ice caps (Motyka et al. 1978, 1980). Heavy snowfall from the northern Pacific produces compact, continuous snow and ice cover over the entire region. Mount Wrangell, in southern Alaska, is heavily glaciated with 10 km^3 of ice at the summit and another 150 km^3 around the flanks (Motyka et al. 1978; Benson and Follett 1986). Benson and Follett (1986) stated that due to Mount Wrangell's high altitude (4000 m above sea level) the summit melting is geothermal in origin. Hence studies of volcanic heat flux have led to a greater understanding of glacier fluctuation (Motyka et al. 1980; Benson and Follett 1986).

2.4.   Effect of Ice Thickness on Eruption Characteristics

Recent research in Iceland and Antarctica has shown that eruptive products reflect the

thickness of the ice. Thin glaciers, such as alpine valley glaciers, or the margins of

larger ice sheets, are composed of snow, firn (intermediate stage of densification) and

fractured ice (Smellie 1999).   As the snow has not been compacted to solid

unfractured glacial ice, melt water is able to migrate through the permeable glacier

(fig. 2.4). Smellie (2000) suggested that, even if substantial melting occurred, pillow

lavas would not form, as the melt water was not ponded over the vent. In essence, for

pillows to form there must be subaqueous conditions and a high pressure meaning a

significant amount of melt water and / or ice. Hence the thin ice eruption would be

explosive in the first instance, but once the initial pyroclastic cone had formed, the

melt water would flow away causing a change to effusive volcanism. Smellie (2000)

also stated that due to melt water flow, some sedimentary flow structures could be

preserved in volcanic sediments or glacial till.
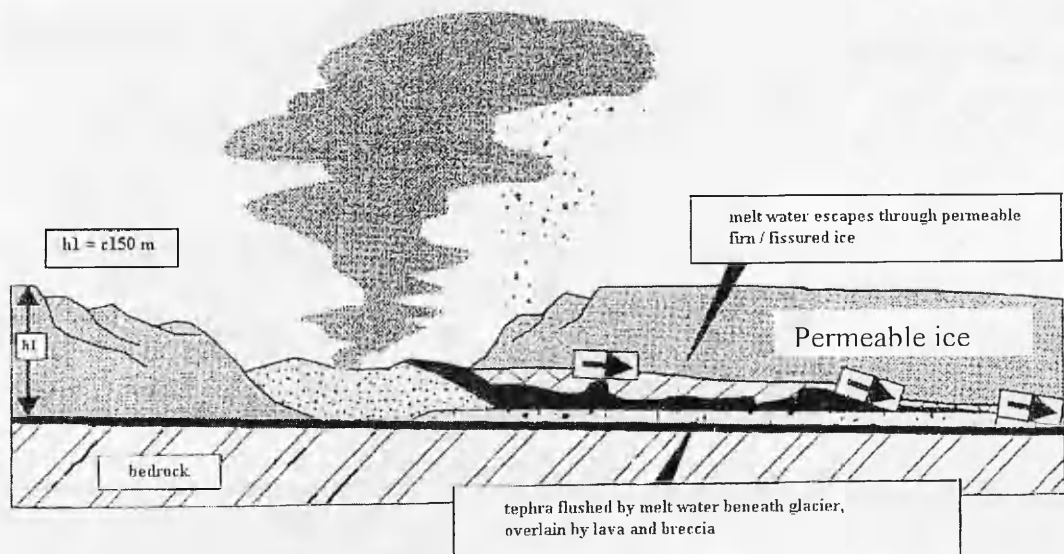
Fig. 2.4 Schematic diagram showing Smellie (2000) model of a subglacial eruption beneath thin permeable ice, where meltwater escapes through fractured ice, and eruption is often explosive.

When subglacial eruptions take place under thick glaciers, those formed of impermeable unfractured ice greater than 150 metres thick (Smellie and Skilling 1994), melt water may be sealed in vaults. Observed subglacial eruptions show that heat transfer from erupting magma to ice is extremely rapid (Björnsson 1983, Björnsson and Guðmundsson 1993, Guðmundsson 2003, Guðmundsson et al. 2004, Smellie 1999, 2002). The formation of ice cauldrons on the surface of ice caps during eruptions is in response to melting at their base (fig. 2.5). If an eruption becomes emergent and breaks the surface then energy is transferred to the eruption plume (Björnsson and Guðmundsson 1993, Guðmundsson 2003).
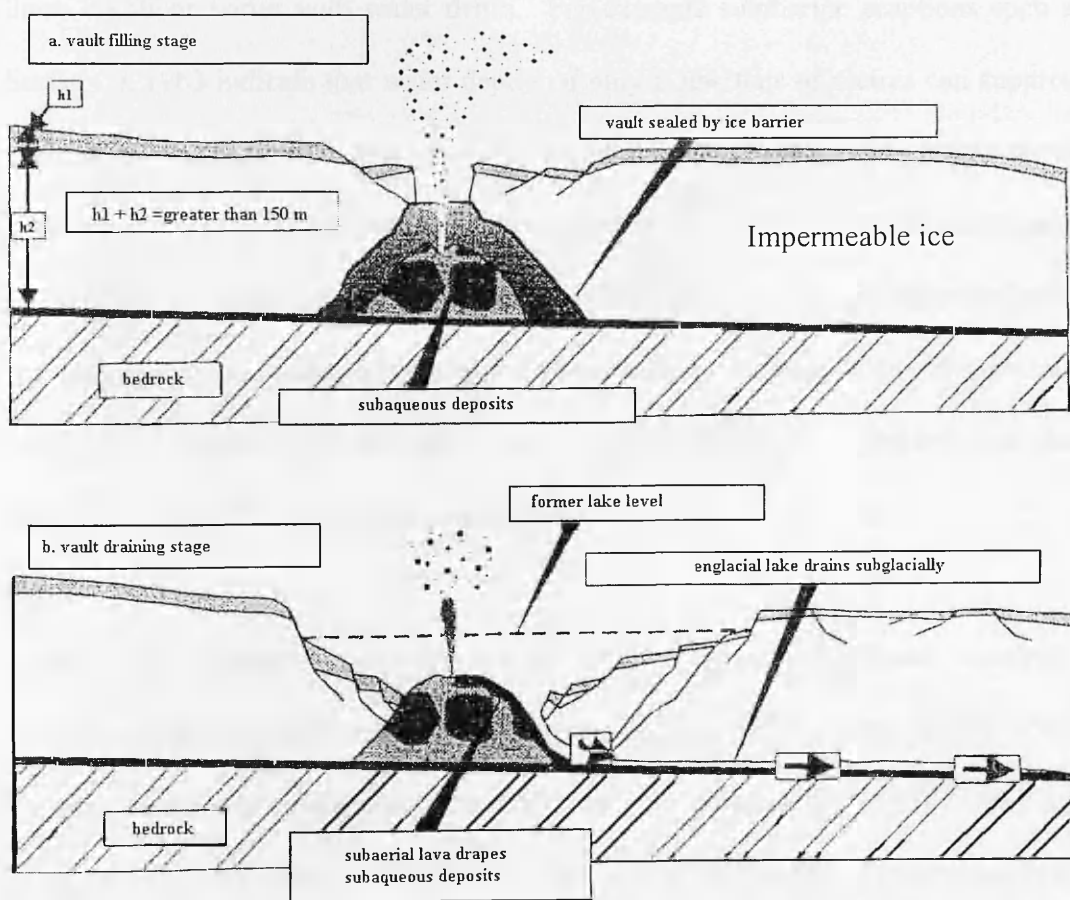
Fig. 2.5 Schematic diagram showing Smellie (2000) model of a subglacial eruption beneath thick impermeable ice, greater than 150 m, with a thin permeable upper layer where melt water is ponded within a subglacial vault. Melt water lake drains subglacially, if ice is breached or is floated.

The volume of melt water within a vault will depend on the volume of magma emplaced and the rate of subglacial leakage (Smellie 2000). Most ice sheets in reality are composed of layers of snow, firn and fractured ice covering impermeable ice, so water will accumulate until it encounters a layer of permeable ice or snow through which it escapes (Björnsson 1988).

For tuyas, hyaloclastite deltas are formed at the top of a subaqueous sequence, and this in turn is overlain by one or more sheet-like columnar jointed subaerial lava flows (Jones, 1968, Skilling 2002). In cases where eruptions cease before the subaerial stage, hyaloclastite ridges called tindars are formed (Jones 1968). The explosivity of these eruptions varies with water depth. For example submarine eruptions such as Surtsey in 1963 indicate that water depths of only a few tens of metres can suppress explosivity. Decker and Decker (1996) found that the critical depth below which submarine lava is not explosive, depends on the dissolved gas content and temperature of the magma. Most submarine eruptions become explosive as the lava pile grows upwards because the pile reaches a level where bubbles can nucleate due to a decrease in pressure. This same process can occur in subglacial eruptions as the lava pile rises to the top of the melt water within the sealed vault.

As the eruptive products emerge through the ice, subaerial lava can directly overlie the subaqueous pillows and tephra (Jones 1970; Skilling 1994). For this to occur, drainage of water from the subglacial vault must take place (Jones 1970). This could occur by leakage of water through the ice barrier but, in the case of impermeable ice sheets, melt water can accumulate in the vault and ultimately float the surrounding ice, releasing the melt water along subglacial channels (Smellie 1999).

Basaltic lava fed deltas, poorly sorted volcaniclastic wedges, can form when subaerial lava flows fragment upon entering water, such as melt water lakes (Skilling 2002). However if the melt water accumulation is sufficient to lift the ice shelf, allowing melt water to escape lava fed deltas will not be formed (Skilling 2002).

2.5. Related Processes

The following section looks in more detail at key processes that occur beneath subglacial basaltic volcanoes, particularly those in Iceland. These processes are included in order to give a better understanding of subglacial volcanic systems, such as Grímsvötn. Because of the inaccessible nature of subglacial volcanoes, the vent and material erupted can seldom be observed directly. Therefore other methods have been used to monitor and study the processes occurring. For example calorimetry has been used to calculate magma volume, and provide information on melt water volumes to give a broader understanding of subglacial volcanic processes (Björnsson 1983).

2.5.1. Subglacial seismicity

Increased earthquake activity before a volcanic eruption is common, although does not occur everywhere. Studies of Mýrdalsjökull (Icelandic ice sheet), seismicity have an annual cyclicity with earthquakes occurring preferentially during the autumn months. Einarsson and Brandsdóttir (2000) explained these phenomena by suggesting a triggering effect such as reduced ice load after a summer's melting and hence elevated pore fluid in underlying bedrock.

Seismic signals associated with volcanic activity have a range of signatures dependent on solid and liquid processes. Increased seismicity has been observed before a number of subglacial eruptions, e.g. the 1969 eruption of Deception Island, Antarctica and the 1996 Gjálp eruption, Iceland. The interaction between water and magma within pores, fractures and faults causes rapid phase changes i.e. water to steam, and this can generate pressure waves that are recorded as volcanic tremor (Vila et al. 1992; Correig et al. 1997; Smellie 2002). Deception Island has a large flooded caldera with high heat flow, and ice-covered flanks. Smellie (2002) stated that the 1969 eruption occurred along a series of en-echelon fissures for a distance of 5 km. A number of earthquakes occurred in the months prior to the eruption. Smellie (2002) suggested that these indicated brittle fractures in the crust and the likely propagation of steam through a previous edifice. For example, as the first eruption column of the 1969 eruption was white, it was probably steam driven Smellie (2002). Smellie (2002) also stated that the large earthquake recorded on the morning of the eruption represented crustal failure and the initiation of the fissure system, leading to the unlocking of the magma chamber in a similar way to the 1996 Gjálp eruption (Guðmundsson et al. 1997, 2002, 2004). During that eruption, seismic activity was initially located below the northwest rim of Bárðarbunga, but during the following twenty-four hours the earthquakes were detected migrating south towards Grímsvötn, accompanied by a high frequency (3 Hz) continuous tremor suggesting magma injection through a feeder dyke (Einarsson et al.1997).

Konstantinou et al. (2000) studied the seismic events leading up to the 1996 Gjálp eruption using temporary and permanent seismic stations around Iceland. They recorded and categorized the events into three groups: (1) low-frequency, (2) mixed

17

frequency and (3) volcanic tremor. Zobin (1999) developed a theory for the movement of magma based on the observed seismic activity preceding the 1996 Gjálp eruption. Zobin (1999) suggested that a magma chamber lying beneath Bárðarbunga, located to the north of Gjálp, covered by dense strong rocks could explain the spatial-temporal seismic features. The main earthquake has caused debate, as suggestions have been made that it was associated with either a propagating fissure, or a dyke intrusion that was recorded as a low-frequency event (Konstantinou et al. 2000). The resulting phenomena allowed the magma to move from the Bárðarbunga magma chamber to Gjálp. This migration of magma caused mixed frequency events (Konstantinou et al. 2000). Zobin (1999) argues that the continuing seismic activity after the initial eruption was associated with the collapse of the emptied part of the Bárðarbunga magma chamber. The volcanic tremor was recorded continuously for 14 days, and showed a variation in frequency (Konstantinou et al. 2000). However there is an apparent conflict between the geophysical and geochemical evidence. Sigmarsson et al. (2000) argues that the chemistry of the Gjálp magma indicated it originated from Grímsvötn. The composition showed no sign of a mixed basaltic magma that would have indicated lateral migration from Bárðarbunga into a chamber beneath Gjálp (Sigmarsson et al. 2000).

Sigmarsson et al. (2000) suggests that the magma did not migrate laterally from Bárðarbunga. They argue that the earthquakes were associated with the propagation of a fracture that intercepted a subsidiary magma chamber to the south of Bárðarbunga. They believe it to be the same magma chamber that was activated in the 1938 Vatnajökull eruption. The volcanic tremor is explained by geothermal boiling of water due to pressure release when the fissure opened (Sigmarsson et al. 2000). This

mechanism combines both the geophysical and geochemical evidence. It is also compatible with previous observations in Iceland, that of lateral migration of fractures, where no magma flow has occurred e.g. during the Krafla eruptions from 1975 to 1984 (Sigmarsson et al. 2000).

2.5.2. Pillow lavas

A pillow represents an individual lava flow unit encrusted by a glassy rind formed by the quenching of magma by water. Pillow lavas are the most common form of volcanic rock on Earth, although most of the occurrences are on the sea floor. Subglacial pillows with a wide range of compositions occur in Iceland. Fridleifsson et al. (1982) studied the relationship between the chemistry of pillow lavas and mean dimensions. All the pillows studied were formed within melt water from subglacial eruptions. Although the exact depth of emplacement is unknown, inferences from thickness of deposits and attitude of tuyas have allowed an estimate of a few hundred metres depth of water (Jones 1968). The study also showed that, regardless of composition or effusion, all small pillows are approximately spherical, but with increasing size gravitational forces have a larger effect, and the pillows are flattened (Fridleifsson et al. 1982). Pillows formed from olivine tholeiite have the largest diameter, and there is a reduction in the size of the pillows with more acidic compositions (Fridleifsson et al. 1982). The glassy crust rapidly attains sufficient strength to prevent further growth. Jones (1968, 1969, 1970) showed that pillow lavas erupted within former subglacial volcanoes in western Iceland, were emplaced in a depth of water from 600 to 715 metres. However, the vesicles that are often used to determine emplacement depth were likely to have been formed after, rather than during emplacement (Fridleifsson et al. 1982). For submarine conditions basaltic magmas containing approximately 1wt% of water would form pillows at pressures

above 5 MPa (~500 m depth) otherwise the water would exsolve and lead to explosive eruptions (Allen 1980, 1982). For a subglacial environment the pressure can either remain constant, if the ice roof remains or can be decrease is ice roof collapses (Wilson and Head 2002). Wilson and Head (2002) state that, if pressure falls below the value at which magma is saturated, more volatiles will exsolve leading to a phreatic eruption.

Using data from a geophysical survey carried out in 1997 on the 1996 Gjálp edifice, Guðmundsson et al. (2002) suggests that the high mean density of the northern area (2200 kg m^{-3}) is compatible with a structure containing pillow lavas. Hence this suggests that the water was ponded during the eruption in order create a subaqueous environment to allow pillow formation (Guðmundsson et al 2002).

2.5.3. Gas driven eruptions

Guðmundsson et al. (1997) observed that magma erupted subglacially is cooled rapidly and may solidify as pyroclastic glass depending on the pressure. These conditions produce little or no latent heat. Highly turbulent convection of melt water and quenched ash is needed to obtain a high rate of heat transfer (Guðmundsson et al. 1997). High melt water temperatures (15-20°C) during the 1996 Gjálp eruption increased the number and size of tunnels allowing for a higher discharge rate (Guðmundsson et al. 1997). Gas temperatures are likely to reach several hundred degrees centigrade in fumarolic vents at the bedrock surface, initiating melting at the base of the glacier prior to the arrival of magma (Smellie 2002). This steam would therefore be the first injected into the atmosphere once it had melted through the ice (Smellie 2002). In the 1969 eruption of Deception Island, a thin ice eruption, the duration of the gas-driven melting period was uncertain, but the seismic record

suggests that abundant gases could have reached the ice-bedrock interface at the same time as the volcanic tremor began (Smellie 2002). Smellie (2002) interpreted this as an unsteady stream of gas in fractures. It is thought that magma did not reach the interface until much later and that there could have been a maximum of 90 minutes for gas-driven melting. Guðmundsson (1997) study of 1996 Gjálp eruption suggested that is a similar process was a work, there would have been sufficient time to produce a sealed vault within the overlying ice for the 1969 Deception Island eruption.

At both the 1969 Deception Island and 1996 Gjálp eruptions, cylindrical ice chimneys were observed, created by gas-driven melting (Guðmundsson et al. 1997; Smellie 2002). Smellie (2002) suggested that a gas-driven melting episode in combination with an associated bubble-generated seismic pressure wave would lead to a mechanical instability in the ice wall when the roof reached within a few tens of metres from the surface. As that section of the overlying glacier, in both thick and thin models, lacks cohesive strength it would readily collapse. Smellie (2002) goes on to infer from this that gas-driven melting is a rapid process leading to the formation of a conical chimney, as melting is greater at the apex than on the walls.

2.5.4. Ice melting

Höskuldsson and Sparks (1997) along with Tuffen et al. (2002a, b) pointed out that subglacial eruptions are dynamic multi-component systems in which ice, water, steam, magma and fragmented magma all interact. Many subglacial eruptions are likely to begin with the intrusion of a sill or dyke at the ice-bedrock interface leading to the production of a cavity. Mafic dykes are driven upwards by magma buoyancy and / or excess pressure in the magma reservoir, typically in conduits one metre wide and at speeds of 1 m s^{-1} (Wilson and Head 2002). The geometries of dykes and sills are

21

efficient at delivering heat to surrounding ice, leading to high melt water volumes,

often in the early stages of eruptions. However Wilson and Head (2002) have shown

that the relationship between melting and pressure is important. In both submarine

and subglacial eruptions it is common for exsolution to be inhibited due to the

pressure of overlying water or ice. Thermal energy released from basaltic lava melts

approximately ten times or more of its own volume of ice (Höskuldsson and Sparks

1997). This leads to pressure differences due to the difference in density between

water and ice, although large changes in pressure are unlikely due to ice deformation

and leakage. Höskuldsson and Sparks (1997) suggested that positive pressure

changes, due to temperature of magma, effusion rates and efficiency of heat transfer,

for rhyolite magmas would lead to deformation and uplift of overlying ice, causing an

escape of water, whereas basaltic magmas were more likely to cause negative pressure

changes leading to sagging structures such as ice cauldrons. Fig. 2.6 is a schematic

diagram, of a fully subglacial eruption, where heat source and water in a cavity,

leading to the creation of ice cauldrons.
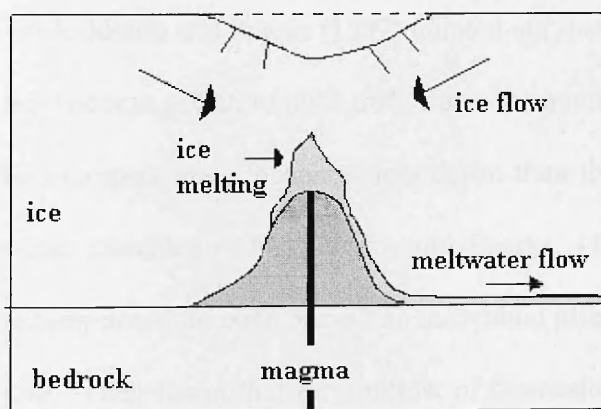
Fig. 2.6 Schematic diagram of a fully subglacial eruption, where magma melts the ice, forming an ice cauldron. If the eruption continues, the pressure could allow the ice to float and melt water to flow beneath the glacier. (Guðmundsson 2003).

Direct observations of subglacial eruptions where ice melting is the dominant

recipient of thermal energy are rare (Guðmundsson and Björnsson 1991,

Guðmundsson et al. 1997, 2002). Generally although some heat is used for the

melting of ice, a larger fraction of the heat dissipates through the eruption plume into

the atmosphere as the eruptions become subaerial. However, the 1938 Vatnajökull

and 1996 Gjálp eruptions used more than 95% of the total available energy for ice

melting (Guðmundsson 2003). The 1996 Gjálp eruption is the best documented of the

two, and Guðmundsson (2003) stated that 3 km^3 of ice was melted in total, of which

two thirds was melted in the first four days of the eruption. The heat flux calculated

(500,000 Wm^{-2}) was too high to be explained by cooling and solidification of pillows

and is believed to be due to quenched ash (Guðmundsson 2003).

Heat is transferred from the lava to the ice by conduction and / or convection.

However cavity distribution is influenced by basal heating and is directly related to

the position of geothermal fumaroles (Höskuldsson and Sparks 1997, Tuffen et al.

2002a). Heat transfer by conduction depends on the volume and dimension of the

lava, along with the rate of cooling. Natural convection is however a major

contributor to melting, as layers of melt water develop between the lava and the ice

through which the heat must be transferred (Höskuldsson and Sparks 1997). However

Höskuldsson and Sparks (1997) pointed out that convective heat transfer in water does

not become effective until melt water temperature is greater than 4°C, as it is above

this temperature it becomes less dense than the cooler melt water found at the ice-

water interface. Höskuldsson and Sparks' (1997) experiments were based on the

assumption that, once buried, an individual pillow would have a minimal heat transfer

rate. They found that for a pillow of dimensions 0.5–1 metres across with a cooling

rate of 10^4-10^5 s^{-1}, melt rates of 2.5x10^{-5} to 3.2x10^{-4} m s^{-1} could be estimated. This is

enough to allow cooling pillows to maintain a cavity in vigorous convection, with a

temperature range of 10-100°C. However, in reality the melt water must circulate

through the developing lava pile, extracting more heat. This may go some way to

explaining why the melt rate of the 1996 Gjálp eruption (3.6×10^{-3} m s^{-1}) is higher than the predictions made by Höskuldsson and Sparks (1997) from their experiments. Fragmentation of the magma followed by rapid cooling could also be used to explain the high heat flux found during the Gjálp eruption (Guðmundsson et al. 2002). Observations made during and following the eruption indicated that the heat released during the 1996 eruption was equivalent to that released by fragmentation of 0.4 km^3 of basic magma and the formation of pyroclastic glass (Guðmundsson et al. 2002). If fragmentation was the cause of the high heat flow then it would be expected that the edifice would be composed of fragmental and mostly glassy material. This was found to be the case by Guðmundsson et al. (2002) for the 1996 Gjálp eruption.

Ice melting and drainage of melt water leads to the production of ice cauldrons on the glacier surface. The ice surface is often smooth and fractures during the early stages of cauldron formation indicating brittle deformation (Malthe-Sørensson et al. 1998). The base of the glacier deforms in a ductile manner, especially at high confining pressures (Tuffen et al. 2002, Guðmundsson et al. 2004). The 1996 Gjálp eruption formed a rapidly widening depression with a diameter of 150-200 metres within the early stages of the eruption, before the roof collapsed. Malthe-Sørensson et al. (1998) described the process of deformation as a combination of melting, sliding, sinking, floating and contact with underlying topography. They pointed out that, away from the central area, a uniform bending of the ice produced a circular series of fractures indicating that the glacier was strained radially as the central region collapsed. This suggests that at least the upper section of ice deformed in a brittle manner (Guðmundsson et al. 2004).

2.5.5. Melt water transport

On most glaciers melt water is formed by heat from solar radiation, which causes surface ablation, and from friction and geothermal energy causing melting at the base or within the body of the ice. Although melt water from the surface may follow a different path to that from the base, both processes involve channel flow (Bennett and Glasser 1996). Movement of melt water through subglacial channels is related to hydrological forces that include changes in melt water input, drainage morphology and mechanical forces such as transfer of overburden pressure between regions of ice. Guðmundsson et al. (2004) stated that, during an eruption, the development of ice cauldrons alters the water potential within the subglacial channels. Kavanaugh and Clarke (2000) carried out a series of experiments to improve our understanding of pressure changes within subglacial water systems. They proposed that pressure pulses could be generated by abrupt glacier motion that either compresses or dilates the hydrological system. Consequently, the high degree of melting and collapse of ice cauldrons in a geothermal region of ice could lead to the production of pressure pulses with melt water. Kavanaugh and Clark (2000) suggested that the pulses would result in rapid transfer of pressure from one area to another possibly leading to the propagation of fractures in the basal region of the ice. Much of the glacial melt water flows through englacial channels rather than along the bedrock surface except in extreme floods, where the ice is floated (Björnsson 1974; Bennett and Glasser 1996).

Roberts et al. (2000) suggested that rapid increases in water discharge generate basal hydraulic pressure in excess of ice overburden, leading to floodwater being forced through propagating fractures onto the surface. Bennett and Glasser (1996) suggest that basal hydraulic pressure is controlled by four main variables: glacier thickness;

melt water supply rate; discharge rate through the channels, and the underlying geology, in particular its permeability. Research on jökulhlaup hydrodynamics in Iceland has shown those shear fractures in shallow ice, result from hydraulic fracturing, i.e. uplift of certain sections of ice (Roberts et al. 2000). The fractures then propagate into thicker ice and Roberts et al. (2000) suggested that the reason for increased flow at the beginning of a jökulhlaup is because of mechanical failure of the ice as opposed to increased melting. Consequently both heat transfer and hydraulic pressure are important in the role of ice melting and water transport.

Englacial conduits i.e. those within the ice, as opposed to beneath it, are oriented perpendicular to surfaces of equipotential pressure and can be classed into two main groups, branching channels and linked cavities (fig. 2.5). Branching channels are known as Röthlisberger Channels (or R-channels). They cut upwards into the ice and tend to be seasonal with the main development in spring increased by surface ablation, then they collapse in winter when melt water volume is reduced (Fountain and Walder 1998). R-channels are enclosed branching networks, with glaciostatic pressures in water filled sections. In close proximity to the edges of ice sheets the pressure can be close to atmospheric due to the combination of melt water and air. Linked cavities or Nye channels are eroded into the bedrock and shaped by local weaknesses that are enlarged by water flow. They are anastamosing, irregular in shape and generally persist throughout the year (fig. 2.7). However due to their irregular shape they are inefficient water carriers (Bennett and Glasser 1996). Under equilibrium conditions R-channel water pressure decreases with increasing discharge because water flux is in equilibrium with channel enlargement. If water conduit pressure exceeds hydraulic

pressure it will force water to spread into the linked cavity system (Roberts et al. 2000).
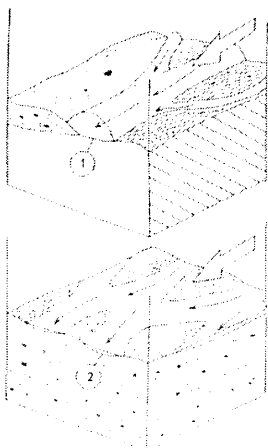
Fig 2.7 Schematic diagram of subglacial drainage systems. Depending on whether the glacier bed is rigid or deformable different types of subglacial drainage systems can be developed.

1. Dendritic network (e.g. R-channels and N-channels)
2. Braided canal network

Taken from (Nye 1976).

Nye (1976) suggested that tunnel enlargement could be explained by melting of ice walls by frictional heat generated by flowing water. His research also indicated that discharge increases with time if the overburden closure is slow and expansion of ice tunnels is due to transfer of frictional heat. Björnsson (2002) suggested that with the assumption of instantaneous heat transfer, water would emerge at the glacier outlet at melting point (0°C). This has been observed in Icelandic jökulhlaups. However, for large floods where water pressure exceeds ice overburden Björnsson (1974, 2002) suggested that the ice is lifted and a sheet flow occurs. Bennett and Glasser (1996) believed that flotation required special circumstances. Their work showed that for the 1996 Gjalp eruption, after drainage, the ice dam returned and the tunnels closed due to ice deformation allowing a subglacial vault to refill until water again reached a critical depth, creating a periodic process. They also indicated that many subglacial lakes appear to drain before the necessary depth for flotation is achieved. Consequently other processes may be involved. The hypotheses put forward by Bennett and Glasser (1996) were that the existing tunnels beneath the Grímsvötn dam were enlarged due to friction during the 1996 Gjálp eruption, or that seismicity damaged the dam.

2.5.6. Volcanic crater lakes

Energy budgets from volcanic crater lakes have been carried out as heat is obtained from the magmatic influx, or hydrothermal fluids, cycling through the lake system Oppenheimer 1997a). Hurst et al. (1991) suggested that heat transferred from a magmatic source at depth can be transferred via a pipe mechanism, and is commonly associated with geothermal systems. Heat is balanced in crater lakes by the input of hydrothermal fluids, precipitation, solar and atmospheric radiative with the output of radiative fluxes from the surface, seepage and overflow (Oppenheimer 1997a). Oppenheimer (1997a) compared bulk crater lake temperatures to surface temperatures and found a possible 13% error when averaging bulk lake temperature. The study concluded that it would be feasible to determine net heat fluxes directly from equations for measured surface skin temperatures. As remote sensing measures only the top layer of the lake it would therefore be possible to use this method for calculating thermal budgets from volcanic crater lakes.

Remote sensing is also used to determine observed water colour and temperature in crater lakes. Oppenheimer (1997c) showed that lake area and heat flux could be derived from Landsat TM imagery of lake colour and temperature. Apparent surface temperatures for an entire lake, are obtained by the inversion of Planck's formula (equation 3.1, section 3.3) leading to a more comprehensive assessment of heat flux (Oppenheimer 1996). A subglacial lake is further complicated by surrounding ice, but heat flux studies of the Grímsvötn caldera lake (Björnsson et al. 1982, Björnsson 1983, Björnsson and Guðmundsson 1993), have shown that even with surrounding ice, it has been possible to determine thermal budgets over a number of years.

2.5.7. Calorimetry and heat flux

Björnsson (1983) showed that Grímsvötn, Iceland, could be used as a calorimeter to estimate heat flow from a geothermal area. The ice sheet covered and insulated the thermal area, stopping heat from escaping to the atmosphere. Therefore any ice melted was a measure of the heat released by thermal activity at the glacier base (Guðmundsson 2003). Björnsson's (1983) work on magma input rates and volume of ice melt, showed that the heat flux of the Grímsvötn drainage basin area was in the order of 5000 MW but declined to 4000 MW from 1850 to 1900 (fig. 2.8). Björnsson (1983) suggested this was due to an increase in the extraction of water penetrating the hot rock boundary of magma at shallow depth. Since 1850, four peaks in heat flux observed were above the base level of 5000 MW. Björnsson (1983) believed these peaks in heat flux were related to unusual jökulhlaups accompanied by volcanic activity. Björnsson's (1983) work concluded that 70% of ice melt was due to geothermal heat, with only 10% due to the intrusion of magma resulting in atypical increases in heat flux during eruptions.
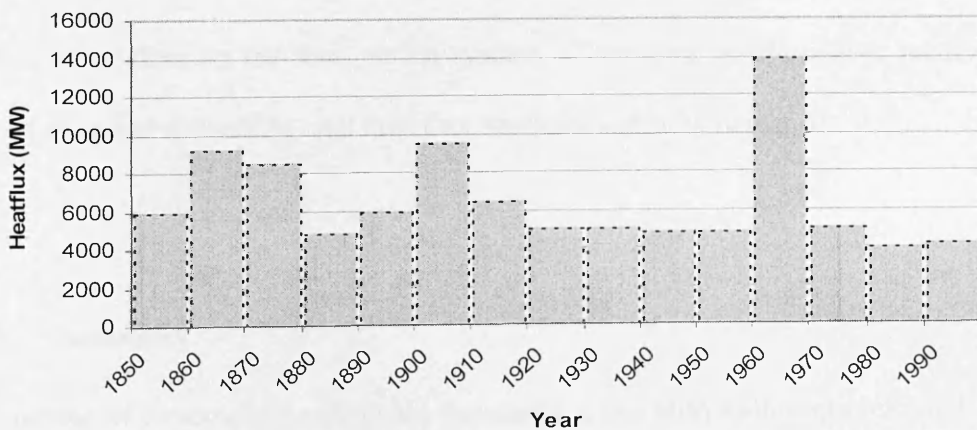
Fig. 2.8 graph of heat flux's derived from Grímsvötn jökulhlaup episodes (Björnsson 1983), showing base heat flux of approximately 5000 MW.

Due to the inaccurate records of jökulhlaup discharge, Björnsson and Guðmundsson (1993) followed up Björnsson's (1983) study by looking at thermal output during the intervals between jökulhlaups. However the extent of the geothermal area was difficult to delimit, and this affected the heat flux measurements. For the 1996 Gjálp eruption, the volume of depressions in the ice surface, coupled with melt water accumulation at Grímsvötn, were used to calculate heat transfer rates using calorimetry. The calculated heat flux was $5\text{-}6\text{x}10^5$ W m^{-2} (Guðmundsson et al. 2004), which was too high to be explained by pillow accumulation (Höskuldsson and Sparks 1997). Thus fragmentation was the most likely eruption mechanism, which was later supported by gravity surveys (Guðmundsson and Milsom 1997, Guðmundsson et al. 2002). In recent years leakage of water through the ice dam at Grímsvötn has made the use of ice melting calorimetry problematic. Moreover at the 1998 eruption site, heat has been lost directly to the atmosphere through small lakes. Consequently, calorimetry can no longer be effectively used at Grímsvötn. However temperatures recorded from crater lakes or ice cauldrons are still fundamental in monitoring Grímsvötn, as precursory evidence of subglacial eruptions is often shown in the melt water rather than on the rock or ice surface. Therefore an alternative method for monitoring and estimating total heat flux would be useful (Chapter 6).

2.6.   Summary

A number of ice-covered volcanoes, especially those with valley glaciers and small summit ice caps, are near populated regions (Cronin et al 1996, Hoblitt et al 1998). Moreover, in some cases most of the volcanic edifice may be concealed beneath hundreds of metres of ice (Björnsson 1974, 1988). Temperate glaciers are at their

pressure melting temperature throughout their thickness, and water can migrate underneath the glacier allowing melt water to flow from the eruption site to the edges of the glacier causing devastating floods known by the Icelandic term, jökulhlaups (Björnsson 1974, Smellie 1999).

In conclusion this chapter has shown that there are many processes involved with subglacial volcanoes, but a key feature is heat flux. Increased heat leads to increased melting, which in turn causes jökulhlaups. Focusing research on thermal energy emitted from subglacial volcanoes would be beneficial for predicting jökulhlaups. Although there has been substantial work on heat flux from Grímsvötn, because it can no longer be used as a calorimeter alternative methods of calculating total heat flux need to be investigated. This study aims to test an alternative methodology (chapter 6).

Active subglacial volcanic eruptions cannot be studied using traditional field based methods, because of poor accessibility and hazardous terrain. Remote sensing offers a potential method for monitoring subglacial volcanoes.

Chapter 3 – Principles of Remote Sensing and Photogrammetry: Applications in Volcanology and Terrain Analysis

3.1. Introduction

Remote sensing is the term used for any observation or measurement of an object without directly being in contact with it (Curran 1992). It is often used to refer to the observation of the Earth using the reflectance or emittance of electromagnetic energy. This chapter will discuss the principles behind remote sensing, specifically for areas composed of bare rock, ice and water, as found at Grímsvötn in Iceland. This chapter also provides a review of the literature on how remote sensing has been used to monitor volcanoes along with icy environments. The ultimate goal of monitoring volcanoes is to predict eruptions and their related hazards. Many of the world's active and potentially active volcanoes are in highly populated developing countries that lack the financial or scientific resources required for adequate regular in situ monitoring (Oppenheimer & Rothery, 1991). Added to this is poor accessibility on most volcanoes making it difficult to mount field-based surveillance (Rothery et al. 1988). Remote sensing offers a low risk method for monitoring volcanoes with a potential for global coverage, allowing the study of a range of phenomena such as thermal and topographic variations over space and time (Oppenheimer & Rothery 1991).

3.2. Electromagnetic Spectrum

Remote sensing is based upon the detection of electromagnetic energy, which is transmitted from an object to a sensor (Elachi 1987). Electromagnetic radiation can

be conceptualised as transverse waves consisting of electric (E) and magnetic (M)

fields (Gibson 2000). Electromagnetic radiation is classified into a number of spectral

regions based on wavelength or frequency. These regions are grouped together and

known as the Electromagnetic Spectrum (fig. 3.1)
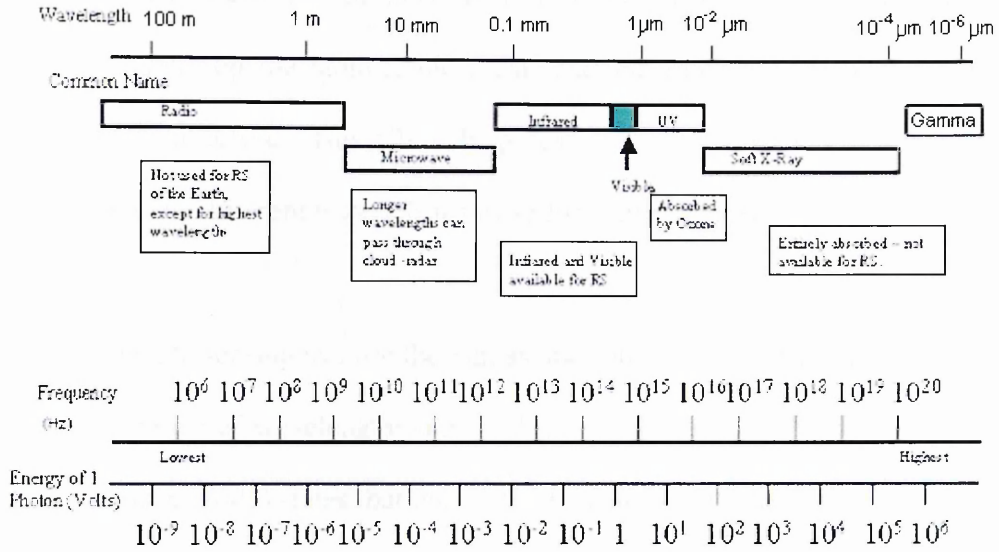
Fig. 3.1 The Electromagnetic Spectrum (taken from Elachi 1987; Mather 1999; Lillesand et al. 2004).

An imaging sensor, whether satellite, airborne or ground based, is sensitive to

upwelling radiation recorded as a series of pixel values known as digital numbers

(DN). The number is proportional to the amount of radiation received in a particular

wave band (Rothery et al. 1995). Many imaging sensors acquire several images of the

same area in different wave bands or channels, resulting in a 'multispectral' image

(Rothery et al. 1995). As electromagnetic radiation interacts with matter the electrons,

molecules or nuclei are put into motion, which leads to an exchange of energy

between the wave and the material (Elachi 1987). The radiation may be reflected,

scattered, absorbed or transmitted depending on the wavelength, angle of incidence

and roughness of the surface. Gibson (2000) states that in reality a combination of all

these processes actually occur. A surface that reflects all incident energy at the same angle is known as specular, and one that scatters all the energy in a number of different directions (isotropically) is a Lambertian surface. In nature no surfaces are of either extreme, but the more Lambertian a surface the more useful it is for remote sensing (Gibson 2000). The radiometric response of different materials in different bands depends on the atomic, molecular and macromolecular composition of the object being observed. This offers the potential of using different band combinations to discriminate different materials using multispectral imagery.

Passive remote sensing can use the Sun as one source of EM radiation. Energy across the entire range of wavelengths travels through the vacuum of space at the speed of light. Gibson (2000) states that only 5×10^{-9}% of the solar radiation actually reaches Earth (the rest is scattered through the atmosphere), but the proportions in each spectral range remain constant. Much of the energy is then absorbed or scattered in its passage through the atmosphere, leaving only regions of low absorbance such as areas of the visible and infrared to pass through zones known as atmospheric windows (Cracknel & Hayes 1991; Lillesand et al. 2004). This makes the visible and infrared bands the most useful for remote sensing (fig. 3.2).
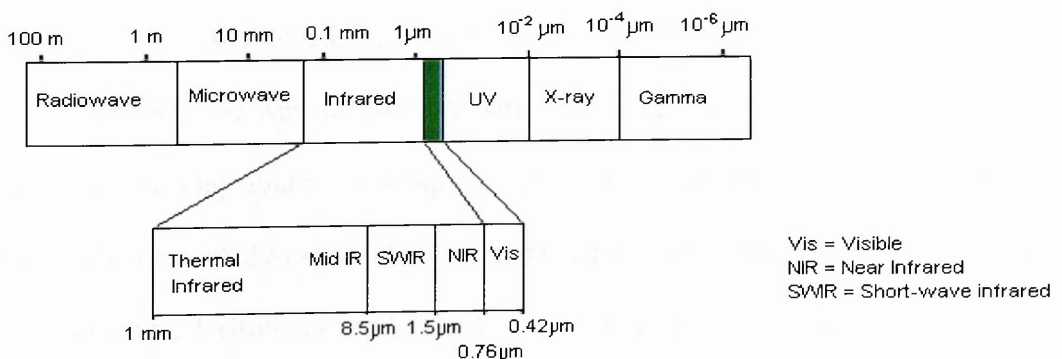
Fig. 3.2 shows a diagram of the wavelengths of the visible and infrared regions of the electromagnetic spectrum, including in detail the division of the infrared region (Cracknell & Hayes 1991).

Infrared energy can also be emitted directly from the Earth's surface. Emitted thermal energy is due to vibrations and rotational motions at the atomic level, i.e. heat energy is produced from the kinetic energy of the random motion of particles and hence collisions (Rees 1999; Lillesand et al. 2004).

3.3. Thermal Emission

Radiance is one of the most important terms used in remote sensing, as it describes what is actually measured by the sensor. It is defined as the total energy radiated over a unit of area and a solid angle of measurement. Spectral exitance is the total energy radiated in all directions by a unit area in a unit time (Curran 1992). Renz (1999) defined a blackbody as a theoretical object that absorbs all the radiation incident upon it, reflecting none. Likewise Gibson (2000) defined a blackbody as an object that emits the maximum radiance across all wavelengths possible.

The Earth is often modelled on blackbodies. Max Planck derived a formula for the spectral exitance that a blackbody should have. Planck's spectral exitance equation is:

$$M_\lambda = C_1 \lambda^{-5} \left[\exp\left(C_2 / \lambda T \right) - 1 \right]^{-1} \tag{3.1}$$

where M = blackbody spectral exitance (Wm^{-3}), C_1 = 3.74 x 10^{-16} W m^2, C_2 = 1.44 x 10^{-2} m K, λ = wavelength in metres, and T = blackbody temperature (K). The formula describes the wavelength distribution of energy radiated from a surface as a function of its temperature. The upwelling radiation recorded as a digital number (DN) can be converted to spectral radiance related to temperature by Planck's formula using equation 3.1 (Rothery et al. 1988). By measuring spectral radiance at a given wavelength, surface temperatures can be calculated through inversion of the formula (Wright et al. 2000b).

Dozier (1981) manipulated the Planck function to look at different surface temperatures providing a method that could be used for looking at regions of high geothermal activity and has become the basis of all thermal monitoring techniques since. The spectral distribution of radiated energy from a blackbody surface at various temperatures can be shown as a spectral exitance curve (fig. 3.3). The area under the curve gives the total radiant exitance coming from the surface of a blackbody (Dozier 1981; Rees 1999; Lillesand et al. 2004). Curves of radiance against wavelength derived from Planck's formula show the greatest change in spectral radiance between 300 K and 1400 K occurs between wavelengths of 1-3 μm, the short wavelength infrared regions (Rothery et al. 1995). Hence short-wave infrared is useful for detecting high temperature anomalies, but thermal infrared bands are useful for detecting lower temperatures, those just above 'normal' environmental temperatures (Dozier 1981; Rothery et al. 1995).
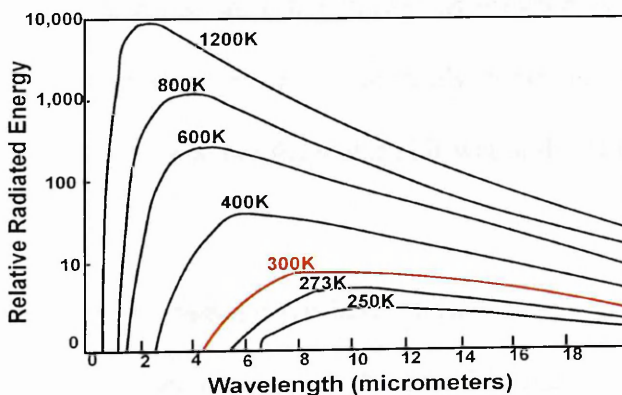
Fig. 3.3 graph to show the spectral radiance emitted by a blackbody at different temperatures according to Planck's formula. Graph taken from Rothery et al. (1995). The area under each curve is the total radiance emitted at the given temperature, showing the greater the temperature of a blackbody, the greater the total amount of radiation it emits at all but particularly lower wavelengths.

However, real materials do not behave as blackbodies, as they emit only a fraction of the energy emitted from a blackbody at the same temperature, but are instead termed 'greybodies' which emit a proportion of the energy they receive (Curren 1992; Lillesand et al. 2004).

3.4. Using Remote Sensing to Measure Emissivity.

Knowledge of radiance or exitance is not sufficient to characterise an object or its temperature. The emitting ability of a real material as compared to a blackbody is a material's emissivity (Renz 1999, Lillesand et al. 2004). Emissivity is the ratio of radiant exitance in proportion to a perfect emitting surface, a blackbody.

$$\varepsilon(\lambda) = \frac{M_\lambda(materialK)}{M_\lambda(blackbodyK)} \qquad (3.2)$$

In order to calculate accurate temperatures from remotely sensed radiance measurements, it is important to have accurate emissivities for each land surface type to be analysed. Emissivity values range from 0 to 1 and vary with wavelength, viewing angle and temperature. Many materials such as water radiate like a blackbody in certain wavelengths. The 8 -14 μm range includes an atmospheric window and is the area of peak energy emissions for most surfaces at normal Earth surface temperatures (Kahle & Alley 1992; Lillesand et al. 2004). Therefore land surface materials are often treated as greybodies in this wavelength range. Close examination of Earth surface materials shows that emissivity can also vary with other conditions i.e. whether the material is wet or dry (Liang 2001; Lillesand et al. 2004).

A number of studies have been carried out to show that emissivity can be directly determined from some remotely sensed images (Kahle & Alley 1992; Kealy & Hook 1993; Wan et al. 1994; Barducci & Pippi 1996; Schmugge et al. 1998; Liang 2001; Buongiorno et al. 2002; Schmugge et al. 2002; Sobrino et al. 2002). All of the studies involved multispectral imagery with more than one band within the thermal infrared region (fig. 3.2). The earlier work showed that, in order to determine accurate temperatures and emissivities, corrected radiance measurements were necessary, and

this required atmospheric corrections across the image. Kealy and Hook (1993) stated that variations in emissivity were related to differences in composition, and their study concentrated on the comparison of a number of methods for extracting emissivities from multispectral data. Liang (2001) showed that an error of only 0.01 in emissivity could cause an error twice that due to atmospheric attenuation; therefore it could be argued that an accurate emissivity value is more important than atmospheric correction.

3.5. Interaction of EM Radiation with Water

Water has a high reflectance at all visible wavelengths but it increases as wavelength decreases (Curran 1992). The majority of radiant flux (total energy radiated in all directions), incident upon water is absorbed or transmitted (Drury 1993). Pure clear water has a high specular reflectance in the visible range (0.4-0.6 μm) but high absorbance in the near infrared above 0.7 μm; hence it appears black on infrared images. Shorter wavelengths can penetrate water bodies to a greater depth, allowing the colour and nature of the bed material to be observed (Gibson 2000). However, for depths greater than 40 m water bodies appear dark as all radiant energy is absorbed (Drury 1993). Scattering due to suspended particles can affect imagery, and is useful depending on the objectives for using remote sensing. Surface roughness is another factor that affects the variability of reflectance (Mather 1999). In the near infrared, water acts as a near perfect blackbody, absorbing almost all incident energy, then emitting almost all in the thermal infrared, allowing surface temperatures to be calculated, as emissivity can be assumed to be one (Drury 1993).

3.6. Interaction of EM Radiation with Rocks.

The interaction of electromagnetic radiation with rocks is controlled by the properties of the constituent minerals, leading to a relationship between rock spectra and chemical composition (Sabine et al. 1994). It was the Landsat 1 Multispectral Scanner (MSS) imagery that first attracted the attention of the geological community (Goetz & Rowan, 1981). Image analysis of rocks has concentrated on topography, erosion and drainage features, thermal anomalies and colour related to mineralogy (Lillesand et al. 2004). Van der Meer (1999) gave a good overview of geological remote sensing, stating that the spectral properties of minerals are required in order to determine the reflective properties of rocks. The dominant factors affecting the spectra of minerals are the distinctive rare ions within their molecular structures (Drury, 1993). Reflectance spectra obtained via laboratory experiments, show that minerals such as quartz and feldspar have a high reflectance. Hence rocks like granite, rich in those minerals, are pale and basalts rich in olivine and pyroxene are dark due to low reflectance spectra (Gibson 2000). Some minerals are characterised by absorption bands at particular wavelengths due to elements within their crystal lattice. Silicate mineral reflectance spectra are dependent on the ions within the crystal lattice whose absorption features vary with wavelength as bond strength changes (Sabine et al. 1994).

The determination of the composition of a rock is further complicated by surface weathering which has its own distinctive spectra. Since the visible and near infrared parts of the spectrum interact with only the outer 50 μm of the surface (Mather, 1999), the spectral properties of fresh minerals rarely affect the reflected radiation used in remote sensing (Drury 1993). Kirkland et al. (2002) emphasised that ground truth

data are essential for interpreting spectral data from land surface types, especially as materials that have weathered or rough surfaces will have different spectral signatures. Examples include iron rich rocks that are hydrothermally altered (Gibson 2000).

Sabine et al. (1994) showed that silicates, particularly quartz, influence the thermal spectra of rocks in the 8-14 μm region of the EM spectrum. With the advent of the Thermal Infrared Multispectral Scanner (TIMS), spectral emittance data, especially for silicates, has been obtained from the thermal infrared wavebands (Kahle & Goetz, 1983). Iron is another important mineral, creating a distinctive absorption band in the visible and near infrared (0.7 and 0.9 -1.0μm). Infrared energy is useful in geological applications for providing bulk mineralogy, dependent on multiple thermal bands, or temperatures, if based on a single thermal band (Van der Meer 1999). An example of the problems involved with remote sensing of rocks, was described by Crisp and Bartholomew (1992) who undertook a number of experiments to look at the possibility of using mid infrared spectroscopy for remote sensing of the Martian land surface. They wished to determine the influence of dust covering igneous rocks and found that even a small amount of ash significantly reduced the spectral emittance of the underlying rock, making it difficult to use remote sensing for identification of rock types covered by dust. Added to this, their experiments were carried out at a constant temperature with no thermal gradient as may be found in the field, particularly in a geothermal region on Earth (Crisp and Bartholomew 1992).

Hyperspectral sensors or imaging spectrometer are instruments that acquire images from very narrow spectral bands through the visible, near and thermal infrared wavebands of the electromagnetic spectrum (Rees 1999; Lillesand et al. 2004). These

systems can discriminate between surface features that have diagnostic absorption and reflectance characteristics that can be lost in the wider bands of multispectral imagery. The Compact Airborne Spectrographic Imager (CASI) is an example of an airborne hyperspectral scanner (NERC ARSF User Manuel 2002b). By using spectral angle mapping it is possible to get a qualitative estimate of the presence of absorption features, which can then be related to mineralogy (Van der Meer 1999).

3.7. Photogrammetry

Photogrammetry is the science of obtaining reliable information about physical environments through interpretation of photographic images (Wolf & Dewitt, 2000). With the increased use of satellite and airborne sensors, photogrammetry has now diversified from simple photographic interpretation (Wolf 1983; Lillesand et al. 2004). The most common use of photogrammetry is for topographic mapping, and with the advent of more sophisticated technologies, orthophotos and digital elevation models (DEMs) are increasingly been used. Wolf and Dewitt (2000) defined orthophotos as aerial photographs, with a uniform scale, producing a map with actual features as opposed to lines and symbols. They also defined DEMs as numerical representations of topography.

Before any image processing is carried out suitable photographs must be acquired. The area of interest is photographed from a plane at a constant height and speed on a series of overlapping flight lines, so that each stripe overlaps by 40% (lateral overlap) as shown in fig. 3.4.
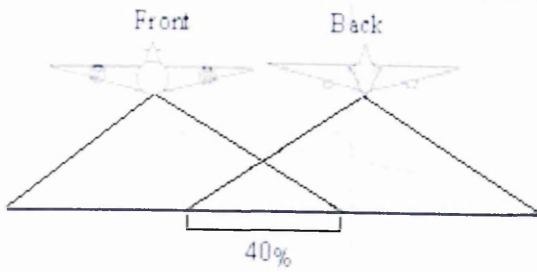
Fig. 3.4 Diagram to show lateral overlaps of aerial photographs. (Blair 1974)

Along flight lines, photographs are taken at frequent intervals so that successive photographs overlap by 60% (fig. 3.5). The time interval between exposures depends on the altitude and speed of the aircraft (Blair 1974).
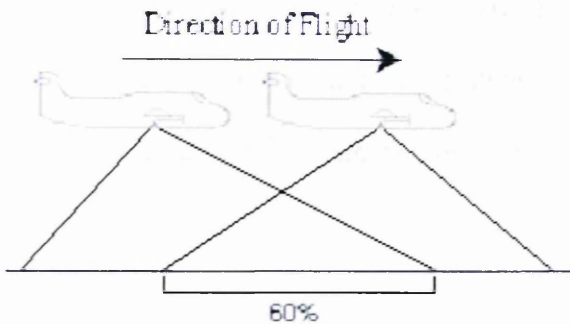
Fig. 3.5 Diagram to show longitudinal overlap of aerial photographs. (Blair 1974)

Vertical photographs are those acquired by a camera aimed directly at the ground surface from above. As the geometrical properties of vertical or near vertical photographs are well established, they form a useful basis for making accurate measurements such as deriving estimates of topographic elevation (Blair 1974).

Aerial cameras are manufactured to include adjustable index marks attached to the camera that are recorded on the photograph during exposure. These are known as fiducial marks (fig. 3.6), and they occur at the sides and corners of a photo. Lines connecting opposite fiducial marks intersect at the principle point or optical centre of the photograph (Wolf 1983).
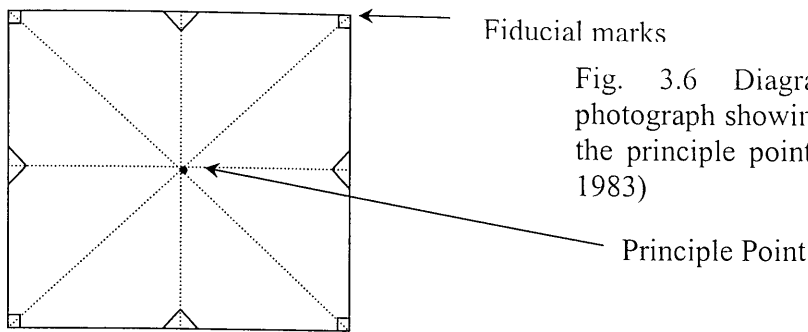
Fiducial marks

Fig. 3.6 Diagram of an aerial photograph showing fiducial marks and the principle point. (Taken from Wolf 1983)

Principle Point

The nadir is the point on the ground vertically beneath the centre of the camera lens (Rees 1999). On a truly vertical picture the principle point and photographic nadir will coincide. However, due to effects of tilt this is unusual and there are often geometric errors or distortions in the vertical photograph such as scale variations and relief displacement (Wolf and Dewitt 2000). Objects positioned directly beneath the centre of the camera lens are photographed so only the top of the object is visible (central object in fig. 3.7).
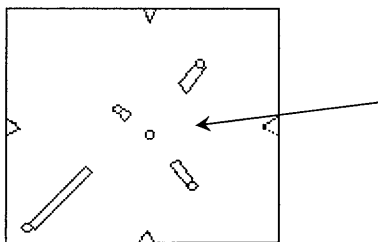
Fig. 3.7 Objects directly beneath the camera show no distortion as it they are in the centre of the photograph. (Blair 1974).

All other objects are positioned so their tops and sides are visible, i.e. these objects appear to lean away radially from the principle point. For tall objects it is clear that the base and top cannot both be in their correct orientation (Wolf and Dewitt 2000). The amount of displacement depends on the height of object and the distance of the object from the nadir.

Atmospheric effects causing refraction of light before entering the camera followed by rays being deflected by the lens aberrations within the camera as well as during the

film processing stage all produce significant distortions. For analysis of aerial photographs Zuidam (1986) stated a number of assumptions that have to be made. These include:

1. intersection of the line joining opposite fiducial marks defines the principle point,

2. lens distortions either do not exist or have been allowed for,

3. film shrinkage does not exist or has been allowed for, and

4. atmospheric refraction does not exist, or is minimal and has been allowed for.

3.8. Stereoscopy

Stereoscopic or binocular vision is the facility that makes it possible to visualise objects in three dimensions, also known as stereoscopy. Put another way, stereoscopy allows for depth perception (Wolf & Dewitt 2000). This can be achieved by looking at an object from two different positions, which results in a pair of images known as a stereopair. An aerial camera collecting overlapping photos at regular intervals, obtains a record of positions of exposure (Wolf 1983). The change of position of an object from one photo to the next caused by the aircraft motion is called the stereoscopic parallax, i.e. parallax is the apparent displacement in the position of an object in neighbouring photos, caused by a shift in the position of the observation (Wolf & Dewitt 2000). For example fig. 3.8 represents the acquisition of stereopairs, and shows the stereoscopic parallax caused by a change in elevation.
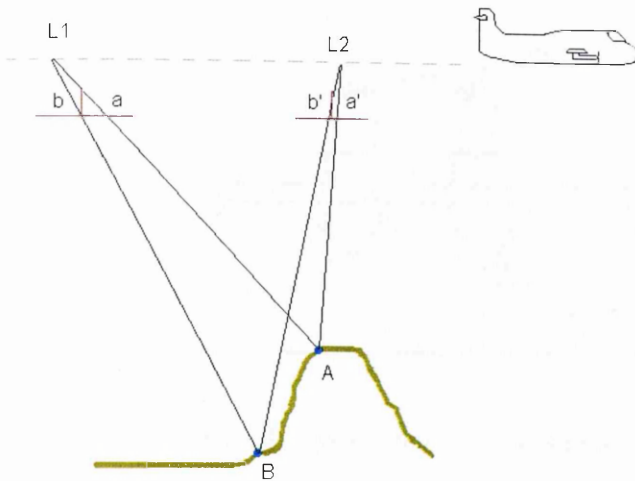
Fig. 3.8 Diagram to show the acquisition of height information from aerial photographs using stereopairs and parallax.
(Taken from Lillesand et al. 2004)

The example in fig. 3.8 shows object points A and B, on overlapping photographs that were collected at exposure locations L1 and L2. On the left photo, points A and B are represented by a, b, but as the aeroplane moved between the exposure locations, the points are represented by a', b'. Movement on the image is greater for point a, meaning that object A has the larger parallax. Wolf and Dewitt (2000) showed that stereoscopic parallax is greater for objects at higher elevations, and hence that parallax is directly related to elevation. Therefore it is possible to determine elevation using stereo photography.

By carefully overlapping the photographs the two-dimensional view in each photograph can be blended and a three-dimensional image of the group appears (Campbell 2002). Stereoscopic 3D images can be seen using stereoscopes (fig. 3.9) and elevations can be manually deduced using the parallax relationship.
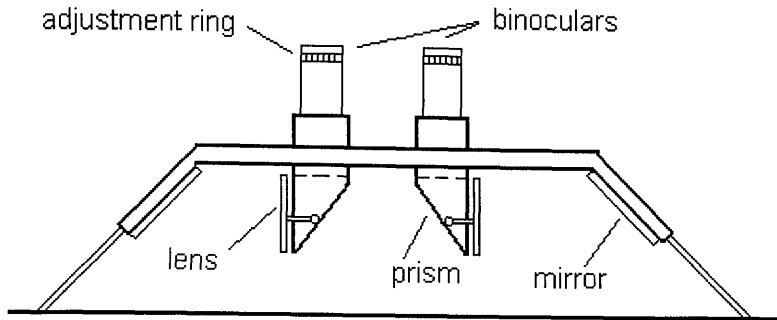
Fig. 3.9 Diagram of the mirror stereoscope (diagram by S.Stewart)

With the widespread use of remote sensing and GIS, photogrammetry has altered, from manual measurement to producing maps directly from digitised stereopairs (Wolf and Dewitt 2000). This allows data to be in digital format that can then be used in a range of ways within a GIS environment.

3.9. Remote Sensing of Snow and Ice

Snow is one of the most reflective natural surfaces in the visible part of the spectrum but reflectance decreases with increasing wavelength in a similar way to water (Drury 1993). Reflectivity of snow is dependent on grain size, shape, surface roughness, impurities and water content (Hall & Martinec 1985). Hence, as it ages, the reflectivity decreases due to compaction, melting and refreezing, and the addition of impurities (Vincent 1997). Therefore as the crystal lattice structure is changed over time, reflectance properties between water, snow and ice, become dependent on their state of matter (Bohren and Barkstrom 1974). Ice has a similar spectral response to snow except for reduced visible reflectance due to compacted ice crystals. However it could be covered by snow thus increasing its reflectivity or impurities within the ice, such as volcanic ash, reducing reflectance in the visible wavelengths (Drury 1993). Within the thermal infrared wavebands, crystal size and water content affect apparent

temperatures (Hall & Martinec 1985). However, in cold regions, contrasts in temperature between ice and water are small, so thermal infrared radiation is not the best way of distinguishing between them (Rees & James 1992), except in the detection of new ice. Rees and James (1992) stated that new ice layers would show a different apparent temperature due to internal structure and reduced snow cover.

The majority of remote sensing work on snow has concentrated on the calculation of snow cover area and ablation rates (Engman & Gurney 1991; Nolin and Dozier 2000; Hodgkins 2001). Nolin and Dozier (2000) used Landsat Thematic Mapper (TM) data to further study ablation rates. They showed that imaging spectrometry data in the near infrared could successfully map grain size of snow, without the effects caused by topography and solar elevation. However they pointed out that dirty snow with >1% by weight of dust will reduce the effectiveness of retrieving grain size. Hodgkins (2001) measured mass balance fluctuations along a glacier snout of Langjökull, Iceland, using aerial photography.

Hyperspectral sensors, such as the Airborne Visible Infrared Imaging Spectrometer (AVIRIS) are increasingly being used to model snow cover area and grain size (Painter et al. 2003), because of the larger spectral capabilities. Other work has involved studying ice elevation changes, especially in relation to geothermal activity beneath the ice. In 1999, Bacher et al. carried out an aerial survey of Vatnajökull ice sheet, Iceland, in order to record accurate elevation changes of the ice surface after the 1996 Gjálp eruption.

Motyka et al. (1978, 1980) determined heat flow by measuring the volume of ice

melted at the summit of Mount Wrangell, Alaska. Benson and Follett (1986) followed

up the research by measuring heat flux from the glacier ice melt from Mount Wrangell

caldera, using a similar technique.

3.10. Applications of Remote Sensing in Volcanology

The launch of Landsat 1 in 1972, initiated the modern era for remote sensing of

volcanoes (Francis and Rothery 2000). Many of the early satellites had no specific

objectives for observing volcanoes but some of their sensors proved useful. Francis et

al. (1989) argued that changes in radiation emitted over time, could be a valuable

monitoring technique, and this has led to the use of remote sensing in hazard

mitigation. It was not until the launch of Terra (Earth Observing Satellite AM-1) in

late 1999, that sensors specific to the study of volcanoes were available (Francis and

Rothery 2000). Terra is concerned with global climate change and environmental

issues. However, various volcanological observations had been made prior to its

missions. The earliest observations indicated the way in which remote sensing and

satellite imagery could benefit science by providing data on remote volcanoes as well

as the more accessible ones (Francis and Rothery 2000).

Sea surface temperature changes of 1°C have been commonly observed since the

earliest meteorological satellites were deployed. However sea surface temperatures

are locally homogenous (Francis & Rothery 2000). Volcanoes generate

heterogeneous anomalies at far higher temperatures than the early sensors were set to

detect. Volcanoes emit detectable radiation across the visible to thermal infrared parts

of the electromagnetic spectrum. Lavas above 1000°C are the obvious phenomena that indicate current volcanic activity, but others include fumaroles emitting gases, pyroclastic deposits, ash columns and lakes of hot water ponded in craters (Harris et al 1995).

Harris et al. (1997) demonstrated the usefulness of Advanced Very High Resolution Radiometer (AVHRR) in monitoring Etna, Krafla, Cerro Negro, Fogo, Lascar and Erebus. They showed that the frequency and real time monitoring capabilities of the AVHRR provided a useful tool for monitoring changes in eruption activity. Thermal data could also be extracted for active lava flows, lakes, pyroclastic flows and active vents. Radar has also been used to look at lava flow textures, topography and deformation of volcanic edifices (Oppenheimer 1997a). Radar has advantages over other remote sensing, as it is an active rather than passive sensor, so can be used at any time of day or night and the microwave radiation used will penetrate clouds. Although radar proves a useful tool, the retrieval of quantitative data requires sophisticated computer processing and an understanding of atmospheric water vapour on microwave transmission (Francis & Rothery 2000). Wadge et al. (2005) have shown the usefulness of a dual mode radar and radiometer called AVTIS (All-Weather Volcano Topography Imaging Sensor). AVTIS was designed to image the distance to lava domes on volcanoes obscured by cloud. It allows thermal and terrain mapping that would otherwise be impossible using other remote sensing methods.

Eruption clouds have also been studied using remote sensing because of potential dangers to aircraft (Sparks et al. 1997). Sparks et al. (1997) stressed the importance of discriminating between volcanic and atmospheric clouds. Injection of eruption clouds

to heights of many kilometres can occur within a few minutes. Long haul flights with limited fuel have few options for diversions. Consequently timely warnings are needed in order to avoid catastrophic engine failure and save lives. During the late 1970s and 1980s the study of volcanic clouds was undertaken using direct sampling methods. With the onset of new technology and sensors such as AVHRR, ATSR (Along Track Scanning Radiometer), and GOES (Geostationary Operational Environmental Satellite), with low spatial but high temporal resolutions, the composition of clouds can be analysed at regular intervals. Rose et al. (2000) retrieved data on the amounts of sulphur dioxide (SO_2), particle radius and mass of particulates in volcanic clouds. Their work related to a number of locations and showed that non-arc eruptions release higher SO_2 than equivalent magnitude eruptions from island arc settings. Sulphur dioxide plumes have been studied widely (Kyle et al. 1990; Anders & Rose 1995; Realmuto et al. 1997; Teggi et al. 1999; Rose et al. 2000) including at Mount Erebus, Antarctica, where SO_2 emission rates correlated with lava lake surface areas. Realmuto et al. (1997) used absorption of emitted radiance by a plume from Kilauea, Hawaii, to determine the concentration and thickness of sulphur dioxide gas. Anders and Rose (1995) gave a good overview of the work that has been carried out using remote sensing to monitor SO_2 clouds. Rose et al. (2000) also indicated that infrared satellite data offers a tool for the study of the transport of fine ash. Both GOES and AVHRR detectors can sense particles between 1 and 12 µm (Rose et al. 2000). This is useful as the larger ash particles fall out close to the eruption site, and it is the finer particles that are transported around the globe leading to climatic and possible health problems (Rose et al. 2000).

Remote sensing of the 1994 Rabaul volcano, Papua New Guinea showed that the eruption cloud contained large amounts of ice. Although the eruption occurred near the sea, and seawater was used to explain the volume of ice, water can also exist due to entrainment of moist air that rises with the eruption column, condenses and freezes. The volume of ash containing ice explains why volcanic ash clouds often have lower temperatures than expected. Rose et al. (2002) describes the particles as icy ashballs, as they still have a spectral signal of ash. In many mid latitude locations the ice observed by satellite would be melted and not be preserved in the deposited ash fall. However at high latitudes, such as the 1963 Surtsey eruption, icy pyroclasts known as hydrometeors where observed (Decker & Decker 1996). Analysis of infrared remote sensing measurements has improved our understanding of the meteorology of such eruption clouds. This is especially useful as there are many volcanoes near oceans and lakes where latent heat can assist in the entrainment of water into the eruption column. Rose et al. (2000) suggested that, when hydrometeors are dominant, eruption clouds could resemble huge thunderstorms or hurricanes.

High surface temperatures and size make lava flows difficult and hazardous to approach. An increasing number of studies are using remote sensing techniques to understand flow and temperature regimes (Oppenheimer & Rothery 1991, 1997a; Harris et al 1995, 1997; Wright et al. 2000a, b; Aries et al. 2001; Pinkerton et al. 2002). Wright et al. (2000b) showed how a series of Landsat Thematic Mapper (TM) images could provide information about emplacement and evolution of a lava flow field produced during the 1991-1993 Mount Etna eruption. They also showed that by combining the data with elevation information in the form of a digital elevation model (DEM), the effect of topography on flow regime and structure could be assessed.

In 1999, EOS (Earth Observing Satellite) was launched. On board was a moderate resolution imaging spectro-radiometer (MODIS), the latest space based sensor capable of low spatial resolution but high temporal resolution data acquisition (Wright et al. 2002). MODIS has become the basis of a global volcanic monitoring system, able to detect a range of volcanic thermal phenomena. Although it is able to accurately determine the volcanic origin of detected hotpots, the low spatial resolution and effects of cloud cover can still cause problems and show that MODIS is not an all encompassing monitoring system, but perhaps the most useful of the systems available at present (Rothery et al. 2003).

3.11. Measuring Radiant Heat from Volcanoes

As noted in section 3.3, Planck's law states that, as temperature increases, so does the amount of energy radiated, especially at shorter wavelengths. Hence short wavelengths are useful for measuring higher temperatures (Rothery et al. 1988). A sensor on board a satellite is sensitive to upwelling radiation that can be converted to spectral radiance, and subsequently to temperature, using Planck's formula (equation 3.1, section 3.3). Volcanic thermal phenomena are often small, high temperature features. A number of studies have been carried out using short-wave infrared (SWIR) areas of the EM spectrum. Glaze et al. (1989) used Landsat TM data to measure radiant energy flux from Láscar volcano, Chile, to show that remote sensing techniques may be used to monitor the activity of a volcano quantitatively, in a way that is not possible using conventional ground studies. A thermal anomaly was noted in July 1985 implying that Láscar was unusually active. This was subsequently confirmed by an explosive eruption in 1986. Glaze et al. (1989) believed that,

although a lava lake had been present, the thermal anomaly prior to the eruption was due to areas of intense fumarolic heating.

Rothery et al. (1988) categorised volcanic thermal phenomena into three main groups: low temperature, high temperature and lava-related effects. Oppenheimer et al. (1993a) established a way of determining each type, on remotely sensed images. For example, fumaroles are represented by individual small-scale, high temperature spots; lava flows appear as long narrow groupings of high temperature pixels; lava lakes are often nucleated pixels with higher temperature lines displaying active rifting. Oppenheimer et al. (1993a) used fumaroles to look at the use of infrared remote sensing for active volcanoes. Oppenheimer et al. (1993b) were able to document the evolution of a lava dome within the crater of Láscar volcano. By using both satellite and field based data, they were able to construct a chronology for dome activity. They showed that it was possible to determine the growth of a new dome before a field party could, especially as Láscar had poor ground monitoring at that time. Oppenheimer & Rothery (1991) showed that satellite and airborne data could provide basic information about the cooling of lava flows, but they were forced to simplify the thermodynamics of flows because of the limitations with the Landsat sensors used. However they found that the use of Short Wavelength Infrared (SWIR) was useful in distinguishing the high from the low temperatures found on the surface of the flow (fig. 3.1). Oppenheimer et al. (1993a) explained further that the distribution of thermal radiance between different wavelengths depends on the surface temperature and area, along with the spatial resolution of the imagery. For instance a large relatively low temperature (100°C) feature would be recorded in the thermal infrared (fig. 3.1), but be poorly distinguished in SWIR, whereas a small high temperature

feature would radiate well in SWIR but be undetectable in the thermal. Hence the reasoning behind studies of SWIR for high temperature volcanic features such as lava flows and active lava lakes.

Matson and Dozier (1981) devised a method for extracting variable temperatures across a pixel by using what is known as the 'dual-band method' (Rothery et al. 1988). The method utilises data from a multispectral scanner with more than one SWIR band. As the pixel area can contain more than one thermal anomaly, the ability to distinguish between the highest and lowest temperatures within that pixel are useful for volcanolgical studies (Oppenheimer 1991). Research using the dual band method has been used to understand high temperature anomalies on volcanoes (Dozier 1981; Matson & Dozier 1981; Oppenheimer 1991; Oppenheimer & Rothery 1991; Oppenheimer et al. 1993a). As the data for this research has only one thermal band, the dual band method will not be used.

Rothery and Oppenheimer (1994) used Landsat TM to study the thermal regime of Mount Erebus lava lake in Antarctica. Mount Erebus is well situated for TM coverage as near the poles it can be observed nine times within one 16-day cycle (Rothery and Oppenheimer 1994). Their study showed a crude estimate for surface temperatures and led to an increased interest in monitoring lava lakes using remote sensing techniques. Oppenheimer and Francis (1997) observed lava and fumarole emissions from Erta'Ale volcano in Ethiopia, using Landsat multi-spectral and thematic mapper images, to study fluctuations of magma level within a conduit. They found that remote sensing allowed for more than one parameter to be looked at simultaneously. Oppenheimer and Yirgu (2002) followed up this work using a small ground based

thermal camera to study the active lava lake, before comparing their results with the Landsat imagery previously analysed. The ground based results appeared to match expected hypotheses better than previous studies of radiant flux. Harris et al. (1999) used Landsat (TM) imagery of Mount Erebus, Erta'Ale and Nyiragongo and Pu'u 'O'o lava lakes to understand the mass balance fluctuations during normal activity. They found that determining whether periods of high flux were atypical events was difficult without regular observations. However they were able to estimate the rate of circulation within a lava lake without determining whether it was due to new magma intrusion or recycling.

Remote sensing is also used to determine observed water colour and temperature in crater lakes. Oppenheimer (1997b) showed that lake area and heat flux could be derived from Landsat TM imagery of lake colour and temperature. Apparent surface temperatures for an entire lake, are obtained by the inversion of Planck's formula (equation 3.1, section 3.3) leading to a more comprehensive assessment of heat flux (Oppenheimer 1996).

Rothery et al. (1992) used the Landsat TM images of the 1992 Etna lava flows in order to understand the behaviour of an active lava flow. Remote sensing allowed rate of effusion, slope steepness, flow form, temperature and viscosity to be studied. However they found there to be significant limitations with the imagery such as time of acquisition. The need for time series imagery caused delays as the repeat cycles produced some cloud covered imagery. The time needed to receive the imagery, and have it analysed added to the delays. However the largest problem was saturation in the short-wave infrared bands due, to the high temperatures of lava flows, meaning the

radiance emitted exceeded the maximum measurable signal of the detector (Wright et al. 2001), and hence reduced the ability to determine meaningful temperatures.

Harris et al. (1995) found that AVHRR data was a useful means of detecting and monitoring eruption activity during the 1984 Krafla eruption, Iceland. The temporal resolution permitted changes in intensity to be monitored over a fortnight. Using both Landsat TM and AVHRR imagery to calculate lava flow effusion rates, Harris et al. (1998) followed up the study to create a spatially and temporally detailed data set. Further work involved using such effusion rates to deduce eruption mechanisms including mass balance and magma supply rates (Harris et al. 2000). Although spatial resolution may vary with sensor data, Harris et al. (2000) argued that satellite data was essential for defining effusion rates, especially where ground based volume data were unavailable. The cessation of the Krafla eruption was reviewed showing that high temperature anomalies occurred during the eruption but a sudden decrease in short wavelength radiation marked the end of the eruption (Aries et al. 2001).

Although primarily developed to monitor global sea surface temperatures, the Along-Track Scanning Radiometer (ATSR) has been used to calculate lava flow cooling rates and flow volume as the short wavelengths bands remained unsaturated (Wooster & Rothery 1997). However Wright et al. (2000b) compared ATSR with Landsat TM imagery and found that, although the results from the ATSR were enhanced and more accurate, they were still prone to over saturation in the longer thermal infrared bands, where the relatively lower temperature anomalies are detected.

Mouginis-Mark et al. (2000) showed how a detailed chronology of events for the 1998 eruption of Volcan Cerro Azul, Galapagos Islands could be assembled from GOES data. They determined that the greatest asset of GOES was the high temporal resolution. Harris et al. (2001) stated that thermal data could be collected every fifteen minutes allowing for progression of volcanic activity to be actively studied. However, only two of the GOES satellites have the necessary short wave infrared bands necessary to detect the high temperature volcanic anomalies (Mouginis-Mark et al. 2000).

Low temperature fumaroles are the most common thermal phenomena detected on volcanoes, as they are characteristic of the waning or passive phases of volcanism (Rothery et al. 1988). Rothery et al. (1995) explained that low temperature anomalies may represent magma intrusion at shallow depth and monitoring of such anomalies could provide an indication of magma movement and possible precursor to eruption. The temperatures of such anomalies are too low to affect SWIR and are better recorded in the thermal infrared range (8-14µm).

3.12. Applications of Photogrammetry for Volcanoes and Terrain Analysis

Photogrammetry is the science of obtaining reliable information about the physical environment through photographic imagery. The nature of the Earth's terrain can lead to improved understanding of the processes at work; therefore any method that can be used to gain information about the Earth's surface is useful.

Chandler (1999) gives a good overview of work that can be achieved and the problems and possible solutions available for photogrammetry in relation to geomorphology. The creation of Digital Elevation Models (DEMs) is one of the major uses of photogrammetry and significant research to ensure accuracy has been carried out (Chandler 1999; Gooch et al. 1999; Lane et al. 2000). With increasingly sophisticated technology and photogrammetric systems, Gooch et al. (1999) showed the importance of accuracy and made suggestions for improving digital photogrammetric techniques. Baltsavias et al. (2001) gives a good review of previous research carried out over glaciers using remote sensing and in particular photogrammetry. Much of the research concentrated on mass balance fluctuations related to climate change in Greenland and Antarctica. Baltsavias et al. (2000) compared topographic mapping methodologies such as laser scanning with the more traditional photogrammetric techniques. They concluded that both methods provided reasonable results and even complimented each other, but there are advantages and disadvantages to both that need to be considered before using them in areas such as ice sheets that have very few textural differences.

With the risks involved with mapping and monitoring active volcanoes and other hazardous environments, photogrammetry has proved a useful tool in understanding the topographic variations on a regular basis. Gwinner et al. (2000), showed how photogrammetry can compliment other remote sensing, and traditional field techniques. Aerial photographs have been used to study volcanoes for many years. Jordan and Kieffer (1981) produced a topographic map of Mount St. Helens to analyse the pre-and post-1980 eruption. Donnadieu et al. (2003) used different digital photogrammetric techniques to look at volcano instabilities and found that

stereophotogrammetry provided a useful method for studying topographic changes on a regular basis. Research into deformation and morphology of volcanoes using photogrammetry has been carried out as an essential part of hazard assessment. Many processes that control the shape of volcanoes can provide useful information on the internal dynamics of volcanoes, such as magma volume, injection rate and the size and direction of collapse. (Baldi et al. 2000; Cecchi et al. 2003; Donnadieu et al. 2003).

Kerle (2002) has used photogrammetry to analyse the volume of material moved during a flank collapse. However, Kerle (2002) showed that it is important to have more than one data set and that by combining photogrammetry with other cartographic data and ground observations it was possible to produce an accurate DEM for flank collapse scenarios.

In terms of volcano-ice interaction, Motyka et al. (1978, 1980) showed that aerial photogrammetry could be used to determine heat flow by measuring the volume of ice melted at the summit of Mount Wrangell, Alaska. Benson and Follett (1986) followed up the research by measuring heat flux from the glacier ice melt from Mount Wrangell caldera, using a similar technique. In 1999, Bacher et al. carried out a precision aerial survey of Vatnajökull ice sheet, Iceland in order to record accurate elevation changes of the ice surface after the 1996 Gjálp eruption. As the ice surface is the most sensitive indicator of increased geothermal activity and further outbreaks, a method of monitoring ice elevation changes could lead to better forecasting of eruptions. Bacher et al. (1999) showed that photogrammetric surveys can be used to produce detailed

maps of the ice surface in remote regions despite the problems with co-ordinates and lack of ground control points.

Natural Environment Research Council Airborne Remote Sensing Facility imagery has been collected from Iceland for measuring glacier mass balance data. Although not directly related to volcanology, aerial photographs collected during the 2001 survey of Langjökull, have been used to measure mass balance fluctuations from the glaciers snout (Hodgkins 2001). The research showed that the aerial photographs were useful for producing digital elevation models when combined with a GPS ground survey.

3.13. Summary

Electromagnetic radiation emitted from the surface of the earth can be harnessed by sensors for use in observing and studying phenomena either not visible by the human eye, or inaccessible by traditional methods. Other advantages of remote sensing are that images have large spatial coverage, quasi-instantaneous measuring within the scene, spatially continuous sampling, and the ability to have regular repetitive monitoring. Different parts of the EM spectrum are useful for observing different land surface types such as thermal infrared for low temperature anomalies or short-wave infrared for high temperature anomalies. However, diverse land surfaces behave in different ways at different wavelengths due to differences in emissivity and spectral reflectance / absorbance characteristics.

In conclusion this review has shown there are potentially many applications for remote sensing in volcanology and terrain analysis. Multispectral and hyperspectral images with more than one thermal band have been used to retrieve accurate surface temperatures and emissivities. Short wavelength infrared data have also been used successfully for studying high temperature thermal anomalies such as lava flows, and lakes. The large spatial coverage can be used to monitor the entire volcanic system as opposed to small-scale features, mapped in the field. Remote sensing therefore has potential in hazard mitigation, in terms of monitoring the temperature, morphological development and effusion rate of lava flows. It also has the potential for monitoring volcanic plumes. Photogrammetry has proved to be a useful tool for producing assisted digital terrain maps to monitor slope instabilities on volcanoes. It has also been used to measure topographical changes in ice surface, leading to heat flux calculations.

The advantages of remote sensing over in situ methods for mapping and monitoring volcanic activity and terrain are tested, developed and evaluated in the current study, in the context of a subglacial volcanic system. The challenges posed by a subglacial volcano include the inaccessible nature of such a remote setting, but in turn provides opportunities for understanding the volcanic processes occurring and could lead to better forecasting of eruptions and hazardous events such as jökulhlaups.

Chapter 4 – The Study Area: Grímsvötn, Iceland

4.1. Introduction

Grímsvötn, Iceland's most active volcano through historical times, lies beneath Vatnajökull, Europe's largest temperate ice sheet (Björnsson and Guðmundsson 1993). This chapter addresses the geographical and geological setting of Iceland before focusing on Grímsvötn directly. The geological structure of the Grímsvötn caldera and a review of the major historical and recent eruptions from Grímsvötn, and their impact on the surrounding area is included, before highlighting the case study areas used for analysis during this research.

4.2. Iceland

The Neovolcanic Zone in Iceland is subdivided into three volcanic zones – the western, eastern and northern (Einarsson 1999). In southern Iceland, NE-SW trending fissures and faults reflect active rifting, while mainly north trending lineations are dominant to the north of Vatnajökull, Europe's largest temperate ice sheet (fig. 4.1) which covers an area of 8300 km^2 in south east Iceland (Einarsson et al. 1997). Some volcanic fissures of the Eastern Volcanic Zone lie beneath the western side of the Vatnajökull ice sheet (Einarsson et al. 1997).

Ice sheets have covered Iceland to varying degrees throughout its history. The last glaciation began 110 ka BP (before present) with warming beginning 14 ka, and this was followed by the cold period of the Younger Dryas (12 ka) (Slater et al. 1998).
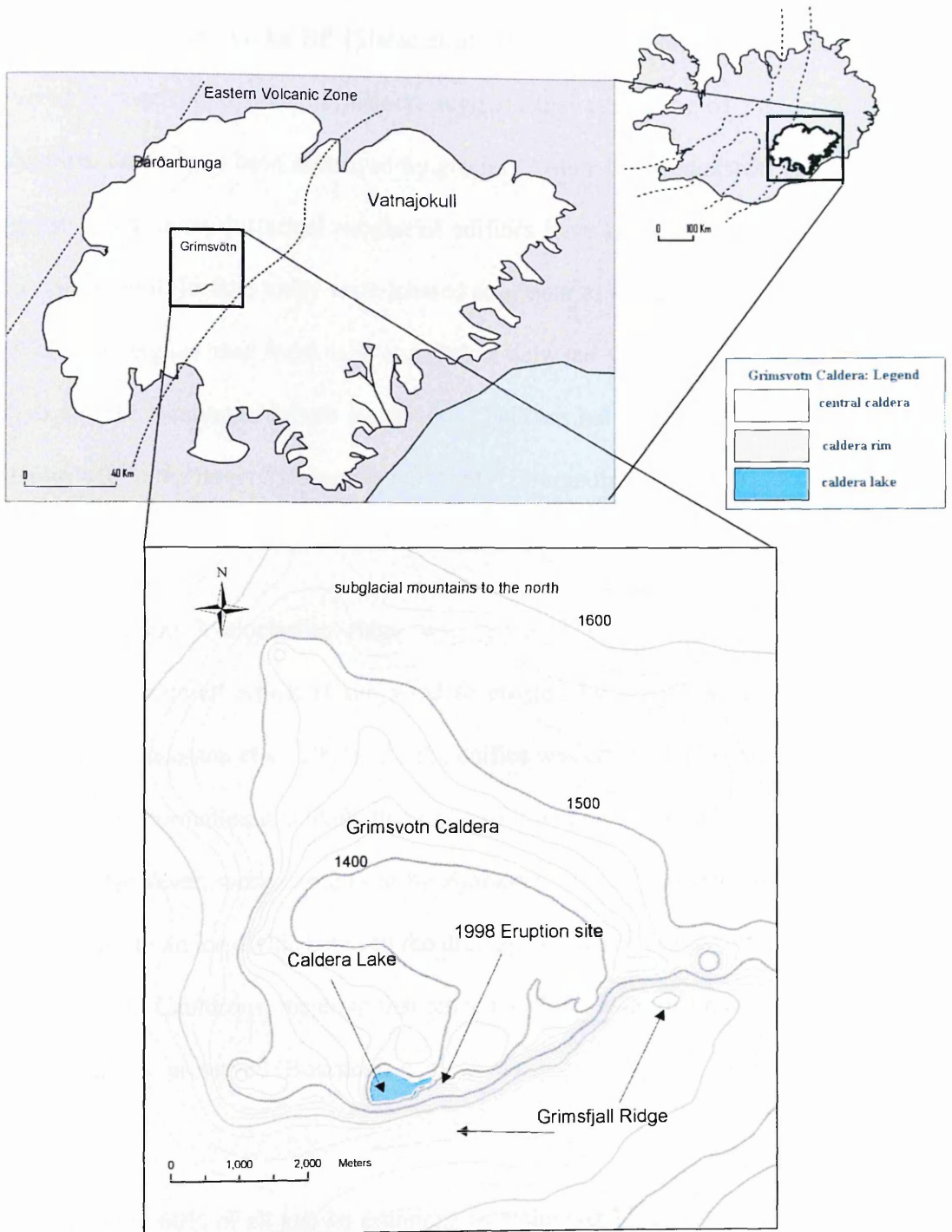
Fig. 4.1 Map to show the location of Grímsvötn within the Vatnajökull Ice sheet. Also shown is the location of the Vatnajökull ice sheet overlying the Eastern Volcanic Zone and its position within Iceland. (Map derived from digitised Modis image, and Icelandic DEM, 2001)

Rapid warming followed that period and led to the retreat of the ice sheets and isostatic rebound by 11 ka BP (Slater et al. 1998). The fact that ice sheets have covered Iceland throughout its history, suggests that a number of the products of volcanism could have been destroyed by glacial erosion. Guðmundsson et al. (2002) suggested that many historical subglacial edifices have been eroded, and that those still preserved in Iceland today were located at or near to ice divides (Bourgeois et al. 1998), who argued that there is a correlation between well-preserved hyaloclastite ridges and the location of former ice divides. This has led to an understanding of flow patterns within the larger Pleistocene ice sheets (Bourgeois et al. 1998).

The 1996 Gjálp hyaloclastite ridge was believed to be composed of poorly-consolidated material which if subjected to erosion by fast flowing ice would be eroded (Guðmundsson et al. 2002). As the edifice was completely covered by ice just a year after its formation it is likely that much of it will be destroyed (Guðmundsson et al 2002). However, work carried out by Björnsson (1982), indicates that the edifice formed close to an ice divide between the drainage basins of Grímsvötn, Dyngjujökull and the Skaftá Cauldrons, meaning that since ice flows away from an ice divide, the edifice could be preserved (Bourgeois et al. 1998).

Approximately 60% of all known eruptions over the last 11 centuries in Iceland took place in ice-covered volcanic systems (Larsen 2002). Saemundsson (1979) defined a volcanic system as consisting of a fissure swarm, where basaltic magma is erupted, and a central volcano, where evolved magmas are erupted. Iceland consists of thirty main volcanic systems, but only five of them more are significantly involved in active

volcanism (Larson 2002). Records of historical eruptions come from written descriptions, tephra layers preserved in ice or soil and associated phenomena such as jökulhlaups (Larsen et al. 1998). These, of course, only account for those eruptions that break through to the surface of the ice, and number approximately two hundred. An unknown number of eruptions have occurred and not been recorded in any way. Tephra deposits from 106 eruptions have been identified in ice and soil and have been correlated geochemically, with their respective systems (Larsen 2002). Eruption frequency has been found to be greatest in the Eastern volcanic zone of the neovolcanic zone of Iceland (Larsen et al. 1998).

4.3. Grímsvötn – Geological Setting

Two of the most active volcanic systems on the Eastern Volcanic Zone are Bárðarbunga and Grímsvötn (Guðmundsson and Björnsson 1991). Both systems are composed of a central volcano and one or two fissure swarms (Saemundsson 1979). Although Bárðarbunga has erupted more magma, Grímsvötn is the more active of the two with about 60 small eruptions that have spread tephra over Vatnajökull in the last 800 years (Guðmundsson and Björnsson 1991; Grönvold et al. 1995; Larsen et al. 1998; Konstantinou et al. 2000). Mapping of subglacial topography with radio echo sounding has shown that Grímsvötn is a central volcano with a caldera, and has also revealed a large circular structure extending from the south flank of Bárðarbunga that encloses Grímsvötn (Björnsson 1982). Although classed as a volcanic system, part of the fissure swarms radiate beyond the Vatnajökull ice sheet, therefore only the central volcano will be the focus for the purposes of this research.

Within the Grímsvötn caldera, intense geothermal activity continuously melts the surrounding ice above at a rate of $0.2 - 0.5$ km^3 yr^{-1} (Björnsson 2002), creating permanent depressions or ice cauldrons above the activity. Due to high overburden pressure, melt water is trapped as a subglacial lake (Björnsson 2002), above which is a floating 250-metre thick ice shelf. Melt water accumulates in the subglacial caldera lake, causing rises of ~10-30 metres per year of the floating ice (fig. 4.2 a, b). The melt water is subsequently released in jökulhlaups when the seal surrounding the lake is breached causing the lake level to lower by 50-100 m within 1-2 weeks, releasing 2-5 km^3 of water every four to six years (Björnsson and Guðmundsson 1993). It is argued that these outbursts can trigger small volcanic eruptions due to pressure release, as in the 1934 and 2004 eruptions (Einarsson et al. 1997; Smithsonian Institution 2004). The high geothermal heat allows for areas of open water to be present at times, thus caldera lakes can be found above particularly intense geothermal activity (Guðmundsson 1989).
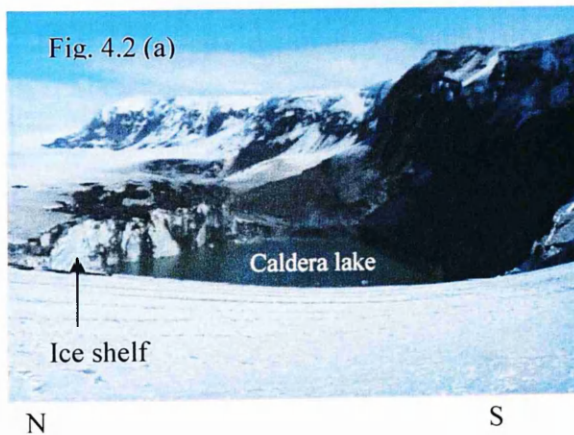
Fig. 4.2 (a) shows the Grímsfjall ridge, and Grímsvötn caldera lake, at its southern extent taken in 2000. The lake level is relatively low, with a large ice shelf to the north. (Photo courtesy of Guðmundsson 2000).
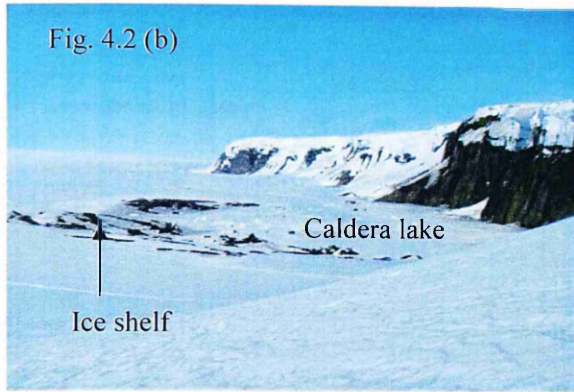
Fig. 4.2 (b) shows the Grímsfjall ridge, and firn covered Grímsvötn caldera lake, at it's southern extent taken in 2004. The lake level is high, and shows only a small ice shelf to the north. (Photo courtesy of Guðmundsson 2004)

4.4. Morphology of the Caldera

Geophysical measurements have produced a clearer topographical understanding of the Grímsvötn caldera (Guðmundsson and Milsom, 1997). The area has been of interest to earth scientists since the 1934 eruption and the resulting jökulhlaup. The main focus of research to date has centred on the size and volume of the caldera and its lake. Björnsson (1988) described the subglacial topography of the caldera as a 6-10 km diameter bowl bordered by the hyaloclastite ridge, Grímsfjall, to the south, and subglacial mountains to the north and east. The caldera is divided into three smaller calderas (fig. 4.3): the main (or south), the north and the east calderas (Guðmundsson and Milsom, 1997).
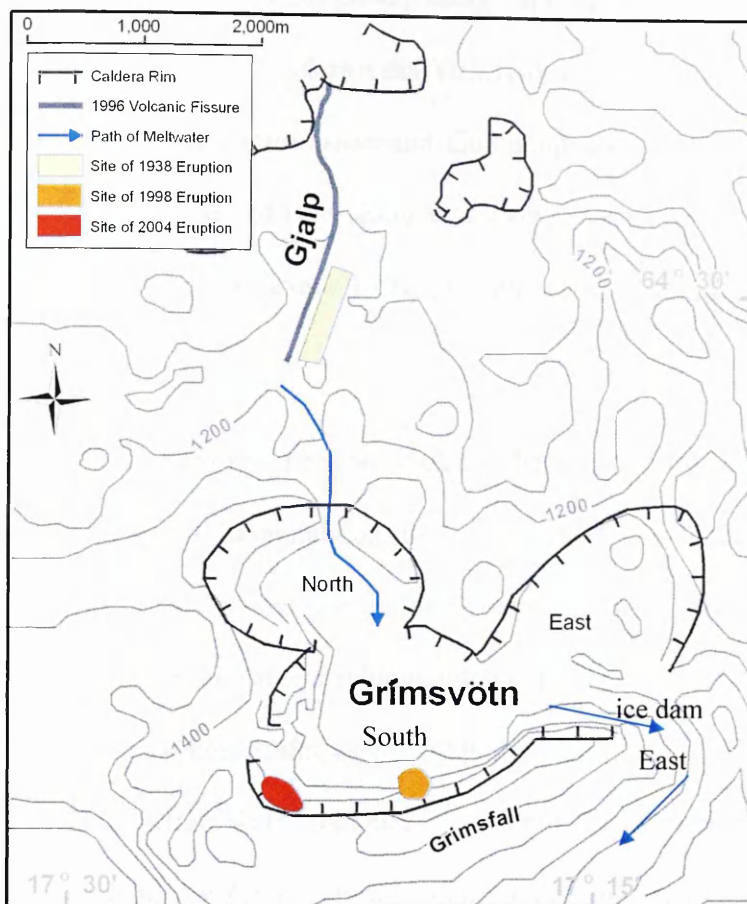
Fig. 4.3 Map (contours in m a.s.l.) of the Grímsvötn and Gjálp areas, of Vatnajökull, taken from Björnsson (1988), and Guðmundsson et al. (2004). The Grímsvötn caldera is shown to have the main caldera in the centre, with two smaller areas to the northeast and northwest. The arrows indicate the inferred subglacial path for melt water. The locations of the 1938, 1998 and 2004 eruption sites, along with the 1996 fissure site are shown on the map. The southern wall of the caldera is called the Grímsfjall ridge.

Guðmundsson and Milsom (1997) described the surface expression of Grímsvötn as a 200-300 m deep depression in the ice surface, caused by geothermal melting at its base. The subglacial lake covers the main caldera but extends into the northern depression at high water levels (Sigmundsson & Guðmundsson 2004). The lake covers the areas of highest geothermal activity, and the eruptions in 1922, 1934, 1983, 1998 and 2004 all took place at its southern margin, where geothermal activity is at its most intense (Guðmundsson & Björnsson 1991; Sigmundsson & Guðmundsson 2004).

Studies of the geothermal power using calorimetry to convert ice melting rates into heat transfer rates have shown that Grímsvötn is one of the most powerful geothermal areas in the world (Björnsson and Guðmundsson 1993). The heat output has been mostly in the range of 1000-4000 MW over the last several decades (Björnsson 1983; Björnsson and Guðmundsson 1993; Guðmundsson 2003; Guðmundsson et al. 2004).

Since 1951, seismic reflection work has been used to determine the depth of the ice shelf and lake (Guðmundsson 1989). In 1987 a joint echo-sounding and seismic survey was carried out within the caldera and this provided clear results on the morphology of the caldera (Guðmundsson 1989). The fact that both techniques were used enhanced the results, as the frequency used for radio echo sounding (1-5 MHz) does not penetrate water, and hence could not survey the lake floor. The results found by Guðmundsson (1989) showed that, at the time of the survey, there was a water depth of 40-90 metres and an ice shelf of 240-260 metres in thickness. The total volume of water within the caldera lake was 0.5 ± 0.1 km^3 (Guðmundsson 1989).

The survey was taken nine months after the 1986 jökulhlaup and the lake level was relatively low, at the time of the survey. The southern wall of the caldera was established to be 500-550 metres high, with the caldera floor dipping 250 m gently northwards (Guðmundsson 1989). There are two subglacial openings, sealed by ice dams for the majority of the time. One is a broad pass at an elevation of 1100 metres above sea level connecting the main caldera to the small northern caldera (fig.4.3). The second opening to the northeast is slightly smaller (fig 4.3), which is also the location of the former ice dam through which jökulhlaups are thought to escape the

caldera on their journey to flood plains at the coast (Guðmundsson 1989). The survey

suggested that the caldera floor is made up of a series of lava flows and sediments and

clear magnetic anomalies tied into seismic profiles show a series of steps believed to

be the edges of lava flows. In the north and east of the caldera the lake floor is

covered with sediments. Seismic reflection from deep within the caldera are believed

to be from buried lava flows and sills intruded at shallow depths into sediments (fig.

4.4). Guðmundsson (1989) suggested that the sediments are likely to be fragmented

hyaloclastites along with some glacial erosion products that have been deposited on

the caldera floor. The deepest reflections are 100 –150 metres below the lake floor,

which corresponds to a 75 metre thick pile of sediments and lavas (Guðmundsson

1989). The lava flows have originated from the southern part of the caldera, which is

thought to be the most volcanically active zone.
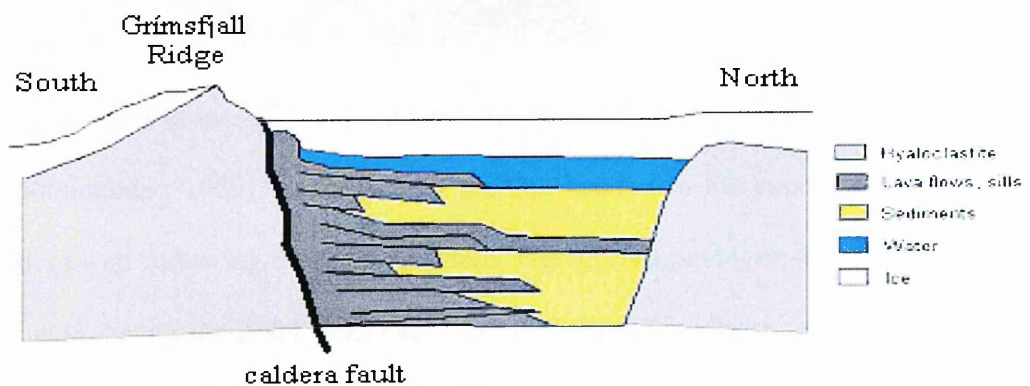
Fig. 4.4 Schematic cross section of the infill of the caldera. Figure is not to scale (from Guðmundsson, 1989). Lava flows and shallow intrusions are believed to constitute a major part of the infill, but hyaloclastite sediments lie in the north.

The Grímsfjall ridge is the only region of exposed rocks within the Grímsvötn caldera,

due to the increased melting around the geothermal regions that lie along the southern

part of the caldera (Björnsson 1988). Fig. 4.5 is an oblique aerial photograph taken in

May 2001, of the Grímsfjall ridge, looking eastwards. The fact that the ridge is

partially exposed could raise the question of the validity of defining Grímsvötn as a subglacial volcano. However the processes discussed in chapter 2, are present at both Grímsvötn and other more typical subglacial volcanoes.

The dominant lithology of the Grímsfjall ridge is hyaloclastite tuffs of basic composition cut by basaltic dykes, sills and lava flows (Guðmundsson and Milsom, 1997).
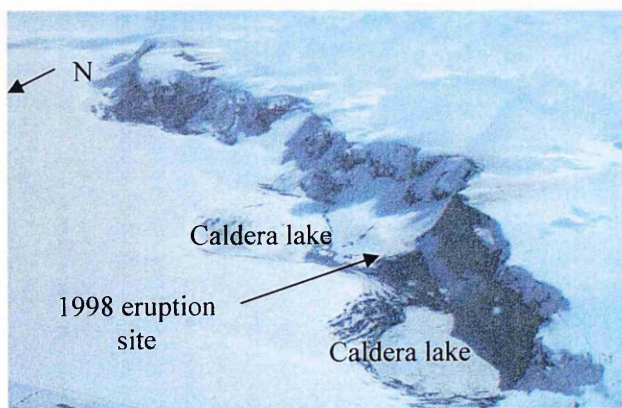
Fig. 4.5 Aerial photograph of the Grimsfjall Ridge, May 2001. (Photo courtesy of Guðmundsson 2001).

The northern slope of the Grímsfjall ridge is considered to be the caldera fault (Guðmundsson 1989), and increased melting has led to the exposure of part of the caldera wall following the 1998 eruption. Fig. 4.6 is a photograph and field sketch of the wall during the 2004 field excursion to Grímsvötn (discussed further in section 4.6). The newly exposed section of wall could be used to gather information about the geological history and evolution of Grímsvötn.

Fig. 4.6 Field sketch and photograph of the southern caldera wall, collected in June 2004. A number of units can be seen such as dark blocky basaltic layers at the top, and finely crystalline altered basalt towards the middle. Beneath that is a section composed of pillow-like structures and columnar jointing. The lowest section looked like layered coarse and fine tephra. Throughout the lower sections there are a number of intrusions, which may have fed higher layers. (Photos by S. Stewart 2004).

Legend

intrusions - sills and dykes

faults

altered basalt possibly high in plagioclase, finely crystalline

Tephra - layered coarse and fine tephra

dark blocky basalt

finely crystalline blocky basalt

columnar basalt

pillow-like strucutures

200 m

Geochemistry could be used to determine separate events in the construction of the wall, but as the cliff is inaccessible, it would be difficult to collect samples. A number of units can be seen in fig. 4.6, but the most interesting section is the lower half, which has a section of columnar joints and pillow-like structures overlying it, shown in more detail in fig. 4.7. If they are pillows, this suggests a subaqueous eruption. The entire cliff shows the subaqueous to emergent units common to subglacial eruption. Much of the Grímsfjall ridge is covered by numerous debris flow deposits, formed due to the high degree of melting (Guðmundsson 1989).
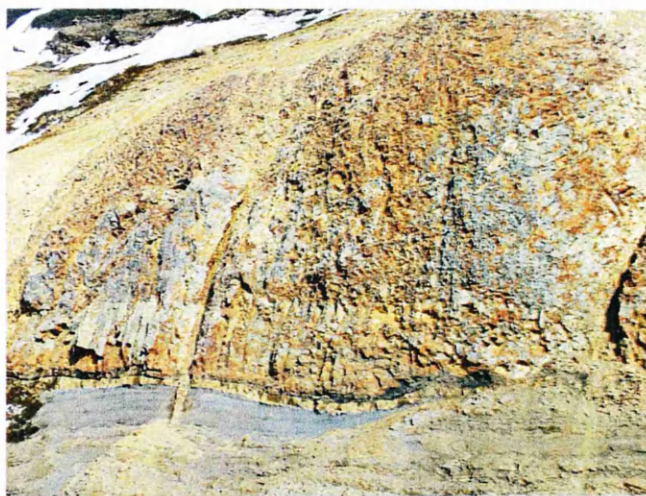
Fig. 4.7 Photograph of the southern caldera wall, approximately 50 metres in height, showing columnar joints at the base, and pillow like structures at the top. There are a number of intrusions crossing through the section. (Photograph by S. Stewart 2004)

As volcanism and geothermal activity are focused along the caldera margins, Guðmundsson and Milsom (1997) carried out a number of gravity and magnetic surveys to map the distribution of anomalous bodies such as subglacial intrusions and magma bodies, to define the sources of geothermal heat. They found that the overall subsurface structure of Grímsvötn inferred that a magma chamber had formed incrementally throughout the lifetime of the volcano, through repeated intrusion and migration of magma. The distribution of geothermal regions is consistent with heat extraction from hot rocks underlain by a magma chamber (Björnsson 1983) and is the principal cause of heat, although a small amount may be due to hydrothermal

alteration from cycling water through the hot rock boundary (Björnsson et al. 1982, Björnsson and Guðmundsson 1993, Guðmundsson et al. 2004).

4.5. Historical Eruptions

Grímsvötn has been active since volcanic records began in Iceland. Prehistoric jökulhlaups that have cut hundreds of metres into glacial canyons in Northern Iceland, for example the river canyon of the Jökulsá á Fjöllum, is believed to have been sourced from the Grímsvötn system and have been recorded as 7100BP, 4600BP, 3000BP and 2000BP (Kristmannsdottir et al. 1999).

Although Grímsvötn has a high eruption frequency (>10 eruptions every 100 years), it does show periods of higher and lower frequency (Thordarson and Self 1993, 2003). Most of the eruptions from Grímsvötn have an explosivity index (Smithsonian Institute 1996) averaging two and occur from central subglacial vents (Thordarson and Self 2003). In 1934, an eruption near the southern caldera wall marked an end to a quiet period for Grímsvötn, and was preceded by a jökulhlaup (Einarsson et al. 1997). An almost entirely sub-glacial eruption on the northern flank of Grímsvötn within Vatnajökull, which breached the glacier at the end of the eruption, occurred in 1938. A peak discharge of 30,000 m^3 s^{-1} was reached after three days, and the Grímsvötn caldera lake was thought to have drained during this eruption (Einarsson et al. 1997). The lava produced a small ridge in close proximity to the location of what became the 1996 Gjálp fissure (Einarsson et al. 1997).

In 1983 a small eruption occurred beneath the ice on the southern edge of the caldera. There was however, no jökulhlaup during this eruption, suggesting the small volume

of melt water had pooled within the caldera lake (Einarsson et al. 1997). This was then followed by a small subglacial eruption in August 1984 (Einarsson et al. 1997). A jökulhlaup in 1986, to the NW of Grímsvötn was followed by a distinct tremor episode, and an eruption triggered by pressure release (Einarsson et al. 1997). Then in 1996, a jökulhlaup to the west of Grímsvötn occurred in February followed by another in August, subsequently leading to a distinctive eruption signature at the end of September (Smithsonian Institute 1996).

4.5.1. 1996 Gjálp eruption

Events leading up to the 1996 eruption possibly started as early as 1974, when a large earthquake of magnitude 5.1 Ms (surface wave magnitude), was recorded and proved to be the first of a series of large earthquakes (Guðmundsson et al. 2002). On the 29th September at 10.48 am, seismographs detected an earthquake measuring 5.4 Ms on the Richter scale (Smithsonian Institute 1996). This was followed by an unusually intense earthquake swarm that included 5 events above magnitude 3 within two hours of the main quake (Einarsson et al. 1997). This continued with increasing intensity until the evening of September 30th when the earthquake swarm suddenly stopped and a distinctive continuous volcanic tremor signalled the start of the eruption (Einarsson et al. 1997).

The next morning (1st October) a subsidence bowl in the glacier surface was seen from the air, and was shown to increase in both size and depth over the day. Three additional bowls in a line, indicative of intensive melting at the base of the glacier, had formed above a 5-6 km long fissure (Smithsonian Institute 1996). As melting occurred along the fissure, the ice shelf above the Grímsvötn caldera, some 15 km to

the south, began to rise, suggesting that the melt water was flowing into the caldera depression (Smithsonian Institute 1996). On October 2nd the eruption broke through the surface of the ice (fig. 4.8), and a eruption column rose 3000 metres before being deflected to the north by a southerly wind at a velocity of 14-20 m s^{-1} (Guðmundsson et al. 2002). By evening, the Grímsvötn ice cover had risen by 10-15 metres due to the rise in the caldera lake level (Smithsonian Institute 1996).

Fig. 4.8 Photograph of the 1996 Vatnajökull eruption, Gjálp, on the 2nd day of the eruption. (Photo courtesy of Sigmundsson F. 1996).

By October 4th the eruption was continuing at a similar pace, but the depression at the eruption site had widened and showed an elongated rift through the ice. By 7.00 pm an increase in the river discharge on the River Skeiðará was recorded, suggesting that the water level had risen and that a glacial burst was imminent (Smithsonian Institute 1996).

By October 10th the eruption had begun to diminish with only occasional explosions of ash high into the atmosphere (Einarsson et al. 1997). A large fissure had opened in the ice, and melt water flowed south into the Grímsvötn caldera lake (fig. 4.9). Guðmundsson et al. (2002) made direct observations of the edifice that was growing within the fissure and suggested that it was predominantly composed of unconsolidated pyroclastic glass fragments. However only a few observations were

made, as the edifice was only exposed for a short time before it was covered by melt water from surface ablation, and the inflow of glacier ice (Einarsson et al. 1997). Geophysical surveys were carried out to map the area of the edifice and calculate the density. The southern part of Gjálp is a narrow ridge with a relief of 200 metres rising steeply to 450 metres in the central section (Guðmundsson et al. 2002). The width of the ridge is 500 metres but widens to the north until reaching a width of 2 km. Guðmundsson et al. (2002) believed that the eastern part of the ridge is centred over the fissure while the western section was formed by migration of volcanic material because of the lack of ice boundaries confining the material. The low mean density (1600 kg m^{-3}) of the central part of the edifice is believed to be due to a high proportion of steam during the eruption, leading to pore spaces in the tephra to be filled by steam (Guðmundsson et al. 2002). After the eruption this is left as air spaces reducing the density of the final hyaloclastite pile (Guðmundsson et al 2002).

Fig. 4.9 Photograph of the 1996 Gjálp eruption on day 10 of the eruption, showing the large canyon formed within the ice. (Photo courtesy of MT Guðmundsson 1996).

The eruption was recorded as ending on the 13th October, but melt water continued to flow south, with no sign of the imminent jökulhlaup (Smithsonian Institute 1996). A high frequency continuous tremor began on the evening of 4th November, indicating the failure of the ice dam, but it was not until 5th that the jökulhlaup arrived at the edge of the ice, increasing the discharge, sediment flow and sulphur content of the Skeiðará River (Einarsson et al. 1997). A peak discharge of 45,000 m^3 s^{-1} and the jökulhlaup caused US $10-15 million worth of damage (Smithsonian Institute 1996).

4.5.2. 1998 Grímsvötn eruption

This eruption was preceded by a small increase in seismicity in the weeks prior to the eruption. An earthquake swarm began on the 17th December 1998, with an increase in activity on 18th, which was replaced by volcanic tremor at 9.20 am on the morning of 18th December 1998 (Smithsonian Institute 1998).

Only ten minutes later, an ash plume was observed, showing that the eruption had penetrated the ice shelf (fig. 4.10).

Fig. 4.10 Photograph of the 1998 eruption Grímsvötn, on day two of the eruption. (Photo courtesy of F. Sigmundsson 1998)

Vents were located along a 1300 m long east-west fissure along the southern flank of Grímsvötn, at the foot of the Grímsfjall Ridge (fig. 4.11). The location of the eruption was similar to the 1934 and 1983 eruptions. The eruption entered the caldera lake and penetrated the ice shelf, melting through approximately 100 metres of ice (Smithsonian Institute 1998).
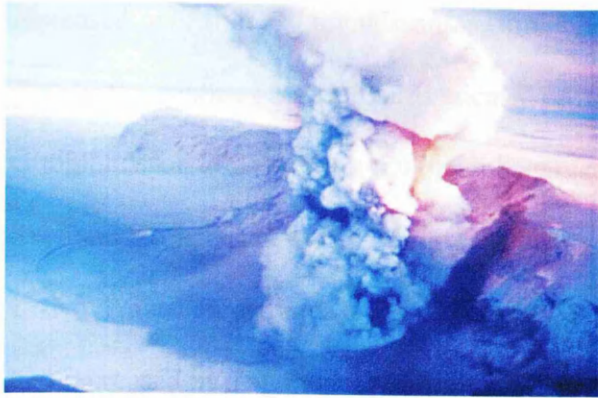
Fig. 4.11 Photograph of the 1998 eruption, day 10, looking east along the Grímsfjall ridge.

(Photo courtesy of Sigmundsson F. 1998)

Activity was most energetic in the main crater, but there were also smaller periodic explosions along the fissure. The eruption lasted 11 days, reducing in activity from the first day when the plume rose 7 km into the atmosphere (Smithsonian Institute 1998). A tephra ring overlying the ice was formed around the edge of the eruption site. (Sigmundsson, 1998). No jökulhlaup occurred because of the low volume of ice melt during this eruption (Sigmundsson 1998).

4.5.3. 2004 Grímsvötn eruption

A number of precursory events led to the 2004 Grímsvötn eruption, including inflation changes since the previous eruption (Sturkell et al. 2003, 2005), lake surface elevation and seismic activity (Vogfjörd et al. 2005). From August 2004, tremor bursts of up to 30 minutes in duration were observed from the Grímsfjall seismic station, indicating an increase in geothermal activity (Sigmundsson & Guðmundsson 2004). During October 2004 periodic icequakes were observed. These are seismic events that occur on floating sheets of ice that have thermal stresses as the major cause of failure (Deichmann et al. 2000).

A periodic tremor pulse was recorded between the 18th and 24th October 2004. This was accompanied by small magnitude earthquakes around the Grímsvötn caldera, that

increased over time (Sigmundsson & Guðmundsson 2004). On 28th October seismic
data to the south of Vatnajökull indicated an imminent jökulhlaups (Sigmundsson &
Guðmundsson 2004). The jökulhlaup began early on the 30th, and water level in the
Skeiðará River began to rise reaching its peak on the 2nd November. In the morning of
1st November an earthquake swarm began beneath Grímsvötn, which by the evening
had increased in magnitude (Vogfjörd et al. 2005). Between 8 and 10 pm, more than
160 earthquakes, up to 2.8 in magnitude, were registered. Volcanic tremor was
observed after a magnitude 2.7 earthquakes at 9.50 pm. The volcanic tremor remained
continuous throughout the night, with an increase between 4 and 5 am on the 2nd
November, when an increase in the eruption plume size was observed on radar
imagery (Vogfjörd et al. 2005). However after the initial activity (fig. 4.12), the
tremor became pulsating and slowly declined until it had all but ceased by the 4th
November (fig. 4.13).
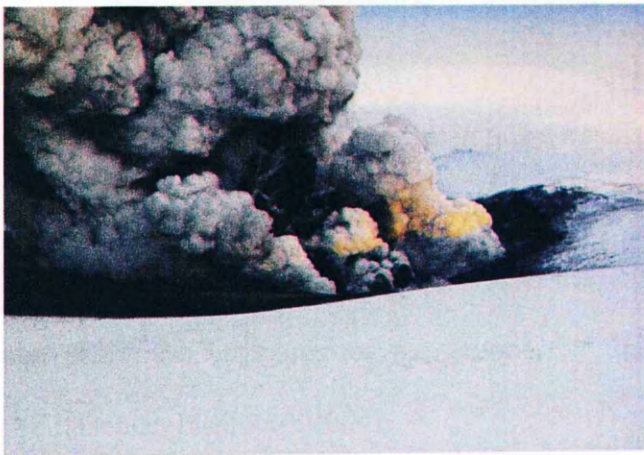
Fig. 4.12 Photograph of the
2004 Grímsvötn eruption, taken
on day 2 of the eruption. (Photo
courtesy of A Jarosch 2004).

The eruption was phreatomagmatic throughout its duration (Sigmundsson &
Guðmundsson 2004). All magma fragmented into pyroclasts that either accumulated
at the eruption site or were carried northwards by the eruption plume (Smithsonian
Institute 2004). The eruption itself was from a 1 km east west trending fissure which
melted a 1 km diameter void in the ice producing 100 metre high ice walls.

Sigmundsson & Guðmundsson (2004) stated that the eruption occurred beneath 150-200 meters of ice, but melted its way through in an hour. The eruption plume was visible by meteorological radar at midnight (Sturkell et al. 2005). On the morning of the 2nd November the eruption plume reached 9 km, with explosive activity varying throughout the day, leading to a maximum plume height of 12-14 km (fig. 4.13). A smaller explosive episode occurred in an ice cauldron near the southeast edge of Grímsvötn, 8 km to the east of the main crater. It issued steam when first observed on the afternoon of the 2nd November (Vogfjörd et al. 2005).
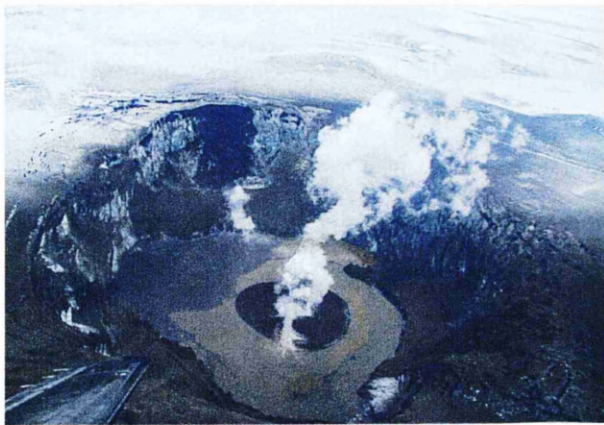
Fig. 4.13 Photograph of the 2004 eruption crater on the last day of the eruption. (Photo courtesy of Svenbjorn Gudbjornsson, 2004).

The effects of the eruption were initially localised, with farmers sheltering their grazing animals in the north of Iceland. However the eruption plume drifted over the north Atlantic as far as Scandinavia, and air traffic was disrupted for an area of 31100 km^2 from the beginning of the eruption to the morning of the 4th November (Smithsonian Institution 2004).

The jökulhlaup preceding the eruption reached a maximum on the morning of the 2nd November with a peak discharge of 3000-4000 m^3 s^{-1}. No damage was caused to roads or infrastructure (Sigmundsson et al. 2004). The 2004 eruption followed a

pattern similar to the 1983 and 1998 eruptions but with less magma erupted (Sigmundsson & Guðmundsson 2004).

The multidisciplinary monitoring approach employed prior and during the 2004 eruption showed potential for monitoring future eruptions and jökulhlaups by enabling real-time hazard assessment (Vogfjörd et al. 2005).

4.6. Case Study Sites

In 2001, an aerial survey over Grímsvötn was carried out by the Natural Environment Research Council (NERC) Airborne Remote Sensing Facility (ARSF). Although the caldera is an average of 8 km across, only the Grímsfjall ridge (i.e. the southern wall of the caldera) was surveyed (fig. 4.14).

In 2004, the Icelandic Glaciology Society invited me to join their annual expedition to Grímsvötn. Their aim of the trip was to take ablation rate measurements, collect DGPS measurements of the Gjálp region, and make new elevation measurements of the highest peak in Iceland. Because of the hazardous terrain, safety precluded individual field work. Nevertheless, selected temperature measurements were made in two areas, and part of the caldera wall was studied, as discussed in section 4.4.
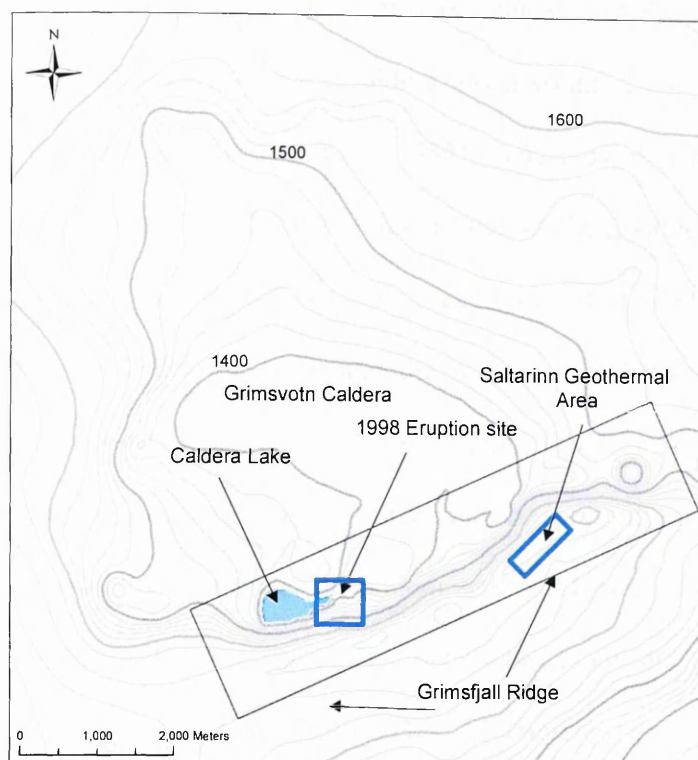
Fig. 4.14 Map to show the location of the 2001 aerial survey (grey rectangle), and the two case study sites, (marked by blue boxes), the 1998 eruption site, and Saltarinn geothermal area.

Following the 2004 field campaign, two areas were selected for detailed analysis. These are the 1998 eruption site (fig. 4.14), because ground based temperatures of that area were made in 2001 and 2004. In addition the 1998 crater lake is exposed in the imagery, and this was used to calculate heat flux. The second area is the Saltarinn geothermal area on the south eastern part of the Grímsfjall ridge (fig. 4.14). This area was chosen as temperature data were collected during the 2004 field excursion..

4.7. Summary

Grímsvötn, Iceland's most active volcanic system lies within the Eastern Volcanic Zone beneath Vatnajökull, Europe's largest temperate ice sheet. Previous studies have shown it to be a caldera with geothermal activity concentrated along the exposed southern caldera margin, known as the Grímsfjall ridge. Melt water accumulates in the caldera lake that is periodically emptied via subglacial channels leading to jökulhlaups every 4-6 years. The Grímsfjall ridge is currently the only region of

exposed rocks within the Grímsvötn caldera. Although Grímsvötn has been active since historical times the caldera has a youthful appearance, believed to be due to recent subsidence (Björnsson 1982). The most recent eruptions, those in 1998 and 2004, took place along fissures on the southern caldera fault (Guðmundsson 1989). As Grimsvötn is such a dynamic environment, it needs to be monitored on a regular basis in order to understand the relationships between geothermal activity, debris flows from Grímsfjall, and jökulhlaups. Studies of the historical formation of the caldera could aid in understanding the present activity. Consequently detailed mapping of the slopes and caldera wall will be useful. Leakage of water through the ice dam following the 1998 eruption has made the use of ice melting calorimetry problematic (Guðmundsson 2003). Moreover, at the 1998 eruption site, heat has been lost directly to the atmosphere through patches of warm open water and crater walls (Guðmundsson et al. 2004), which may not always be accessible. Alternative methods, such as remote sensing, for monitoring the geothermal activity would be advantageous.

Chapter 5 – Image Processing Methodology and Analysis

5.1. Introduction

The data used for this research were collected using airborne sensors at a height of approximately 1000 metres above the surface of the Earth. The principles involved with remote sensing are the same for either space or airborne sensors as they rely on the measurement and interpretation of electromagnetic radiation (Mather 1999). A major area of this research concentrates on analysing remotely sensing data provided by the NERC ARSF, and building on ground based calorimetric research. This chapter will therefore introduce the data used for this research in more detail, along with some of the issues involved with geocorrection and the processing methodology undertaken in order to prepare the data for further analysis. In order to calculate temperatures from the radiance values the emissivity of the land surface is needed, hence it is necessary to classify the imagery for the land cover types that can be associated with a specific emissivity value. This chapter discusses the methodology and statistics involved with classification, along with an assessment of the accuracy.

5.2. Airborne Remote Sensing Facility

The Natural Environment Research Council (NERC) has supported its research scientists and academics by providing an airborne remote sensing system since 1982, when an aircraft was purchased and converted for aerial surveying (Wilson 1997). Since then a series of scanner updates and the development of an integrated data system (IDS) to allow for an enhanced geometric correction within the ground data

processing system, has led to the establishment of the Airborne Remote Sensing Facility (ARSF) in 1993 (Wilson 1997), known as the Airborne Research and Survey Facility since January 2005. The instruments onboard in 2001 at the time of the aerial survey of Grímsvötn, consisted of the Daedalus 1268 (AZ-16) Airborne Thematic Mapper (ATM) that has spectral channels similar to the Landsat Thematic Mapper (TM), Wild RC-10 camera that can produce stereo photographs and the Itres Research Compact Airborne Spectrographic Imager (CASI), a CCD (charge coupled device) array pushbroom imager with a spectral range of 390 –950 nm.

5.2.1. The Airborne Thematic Mapper

The ARSF's airborne thematic mapper (ATM) sensor is a Daedalus 1268 AZ-16, a passive remote sensor designed to detect radiation reflected and emitted from Earth's surface from an airborne platform. The scan head optics and detector layout separates the incoming radiation into 11 spectral bands (table 5.1) ranging from blue in the visible part of the spectrum to thermal infrared (Azimuth System, 2001). Bands 1-8 cover the visible and near infrared part of the spectrum, bands 9 and 10 are short wave infrared and band 11 is thermal infrared.

Table 5.1 Airborne thematic mapper bands

Band	Wavelength (µm)	
1	0.42-0.45	Visible
2	0.45-0.52	
3	0.52-0.60	
4	0.60-0.62	
5	0.63-0.69	
6	0.69-0.75	Near infrared
7	0.76-0.90	
8	0.91-1.05	
9	1.55-1.75	Short wave infrared
10	2.08-2.35	
11	8.5-13.0	Thermal infrared

The ATM splits the radiation between 0.42 and 1.05 μm (the visible and near infrared bands) by a prism before imaging it onto a silicon detector array. The short wave and thermal light is split, and imaged onto a single detector. The thermal band is calibrated in "real time" using two on-board blackbodies (ARSF User Manual, 2002a), which are imaged by the sensor during every scan before and after the scene pixels on a scan line.

Although the infrared part of the electromagnetic spectrum extends from 0.7 μm to 1 mm, the atmosphere absorbs much of the emitted radiation beyond 3 μm in wavelength. Sensors such as the ATM detect radiation between 8 and 14 μm as that wavelength allows thermal anomalies to be detected through an atmospheric window (Mather 1999). Band 11 of the ATM covers the same wavelength interval as band 6 of the Landsat Thematic Mapper.

5.2.2. The Wild RC-10 camera

The Wild RC-10 aerial camera system is designed for taking near vertical exposures from the air. The camera is aligned and levelled during the flight by the operator to correct for aircraft roll pitch and yaw. The focal length of the camera has been calibrated as 153.435 mm. The standard negative format is 230 x 230 mm. The final outputs are a series of large format hard copy colour prints of 252 x 238 mm.

5.2.3. The Compact Airborne Spectrographic Imager

The Itres CASI sensor collects an image frame of 512 spatial pixels of the surface, building up a flight line as the aircraft moves. Light is dispersed for each pixel scanned, over the 0.39 – 0.95 μm spectral range by a reflection grating, then recorded by 288 detectors on the CCD. The Charge Coupled Device (CCD) is an electron

series of light sensitive cells that record the image electronically. The spatial mode records data from all 512 spatial pixels but for only a limited number of programmable bands, 13 in the case of this survey (table 5.2), by the selection and addition of 0.018 μm resolution detector elements.

Table 5.2 Compact Airborne Spectrographic Imager, spatial mode bands.

Band	Centre (μm)	Width (μm)	Start (μm)	End (μm)
1	0.402	20	0.392	0.412
2	0.432	20	0.422	0.442
3	0.480	20	0.470	0.490
4	0.501	20	0.491	0.511
5	0.547	20	0.535	0.556
6	0.610	20	0.600	0.620
7	0.660	20	0.650	0.670
8	0.678	5	0.676	0.681
9	0.705	10	0.700	0.710
10	0.744	15	0.737	0.752
11	0.760	5	0.758	0.763
12	0.766	20	0.756	0.776
13	0.815	10	0.810	0.820

The CASI data provided for this research was in spatial mode but the hope was to use spectral data within the CASI imagery to map compositional variation on the ground. A preliminary analysis (appendix f) has been made to determine the potential of using 13 CASI bands for compositional mapping. However in order to fully test the imagery hand specimens would be required. These were unavailable, due to lack of ground observations at the time of the aerial survey. Therefore this research will concentrate on the thermal band of the ATM and the aerial photography.

5.3. Aerial Survey 2001

The 2001 aerial survey was carried out on the 10th and 14th June over the Grímsfjall ridge. Three Airborne Thematic Mapper (ATM) flight lines were collected on each day of the survey, producing 6 images. However, the central flight line for each day

was chosen for all subsequent analysis this adequately covered the entire scene of the Grímsfjall ridge area [appendix B1]. A set of aerial photographs was collected from the central flight line on the 14th June 2001, allowing a number of stereopairs to be assembled. These are further analysed and discussed in chapter 7. Compact Airborne Spectrographic Imager (CASI) data were also collected on the 2nd day of the survey, 14th June 2001, again in three flight lines.

5.4. Geometric Correction

The first stage in processing the ATM and CASI data was geometric correction carried out using AZGCORR software on a UNIX workstation. Remote sensing images are often integrated into a Geographical Information System (GIS), or presented in a map like form. Geometric correction is the transformation of an image so that it has the scale and projection properties of a map.

The ARSF found that the development of algorithms for remote sensing data analysis and the level of technological expertise needed by non-specialists was reducing the number of users. In order to address this problem a processing chain developed by NASA (Wilson 1997) was established. Raw data acquired from the ATM and CASI sensors (level 0) are radiometrically calibrated by the ARSF (Level 1b). These data are then transferred to the user in the form of hierarchical data files (hdf), saved on CD Rom. The user can then apply specific geometric correction (level 3a) for a user defined map projection.

AZGCORR combines the scanned image data with pre- or post- navigation records and then interpolates a map projection, referenced to the output image that has been corrected for aircraft position and altitude. The navigation is converted from geographic co-ordinates on GPS satellite datum, to a suitable survey map projection. A map projection is a device that represents a curved surface on a flat sheet of paper. All the navigation is referenced to a set of axes and a model that describes the static and dynamic geometry of the earth in that area. This is known as the geodetic datum or geiod. The current GPS datum is the WGS84 (World Geodetic System agreed in 1984). For the geocorrection of the ARSF imagery of Grímsvötn, the WGS 1984 geodetic datum was chosen, along with UTM zone 28, as this is the projection being increasingly used by Icelanders. The advantage of using the UTM projection is that it reduces the distortion acquired due to the high latitudes of Iceland.

The three-dimensional spheroid is obtained from the representation of the Earth as an ellipse rotated about Earth's North-South axis. To relate the two figures, the geoid and the spheroid, a local origin is chosen with measured lateral position and assigned vertical position. This technique is not without errors but they are minimised compared to angular triangulation methods carried out manually prior to correction. The relationship between a simple spheroid and its geoid is obtained by a combination of satellite orbit observation and satellite height above sea level. The highest accuracy can only be achieved with GPS ground control points.

Another significant source of error comes from altitude, especially if the image is well above mean sea level. As Grímsvötn has an average altitude of 1500 metres above sea level this needs to be taken into account. Without a DEM, the ATM flight line would

be much wider, as by default the scans are projected down to sea level or the spheroid surface if no geoid-spheroid correction is applied. The area is dynamic and hazardous. There are few locations that would remain unchanged and easily recognisable from the air, due to the intense geothermal activity continuously melting snow and ice, so there were no ground control points collected specifically for the correction of the imagery.

The NERC ARSF uses on-board GPS data to give three-dimensional positions relating dynamic platform observations to static field sites, as well as relating to existing maps. This then requires further adjustments, such as the transformation of aircraft position on the GPS datum to a local mapping datum. Both ATM (rotating mirror) and CASI (pushbroom) have positions calculated for every pixel and the image is then interpolated to a rectilinear grid.

An example of the command code used to carry out the first stage of processing using UNIX is as follows:-

azgcorr –v –be –d7 0 -73 46 -86 0 0 0 0 –mUTMZ 28 –p 5 5 -1 (input file) –es sphsep –hsu –hs - XX -3 (output file)

where -v -be is the listing code, -d7 is the spheroid code, -mUTM is the Universal Transverse Mercator Zone 28, -p 5 is the pixel size in metres, -es geiod spheroid separation grid path file name, -hsu height correction for WGS84 and file sphsep (as not processing UK data), -hs -XX average height in metres of the terrain.

A specific example for image a161133a for the 10th June 2001 is:

azgcorr –v –be –d7 0 -73 46 -86 0 0 0 0 –mUTMZ 28 –p 5 5 –1 a161131b.hdf –es sphsep -hsu – hs 1550 –3 hdf3a a161133a.hdf

The second stage of the process converts the hdf files into a usable format that can be imported into ERDAS Imagine (see section 5.5). This involves the use of AZEXHDF, which produces a band-interleaved file (bil) that can be imported as a generic binary type file before being converted in to ERDAS image files.

The command line for azexhdf would be as follows:

azexhdf –h (hdf file name) –B (bil output name) –Bv

A specific example for the image file a161133a for the 10th June 2001 is:

azexhdf –h hdf3a/a161133a.hdf –B bils/a161133a.bil –Bv

During this process the rows (lines) and columns (pixels) of each image are stipulated and are recorded for import into ERDAS Imagine.

The third stage of the geometric correction, outputs the image co-ordinates corrected for UTM Zone 28. The command used is:

azexhdf –h (file name) –v 8

E.g. azexhdf –h a161133a.hdf –v 8

Despite the lack of ground control points, the ARSF imagery could be geocorrected using the on board GPS coordinates.

5.5. Importing to ERDAS Imagine Version 8.7

ERDAS Imagine is a collection of software tools designed specifically to process imagery and extract useful information from data (ERDAS 1999). Geographic data are often presented in terms of multispectral imagery including aerial photographs, as well as vector data. ERDAS Imagine can be used for both vector and raster data but is particularly useful for raster data. It has useful enhancement techniques such as principal components analysis and classification, both of which are used in this

research (ERDAS 1999). Images can be easily exported from ERDAS into Geographic Information Systems (GIS) environments for further analysis due to its high compatibility (Longley et al. 2001). GIS is defined as an organised collection of computer hardware, software and geographical data, that can be used to capture, store, intergrate, manipulate, analyse and display data related to a position on the earth's surface (ESRI 1993). ARCMAP is the GIS software used for analysis of aerial photographs and the display of data used in this research.

Within ERDAS Imagine, there are a number of different file types that can be imported and converted to .img files. The output from the AZEXHDF file conversion creates a .bil file, which is a generic binary type file, and is listed in the import file type index of ERDAS Imagine. The number of rows, columns and bands has to be entered into the relevant areas and the program then imports and converts the bil file into an image file format (.img) that can be viewed in the ERDAS Imagine viewer as well as within an ARCGIS environment. This allows the image data to be processed within the Data Preparation, Interpreter and Classifier sections of ERDAS Imagine, along with using ARCGIS spatial analyst and georeferencing tools for creating maps and output imagery.

5.6. Band Combinations

Digital images are typically displayed as colour composites using the three primary colours red, green and blue (RGB). When three wave bands are combined for display purposes using RGB for each band, a 'false colour' composite image can be produced. It is 'false' in that the colours do not correspond to true colour of the ground surface

(Rothery et al. 1995). Image interpretation can be aided by varying the colour combination across the bands in order to display the different land surface spectral properties. This is achieved in ERDAS Imagine by changing the band combinations within the Raster menu. The ATM imagery collected during the aerial survey of Grímsvötn in 2001 contains 11 bands, and these were used in different combinations to construct false colour composites for initial visual inspection and subsequent interpretation.

5.7. Principal Components Analysis

Digital images consisting of various spectral bands often show uniformity across those bands (Mather 1999; Lillesand et al. 2004). This correlation across an image can hinder image analysis by concealing some of the less obvious pixel information (Richards and Jia 1999). Principal Components Analysis (PCA) is a technique used to enhance imagery prior to visual interpretation as well as a preprocessing procedure before classification (Cracknell and Hayes 1991). It is also a method of data compression as it allows data to be compacted into fewer bands, reducing the dimensionality of the source data i.e. creating a new set of bands in which the information is not distributed evenly but concentrated into a small number of bands (Cracknell and Hayes 1991). PCA was applied to the ATM and CASI data in the present study in order to enhance the imagery prior to visual analysis and classification.

If two variables are perfectly correlated they will be plotted as a straight line on a scatter diagram (Mather 1999). Different bands within multispectral images are not

perfectly correlated but do usually have a dominant direction of scatter producing an

ellipsoid. Fig. 5.1 shows the dominant direction of variability (AB) as the major axis,

which is known as the first principal component. Therefore as the axis is in spectral

space it measures the highest variation within the data (Curren 1985). The second

principal component is the widest transect of the ellipse that is orthogonal to the first

principal component, and shows the largest amount of variance within the data, not

already described in the first component (ERDAS 1999).
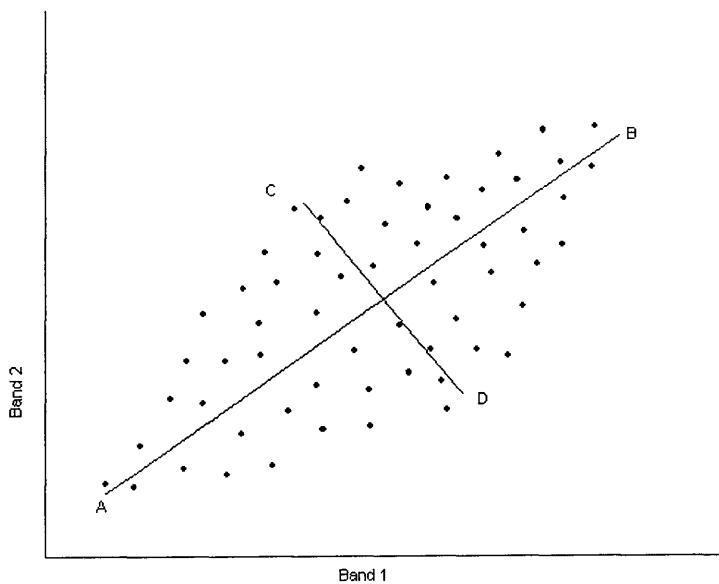
Fig. 5.1 Diagram to show principal component analysis ellipsoid with first and second components along dominant axes.
(Taken from Mather 1999)

Each successive component accounts for a decreasing amount of variation within the

data, which is not already accounted for by previous principal components (Mather

1999; Lillesand et al. 2004). Curran (1992) suggests that 90% of the total variance is

often compressed into the first principal component with subsequent components

containing increasingly more negligible variance. The direction of each component is

known as the eigenvector and the length is known as the eigenvalue. Eigenvalues are

measured in terms of units of variance (Mather 1999).

A rapid fall in size of eigenvalues indicates original bands exhibit high correlation and a significant result can be obtained from transforming the image using principal components analysis (Richards & Jia 1999). The eigenvectors scaled by square roots of eigenvalues can also be interpreted as correlations between abstract principal components and individual bands of multispectral image. Correlations are used rather than co-variances in principal components analysis because the linear relationship between two variables is used rather than the distribution (Mather 1999), i.e. the diagonal and off diagonal relationships as opposed to scattered distribution. However the eigenvalues can be used to see the percentage of the total variance shown by each component using the following equation:

$$\%_p = (\lambda_i \times 100) / \sum_{i=1}^{n} \lambda_i \qquad (5.1)$$

where λ_i is the ith eigenvalues, and $\Sigma\lambda_i$ is the sum of all eigenvalues. In order to correctly interpret the image it is important to evaluate how each band corresponds to each principal component using factor loadings. Depending on which band is loaded in which component it is possible to ascertain which principal component to look at in order to analyse a particular feature. The individual factor loadings can be calculated using the following equation:

$$R_{kp} = \frac{a_{kp} \times \sqrt{\lambda_p}}{\sqrt{(Var_K)}} \qquad (5.2)$$

where a_{kp} = eigenvector element for band k and component p, λ_p = pth eigenvalue, Var_k = variance of band k in variance-covariance matrix (Jensen 1996). Jensen (1996) described as the comparison of two variables from the diagonal and off diagonal.

In constructing a colour image only three dimensions can be mapped to the three primary colours for example assigning the first three components to red, green and

blue (Richards & Jia 1999). However by visually comparing loading factors it is possible to decide on the appropriate component combination in order to extract the best possible information from the image produced. Decorrelation, a statistical procedure for reducing distortions within the data, enhances the colour separation on an image exaggerating colours and improving the visual impact of features (Mather 1999). If decorrelation of the data is all that is required in order to aid analysis, all components should be retained (Mather 1999).

ERDAS model maker has a variety of graphical models that can be adapted and combined by the analyst in order to construct particular image processing procedures. There are two methods for carrying out a principal component transformation. The first method uses the modeller for the entire conversion, using a generalised model that can be changed for the correct image (fig. 5.2).
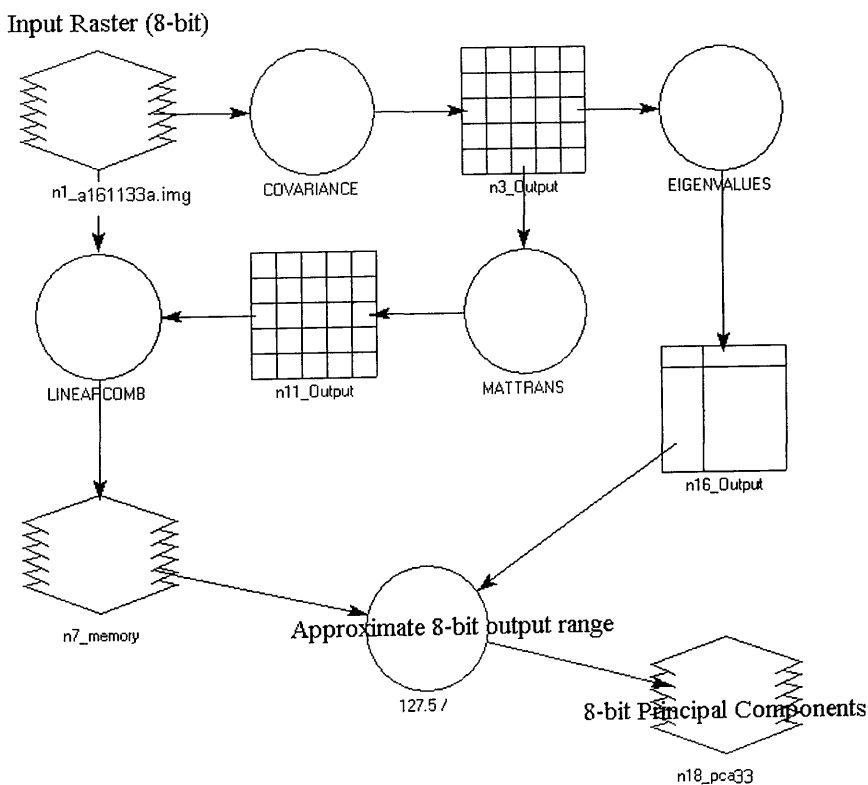
Fig. 5.2 flow chart showing an example model for principal components transformation, for image a161133a.img.

Once the software runs the model, two matrix files for the eigenvalues and eigenvectors, the variance-covariance matrix, and a table of eigenvalues, along with the output image are produced [appendix B2].

The second method is to carry out the covariance calculation using the modeller producing the variance-covariance matrix (fig. 5.3)
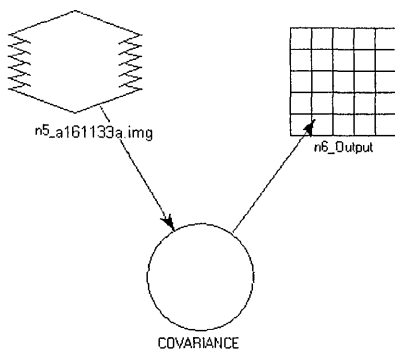
Fig. 5.3 Flow diagram to illustrate ERDAS model for covariance calculation for principal components calculation.

This is followed by the principal components transformation under the ERDAS Interpreter / Spectral enhancement drop down menus. On entering the image to be transformed the eigenvectors and eigenvalues produced during the transformation can be saved to a file of the analyst's choice. The output is stretched to an 8-bit range of data values, the standard data output for thematic images with 256 or fewer classes. Both methods were carried out but the results were found to be identical. For the rest of this analysis the 2nd method was chosen due to the format of eigenvector and value output, which allowed for import into Microsoft EXCEL for further calculation.

In order to choose the optimal components for visual interpretation of classification, calculation of the factor loadings is required. If there is a large drop off in percentage variance (equation 5.1) from the first component, it is likely that the transformation will aid in the analysis and interpretation of the image by reducing the level of

correlation. For example, using the image for the 10th June 2001 (a161133a.img) and band 1, principal component 1 the percentage variance is:

$$\%_p = (\lambda_i \times 100) / \sum_{i=1}^{n} \lambda_i$$

$$\%_P = (598278975 \times 100) / 605861816$$
$$= \mathbf{98.75\ \%}$$

This means that 98.75% of all the variance is in band one; hence almost all the information in the image is in the first principal component. The second stage of the calculation for factor loadings, uses equation 5.2. For example:

$$R_{kp} = a_{kp} \times \sqrt{\lambda_p} / \sqrt{(Var_k)}$$

$$R_{kp} = 0.446362 \ \times \ \sqrt{(598278975)} / \sqrt{(119305158.06)}$$

$$= \mathbf{0.99}$$

The factor loading (R_{kp}) in this example is almost 1, meaning that band 1 has a strong contribution to principal component 1.

Once this procedure has been carried out for all bands, a series of factor loadings is produced [appendix B2]. It is then possible to choose the three principal components with the highest values to incorporate in to a RGB image, allocating each principal component layer to a colour. Fig. 5.4 shows an example of principal components analysis on image a161133a from the 10th June 2001. The combination of components to view as a RGB image was chosen by comparing the factor loading results for each component. Those components with the most positive numbers were deemed the most useful. The factor loadings for image a161133a suggested that principal components, 2, 4, and 7 held the most useful data after component 1. However depending on the elements of most importance to the analyst this combination may not be the most beneficial. The combination of components 2, 4, 7

showed some detail of the cliff edge and the icebergs in the narrow lake, however the

1998 eruption site was all one colour. As this research looked at the 1998 eruption

site in more detail it was important to change the combination of components to show

hidden information, not visible within other combinations of principal components.

The next component from the factor loading results was 11, so a combination of

components 2, 4, 11 was used (fig. 5.4). The combination shown in fig 5.4, allows for

both the information from the suggested ideal factor loadings, 2, 4, 7, to be viewed, as

well as some of the hidden details from within the 1998 eruption site, such as the

crater lakes shown by bright blue in the image.

bright blue areas depict lakes
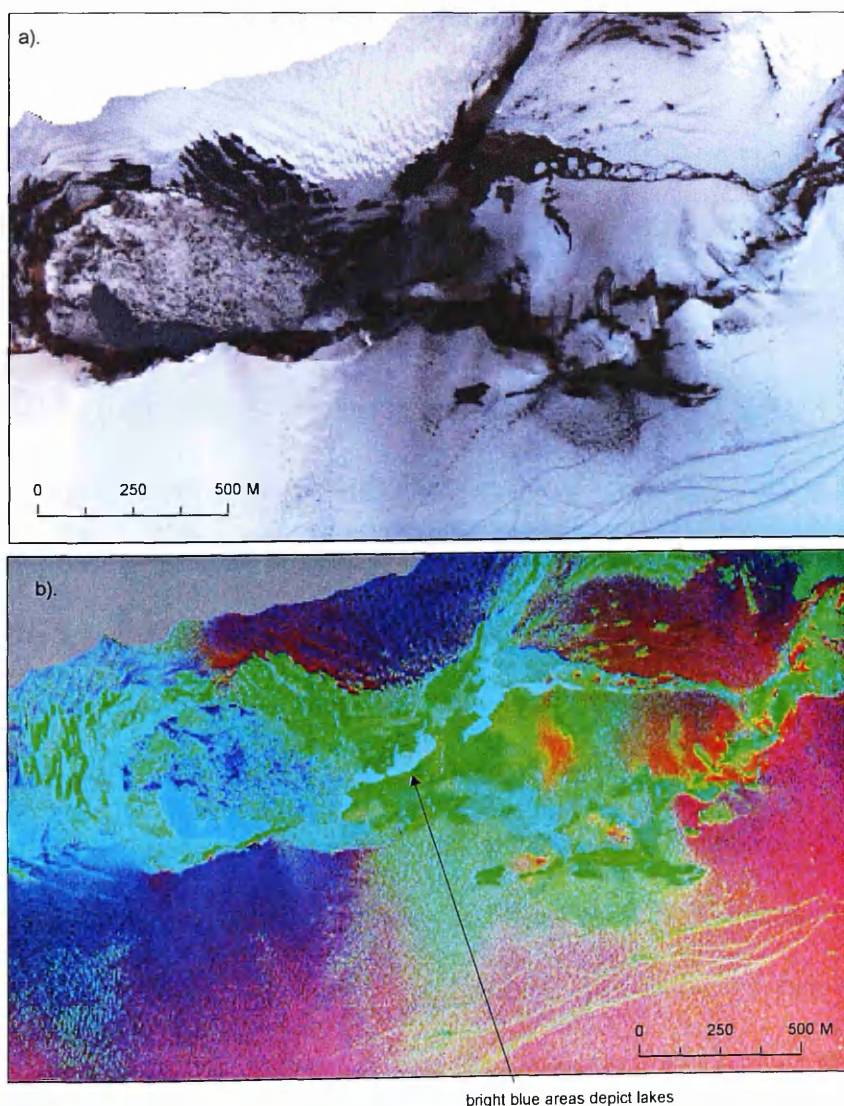
Fig. 5.4(a) False colour composite of the 1998 eruption site and caldera lake in RGB bands 1,2,3. (b) Principal components image with RGB, PC 2, 4, 11 depicting hidden details, such as the crater lake and other water bodies in bright blue.

5.8. Classification

Classification is a form of pattern recognition in which pixels are clustered and labelled. The overall objective is to automatically categorise all pixels in an image into land cover classes (Lillesand et al. 2004). Pixel clustering can be supervised or unsupervised. The main variation between these two techniques is the amount of user input that is needed for the process. Unsupervised classification is an automated process where the computer naturally clusters pixels of similar spectral properties. It automatically classifies the clusters, and the user then evaluates the outcome. By contrast, with supervised clustering the analyst defines the pixel categories at the outset, and the computer then uses the numerical descriptors to classify the image.

For the purposes of this research, classification of the ATM imagery is required in order to assign emissivity values to each land cover class for the purpose of calculating temperatures from radiance data (Liang 2001).

5.8.1. Unsupervised clustering and classification

Remotely sensed images are often composed of spectral classes that are reasonably uniform in terms of brightness across several bands. Unsupervised clustering defines and labels these natural classes (Campbell 2002). Sometimes insufficient land cover data is available to the analyst, so an automated clustering of pixels allows labels to be added after the classification has been done (Mather 1999). The identification of spectral classes created by unsupervised clustering is achieved by using information available to the analyst from fieldwork, maps or aerial photography. The advantage of unsupervised classification is that no prior knowledge of the area is needed, and human errors are reduced due to minimum user input. However, the creation of spectral classes that do not correspond with categories of interest to the analyst is

common (Campbell 2002). As unsupervised classification is highly automated, the methodology only involves specifying the input image, output file name, and number of classes to be produced. Fig. 5.5 shows the result of unsupervised clustering and subsequent classification on an ATM image.
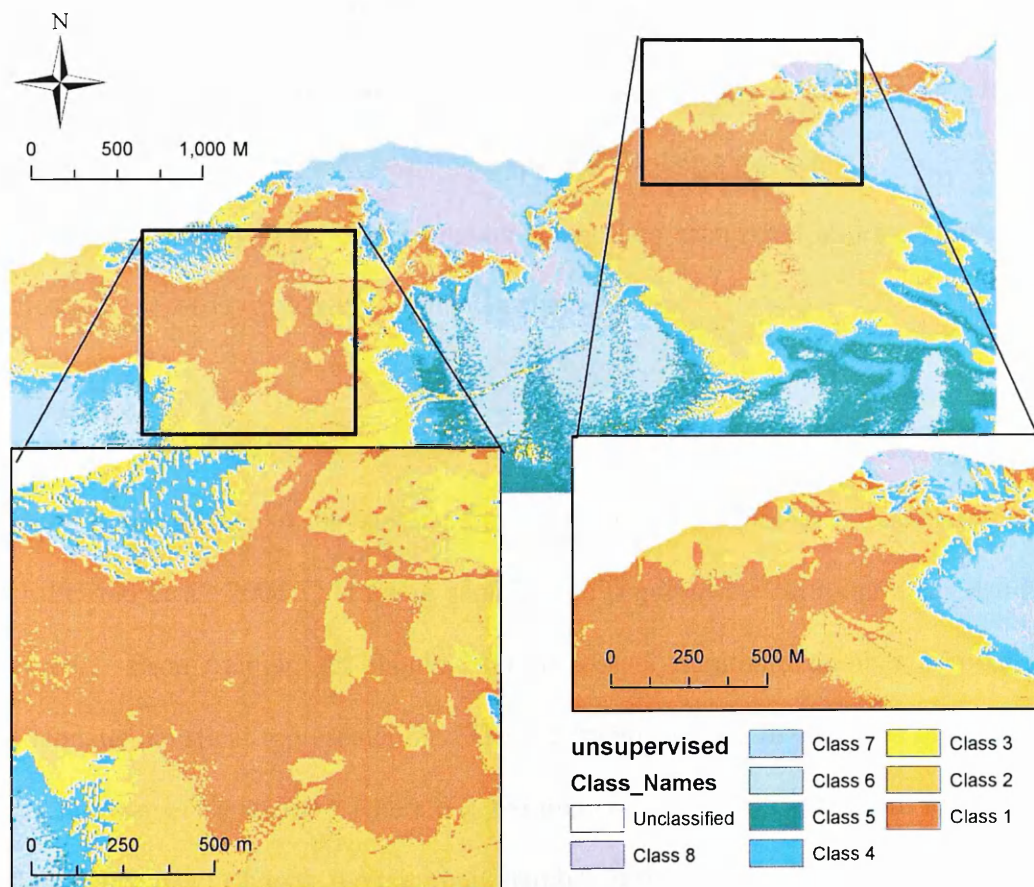
Fig. 5.5 Unsupervised classification of image a161133a.img for the 10th June2001 with 32 classes merged into eight land cover classes.

There is poor detail shown by large areas dominated by only one class, especially around the areas of the 1998 eruption site and Saltarinn geothermal area, which are key areas for this research. Because of this shortcoming, supervised clustering was used.

5.8.2. Supervised clustering

A number of statistical methods are available for carrying out a supervised classification. In this research, several methods were investigated before a suitable methodology was chosen. The following section discusses the various classification procedures available. Lillesand et al. (2004) defined supervised classification as having three stages: the training stage or clustering, where the analyst identifies representative training areas containing spectral attributes of each land cover type; the classification stage, where the computer categorises each pixel into the land cover it most closely resembles; and the output stage.

The majority of classification is automated but the training requires a large manual input as the quality of the training stage determines the success of the classification (Lillesand et al. 2004). Training samples are acquired by outlining areas using the cursor. Each training set should have at least a minimum number of pixels for adequate statistical representation. The minimum number of pixels is dependent on the number of bands (n+1 where n is the number of bands). Therefore for the ATM data which has 11 bands, the minimum number of pixels in each training set is 12.

An image can be clustered and classified using any combination of spectral bands present in an image. For the purposes of explanation, two bands will be used. The digital values attributed to pixels can be expressed graphically by plotting two bands against each other on a scatter plot (fig. 5.6). For example if a pixel in band 1 had a DN value of 10, and the same pixel had a DN value of 68 in band 2 the co-ordinate would be (10,68) in graphical measurement space. As pixels are clustered they can be

classed into different cover types. There are two main types of algorithms from which the classified image is derived, statistical and neural.
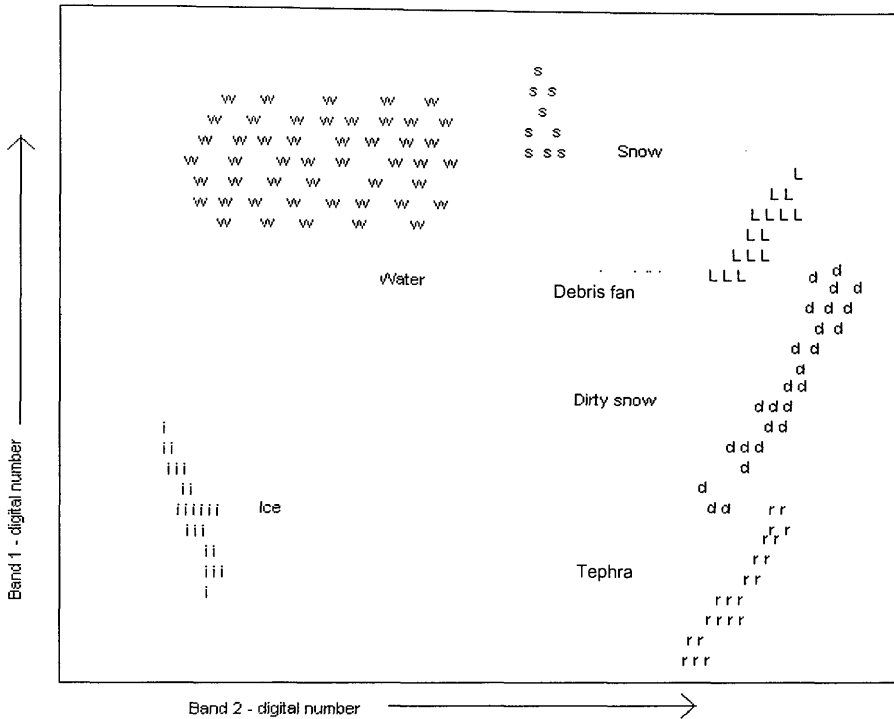
Fig. 5.6 Pixel observations from selected training sites plotted on a scatter diagram. Diagram adapted from (Lillesand et al. 2004).

Mather (1999) defined statistical algorithms using parameters derived from training data such as minimum, maximum or mean values of individual clusters. Neural methods do not rely on statistical information at all, relying instead on training classes and can be strongly influenced by misidentification of pixels as well as the size of the training set.

5.8.3. Supervised classification

A statistical method known as the Parametric Rule can be used to locate unknown pixels and classify them into the correct area. Although it is easy to extract training samples it is difficult to ensure that those sets are not contaminated by mixed pixels and therefore atypical of the class they are supposed to represent (Mather, 1999). This

can be a particular problem for the present study site in Iceland, which contains areas of snow and tephra intermixed with steam vents. A number of statistical options are available to reduce the error involved with mixed pixels.

5.8.3.1. Minimum distance

The mean spectral value in each band for each category is determined to give a mean parameter space location for each category (indicated by +) in fig. 5.7. A pixel of unknown identity can be classified by computing the distance between the pixel and the mean location for each category. The Minimum Distance method then assigns the unknown pixel to the closest class (fig. 5.7). This method is mathematically simple and computationally efficient but is insensitive to different degrees of variance within the data.
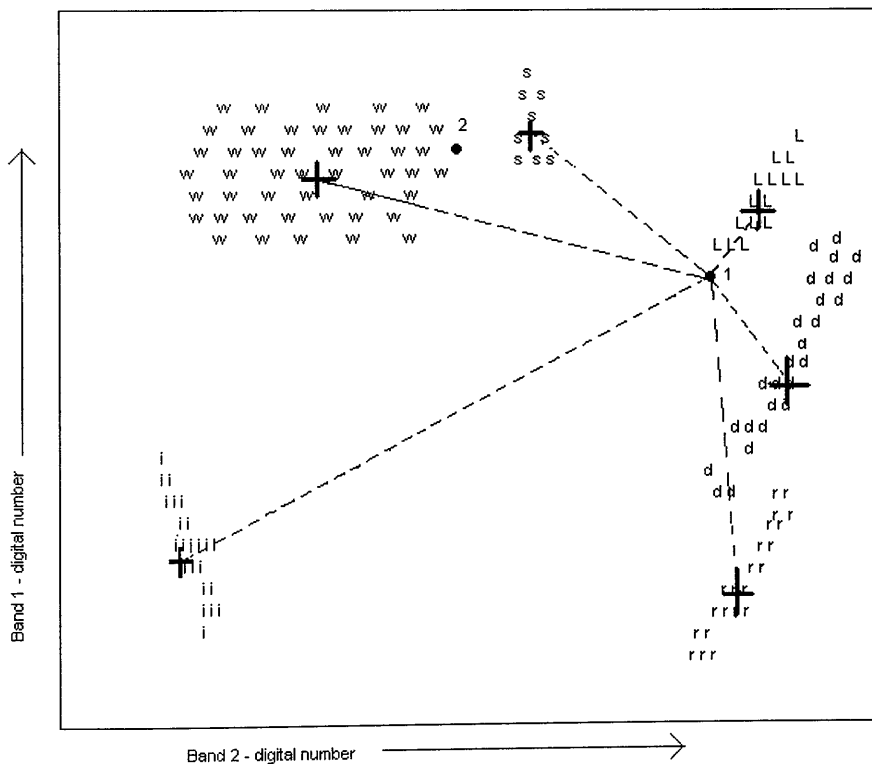
Fig 5.7 diagram to show an example of the minimum distance classification methodology. Point 1 would be placed in Class L (Debrisfan), as that is the minimum distance from the mean vector. Diagram adapted from (Lillesand et al. 2004).

For example in fig. 5.7 point 1 would be correctly categorized as part of debrisfan (L) cover class, but point 2 would be assigned to snow (s) due to shorter distance to the mean vector, but the water class (w) has great variability and would be a better class to assign it to. Minimum distance is not normally used for analysis in situations where there are spectrally similar classes or high variability between pixels.

5.8.3.2. Parallelepiped

A parallelepiped is a simple geometrical shape consisting of a parallel-sided body defined by the highest and lowest pixel values (Mather 1999). In a two-dimensional scatter diagram it appears as a rectangle, allowing unknown pixels to be classified according to the region in which they lie.

This method of classification is fast and efficient but not always accurate as points may lie within one or more parallelepiped areas and be automatically categorized into one or both classes (Lillesand et al. 2004). In fig. 5.8 dirty snow (d) has a positive covariance, and point one would be classed as dirty snow although it is situated away from the main cluster. Covariance is the tendency for spectral values to vary similarly in two bands, i.e. pixel sets are clustered in a positive slant that poorly fits the decision rule space. The water category (w) has a near circular distribution, hence no covariance and allows for a square parallepiped, within which point 2 can be clustered.

Band 1 - digital number

Band 2 - digital number
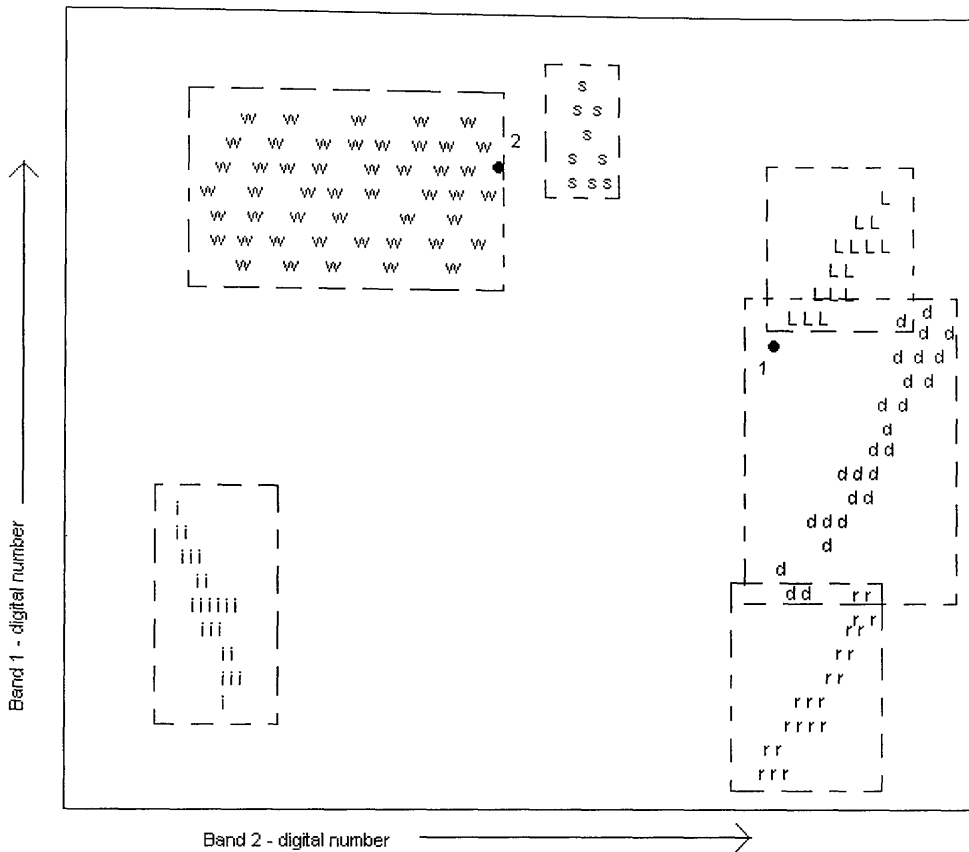
Fig. 5.8 diagram to show parallelepiped classification method. Point 1 would be classed as dirty snow (d) according to this classification, although it appears to be more like debris fan (L) in terms of clustering. Point 2 is correctly categorised as water as there is no covariance for water. Diagram adapted from (Lillesand et al. 2004).

Use of minimum distance along with Parallelepiped allows the area of overlap to be reduced, leading to improved results.

5.8.3.3. Maximum likelihood

This classification process is based on the assumption that the distributions of spectral pixels in the training categories have a normal distribution (Gaussian). The training sets are used to determine the shapes of distribution for each class (Mather 1999). This means that the computer calculates the probability of a pixel value occurring in a certain class compared to it occurring in another (Lillesand et al. 2004). After

evaluating the probability for each category, the unknown pixel would be assigned to the most likely class. An important advantage of the maximum likelihood approach is that prior knowledge can be taken into account, i.e. not just the mean vector and covariance as in Minimum Distance and Parallepiped but also the analyst's own knowledge.

5.8.3.4 Fuzzy classification

Whatever method of classification is used, there may still be a high proportion of pixels that are classed as unknown due to poor knowledge of the area, or mixed pixel training sets. Fuzzy classification presents the analyser with a higher degree of control over which class a pixel may belong to. Instead of having hard boundaries between categories, fuzzy regions are established, allowing unknown pixels to be categorised into more than one class, or more accurately partial membership. This means that a pixel can be assigned a membership grade such as 0.3 for water and 0.7 for snow in recognition that the pixel may not be properly assigned to a single class. Campbell (2002) argued that fuzzy classification can marginally improve upon standard classifications but stated that this error is difficult to prove.

5.8.4. Methodology adapted in the present study

Using aerial and ground based photographs, and personal knowledge of the site, training classes were chosen from groups of pixels in the ATM image. Small groups of the same pixel type are generally accepted as being more accurate than one large area of similar pixels. Thirty-two clusters, with four of each land cover type taken from different parts of the image, were used during the supervised clustering stage (see fig.5.9). They were then merged into 8 land cover classes for use in the classification stage. The band combination of the image being classified had to be

chosen by the analyst prior to classification. The main objective of image classification in this research was to assign an emissivity value to each land cover class, for calculating temperatures. A combination of bands 2, 4, 11 was used for the classification derived from the principal components analysis outlined in section 5.7, incorporating the thermal band. Classification decision rules were then stipulated using the parallelepiped and maximum likelihood methods, as discussed in section 5.8.3. An additional reason for using maximum likelihood classification in this analysis is because it is insensitive to atmospheric attenuation (Hoffbeck and Landgrebe 1994). This is important because no atmospheric corrections were carried out on the imagery, because of a lack of atmospheric data collected at the time of the survey.

Fig. 5.9 shows the result of image a161133a.img for the 10th June 2001 using a supervised classification. It shows considerably more detail in the water and tephra regions of the case study sites than the unsupervised classification in fig. 5.5. When a visual comparison was made with aerial photography and imagery, there were some errors in the classification. For example there are a large number of debris fans and slumps along the central part of the ridge but they are not as extensive as suggested by the classification. Therefore a formal accuracy assessment is needed to determine the confidence that the analyser can have in the classification.
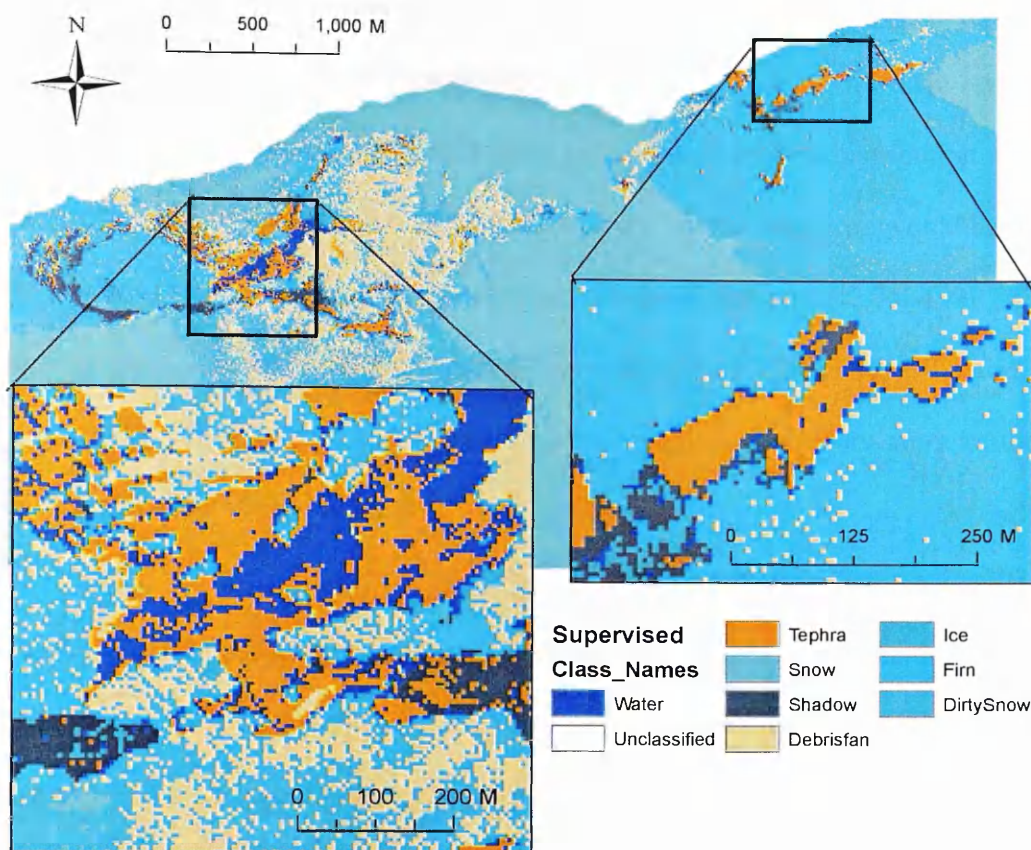
Fig. 5.9 Supervised classification image of a161133a.img for the 10th June 2001, showing 8 classes. The two case study sites are shown, the 1998 eruption site, with the crater lake, and the Saltarinn Geothermal area, depicted by tephra.

5.9. Accuracy Assessment

A number of errors can occur throughout a remote sensing project, for example, during data acquisition, processing, analysis and final presentation.   Accuracy assessment is conducted in order to understand the quality of the information extracted from the data and to determine the usefulness of the data (Congalton and Green 1999), allowing for a degree of confidence in the information extracted (Richards and Jai 1999).   Most assessments of accuracy use the same data set used for the training classification, which can over estimate the accuracy (Congalton 1991).   Therefore aerial photographs and ground observations can improve the assessment of accuracy. An assessment of accuracy requires sampling the data but this can lead to inaccuracies.

For instance, the classification scheme makes it possible to produce characteristic landscape features in order to be readily recognisable and forms the basis for accuracy assessments. The image sampling technique is driven by the distribution of the information across the image i.e. large areas covered by one class type would be more heavily weighted during the random sampling methods (Richards & Jai 1999). The level of detail, i.e. the number of categories in a classification scheme, influences the time needed for an accuracy assessment. Most classification errors are a result of misidentification of pixel identities.

The basis of accuracy assessment is to choose a set of pixels in the classified image that are then compared with aerial photographs and ground observations. The sample size must be a compromise between statistical validity and practical consideration of the time required to assess the data. Simple random sampling tends to under sample the more important areas (Richard & Jai 1999). However, stratified random sampling allows a variation in the number of pixels sampled for each land cover class, so that the more useful and interesting pixels can have a higher proportion of randomly chosen pixels to ensure their accuracy (Congalton 1991).

However it must be remembered that the quality of the accuracy assessment is dependent on the information used to establish the true land cover types (Lillesand et al. 2004). Therefore any errors present in the reference data will be incorporated into the accuracy assessment process. For this research, where there was limited ground data, the process of assessing classification accuracy was dependant upon the efficiency of the manual interpretation of aerial photographs.

The most common method for representing the degree of accuracy is in the form of an error matrix (Congalton 1991; Congalton & Green 1999; Mather 1999). The error matrix is the starting point for a number of descriptive and analytical statistical techniques of which overall accuracy is the simplest. However overall accuracy only incorporates the major diagonal data and excludes individual pixel errors classed as omission and commission errors. A commission error is defined by Congalton and Green (1999) as including an area in a category that it does not belong to, and an omission error excludes that area from the category in which it truly belongs. Congalton (1991) calls for a normalized overall accuracy, which is a better representative because it contains the off diagonal omission and commission error values. A normalised accuracy can be computed for each matrix by summing the major diagonal values, and dividing this sum by the total for the entire matrix.

For the images used in this research, snow covers the majority of the image. Consequently, when a number of pixels are chosen randomly the vast majority will be from the snow cover class. This allows a bias towards increased accuracy. Therefore each image had 150 pixels chosen using stratified sampling. Each pixel class was then checked against the ground observations from the 2004 field visit and aerial photographs. An accuracy report was produced that showed the percentage accuracy for each land cover class and an overall accuracy assessment [appendix B3]. The accuracy of the two images used for analysis was found to be 79.33% and 74% respectively. Consistent with the work of Foody (2002) accuracy of 70% and over was deemed to be acceptable; therefore there is a good degree of confidence in the classified imagery.

To further quantify the classification accuracy a KHAT statistic (kappa) was produced
using the following equation (Lillesand et al. 2004).

$$k^{\wedge} = \frac{N\sum_{i=1}^{r} x_{ii} - \sum_{i=1}^{r}(x_{i+}x_{+i})}{N^2 - \sum_{i=1}^{r}(x_{i+}x_{+i})} \qquad (5.3)$$

where r = number of rows in the error matrix, x_{ii} = number or observations in row i
and column i on (major diagonal), x_i = total of observations in row i, x_{+i} = total of
observations in column i, and N = total number of observations included in the matrix.

The result of this calculation indicates the extent to which the errors are due to chance
or a true agreement. The closer the value to one, the truer the agreement. The results
produced were 0.66 and 0.69 respectively. This means that the images can be taken as
being 66 and / or 69 percent better than a random agreement. Mather (1999) states
that a Kappa value less than 0.4 is classed as poor, whilst a figure over 0.55, is good
Therefore the results from this research can be classed as good.

5.10. Summary

A number of stages of pre-processing are required before analysis of the data can be
undertaken. This chapter described the processes applied to transform the raw data
collected during the 2001 ARSF survey of Grímsvötn to meaningful data. The initial
geometric correction and conversion of imagery to a usable format was the first stage
of processing.

The Principle Component Analysis (PCA) was used as a method of data compression.
It allows redundant data to be compacted into fewer bands, reducing the

dimensionality of the data. The bands of PCA data are non-correlated and independent, and are more interpretable than the source data. The calculation of factor loadings allowed the optimum band combination for visual and statistical analysis to be chosen.

A process of supervised clustering and classification was applied to the ATM data. In order to classify the images, assumptions of the land cover classes were made based on the ATM imagery and aerial photographs, and information from the Icelandic collaborators on the different surfaces present. A number of classification techniques were tested before using the optimum decision rules, the parallelepiped and maximum likelihood. This produced a land cover map of acceptable accuracy for use in subsequent analytical stages.

Accuracy assessment of the classified image file was carried out and showed an accuracy of 79 % and 74 % for the two images used for all the analysis. They had a Kappa (k) value of 0.68 and 0.66 respectively. Although accuracy percentages above 65%, or k value above 0.55 are classed as good, the classification could have been improved with ground observations of the land cover classes. However, because it was difficult to access some areas on the ground, it was not possible to make any additional improvements to classification accuracy.

Chapter 6 – Assessment of the geothermal output of Grímsvötn

6.1. Introduction

One of the major objectives of the over flights of Grímsvötn on 10th and 14th June 2001 was an assessment of the geothermal output from this volcano using the thermal band of the airborne multispectral imagery on the NERC ARSF aircraft. This chapter will show how the airborne thermal imagery data collected on 10th and 14th June 2001 can be converted into images that allow temperatures to be calculated for two case study regions. The first region is the 1998 eruption crater, where ground point temperatures were measured at the time the ARSF over flight took place, and the second is the Saltarinn geothermal area. A critical component of this research was an assessment of the usefulness of the NERC ARSF thermal data and a comparison with ground based measurements. The chapter begins with a calculation of temperature values derived from the ATM data, followed by a comparison of ground and airborne temperature data. By building on ground based calorimetric research, this study aims to use the thermal imagery collected by the ARSF to calculate heat flux for an inaccessible and remote environment where in situ data is limited. Previous heat flux research has taken place from the Grímsvötn caldera lake, but since 1998 leakage has meant that alternative methods must be found. A method for calculating heat flux from the crater lake is described and the results are interpreted.

6.2. Radiance to Temperature Conversion

The data acquired from the ATM was in the form of digital numbers measured in radiance (μW cm^{-2} sr^{-1} nm^{-1}). Although radiance values are adequate for analysis, ground data collected by thermometers, in degrees Celsius will be used for comparison with, and informal validation of, the thermal imagery. Therefore conversion from radiance to temperature is necessary to extract temperature information from the ARSF ATM band 11 data.

The total radiance leaving a given area is known as the Radiant Exitance (M). The relationship between spectral radiance (amount of energy released over a give area, at a fixed angle over a range of wavelengths), and radiant exitance is given by:

$$L_\lambda = M_\lambda / \pi \tag{6.1}$$

where L$_\lambda$ is spectral radiance and M$_\lambda$ is radiant exitance. This relationship, along with Planck's law (equation 3.1), discussed in chapter 3, is the basis for the conversion of radiance to temperature using a temperature conversion program devised by Wilson (personal communication, 2003). The algorithm includes a correction for sensor response and wavelength [see appendix C1].

The pre-processing carried out by the ARSF converts at-sensor radiances to surface radiances, as discussed in chapter 5, section 5.2. In this conversion, it is assumed that the ground surface acts as a blackbody. Consequently, an emissivity of 1 is used in Planck's law to calculate temperature. As this is an unrealistic approximation for most materials, the calculation of accurate temperature data requires the inclusion of more realistic emissivities. In the current analysis, a map of emissivity was derived by

firstly constructing a land cover map using a supervised classification of the ATM data as discussed in Chapter 5. Fig. 6.1 shows the land cover map.
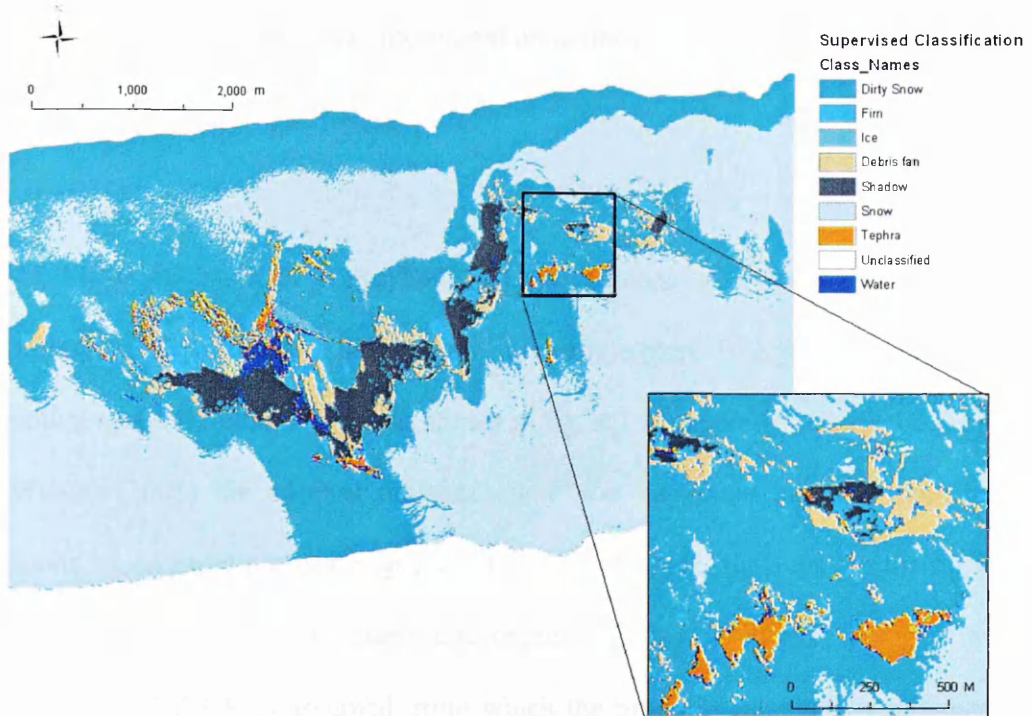
Fig. 6.1 Land cover map derived from supervised classification of ATM data.

A specific emissivity value was then allocated to each land cover class based on published values (Table 6.1) taken from Lillesand et al. (2004).

Table 6.1 Emissivity values (Lillesand et al. 2004) allocated to Land cover classes

Land Cover Class	Emissivity
Ice	0.975
Dirty Snow	0.975
Basalt	0.96
Firn	0.975
Water	0.985
Screefan	0.96
Tephra	0.96
Snow	0.98
Shadow	N/A

Using Environment for Visualising Images (ENVI) Version 3.5, an array was produced [appendix C2], allowing each pixel to be allocated an appropriate emissivity, dependent on its land cover class. A second array was produced in ENVI, to produce a new blackbody radiance based on radiance emissivity principles:

$$M_g = M_b \varepsilon \qquad (6.2)$$

$$M_b = M_g / \varepsilon \qquad (6.3)$$

where M_g is radiance of a greybody, M_b is radiance of a black body and ε is emissivity. According to Planck's law, the temperature is equivalent to the area beneath a spectral radiance curve as shown in fig. 4.3 (Chapter 4). Using the program of Wilson (2003) the spectral radiance curve was separated into 141 wavelength divisions based on the sensor response. These wavelength divisions are then used as the wavelengths for temperature conversion. Using Planck's law, an initial temperature of 273 K is assumed, from which the program calculates a radiance for the given wavelength band, sensor response and temperature.

The following equation is a variation of Planck's formula, with the added sensor response from the Wilson (2003) program:

$$M_\lambda = \frac{C_1 \lambda^{-5} resp}{\exp(C_2 / \lambda T) - 1} \qquad (6.4)$$

where spectral radiance constants $C_1 = 119095879.96$ Wm^2 and $C_2 = 14387.75225$ Wm^2, resp = sensor response, λ = wavelength (μm) and T = temperature (K).

The program iterates the temperature until the radiance matches the radiance from the image for a given pixel. This process continues for every pixel in the image until all pixels have a temperature assigned within a new array [appendix C2].

The images were exported from ENVI as GeoTiffs, for subsequent analysis in ERDAS Imagine and ArcGIS. The images were imported into ArcMAP where, to aid further interpretation, they were classified into fourteen temperature bands, each with a specific colour attributed to a 5°C range. Fig. 6.2 shows a colour composite ATM image, overlain by a temperature image with colour pallet of 5°C intervals. All temperatures below 0°C are shown as colourless, to reflect the snow and ice cover. The higher temperature areas are either in the crater lakes, or are areas of rock or ice covered by tephra, such as the 1998 eruption site, shown in the inset of fig. 6.2. The dark area is the topographic shadow of the Grímsfjall ridge for which no temperature data were able to be collected by the ARSF aircraft.
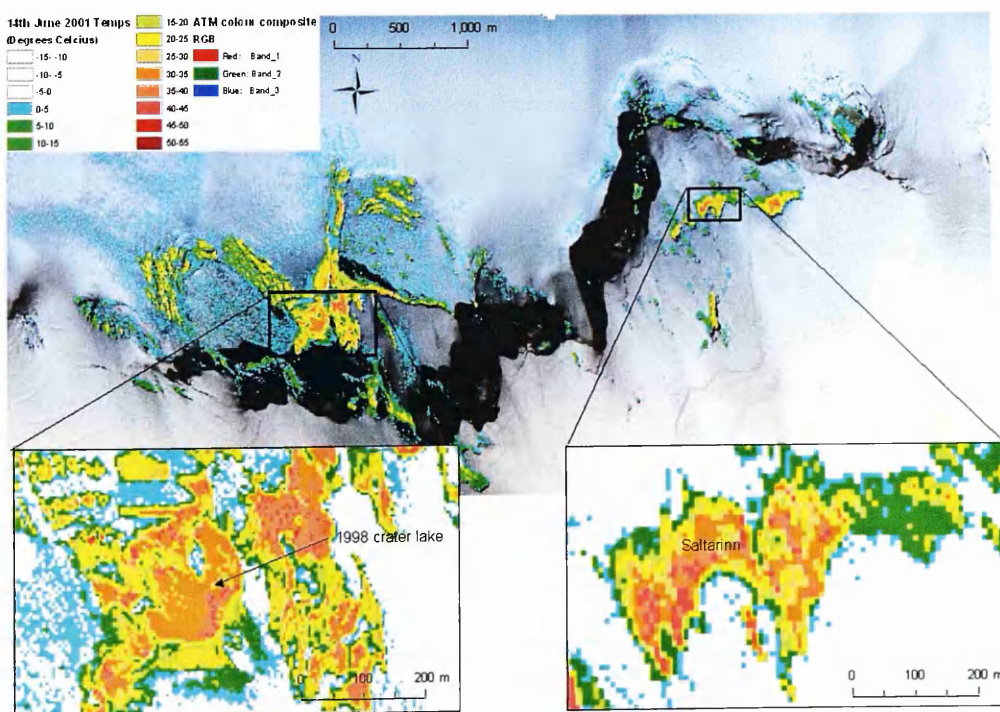
Fig. 6.2 A temperature image, overlying a colour composite ATM image (Bands 1, 2, 3 in RGB). All the temperatures above 0°C are colour coded in 5° intervals. Also shown in the inset are the two case study areas: the 1998 eruption site and the Saltarinn geothermal area.

6.3. Analysis of Temperature Images

Two areas of Grímsvötn were identified for detailed temperature analysis (fig. 6.2.). The 1998 eruption crater at the base of the Grímsfjall ridge, was chosen as a case study site as ground based temperatures were acquired there in June 2001 at the time of the aerial survey, and again in June 2004. The Saltarinn geothermal area, approximately 3 km from the 1998 eruption site, is an active geothermal region on the top of the ridge that is rarely snow covered. Ground based temperature data were collected from Saltarinn in June 2004. Using remote sensing in parallel with ground based data allows validation of remotely sensed data and a greater understanding of the geothermal activity.

6.3.1. Comparison of 2001 field and airborne data: 1998 eruption site

Ground based temperature data collected from unconsolidated tephra within the 1998 eruption crater on 4th June 2001 by Icelandic collaborators were overlain on the thermal images. The co-ordinates of the sample points were collected using a Trimble Pathfinder differential global positioning system (DGPS) instrument with an accuracy of 1-2 m. The point source temperatures were collected from the top 10 cm of tephra, using an Ebro platinum thermometer probe, with a precision of 0.1°C and accuracy of 0.3°C, along seven northwest southeast lines, with approximately three points on each line, dependent on accessibility.

Initially an attempt was made to compare the airborne and ground based temperature data by identifying specific pixels (5 x 5 m in size) within which each of the ground sample points were located. However, this revealed that the geometric correction of the ATM imagery was insufficiently accurate to allow this point within specific pixel comparison. The inadequate geometric correction of the imagery was attributable to

the inability to incorporate a DEM of adequate spatial resolution into the geocorrection procedure. This problem could not be resolved by using ground control points to perform further geocorrection of the imagery as no such ground survey points that were also identifiable in the imagery, were available. A further difficulty in comparing airborne and ground targets was that each ground measurement recorded the temperature of the small local area in contact with the thermometer, whereas the temperature recorded in the ATM data was an integrated value derived from a 5 x 5 m area of ground. Within each 5 x 5 m area considerable variability in surface temperatures may exist due to spatial variations in surface properties, in which case a single point temperature measurement is unlikely to be representative of the area as a whole. Fig. 6.3 shows how variable the temperatures across a specific area of the ground can be, especially in areas of high geothermal activity, where there are numerous fumaroles and steam vents. In order to attempt to overcome this problem and the difficulties associated with geocorrection of the ATM imagery, the following method was adopted for comparing ground and airborne temperature data.

Fig. 6.3 Photograph of Kirsty Langley, holding the DGPS used to collect co-ordinates for ground based temperature points, at a fumarole within a snow patch. The snow patch would cover a number of pixels producing a lower overall temperature, whereas the individual point temperature would be high for the fumarole.

An image composed of pixels of the same size as the ARSF data (5 x 5 metres), was constructed by interpolating the ground based point temperature data. A number of

interpolation techniques are currently used in geographic information systems (Oliver & Webster 1990). Some of the more statistically simple systems lose detail due to smoothing (Oliver & Webster 1990). Kriging is a technique based on the statistical approach of regionalized variable theory. It was selected because it allows for optimisation of unbiased results along with an indication of the confidence limits in the analysis of individual data sets shown by a variogram created during this type of analysis. A variogram is a measure of the variance between data as a function of distance (Mather 1999). The ordinary linear kriging method available within ArcMap was used, with the z field being temperature, a search radius of 10 and output cell size of 5 metres, to produce a pixelated rectangular grid.

The kriging method assumes that each spot measurement is representative of an entire pixel. However for most measurements this will be invalid. Fig. 6.4 shows that adjacent pixels can have a difference of up to 25°C. Consequently temperature variations greater than 25°C may not be unusual within one pixel. There is also a natural tendency, when making measurements in the field, to be drawn to the highest temperatures even within random sampling. There is less confidence in regions away from the sampling sites, as those areas may have the highest variance.

Two profiles, (a 200 and 300 m profile) are used to compare the ground based and ATM temperatures. A linear 200-metre profile was constructed on the interpolated image, passing through the area covered by the original ground measurement sites (i.e. the area within which we can have most confidence in the interpolation results as indicated by minimal variance). Fig. 6.4 shows the locations of the original temperature sample points, the interpolated temperature image and the location of the

profile. Blocks of three pixels astride the profile line were averaged to produce the temperature value for each location along the profile (fig. 6.4 inset).
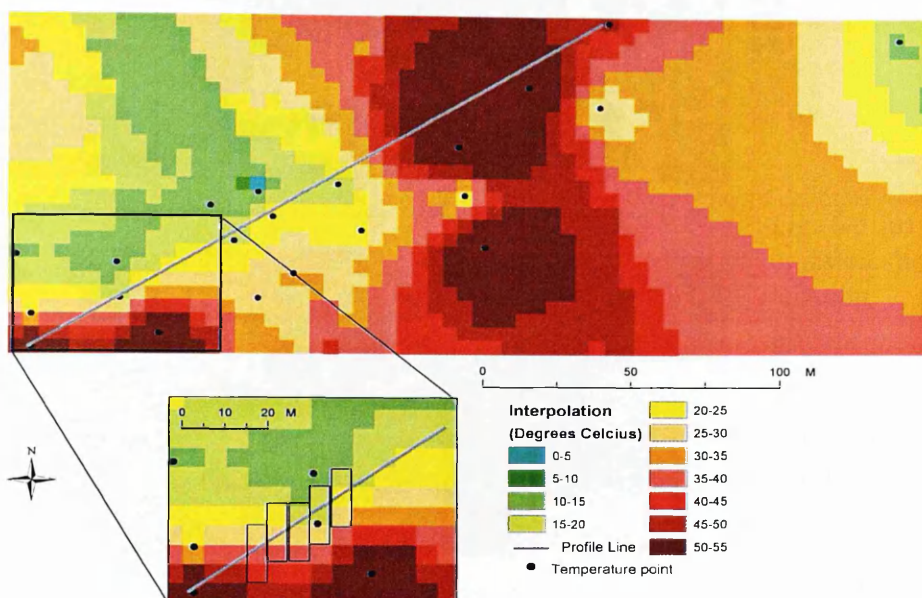
Fig. 6.4 The interpolated temperature image showing the locations of the ground based temperature sample points. The line of the profile is shown in grey. In the insert, 3 pixel-long boxes show how the average temperatures were created along the profile.

Fig. 6.5 (a), shows the 1998 eruption site, with the location of the 2001 ground based temperature points on top of the ATM image, and (b), the interpolated 2001 temperature image. The two profiles used for comparison of the ground based and airborne data are also shown. Comparison of the two images using the coloured pixels shows the two approaches, in some cases, produce similar temperatures. The difference in colour depicted in the two images is explained by the fact that the ground based images have overall higher temperatures due to the high temperature sampling points. However the key point to make is that if an area is predominately covered by red coloured pixels, it is high temperatures, and the same area on the ATM temperature image can show a similarity, even if the temperatures are predominantly lower due to averaging.
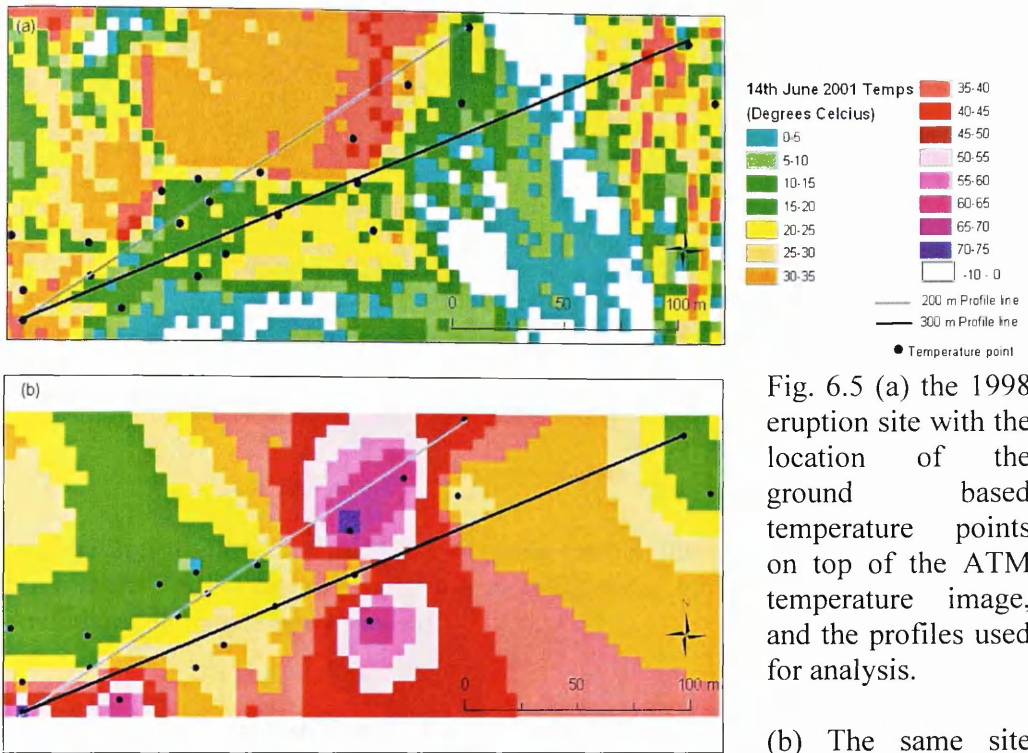
Fig. 6.5 (a) the 1998 eruption site with the location of the ground based temperature points on top of the ATM temperature image, and the profiles used for analysis.

(b) The same site with interpolated 2001 temperatures.

A 200 m long, 15 m wide profile was taken along the same profile line from the ATM temperature images (10th and 14th June 2001) and the ground and airborne temperatures were compared. Fig. 6.6 is a graph showing the three temperature profiles. The black dotted line (4th June 01) is the interpolated data from the ground measurement, and grey lines (10th & 14th June 2001) are the two ATM temperature image profiles. The graph shows that there are high temperature areas in the first 20 metres and the last 80 meters of the ground based temperature profile compared with the ATM data. However, along the central part of the profile from 40 to 120 metres the temperatures are similar, with the ATM profiles showing slightly elevated temperatures compared with the ground based ones.
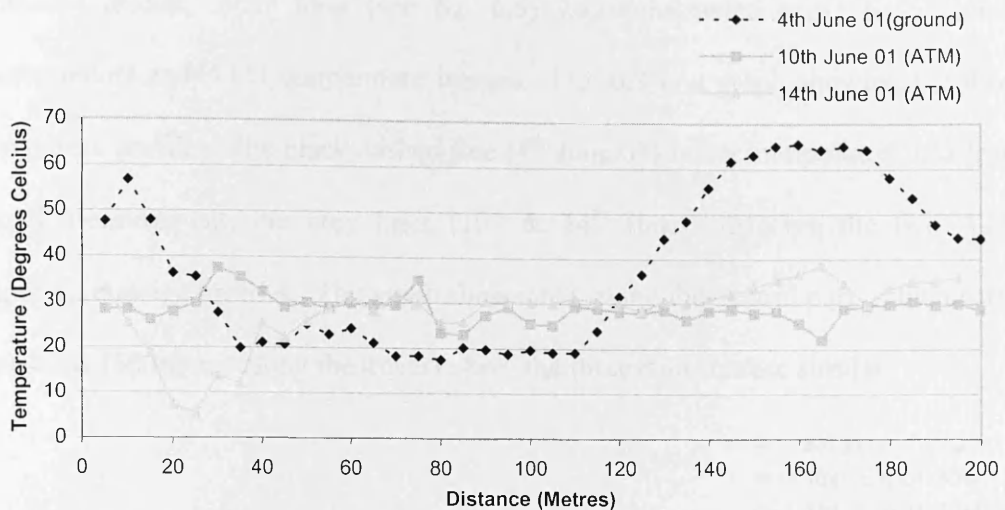
Fig. 6.6 Graph to show 200 m, least variance temperature profiles, within the 1998 eruption crater, including the ground based, interpolated temperatures (black dashed), and two thermal images (grey shades).

The similarity is further shown by the visual spatial pattern, in fig. 6.4, shown by similar coloured pixels between the interpolated image and the ATM temperature image. The drop in temperature from 4th June to the 10th and 14th, as shown in fig. 6.7, would suggest that the areas that where particularly high in temperature have dropped by 20 to 40 °C.
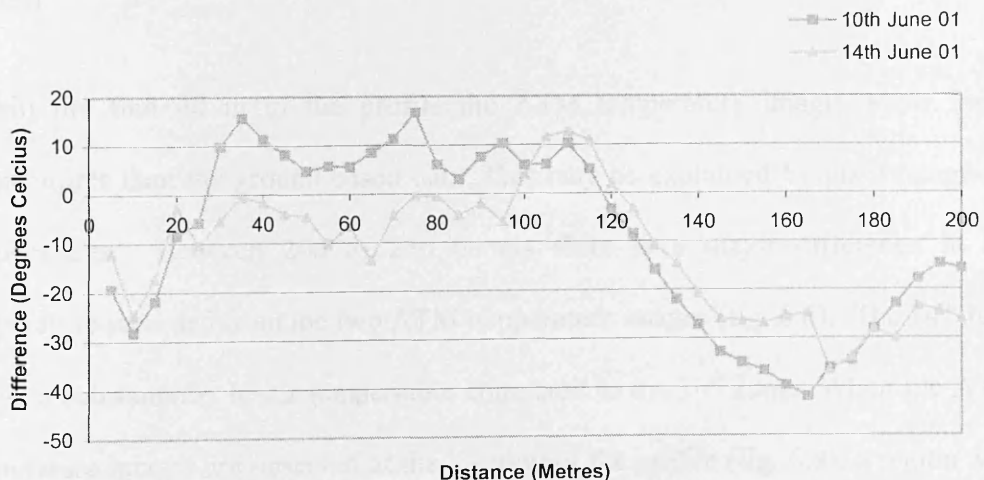
Fig. 6.7 Graph to show positive and negative temperature differences for the thermal images compared to the ground based temperatures collected in 2001, along the line of least variance.

A second profile, 300m long (see fig. 6.5) was constructed using both ground measurements and ATM temperature images. Fig. 6.8 is a graph showing the three temperature profiles. The black dashed line (4th June 01) is the interpolated data from ground measurement; the grey lines (10th & 14th June 2001) are the two ATM temperature image profiles. The graph shows that, along the central part of the profile from 40 to 150 metres along the traverse line, the three data sets are similar.
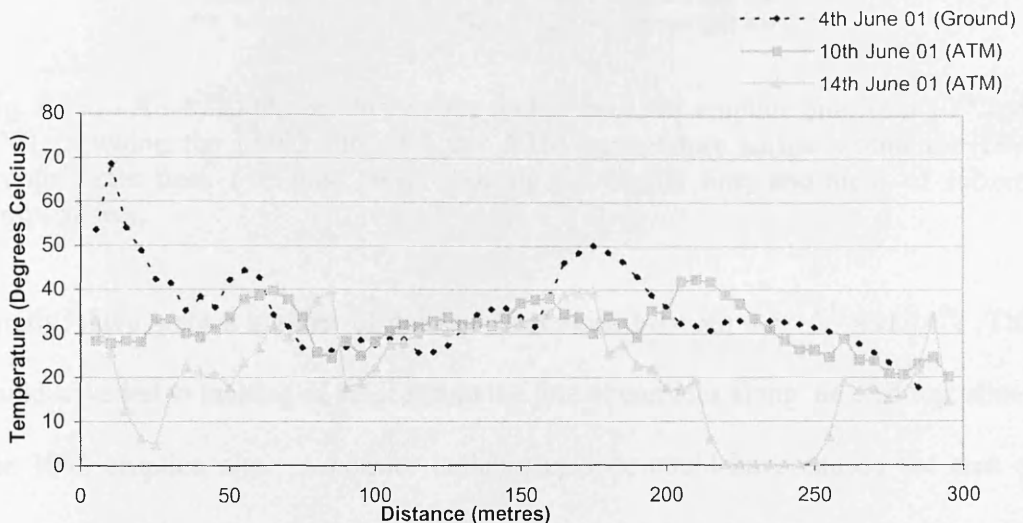
Fig. 6.8 Graph to show 300 m profile, within the 1998 eruption crater, including the ground based interpolated temperatures (black dashed), and two thermal images (grey shades).

Within the first 40 m of the profile the ATM temperature images show lower temperatures than the ground based data. This may be explained by pixel integrated temperatures. Between 200 to 250 meters there is a major difference in the temperature recorded from the two ATM temperature images (fig. 6.8). The 14th June shows a substantially lower temperature compared to the 10th June. When the ATM temperature images are observed at the location of the profile (fig. 6.9), a region with sub-zero temperatures can be seen on the central part of the image of the 14th that was not present on 10th June 2001. Possible reasons for this are as follows.
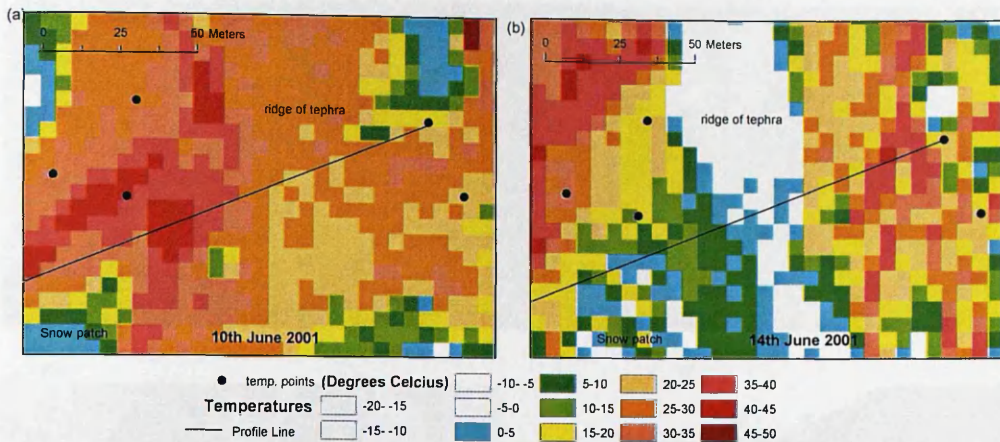
Fig. 6.9 (a) An ATM temperature image within the 1998 eruption site from 10th June 2001, showing the profile line. (b) An ATM temperature image within the 1998 eruption site from 14th June 2001, showing the profile line, and areas of subzero temperatures.

Firstly, there were a number of days of clear skies between the 10th and 14th. This could have led to melting of the ice from the line of cornices along the cliff top, above the 1998 eruption site. A cornice collapse episode could have caused the area of ground crossed by the profile to have become covered by snow and ice (in the period between the 10th and 14th June 2001), leading to the difference in temperature between the two images. However, when the same area of the ATM colour composite for the 14th June 2001 is examined (fig. 6.10a), there are no snow patches in the area with low temperatures (see blue box in fig. 6.10b). A photograph taken during the ground based survey on 4th June 2001 shows a ridge of tephra (fig. 6.10c), which could lead to shadowing. A second possible explanation for the temperature differences between the 10th and 14th June 2001, could be differences in the conditions under which the images were collected. Differences in slope, aspect and the position of the sun, due to times of acquisition of the imagery over the two days, could cause variations in shadowing.
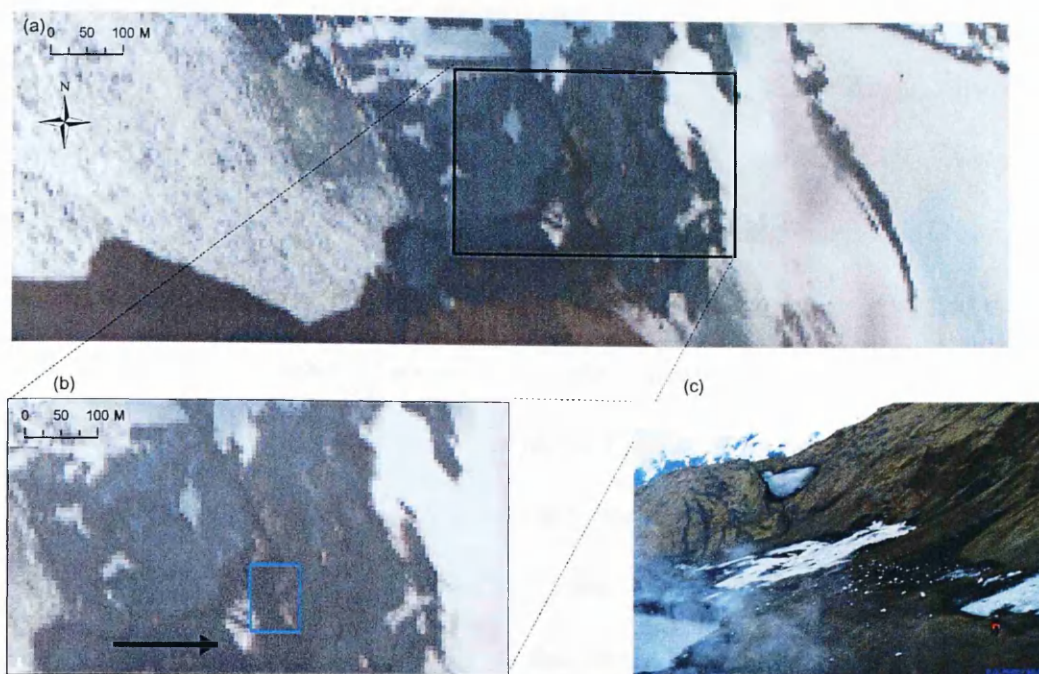
Fig. 6.10(a) True colour composite ATM image (bands 4, 3, 2 in RGB) showing the 1998 eruption site. (b) The area of interest shown by the small blue box, from which the two temperature images in fig 6.9 were taken. (c) Ground based photograph taken 4th June 2001, showing tephra ridge in the distance beyond the snow patch and a person for scale.

A point in the last 20 metres of the profile for both images shows substantially higher temperature compared with the ground data (see fig. 6.8). Low atmospheric pressure (823 and 825 hPa, hectopascal) measured from the Grímsvötn meteorological station at 1640 metres above sea level (m asl) provides one explanation for this as it would have caused a larger number of steam emissions and hence higher temperature anomalies on the images than recorded on the ground on the 4th June 2001. This would still apply, even considering the air pressure was lower on the 4th June 2001 (808 hPa), as it was the ground that was directly sampled.

A second method for comparing ground and airborne collected temperatures is to use image change detection. Change detection is an image processing tool used to discriminate land cover changes between different times of acquisition (Lillesand et

al. 2004). One method of change detection is to use image subtraction, where a pair of co-registered images of the same area, are subtracted from each other to assess the degree of change (Mather 1999). Image differencing is carried out on a pixel-by-pixel basis. Fig. 6.11(a) is the variogram for the ground based interpolated points. A nominal variance at or below 1000 was chosen for the area of change detection, in order to reduce the number of anomalies, which corresponds to an area of 15 km^2. Fig. 6.11(b) shows the change in degrees Celsius between the 4th (ground measurement) and 10th June (ATM temperature measurement) 2001. The change is divided into 10°C increments. An area of 7.5 km^2 shows a change in temperature of 10°C or less, which equates to 26.2% of the pixels, meaning that 73.8% of pixels shows a greater change in temperature. However only 44.9% of pixels are within the 10°C variation for the period 4th to 14th June 2001, hence 52.6% of pixels show a greater change. The corresponding areas from the two ATM temperature images, collected on 10th and 14th June 2001, were subtracted. This showed that 55.1% of the pixels showed a greater than 10°C difference. Fig. 6.11(c) shows the results of the image differencing. These results suggest that, although there has been has been a change in temperature over the 4 days between the two flights, there has been a greater change since the ground based data were collected. When related to the 200 m profile, the spatial change in temperature depicts the variation, seen in the profile in fig. 6.6.
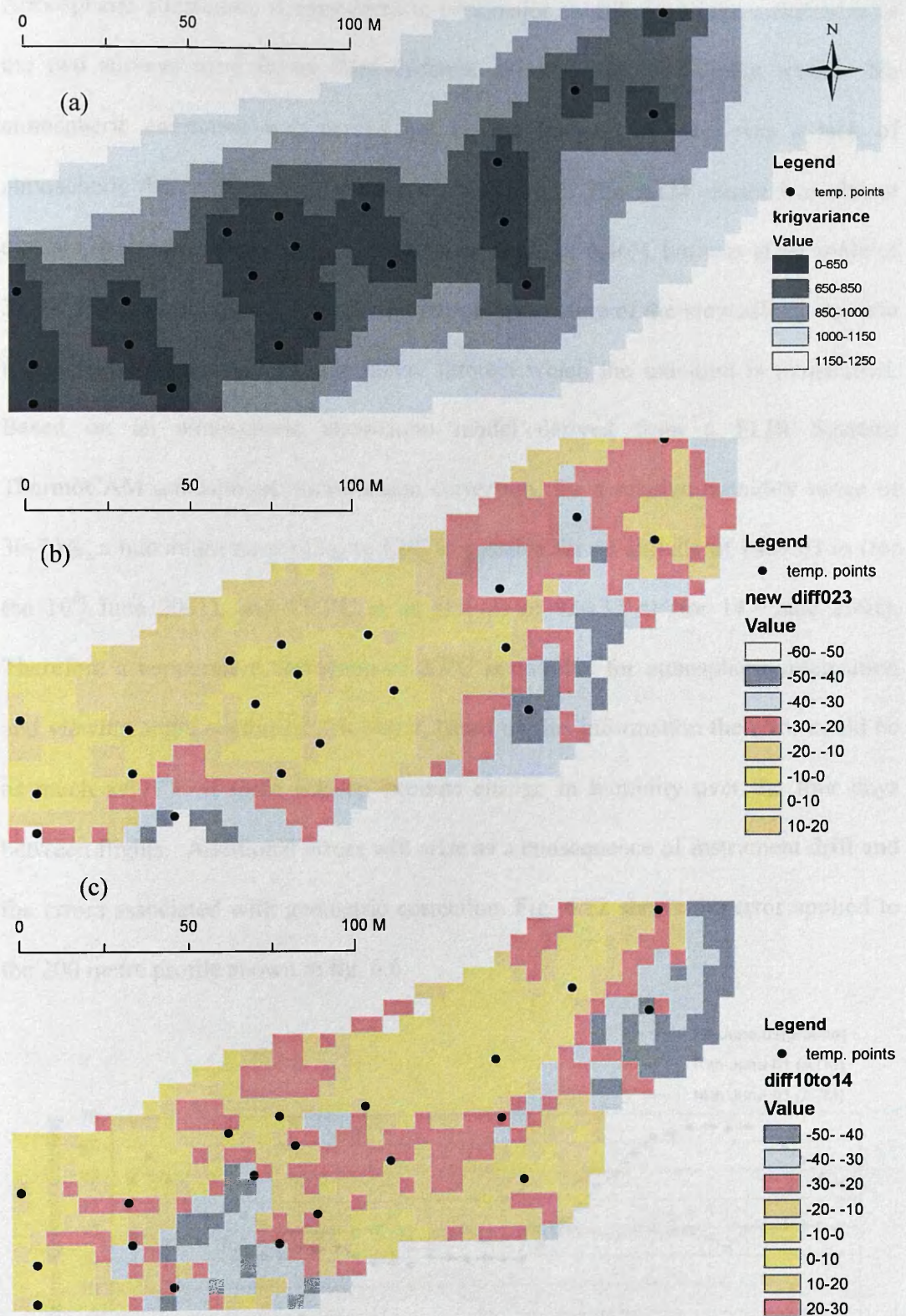
Fig. 6.11(a) The variogram for interpolated ground based temperature measurements from the 4th June 2001. (b) The change detected from 4th June 2001 to 10th June 2001, for an area of 15.33 km^2. (c) The image differencing from 10th June 2001 to 14th June 2001 for the same area as in (b).

Atmospheric attenuation is considered to be a major contributor to the differences as the two surveys were flown from different altitudes and at different times. No atmospheric correction was carried out on the images, as there was a lack of atmospheric data collected at the time of the survey. The ATM sensor was almost directly above the lake on the 14th June (at an angle of 6.46°), but was at an angle of 37.87° from normal on 10th June 2001. The oblique nature of the view affects the area imaged, and the amount of atmosphere through which the radiation is transmitted. Based on an atmospheric attenuation model derived from a FLIR Systems ThermoCAM atmospheric transmission correction, for a relative humidity range of 30-70%, a maximum error of up to 17°C is possible for an altitude of 1469.03 m (for the 10th June 2001), and 15.3°C at an altitude of 924.37 m (for 14th June 2001). Therefore a temperature correction of 2.3°C is possible for atmospheric attenuation and viewing angle combined. However, based on this information the error could be as much as 17°C if there was an extreme change in humidity over the four days between flights. Additional errors will arise as a consequence of instrument drift and the errors associated with geometric correction. Fig. 6.12 shows the error applied to the 200 metre profile shown in fig. 6.6.
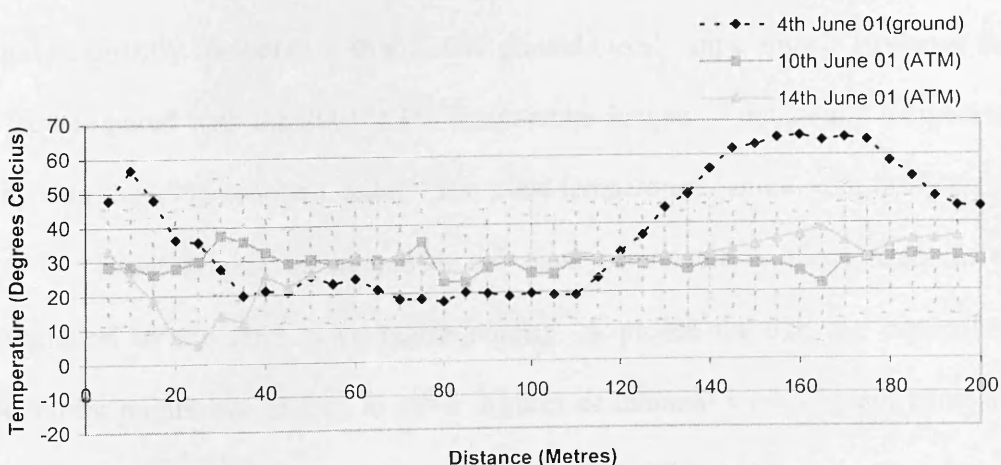
Fig. 6.12 Temperature comparison of ground and airborne data for a 200 metre profile in the 1998 eruption site. This graph shows the maximum error of 17°C.

Given the size of the error bars, the temperatures are very similar, save for a few high ground based temperatures at the beginning and end of the profile.

Comparisons of ground based temperature data with ATM temperature imagery reveal similarities in results. However there are problems combining the different techniques as it is difficult to compare temperatures at specific locations and times, due to pixel integrated temperatures and topographic variations. It is possible to derive spatial variations and change over time, but there ideally needs to be a longer time frame between the acquisitions of temperature imagery.

6.3.2 Comparison of 2004 field and 2001 airborne data: 1998 eruption site

During the field visit in June 2004 surface temperatures were measured at a number of locations within the 1998 eruption crater (fig. 6.13). The temperatures were collected using a 10 cm Digitron probe thermometer, and the co-ordinates were collected using a handheld Garmin 12XL GPS receiver. The temperatures were collected in a rough grid, approximately 3 metres apart where possible. Unfortunately as the lake level had risen considerably since 2001, the locations of the original 2001 temperature measurement points were beneath the lake. Consequently, the 2004 temperatures cannot be directly compared with the 2001 ground based temperatures. However they can be compared with the 2001 ATM temperature images to detect any temperature changes in the 1998 eruption crater. The 2004 temperature points were interpolated, using the linear kriging method, with the same parameters as those used for the interpolation of the 2001 temperature points. A profile through the interpolated temperature points was chosen to cover an area of minimal variance, and compared with a profile taken from the same location on the two 2001 ATM temperature images (fig. 6.13).
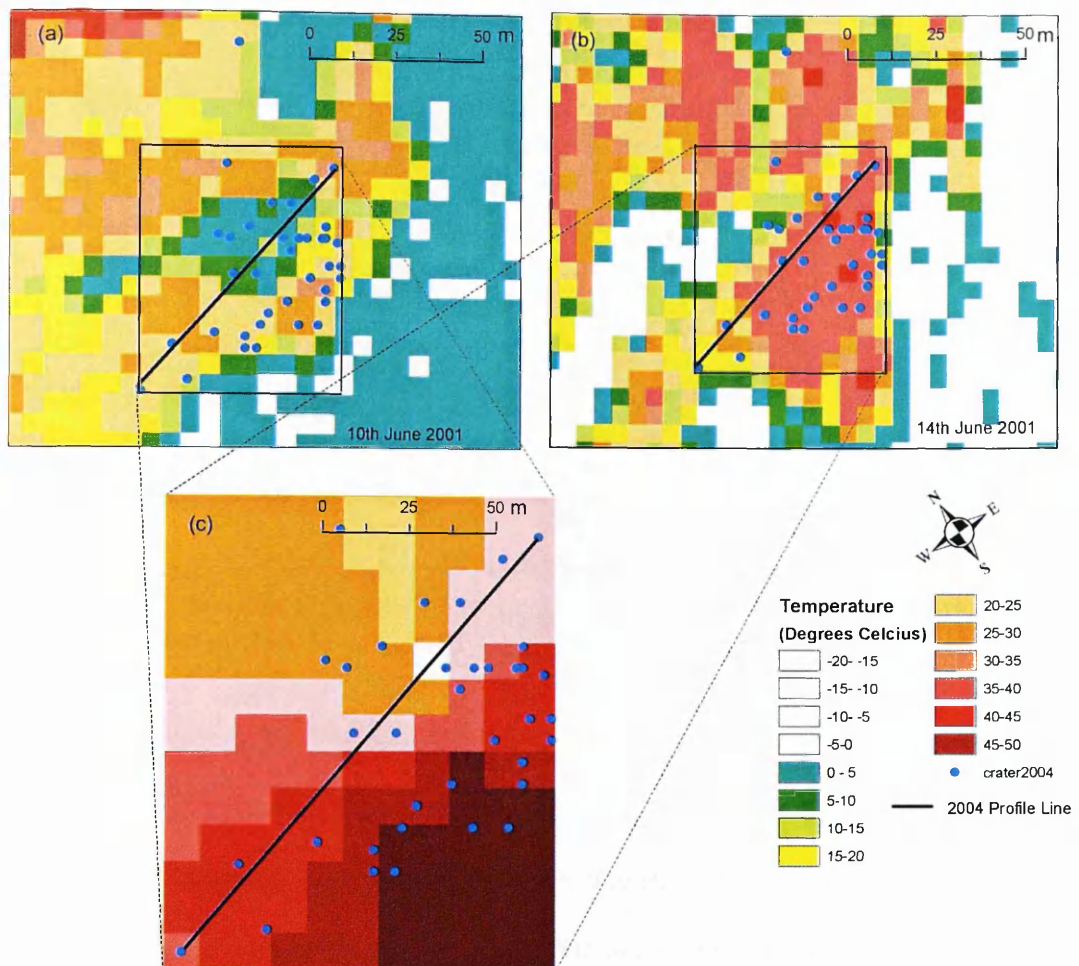
Fig. 6.13(a) Location of the 2004 temperature points and profile within the 1998 eruption crater, on the ATM temperature image for 10th June 2001. (b) Location of the 2004 temperature points and profile on the ATM temperature image for 14th June 2001. (c) Interpolated 2004 ground based temperature image.

Fig. 6.14 shows a graph of the three temperature profiles. The black dashed line represents the interpolated ground based temperature data recorded in June 2004; the grey lines show the ATM temperature data for 10th and 14th June 2001. The temperatures for the 10th June 2001 follow a similar pattern to the 2004 temperatures. At the start of the profile, the temperatures are higher, indicating a more intense geothermal region that then cools along the profile. However, the temperatures have increased by 20°C from 2001 to 2004.
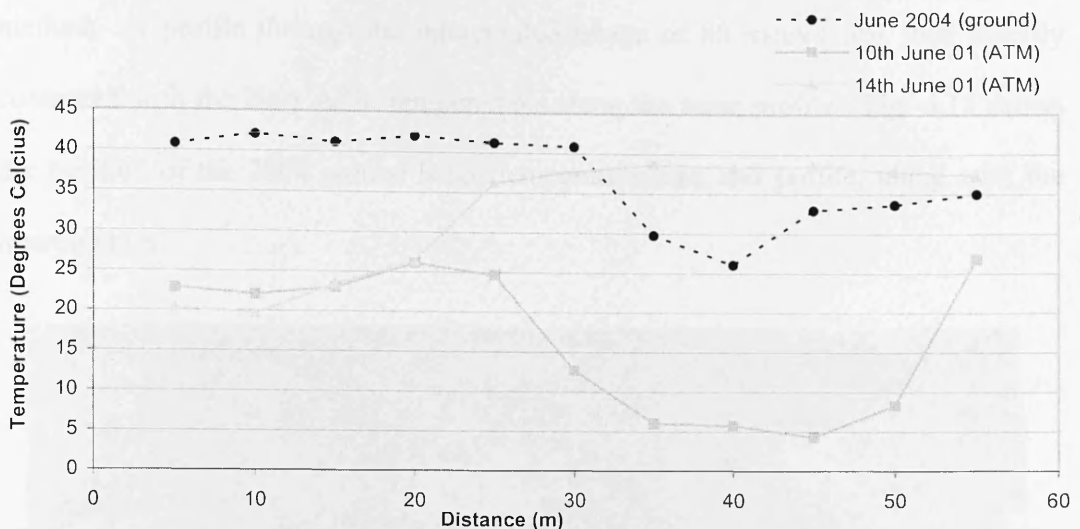
Fig. 6.14 Graph to show three temperature profiles, within the 1998 eruption crater. These are 2004 ground based interpolated temperatures (dashed), and two sets of ATM temperature data (grey) from 2001.

These results are interesting as it could suggest that the geothermal activity within the 1998 eruption crater has increased over the three years since the ATM temperature images were collected, especially as we know that there was an eruption in November 2004. However, the profile for 14th June 2001 is not the same as either the 10th June 2001 or the 2004 profile. The first 25 meters of the 14th June profile is similar to the 10th June but then the temperature increases to an average of 32°C for the remainder of the profile. An explanation for this could be that clear skies for the four days between the flights had caused an increase in solar radiation and induced melting which led to more water cycling through the tephra, which in turn led to more steam vents. This increased temperatures across the majority of the profile.

6.3.3 Comparison of 2004 field and 2001 airborne data: Saltarinn

The second case study area, Saltarinn, is a geothermal region to the south east of the 1998 eruption crater (fig. 6.15), which is so active that it is never covered by snow, even in winter. A number of surface temperature measurements were made within this area in June 2004, and the point data were interpolated using the linear kriging

method.   A profile through the interpolated image of 80 metres was then directly compared with the 2001 ATM temperatures along the same profile. Fig. 6.15 shows the position of the 2004 ground based temperature data and profile, along with the interpolation.
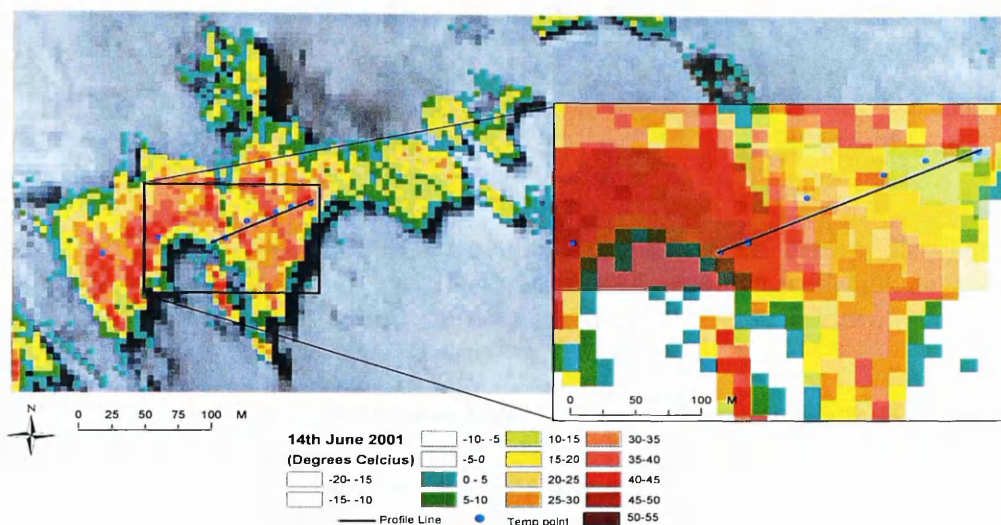
Fig. 6.15 Map to show the location of the Saltarinn geothermal area, and the position of the 2004 temperature points and profile. The inset shows the 2004 interpolated image overlying the ATM temperature image. The interpolation is shown at 40% transparency to show the spatial correlation across the pixels.

A comparison between the 2004 temperature profile across the Saltarinn geothermal area and the 2001 ATM temperature images for the 10th and 14th June was carried out. Fig. 6.16 shows the three temperature profiles. The Saltarinn 2004 data shows a steady decrease in temperature along the profile, suggesting a particularly intense region of geothermal activity that cools to the east. The ATM image data from 10th and 14th June 2001 are similar but show more variation along the profile than the interpolated ground data. This may be due to the fact that there will be areas along the ground based temperature profile where there were no original data points and the values have been interpolated creating the effect of a smooth variable temperature profile.
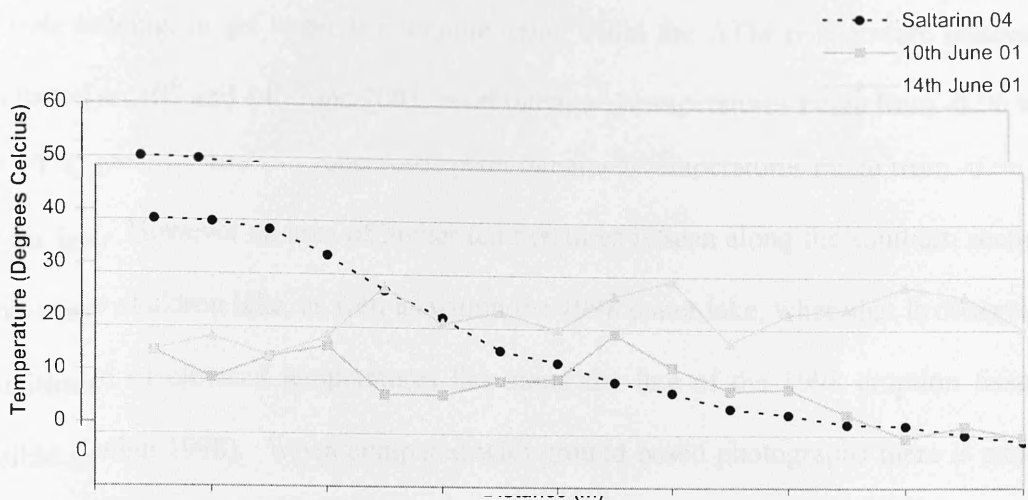
Fig. 6.16 Graph to show three temperature profiles, from across the Saltarinn geothermal region, Grímsvötn. The 2004 interpolated temperatures (black dashed) are compared with the two sets of airborne data taken in 2001 (grey shades).

The first part of the 2004 profile has higher apparent temperatures than both of the 2001 profiles and corresponds to the results found in the 1998 eruption crater. The 14th June data shows an apparent increase in temperature from the 10th to the 14th June 2001. This may be caused by an increased heat flow, and possible steam emissions similar to that in the 1998 eruption crater for 14th June 2001 data. While the first 20 m of the 2004 profile is higher than either of the 2001 profiles, the second half of the 2004 is similar to the 10th June 2001. When the spatial variation is observed (fig. 6.15), the western part of the Saltarinn appears to have higher temperatures, and the eastern region appears to be cooling.

6.3.4. Collection of temperature data from inaccessible locations

The NERC ARSF visible and thermal infrared images reveal the presence of a number of ice cauldrons around the Grimsvötn caldera together with areas that cannot be measured in the field. This includes inaccessible parts of the Grímsfjall ridge such as the small water filled ice cauldron on the eastern edge of the caldera (fig. 6.17). The ice cauldron has steep sided ice walls meaning there is no way, other than by using

remote sensing, to get water temperature data. From the ATM temperature images, collected on 10th and 14th June 2001, pixel integrated temperatures range from -0.96 to 25.09 °C. However an area of higher temperatures is seen along the southern section of the ice cauldron lake, as well as within the 1998 crater lake, when that is observed. The trend of elevated temperatures lies along the line of the 1998 eruption fissure (Smithsonian 1998). When compared with ground based photographs there is steam visible across these sections of the lakes. These areas of increased heat output, may indicate the location of the caldera fault (Guðmundsson 1989). This is a zone of weakness, and hence a possible pathway for magma intrusion (Einarsson et al. 1997; Konstantinou et al. 2000; Wilson & Head 2002).
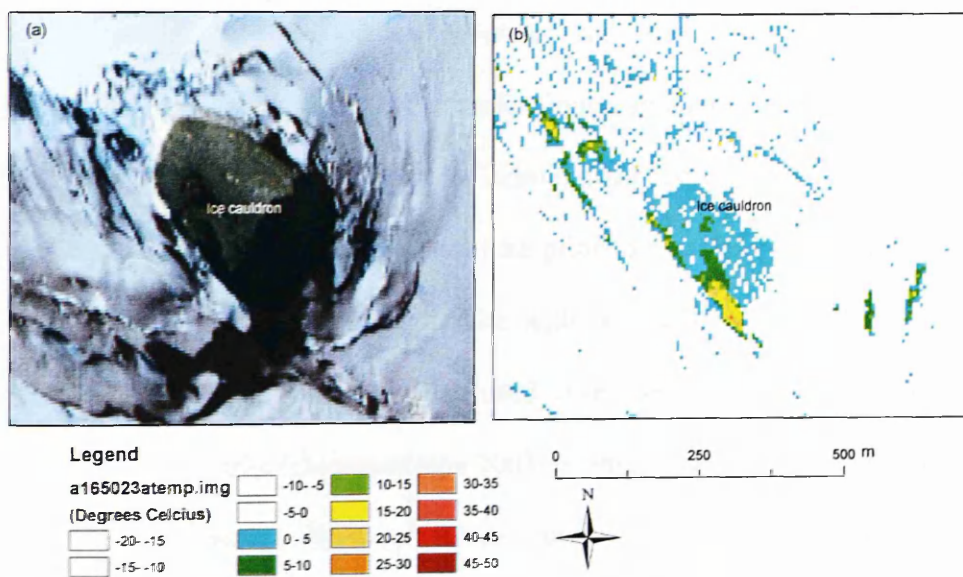
Fig. 6.17(a) True colour ATM composite of an inaccessible ice cauldron to the east of Grímsvötn caldera. (b) ATM temperature image of the inaccessible ice cauldron, showing the higher temperatures in the southern section of the lake

The more data that are available, the greater the chance of understanding the processes at work, within the Grímsvötn caldera. This research has shown that, despite the issues involved with geocorrection and co-registration of the ground based temperature points and ATM imagery, it is possible to compare ground based and

aerial data sets for a remote region, to show similarities in thermal anomalies, and combine the results to give a broader understanding of the processes at work. The results in this section have shown that both spatial and temporal changes in temperature can be observed, along with temperatures from otherwise inaccessible regions.

6.4. Heat Flux

Precursory evidence of subglacial eruptions is often shown in the melt water rather than on the rock or ice surface. Measurements of the variations in the thermal output of Grímsvötn caldera have been made over a 69-year period (Björnsson & Guðmundsson 1993). The ice covered Grímsvötn caldera lake was a unique calorimeter for measuring the heat transfer from magma to ice and melt water, and the rate of accumulation of melt water (Guðmundsson 2003). However this work was carried out on the Grímsvötn caldera lake prior to the 1998 eruption, when the lake was believed to be an enclosed system with no leakage. Since the 1998 eruption, increased melting at the ice dam that used to seal Grimsvotn caldera lake has led to leakage from the lake (Guðmundsson 2003). Consequently, calorimetry can no longer be effectively used. However temperatures recorded from crater lakes or ice cauldrons are still fundamental in monitoring Grímsvötn. Heat lost via radiation directly into the atmosphere from exposed rock outcrops (nunataks) and open water, cannot be measured using calorimetry based on ice melting.

The original proposal for the airborne survey in 2001, was to collect data for use in calculating heat flux from the Grímsvötn caldera lake. However, during the 2001 ground survey the caldera lake was inaccessible; hence measurements such as depth

and volume of water were not collected. Previous work on heat flux has been based

on melt water volumes but because of the leakage and the continuous change in lake

level, an alternative method had to be used. Remote sensing allows temperatures to be

collected from lakes and areas of open water where volumes are unknown. In this

section, a method will be presented to show how surface temperatures along with

meteorological measurements can be used to study heat flux from the 1998 eruption

crater lake to the atmosphere, using ATM thermal imagery.

Fig. 6.18 shows the location of the 1998 crater lake.
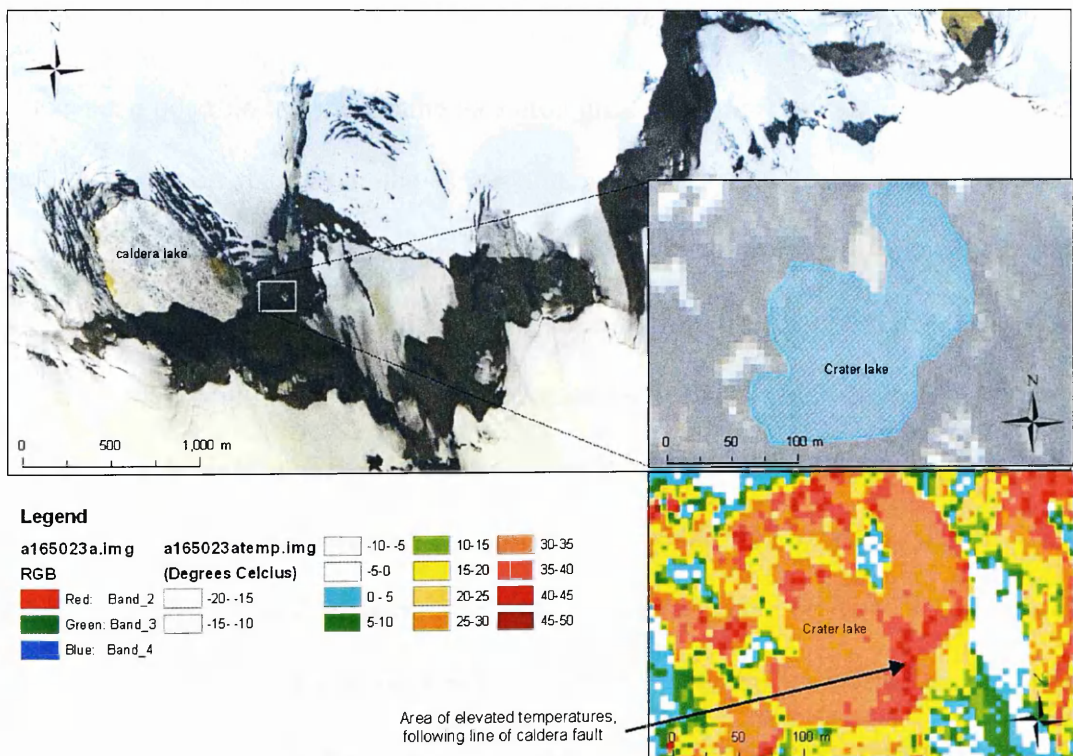
Fig. 6.18 Colour composite ATM image, with the 1998 crater lake inset, and a temperature image of the lake from which the temperatures were taken to calculate heat flux.

Fig. 6.19 is a frequency distribution curve of the 1998 crater lake temperatures from

the two ATM temperature images. This shows that the overall distribution of

temperatures is similar for the two dates. For the calculation of heat flux, a mean

temperature was taken from the distribution in fig. 6.19.
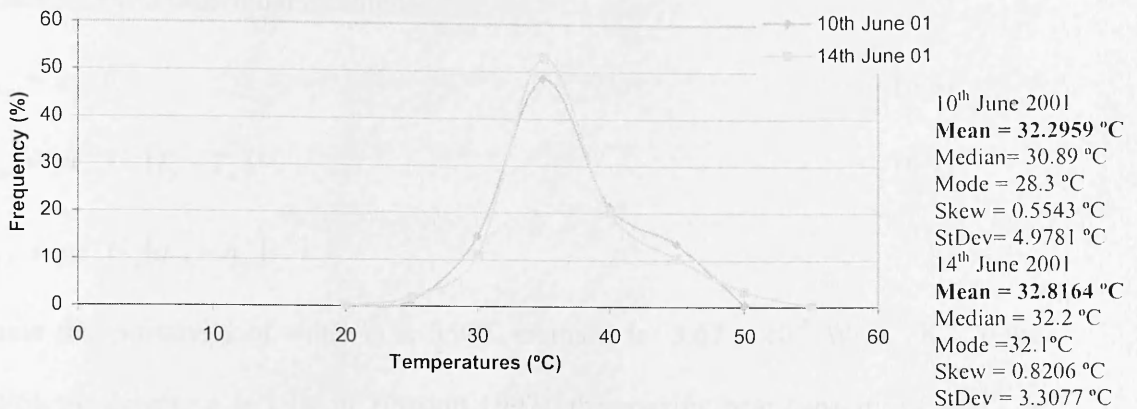
Fig. 6.19 Histogram of temperature within the Grímsvötn 1998 crater lake for the 10th
and 14th June 2001.

It has been possible to estimate the meteorological conditions at the time of the aerial

survey based on data from the Grímsvötn weather station [appendix C4 & C5].

However only air pressure and temperature were available from the Grímsvötn station

so wind speed and cloud cover data has been taken from the Skaftafell meteorological

station 30 km south of Grímsvötn, courtesy of the Icelandic Meteorological Institute

http://www.vedur.is/english/. However it should be noted that Skaftafell is at a lower

altitude than the study site and not on the ice sheet. The relative humidity data

necessary for the calculations came from an average of two other nearby

meteorological weather stations, neither of which are located on ice sheets. Although

data from six weather stations were available, only two have relative humidity

measurements.

The total upward heat flux (Q_T) from the Grímsvötn lake is the sum of all the fluxes

from individual processes (Jones et al. 2005, Gill 1982), namely,

$$Q_T = Q_{Lo} + Q_{Sh} + Q_{LE} - Q_{Si} \qquad (6.5)$$

where Q_{Lo} is the net upward long wave radiation, Q_{Sh} is the sensible heat flux, Q_{LE} is

the latent heat flux and Q_{Si} is the incoming short wave solar radiation. Each parameter

is derived from individual equations.

$$Q_{Lo} = \varepsilon_s \sigma T_s^{4} \qquad\qquad (6.6)$$

$$Q_{Sh} = \rho C_p U_a \left(T_s - T_a\right) \qquad\qquad (6.7)$$

$$Q_{LE} = \rho C_e U_a \left(q^*_s - q_a\right) \qquad\qquad (6.8)$$

where the emissivity of water ε_s is 0.985, sigma σ is 5.67 x 10^{-8} W m^{-2} K^{-4} (Oke

1995), air density ρ is 1 kg m^{-3}(Garratt 1992), the specific heat capacity of air C_p is

1005 J Kg^{-1} K^{-1}(Gill 1982; Garratt 1992), transfer coefficients for sensible and latent

heat C_e is 1.4x10^{-3} W m^{-2} K^{-1} (Hicks 1972; Jones et al. 2005), U_a is wind speed m s^{-1},

T_s is lake surface temperature in K, T_a is mean air temperature in K, L is latent heat of

evaporation 2.5 x 10^6 J kg^{-1} (Gill 1982; Garratt 1992), q^*_s is saturated specific

humidity at water surface is, and q_a is specific humidity at reference height.

As specific heat capacity, density and latent heat of evaporation varies only slightly

with temperature (Jones et al. 2005); constant values have been assigned from the

literature. To calculate outgoing long wave radiation, Q_{Lo}, a correction for cloud

cover and back radiation is added to the basic equation. For example,

$$Q_{Lo} = \varepsilon_s \sigma T_s^{4} \underbrace{\left(0.39 - 0.05e_a^{1/2}\right)}_{x} \underbrace{\left(1 - 0.6n_c^{2}\right)}_{y} \qquad\qquad (6.9)$$

where x is the correction factor for back radiation in the absence of clouds, where e_a is

the vapour pressure of water at a standard height, y is the correction for cloud effects

based on cloud cover (n_c) measured at the Skaftafell Meteorological station on the

days of the aerial survey 10th and 14th June 2001.

For sensible heat flux, equation 6.7 is used and is straightforward, as the input values are taken straight from the literature and meteorological stations. Latent heat flux (equation 6.8) is however more complicated as it requires that saturated specific humidity at the surface ($q*_s$) is calculated from saturated vapour pressures ($e*_s$), at the surface. The same equation is then used to calculate specific humidity of the air (q_a) from vapour pressure of the air (e_a).

(a) $q^*_s = \dfrac{\lambda e^*_s}{P_o + (\lambda - 1)e^*_s}$ (6.10)

(b) $q_a = \dfrac{\lambda e_a}{P_o + (\lambda - 1)e_a}$

where $\lambda = 0.622$, and is the ratio of gas constants for dry and moist air (Garratt1992) and P_o = air pressure in hPa (from meteorological station at Grímsvötn).

In order to calculate the required vapour pressures the following equations are required. Firstly the saturated vapour pressure of the surface (6.11), and then the saturated vapour pressure of the air (6.12), followed by a correction from the known relative humidity (6.13), to result in the vapour pressure of the air.

$e^*_s = 6.112 \exp\left[\dfrac{[17.67(T_s - 273.15)]}{(T_s - 29.65)}\right]$ (6.11)

$e^*_a = 6.112 \exp\left[\dfrac{[17.67(T_a - 273.15)]}{(T_a - 29.65)}\right]$ (6.12)

$e_a = relative humidity \times e^*_a$ (6.13)

Equations 6.11 and 6.12 are identical, except for substituting the air temperature for the surface temperature. In this study, data from six nearby meteorological stations was collected [appendix C4], but relative humidity readings were only available from two of those for June 2001. Therefore relative humidity was taken as an average of the two. When the products of equations 6.10 to 6.13 are placed into equation 6.8, a figure for the latent heat flux results.

The final parameter needed for the total upward heat flux is the incoming short wave solar radiation. As this was not collected at the time of the survey a figure has been taken from the literature. In 2001, Guðmundsson et al. (2003) derived a number of models for summer ablation on Langjökull ice sheet, Iceland, using climatic data necessary for heat flux calculation. Their measure for incoming short wave solar radiation was 280 W m^{-2}, which has been used for this research. An average constant for the proportion of solar radiation reflected over lakes has been taken as 70% from Oke (1995) to obtain a downward flux of 260.4 W m^{-2}.

Using data from the 10th June 2001, and the parameters listed below in table 6.2 and equation 6.5, the total upward flux in W m^{-2} can be calculated [appendix C3].

Table 6.2. Parameters used in the calculation of heat flux.

Parameter	Value
ε_s	0.985
σ	5.67 x 10^{-8} W m^{-2}K^{-4}
ρ	1
C_p	1005
C_e	1.4x10^{-3}
U_a	6.78 m s^{-1}
T_s	305.44 K
T_a	274.15 K
L	2.5 x 10^6 J kg^{-1}
q^*_s	0.0374
q_a	0.0039

$$Q_T = Q_{Lo} + Q_{Sh} + Q_{LE} - Q_{Si}$$

$$= 107.597 + 298.490 + 794.141 - 260.4$$

$$= 939.828 \text{ W m}^{-2}$$

For the lake area of 10625 m^2 this equates to a total energy of approx 10 MW. If you take the average caldera size as 5 km^2, the total heat flux would be 5495 MW. This

figure corresponds with that of Björnsson and Guðmundsson's (1993) calculations of
heat flux for the entire Grímsvötn caldera.

The above result is based on a mean temperature value for all the pixels across the
lake surface. However, it is possible to calculate heat flux for each individual 5 x 5
metre pixel. Fig. 6.20 is a histogram of the heat flux values found across the lake
derived from calculating heat flux for every pixel in the lake. It shows that, based on
a constant set of values for wind speed, air temperature and relative humidity there is
some variability over the lake for the two dates surveyed. The histogram for 14th June
shows a near normal distribution, but the 10th June histogram shows greater variability,
with higher heat flux values being evenly distributed. The greatest difference is that
the overall heat flux is higher on the 14th June 2001, with a mean value of 1099 W m^{-2}
compared to 1035 W m^{-2} for the 10th June. This corresponds to the temperature data
compared in section 6.3 which showed that the temperatures appeared higher on the
14th June 2001.
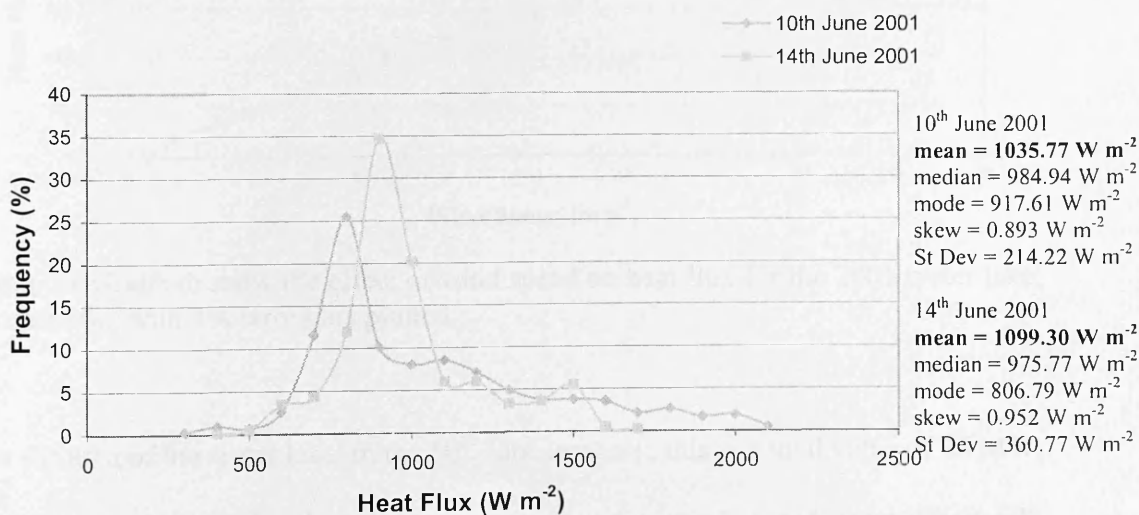
Fig. 6.20 Histogram distribution for heat flux, pixel by pixel across the 1998 crater
lake, for 10th and 14th June 2001.

This calculation of heat flux was based on wind speeds of 6.78 m s^{-1} (10th June 2001) and 6.68 m s^{-1} (14th June 2001), which were the average wind speeds taken from the Skaftafell meteorological station. Wind speed is a major variable in the calculation for heat flux as the faster the heat is removed from the surface the greater the heat flux. To show the importance of wind speed, and hence the variability of heat flux, the calculation was carried out for a range of wind speeds. Fig. 6.21 shows the results of the heat flux against wind speed for a range of 1-20 m s^{-1}. There is a linear trend, showing the importance of being able to define the wind speed. For example a change in wind speed of 10 m s^{-1} can cause a change in the heat flux of 1500 W m^{-2}. A wind speed of 16.6 m s^{-1} was recorded during the 1996 Gjálp eruption. This equates to a heat flux of approximately 2500 W m^{-2} from fig.6.21.
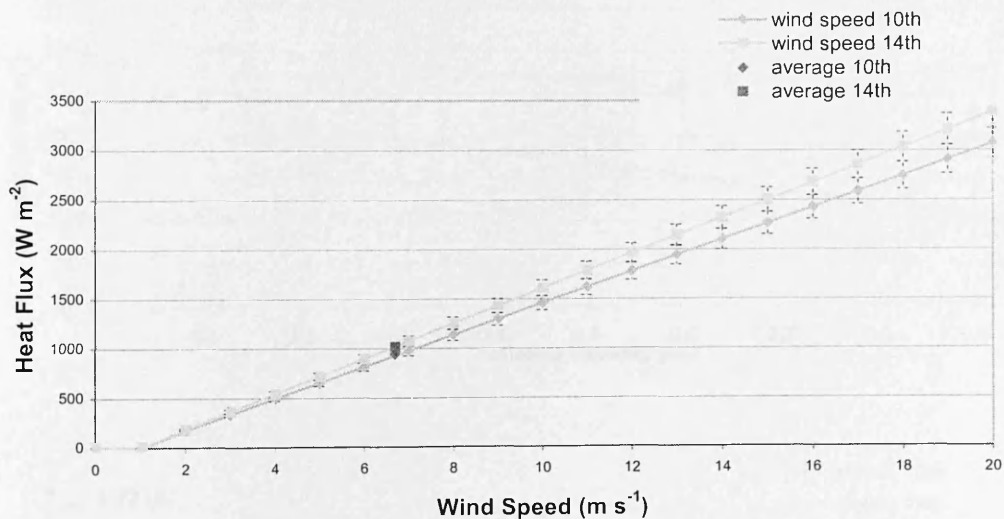
Fig. 6.21 Graph to show the effect of wind speed on heat flux for the 2001 crater lake, Grímsvötn., with 5% error bars plotted.

For the area of the crater lake, in the 10th June imagery, this is a total value of 26 MW, compared to 10 MW using the average value for wind speed from Skaftafell. Consequently, it is important to collect accurate wind speed data on an ice sheet such as Vatnajökull, where wind speeds and weather can be extreme and change rapidly.

The other parameters that were estimated for use in the heat flux calculation have been looked at in terms of their effects on the total heat flux produced from Grímsvötn crater lake. Fig. 6.22 shows three of these parameters: relative humidity, air temperature and cloud cover. Relative humidity, fig. 6.22(a), has a gentle linear relationship. With a 5% error assumed, relative humidity has an effect on the heat flux. The effect of relative humidity may not be observed if a 10% error is assumed in calculations, but if a 5% error is used then the affects are detectable. Therefore relative humidity should be recorded as accurately as possible for heat flux calculations.

Fig. 6.22 (a)
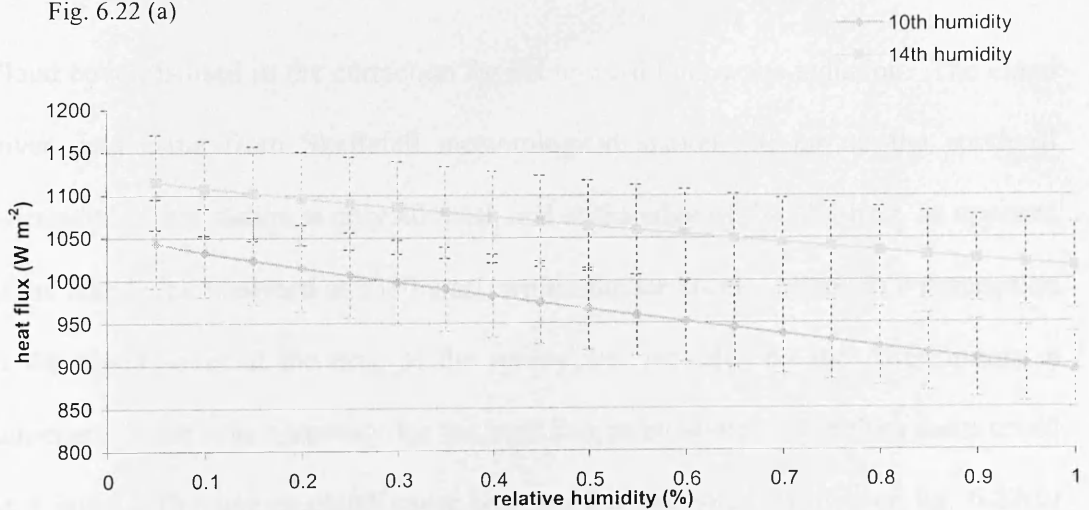
Fig. 6.22 (b)
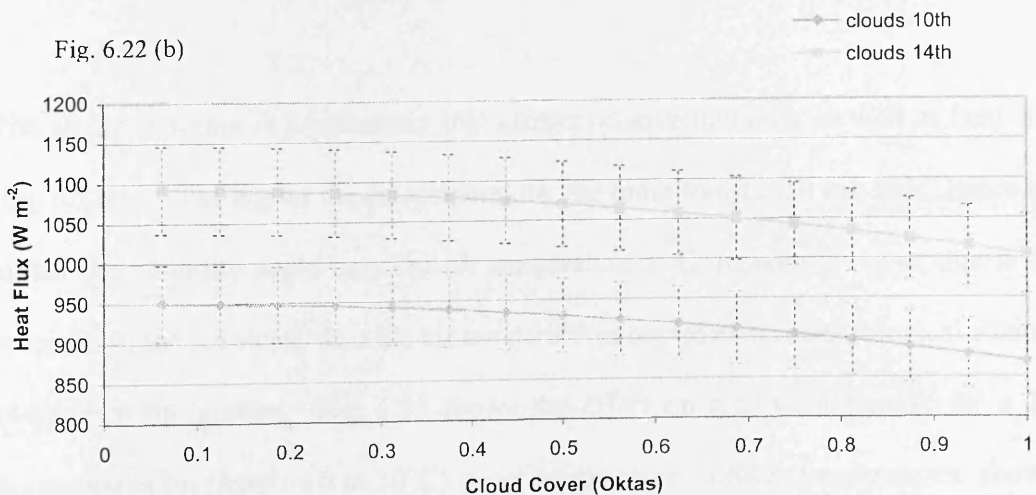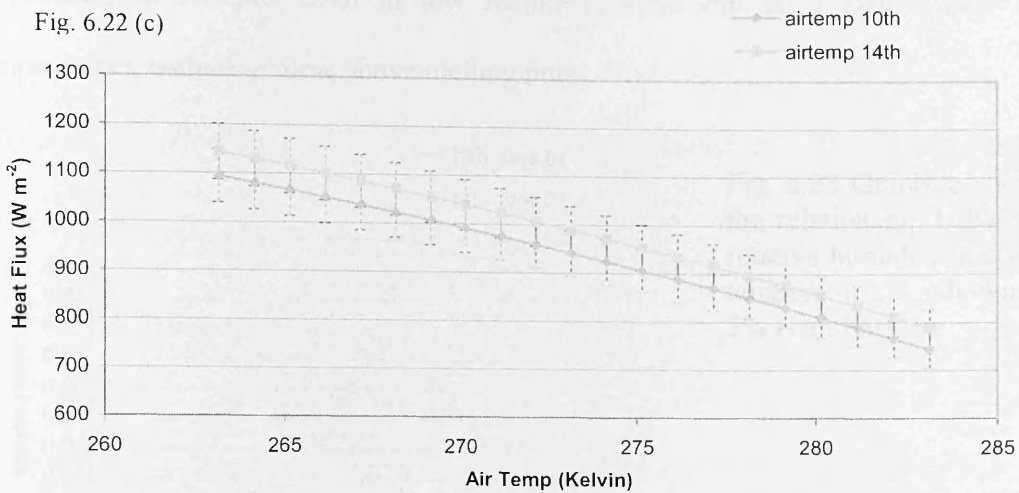
Fig. 6.22 (c)

Fig. 6.22 Graphs to show effect of (a) relative humidity, (b) cloud cover and (c) air temperature on heat flux, all showing 5% error bars.

Cloud cover, is used in the correction for net upward long wave radiation. The cloud cover data came from Skaftafell meteorological station, 30 km to the south of Grímsvötn. This station is only 40 masl, and at the edge of the ice sheet, as opposed to the lake being analysed at 1380 masl, within the ice sheet. Although a description of the cloud cover at the time of the survey was recorded by the ARSF pilots, a numerical figure was necessary for the heat flux calculations. Therefore there could be a large difference in cloud cover between the two sites. However fig. 6.22(b) shows that the effect of cloud cover on heat flux is minimal.

The air temperature is a parameter that affects relative humidity as well as heat flux (fig. 6.22(c)). The higher the air temperature, the more moisture it can hold, hence the higher the humidity could be. The air temperature at Grímsvötn is lower, due to the presence of the ice sheet, than the air temperatures recorded at meteorological stations away from the glacier. Fig. 6.23 shows the effect on relative humidity, for a 20-degree variation (from –10 to 10°C) in air temperature. Lower temperatures, show a lower relative humidity as would be expected. However with 5% error incorporated it

is possible to see that even in low humidity, there can be a large range of temperatures, including some above melting point.
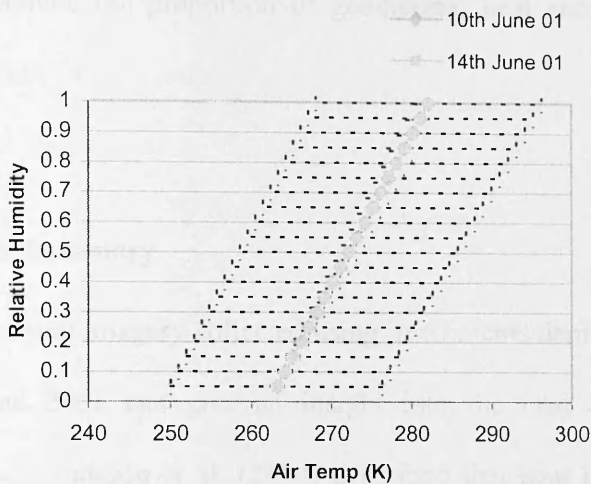
Fig. 6.23 Graph to show the relationship between relative humidity and air temperature, showing 5% error bars.

However there is still only 200 W m^{-2} variation per every ten degrees (see fig. 6.22(c)), which, when compared to figures of 1500 W m^{-2} variation from wind speed, can be classed as a minor effect.

In conclusion, this study has shown that it is possible to calculate heat flux values from lake surface temperatures and meteorological data. The work has also looked at the sensitivity of the input parameters, and shown that wind speed has the greatest effect. It is difficult to quantify the accuracy of heat flux, as this research has only shown that the methodology can be used in a poorly accessible environment. However, the assessment of the input parameters has shown that it is essential that accurate ground measurements are collected at the time of aerial surveys, particularly for dynamic regions like Grímsvötn.

In order to calculate the total thermal budget for the Grímsvötn caldera using this method, surface areas and temperatures of water bodies would need to be derived

from remotely sensed data, along with accurate meteorological data. Once a total thermal budget for the entire caldera has been calculated it would be possible to calculate the proportion of geothermal heat energy generated from the crater lake alone.

6.5. Summary

Thermal imagery collected using instruments deployed on the NERC ARSF aircraft in June 2001 can give an insight into the heat output along the Grímsfjall ridge. Guðmundsson et al. (2004) described that heat is lost through open areas of water; therefore the ATM temperature images provide a method for easily identifying heat lost across the entire region. The temperature images reveal elevated temperature regions that were not detected during ground based measurements, allowing previously inaccessible areas to be monitored. Also thermal anomalies have been observed following the trend of the caldera fault (Guðmundsson 1989).

Guðmundsson et al. (1997) stated that melt water at 20°C increased the englacial and subglacial tunnels allowing water discharge rates to increase. In addition, Björnsson's (1983) research concluded that 70% of ice melt was due to background geothermal activity. The ARSF imagery in this research has shown that the melt water lakes along the Grímsfjall ridge have an average temperature over the critical temperature of 20°C, mid way between two eruptions. This suggests that even with rapid magma input into the system, there would already be discharge tunnels available before any eruption occurred. Although the tunnels could have formed during the 1998 eruption, the geothermal activity has allowed the melt water temperature to remain above 20°C. Leakage of melt water after the 1998 eruption has been discussed in this research,

related to the calculation of heat flux. Leakage of the Grímsvötn caldera lake since the 1998 eruption, has made the use of melt water volume calorimetry invalid (Guðmundsson 2003), but this research has shown that it is possible to use remotely sensed imagery along with meteorological measurements to calculate heat flux from the 1998 crater lake. The presence of discharge tunnels that have remained open due to high geothermal heat flow could be the reason for the leakage of the Grímsvötn caldera lake.

Two thermal images, collected four days apart have shown that there are small apparent temperature differences on this time scale. The possible reasons for these are varied, including reflected solar radiation, atmospheric attenuation and image acquisition differences. Although cornice collapse was discarded for the study regions discussed here, it is still a valid process that may affect temperatures elsewhere along the Grímsfjall ridge. If these phenomena were unknown to the analyst, it would look at first glance as though there had been a fundamental change in ground surface temperature over a short period of time. This will have to be taken into account during any future surveys, along with the need to ensure there are adequate ground observations, good on-board GPS, day and night imagery, and atmospheric measurements at the time of the flight.

In conclusion, despite issues with geocorrection, the ground based and ARSF temperatures are in agreement, although the error bars and values are quite large. Ultimately if detailed meteorological data can be collected at the time of any future surveys, an accurate measure of heat flux could be calculated, and this in turn could allow the thermal budget for the entire Grímsvötn system to be calculated.

Chapter 7 – Geomorphological Terrain Analysis

7.1. Introduction

Terrain analysis covers many topics related to landforms and their environment, and the results are generally expressed in the form of maps. Geomorphology is the study of landforms and landscapes, including the description, classification, origin, development, and history of the Earth's surface (Zuidam 1986). Aerial photographs are used extensively in terrain analysis and classification. The observation of aerial photographs allows for the determination of different surface forms present within an area, as well as different textures relating to land units i.e. landslide / slump deposits (Wilson & Gallant 2000). Since geomorphology is a dominant part of terrain classification, aerial photography can be used effectively in such studies.

The reliability of a map based on aerial photography depends on a number of factors including the method of interpretation, ground observations, and method of mapping. For geomorphological interpretation the boundaries between land cover types have to be distinguished including topographical variations and landforms (Verstappen 1977). Terrain classification is a useful means of mapping natural hazards, particularly for dynamic areas such as volcanic systems that may feature earthquake, flooding, subsidence, and slope stability hazards (Owens & Slaymaker 2004).

The aims of this chapter are to develop techniques for analysis, and derive digital products from aerial photographs collected during the 2001 NERC ARSF survey, and to interpret and evaluate those products. This chapter will discuss specifically the processes involved with, and the usefulness of, aerial photography for producing

geomorphological maps for a dynamic subglacial volcanic system. Morphological features such as crevasses and ice caves will be mapped from the aerial photographs. The ability to create digital elevation models from remote platforms is a useful tool for determining slope stability, volcanic inflation and ice reduction for inaccessible areas. This chapter shows the methodology involved with the generation of a high resolution digital elevation model (DEM) for Grímsvötn.

7.2. Photograph Preparation

The key factor in using aerial photographs with a stereoscope is the stereoscopic parallax. This is the change in position of a single point on two consecutive photographs, caused by the position of the camera, as stated in Chapter 3, section 3.8. The stereographic parallax of an object is a measure of its height. The parallax difference is the distance between the corresponding points and is measured using a parallax bar. In order to correctly determine parallax measurements, the aerial photographs must be positioned correctly. Determining the principal point and flight line is the first step in achieving this. The principal point is determined by connecting the fiducial marks as seen in fig. 3.6 (Chapter 3). The principal points are then transferred to each consecutive photograph and a line drawn between them as shown in fig. 7.1.
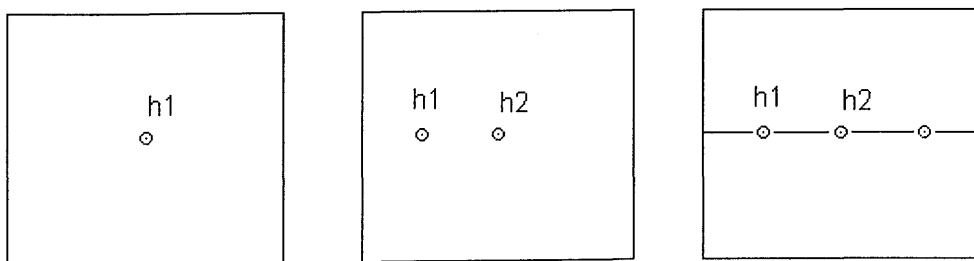
Fig. 7.1 Sketch diagram showing the principal point (h1) transferred onto the

consecutive diagram. Once the principal points are transferred a line can be drawn connecting them. This indicates the flight line.

Once the flight line is drawn, a number of photographs can be aligned to show the flight path of the aerial survey. Although lines of adjacent points will coincide the flight line may not be a straight line due to movement of the aeroplane during the survey (fig. 7.2).
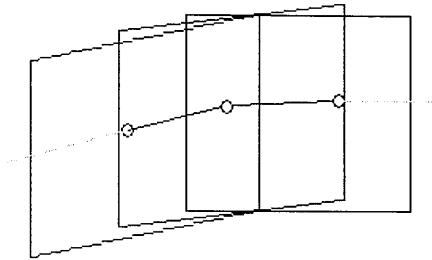
Fig. 7.2 Diagram to show position of photographs and flight line.

The photographs are then oriented along their flight line so that the principal points are aligned, beneath the stereoscope. The scale of the photographs can be calculated by: focal length of the camera / average terrain height.

$$\text{Thus, scale} = \frac{f}{H-h} \qquad (7.1)$$

where f is focal length = 153.435 mm (for the Wild RC-10 camera used in this study), H is mean altitude above sea level = 2524.76 m (for the NERC aircraft), h is mean height of terrain above sea level, = 1577.5 m (at Grímsvötn).

$$\text{Scale} = \frac{153.435 \text{ mm}}{2524.76 - 1577.5 \text{m}} = \frac{153.435 \text{mm}}{947.26 \text{m}} = \frac{0.153435 \text{ m}}{947.26 \text{m}} = 0.000162$$

Thus, the scale for the photographs used in this project is 1:6000, meaning that a distance of 1 cm on the photograph is equal to 60 m on the ground. As there are few easily identifiable objects on the aerial photographs of Grímsvötn, because of the lack

of infrastructure, knowing the scale of the photographs helps in judging the size and identifying features on different photographs.

7.3. The Geomorphological Map

Geomorphology is the science that investigates landforms and the processes that create them (Ahnert 1996). An appreciation of the role of geomorphology is important to society; both for the effects that people have on the environment, e.g. deforestation, erosion, but also the geomorphologic hazards that affect society. Owens and Slaymaker (2004) included avalanches, landslides, debris flows, jökulhlaups, earthquakes, and volcanic eruptions as geomorphologic hazards, with eruptions also including specific hazards such as, ash falls, pyroclastic flows and surges, lahars and lava flows. It is therefore important to understand the processes in order to reduce the detrimental effects of such hazards on society, through hazard monitoring, mapping and risk assessment. The advent of remote sensing has increased the ability to predict and prepare for hazards, as well as visualizing, and researching more remote regions. With aerial photographic interpretation the landform itself is visible so there can be direct observation, with only a small amount of deduction required to infer the processes involved (Verstappen 1977). Volcanoes are dynamic regions and, as such, geomorphological processes tend to occur more frequently than in other environments. Grímsvötn is an atypical volcanic environment, as it consists of a range of geomorphological environments. Most volcanoes are mountain type environments, with high elevations, steep slopes and snow and ice. This environment yields many volcanic processes and hazards including ash falls and jökulhlaups (Björnsson 2004).

7.3.1. Methodology

Of the aerial photographs collected during the 2001 survey, a series of twelve colour

prints, taken from the central flight line, showing the entire Grímsfjall ridge (chapter

4, fig.4.13), were chosen for analysis. Many of the other photographs from the survey

showed no easily identifiable areas, being covered only in snow. The photographs

were scanned, as both digital and hardcopy photographs were needed for use in

digitising and stereoscopy, using an Epson Expression 1640XL A3 scanner, with a

resolution of 300 dpi. They were then co-registered to a geometrically corrected ATM

image, within ERDAS imagine. The photographs were used to create a Digital

Elevation Model (DEM), allowing the temperature imagery to be overlain.

Geomorphology is systematic (Ahnert 1996), the first stage being detection, i.e. a

selection of the objects are identified that are believed to be of interest to the study. In

digital mapping, features can be represented by points, lines or polygons. In this

research a number of map symbols were chosen to represent the different features

seen on the ground, including a steep cliff (30° to near vertical), a short slope (30° or

less), crevasses, water and snow. A shape file, either polygon or polyline, was created

for each feature in ArcGIS. The second stage of geomorphological analysis is the

recognition and identification stage. Using a stereoscope, and the original hard copy

photographs it was possible to determine topographic features, such as the Grímsfjall

ridge cliff line, and ice cauldrons that represent increased geothermal activity.

Tracings of the major features from the photographs aided in the identification of the

major features. The features were then outlined (digitised) onscreen within ArcMap.

The final stage of the process is the interpretation and analysis of the geomorphology,

including deducing the relationships between landforms and processes. The initial

analysis of the aerial photographs shows that, although the photographs are colour, there is a basic distinction between black and white areas (fig. 7.3). This is because large areas of the ground surface are snow covered, and appear white in the photographs, while bare rocks appear black. However on closer inspection slight changes in tonal colour represent different surface features.
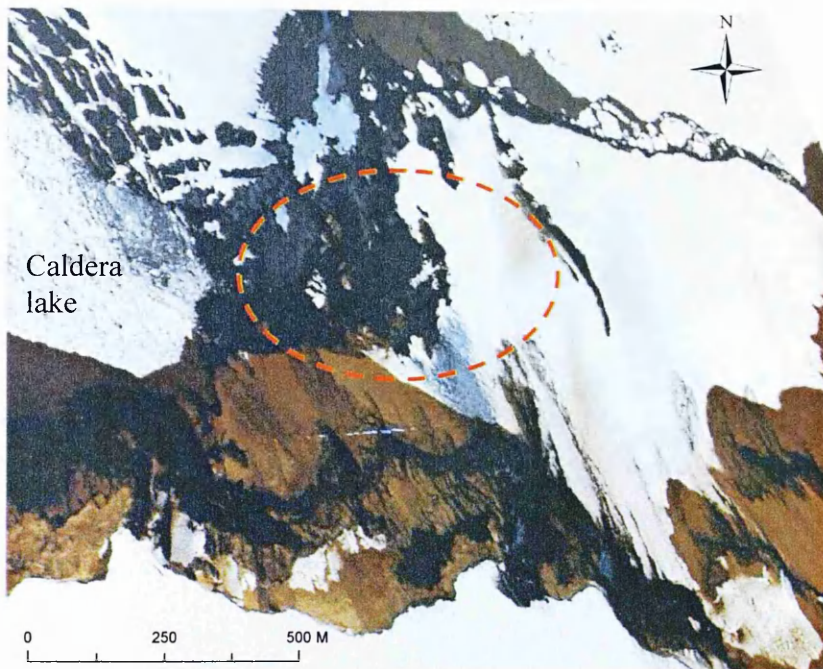
Fig. 7.3 An example of the aerial photographs collected during the 2001 survey. This example shows the approximate location of the 1998 eruption crater (orange oval).

7.3.2. Interpretation of the geomorphological map

Detailed analysis of the ARSF aerial photographs has been undertaken. The resulting geomorphological map (fig. 7.4) contains a few spot heights from an Icelandic DEM which helped in the interpretation of the photographs. Fig. 7.4 shows that the most obvious landform defined, is the Grímsfjall ridge cliff. To the south of the cliff there is a gentle incline up to the edge, which is more defined in the western region. The highest point of the Grímsfjall ridge, Svíahnúkur vestri shows a slightly steeper slope shown by the short slope symbol on the map (fig. 7.4). There are also a large number

of crevasses clearly visible in the snow by slightly different tones of white and pale grey, along the entire length of the cliff. The crevasses show a clear pattern, predominantly parallel to the cliff edge, suggesting that the ice above the cliff is unstable, which may be attributed to relatively high geothermal heat flow beneath the ice. A number of ice caves in the eastern section provide evidence of geothermal activity to the south of the cliff.
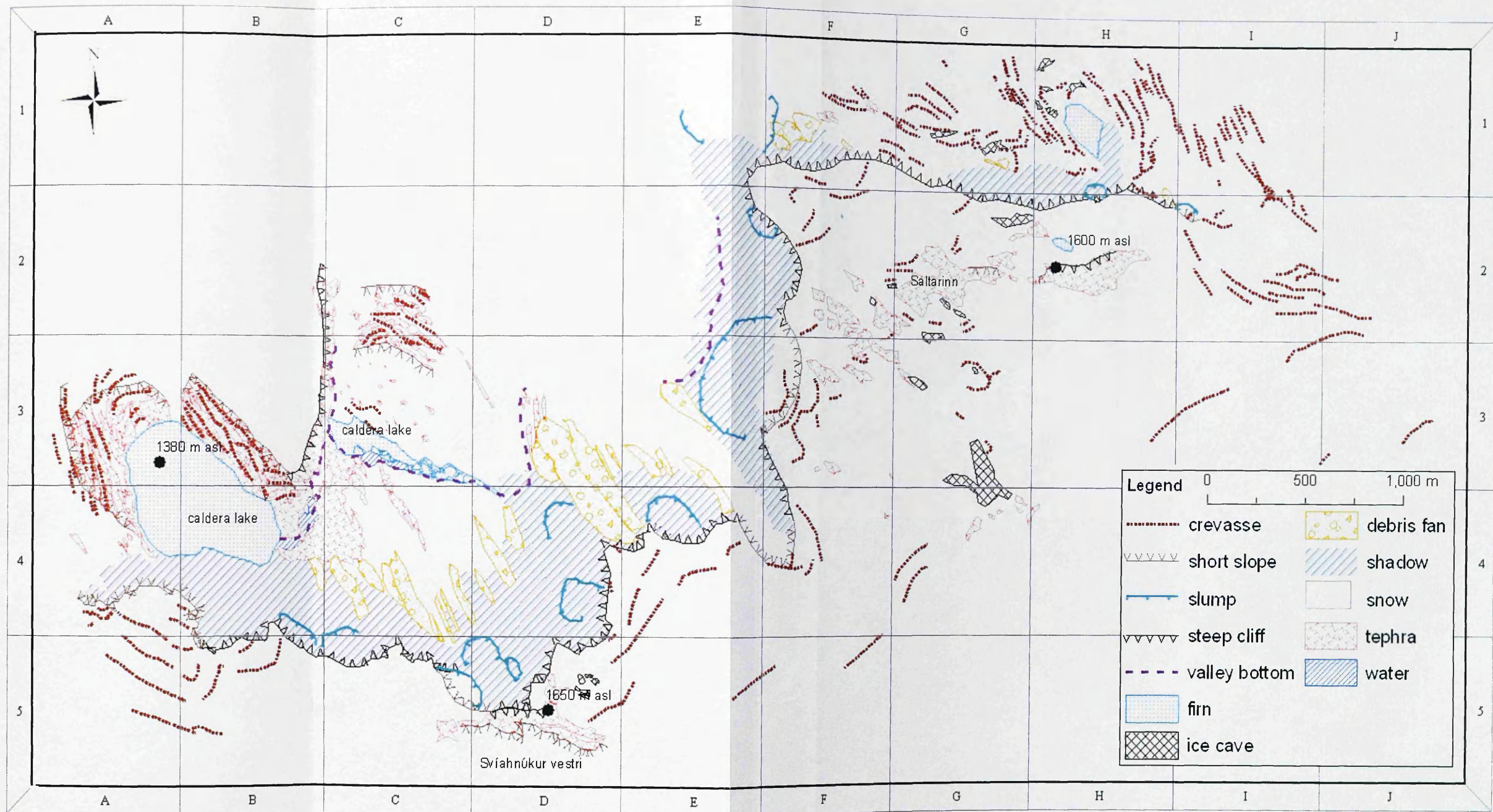
Fig. 7.4 Geomorphological map of the Grímsfjall ridge, Grímsvötn, showing the caldera lake, 1998 eruption crater, Svíahnúkur vestri and the Saltarinn geothermal region. This map based on aerial photographs collected in June 2001, but due to caldera lake fluctuations many of the features (within the 1998 crater particularly) had changed by 2004. Appendix D2 contains the aerial photographs from which this map was derived.

The cliff itself varies from near vertical to a slope of approximately 45° where cornices have collapsed. To the north of the cliff a topographic shadow obscures some features. However a number of slumps are visible. For the purpose of this map slumps were defined as areas where the cornice had collapsed partially down the cliff, as opposed to debris fans, which tend to be long narrow features that fan out at the base of the Grímsfjall ridge. Not all the debris fan deposits are fan shaped, and appear to be similar to debris flow deposits. However, as they are not topographically constrained by valleys they are more likely fans that have become covered by fresh snow or eroded by subsequent avalanches. A number of slump features are clearly visible along with exposed regions of the caldera wall, especially along the western section of the cliff. It was possible to see some slump and debris fans from the visible area into the shadow. The point at which the width of the debris fans increase is a good indicator of slope angle change (fig. 7.4, D3).

In the west, moving north from the cliff, the most obvious feature is the Grímsvötn caldera lake (fig 7.4, B4). A layer of firn covers the lake with the surface dotted in tephra that is most likely of wind blown origin. At the northern edge of the lake there is a gentle slope up the ice. Around this slope the ice is heavily crevassed, allowing layers of tephra from the 1998 eruption to be visible. Within the 1998 crater itself, the distinction between units is difficult, as the majority of the area is dark with little contrast due to the topographic shadow caused by the Grímsfjall ridge. However, by increasing the image brightness and contrast in this area, it is possible to distinguish two small lakes. The rest of the crater contains tephra formed during the 1998 eruption. In the valley north of the eruption site (fig. 7.4, C3), there is a lake, 900 m long by 100 m wide at it greatest. A layer of firn covers much of the lake, but there are small areas of open water with a number of icebergs. There is clearly enough geothermal heat to

allow the water to remain in a liquid state. A gentle incline to the north with tephra visible on the ice surface (fig 7.4, C2), signifies the move from the Grímsfjall ridge and caldera lake, to the main dish of the Grímsvötn caldera.

In the central section of the Grímsfjall ridge, a massive cornice collapse (centred on fig. 7.4, E3,4 & F3,4), has created a gentle snow covered slope, with an number of semicircular crevasses (fig. 7.4, F4) around the southern edge showing a likelihood of further collapses at this site. The geothermal region to the south east of the cliff implies that areas of tephra are continuously exposed due to high heat flow. To the north east of the cliff a number of slumps have occurred, but the cliff itself is generally clear of snow (fig. 7.4, F1). This area is the exposed section of the caldera wall that was sketched in June 2004, and discussed in Chapter 4. High heat flow along the base of the cliff has prevented snow accumulation, but the stable near-vertical cliff has reduced the number of debris flows in this area. However there are a large number of crevasses and a small firn covered ice cauldron (fig. 7.4, H1), in the path of the outwash river formed during jökulhlaups. The majority of recent eruptions have occurred in the south western region of the caldera. The intense geothermal heat melts the ice, which then forms a river that flows along the southern wall of the caldera, escaping out the eastern side (Guðmundsson 1989). As the melt water river is relatively warm it leads to a destabilization of the covering ice, and results in a large number of crevasses (fig. 7.4, G1).

For a more detailed interpretation of the map, two case study areas, the 1998 eruption site, and Saltarinn geothermal area were examined in more detail. The 1998 eruption site (fig. 7.5, C3) is a complex region and incorporates all the major geomorphological units. Svíahnúkur vestri is a high peak to the south east of the eruption site. Numerous

debris fans and slumps cover the cliff along this section of the Grímsfjall ridge (fig. 7.5, C4). Unlike the exposed caldera wall in the east, the slope has a slightly gentler incline. Additionally, residual heat from the 1998 eruption allows for the build up of numerous debris fans and slumps.
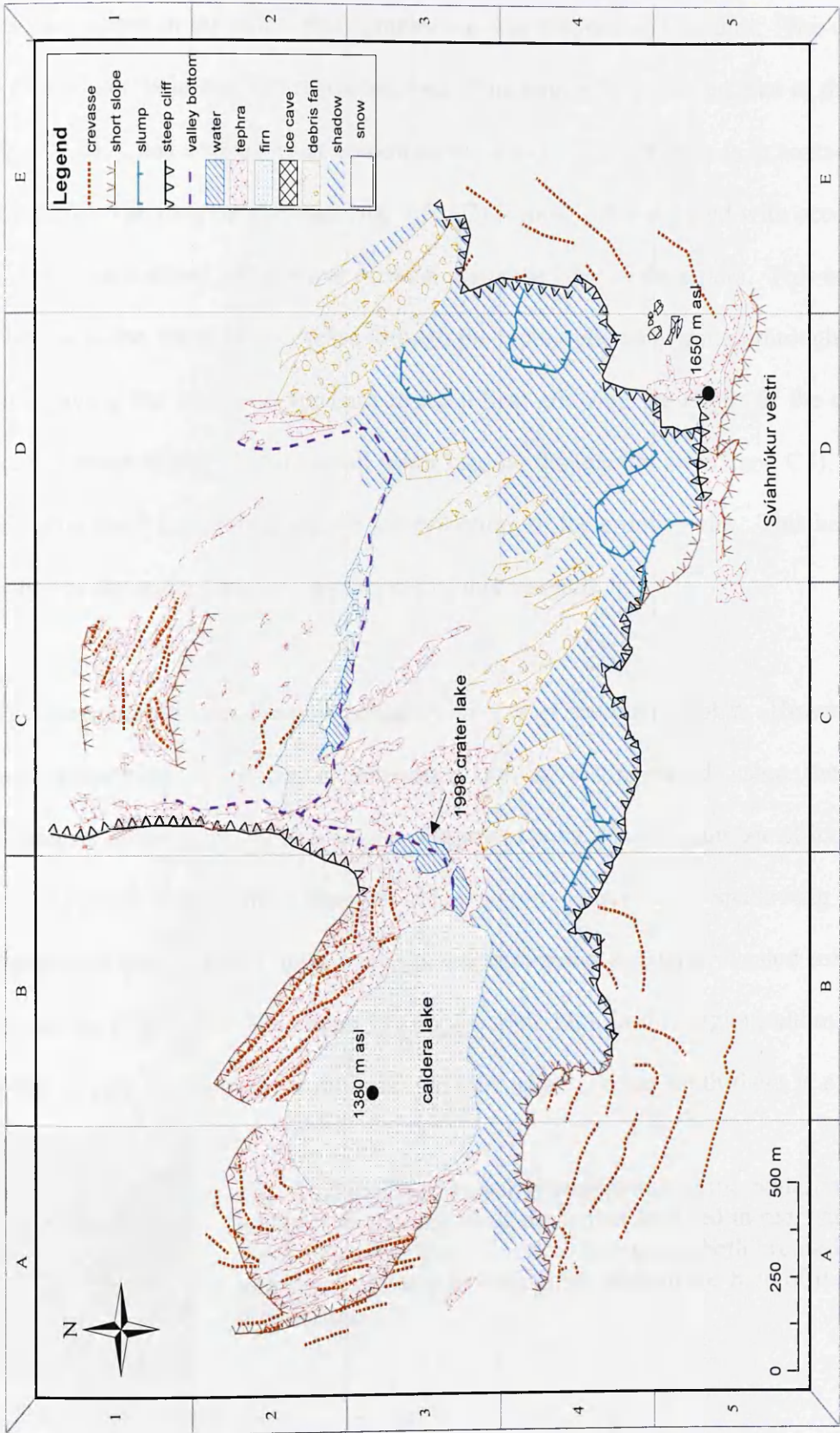
Fig. 7.5 Geomorphological map of the 1998 eruption site. The map also shows the location of the caldera lake and Grimsfjall ridge. Appendix D2 contains the aerial photographs from which the map was derived. Map accurate for June 2001.

Circulation of water through the poorly consolidated debris piles leads to more instabilities in the region. The large area of tephra in the 1998 crater appears to be undifferentiated in the aerial photographs and was mapped as one unit. The caldera lake, however, is in two distinctive sections. The largest firn covered lake to the west (Fig. 7.5, B3), has a small water section on the eastern edge where it is in contact with the tephra. The long narrow lake (fig. 7.5, C2) is mostly firn covered with occasional icebergs, but it shows a thin sliver of water along the edge of the tephra. This is likely to be due to the water being cycled through the tephra pile and emitted through steam vents, giving the tephra an apparent residual heat allowing the edges of the caldera lake to remain liquid. A third small water lake (at the junction of B3 and C3), within the tephra itself is visible along the valley bottom of the eruption site. This has been defined as the crater lake for the purposes of this research.

The Saltarinn geothermal area is primarily an area of snow and tephra. However, on closer inspection a number of crevasses can be distinguished using the tonal differences in the snow. The area also appears to have a higher number of ice caves than anywhere else in the Grímsfjall ridge region. Because of shadowing in the photographs the ice caves appear as exposed tephra and are only revealed using the stereoscope (Fig. 7.6). The tephra is a topographic high in this region, although the incline is very gentle to the north until the cliff edge. To the south there is a gentle

Fig. 7.6 Section of an aerial photograph at the Saltarinn geothermal area, showing the tephra outlined in red, and the ice caves in blue. On the photograph both are dark and hence difficult to distinguish without the help of the stereoscope.

slope, which evens out to an almost flat plane in the area of the largest ice cave (fig. 7.7, B5), which is 180 m by 40 m. The majority of the caves are adjacent to the tephra, and there is a high probability of more that are not easily distinguishable in the photographs, because of their closeness to the dark coloured tephra, and their scale.
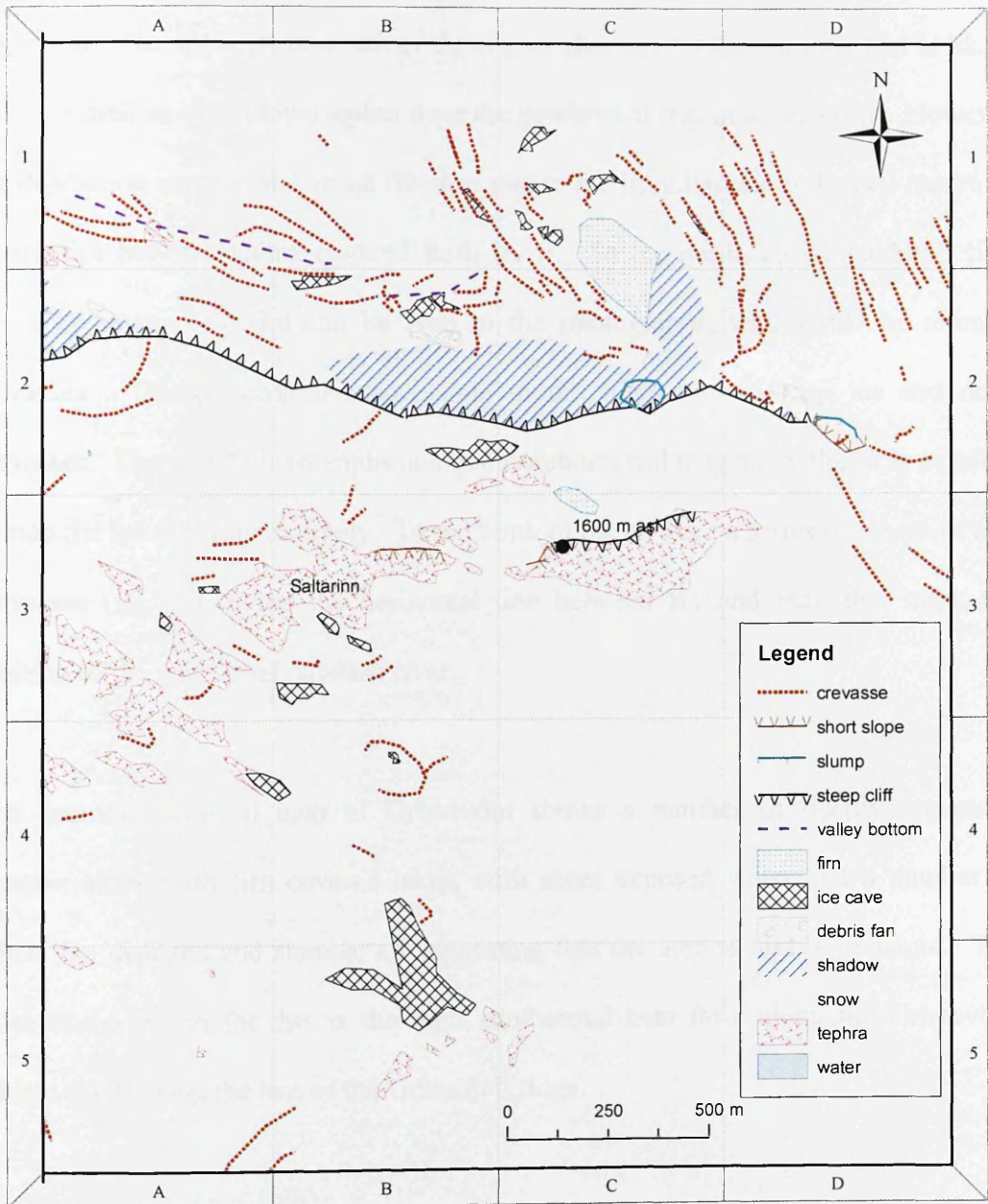
Fig. 7.7 Geomorphological map of the Saltarinn geothermal region, southern Grímsvötn. Appendix D2, contains the aerial photographs from which this map was derived. Map accurate for June 2001.

The geomorphological map for the Saltarinn geothermal region (fig. 7.7) shows the major ice caves that are most easily distinguished. The ice caves tend to be highly dynamic, changing in volume and morphology (Guðmundsson, personal communication, 2004). The largest ice cave in the area appears to be fairly stable (fig. 7.7, B5), being visible in both the aerial photography, and during the 2004 field excursion. The snow to the south of the region also has a different tone and is likely to be covered in wind blown tephra from the geothermal region to the north. However the distinction was not shown on the map due to the irregular and indistinct nature of boundaries between tephra covered fresh snow. To the north, an ice cauldron (fig. 7.7, C1) covered by firn can be seen in the photographs, surrounded by circular crevasses. The cauldron is inaccessible in the field due to steep ice and deep crevasses. The aerial photographs and geomorphological map show that it is possible to map the ice cauldron remotely. To the north of the cliff are a series of ice caves and crevasses (fig.7.7) (along the horizontal line between B1 and B2), that mark the position of the subglacial outwash river.

The geomorphological map of Grímsvötn shows a number of deeply crevassed regions, along with firn covered lakes, with some exposed water and a number of debris fan deposits and slumps, all suggesting that the area is highly dynamic. The most likely reason for this is the high geothermal heat flow along the Grímsvötn caldera fault, along the line of the Grímsfjall ridge.

The geomorphological map was produced and interpreted from the aerial photographs, and was taken into the field in 2004. An accurate assessment of the map could not be

made in 2004, due to lake level changes which had obscured many of the features that
had been visible in the 2001 imagery.

7.4. Quantitative Analysis of Aerial Photography

Detailed analysis of terrain can improve our understanding of the processes involved
in the formation of landscape.   Consequently, accurate representations of surface
shape are beneficial to geomorphologists. Terrain models represent an altitude surface
derived from altitude data using interpolation algorithms. Assuming that the lowest
ground surface elevation is known, the calculation of height difference can be used to
generate a high resolution Digital Elevation Model (DEM).   A DEM is a digital
representation of the Earth's surface in terms of terrain relief (Rees 1999), and is used
for a range of purposes such as deriving slope angles, visibility analysis and multi-
criteria evaluations in GIS.   An accurate high resolution DEM can also be used to
improve geometric corrections and correct for terrain illumination effects in remotely
sensed imagery (Mather 1999).   DEM generation has traditionally been carried out
using aerial photography and stereopairs, but can also be done using other types of
remotely sensed imagery, and laser scanning (Rasemann et al. 2004).   The resulting
DEM is dependent on the source data and the interpolation techniques used.
Rasemann et al. (2004) analysed different interpolation techniques for use in
producing terrain models. They concluded that the algorithms used are dependent on
the final application, but that ordinary kriging produces the most useful result with a
regular and smooth surface.

A DEM of Grímsvötn and the Grímsfjall ridge would allow for a greater
understanding of the relief and the potential to locate and map areas of increased

melting in the ice surface. Fig. 7.8 was derived from a 100 m resolution DEM created using differential GPS, by the Icelandic collaborators, in 2001 at the time of the aerial survey. However a higher resolution DEM would be more useful when studying small features such as the 1998 crater lake, and ice cauldrons, which would show the first evidence of increased heat flux.
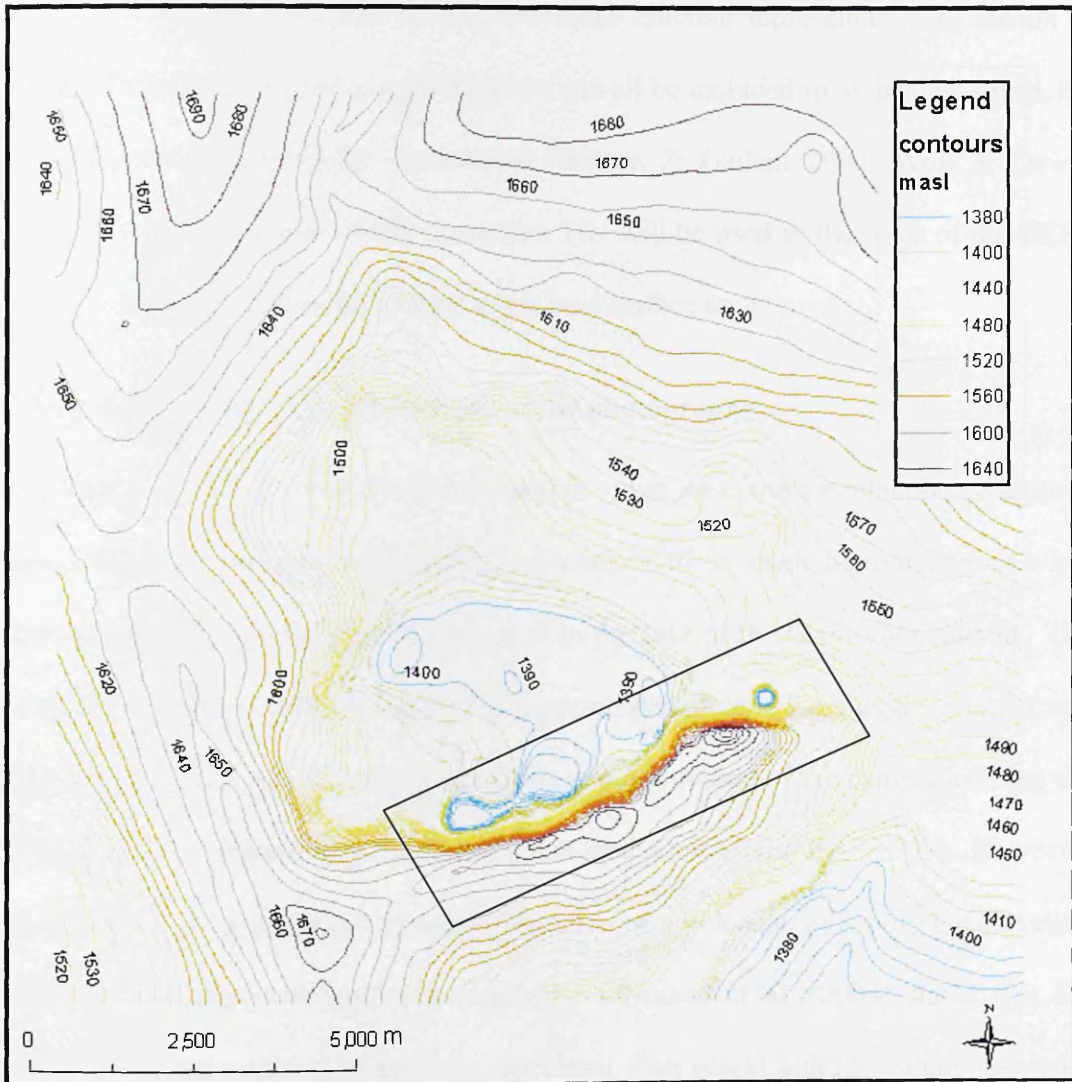
Fig. 7.8 Contour map created from the 2001 Icelandic DEM. This map shows the entire Grímsvötn caldera as a large depression. The box shows the Grímsfjall ridge and caldera lake region from which the aerial photographs were collected for the present study.

There are two main forms of DEM. The regular grid, such as that used for the 2001

Icelandic DEM (fig. 7.8), which uses a square mesh and has become the most widely

used data structure recently (Wilson & Gallant 2000). Regular grids need high

computational efficiency and do not handle abrupt changes in elevation well. An

alternative format is the triangulated irregular network or TIN, which is a simple

surface where specific points of interest such as peaks and breaks in slope form an

irregular network. The TIN format is a more efficient representation of terrain in

terms of data storage, and as critical points can all be included in an irregular grid, the

land surface is often better represented (Wilson & Gallant 2000; Wolf & Dewitt

2000). For the purposes of this research a TIN will be used as the basis of the DEM,

as the points used will all be critical to the land surface structure.

7.4.1. Calculation of elevation from aerial photographs

In order to create a DEM for the Grímsfjall ridge area, the calculations of altitude

above sea level along with the exterior orientations of the camera are necessary when

there is a lack of ground control points, as in the case of the Grímsvötn caldera. The

Wild RC-10 camera has no exterior orientation parameters, such as the angular and

rotational co-ordinates defining the position and orientation of the camera, making the

calculation of elevation impossible using this methodology (ERDAS 1999). However,

in order to look at either subsidence or inflation of a volcanic area, only the elevation

difference between two points is required. Lillesand et al. (2004) stated that the

difference in elevation is often more important than actual altitude values for many

applications. Whilst the exact elevation of the ground surface is unknown, it is

possible to calculate the height difference between different points on the photograph

by using a parallax bar. The accuracy of the parallax bar measurements was

determined using the mean square error of 10 parallax readings of the same point in two photographs.

The aerial photographs were set up in their stereopairs along the flight lines, as described in section 7.2. A point that was clearly identifiable on two photographs in a stereopair was chosen and the bar placed in the correct position, with the floating points lying on the feature of interest on both photographs. Parallax readings were taken and repeated ten times to calculate the mean [appendix D1]. Then the mean square error (m.sq.e) was calculated using the following equation:

$$m.sq.e = \frac{\sum V^2}{n-1}$$

(7.2)

where V = deviation of parallax reading from mean, $\sum V^2$ = sum of the squares of 10 V values, and n = no. of readings. An acceptable mean square error for height determination is 0.02. This exercise was repeated three times to ensure an accurate use of the parallax bar. An average mean square error of 0.00160 was calculated which is well within the acceptable accuracy for such height determination. In order to extract height information from the aerial photographs, information such as the focal length of the camera (for scale), and height of the aircraft are required.

To calculate the height difference the parallax equation (Lillesand et al. 2004) is used:

$$\Delta h = \frac{\Delta p}{Pa + \Delta p} \times Za$$

(7.3)

where Δh = height difference, Δp = differential parallax (elevation difference), Pa = stereoscopic parallax of highest point, and Za = flying height above terrain. In order to use the parallax equation, each of the parameters need to be calculated separately first. Therefore the aerial photographs were prepared, oriented and a number of

distinctive objects were identified. With the parallax bar, the floating mark was placed at the top of the object (Ma) on both photos and the bottom (Mb) of both. The difference in elevation between these two points is the differential parallax (Δp), i.e. equation 7.4.

$$\Delta p = Ma - Mb \qquad\qquad (7.4)$$

The stereoscopic parallax is calculated using equation 7.5, where the parallax difference between the subsequent principal points (Fig. 7.6) is measured and compared on each photograph. The average measurement is used.

$$Pa = (h2 - h1) \div 2 \qquad\qquad (7.5)$$

The average flying height (Za) is the distance between the camera position at exposure and the ground elevation:

$$Za = Zo - hm \qquad\qquad (7.6).$$

where Za = average flying height above the terrain, Zo = average aircraft altitude, hm = relative terrain elevation of the lowest point.

This is an example calculation from the aerial photographs:

Average aircraft elevation, Zo = <u>2524.76 metres</u>

Relative terrain elevation, hm = <u>1380 metres.</u>

Thus Za = 2524.76 – 1380 = 1144.76 metres.

Δp = Ma – Mb therefore

Ma = 29.19

Mb = 24.26 Δp = 29.19 – 24.26 = <u>4.93</u>

Pa = 82.5 mm

Therefore the height difference between the two points equals:

$$\Delta h = \frac{4.93}{82.5 + 4.93} * 1144.76 = \underline{64.55\ m}$$

This methodology has been used to create a high resolution DEM of the Grímsfjall ridge.

7.4.2. High resolution DEM generation

In order to create a DEM of the area, a number of height differences were needed in order to build up a grid or TIN. Sixteen points were chosen around the edges of the caldera lake (fig. 7.5, B3), and small ice cauldron to the east of the Grímsfjall ridge (fig. 7.7, C1), along with another 16 points along the cliff top, and other higher elevations and changes in slope, that were easily identifiable on both the aerial photographs and the ATM imagery. The points were chosen to illustrate the overall form of the landscape. The parallax equation (equation 7.3) was then applied to those points to calculate the height differences.

The lowest elevation, in the Grímsvötn region, the caldera lake surface, was taken from the 2001 Icelandic DEM (fig. 7.8). It should be noted that the lake level is continually changing due to ice melt and discharge via jökulhlaups, In this study ground GPS used for the Icelandic DEM were acquired at the same time as the aerial survey. Consequently this technique would be inappropriate if the photographs were collected at a different time to the ground based DEM.

The height differences for each point calculated from the aerial photographs were added to the lowest elevation from the Icelandic DEM to give the height in metres above sea level for each point. The points were then interpolated in ArcMap, using ordinary kriging, to produce a 2D elevation TIN, with a 5 metre resolution. This corresponds with the resolution of the ATM and temperature imagery. DEMs were only produced for the extreme eastern and western ends of the Grímsfjall ridge as the

water level is known for the caldera lake (at 1380 masl, fig. 7.5 B3) and ice cauldron (at 1380 masl, fig. 7.7, C1). This was because the lowest elevations in the areas away from open water along the central part of the ridge were unknown. Fig. 7.9 shows the DEM and contour map produced for the 1998 eruption area using the aerial photographs. The area was chosen because the caldera lake is clearly visible on the aerial photographs in this area, and the altitude could be obtained for a number of points around the lake area. Fig. 7.10 shows the grid and contour map produced from height information extracted using photogrammetry for the eastern part of the Grímsfjall ridge. The small ice cauldron to the northeast was used as the basis for the lowest altitude levels. If adequate ground control measurements, with accurate elevations could be made along the central section of the ridge then it would be possible to create a DEM for the entire section. Those areas away from points have increasing errors due to the interpolation methods used during the creation of the DEM.
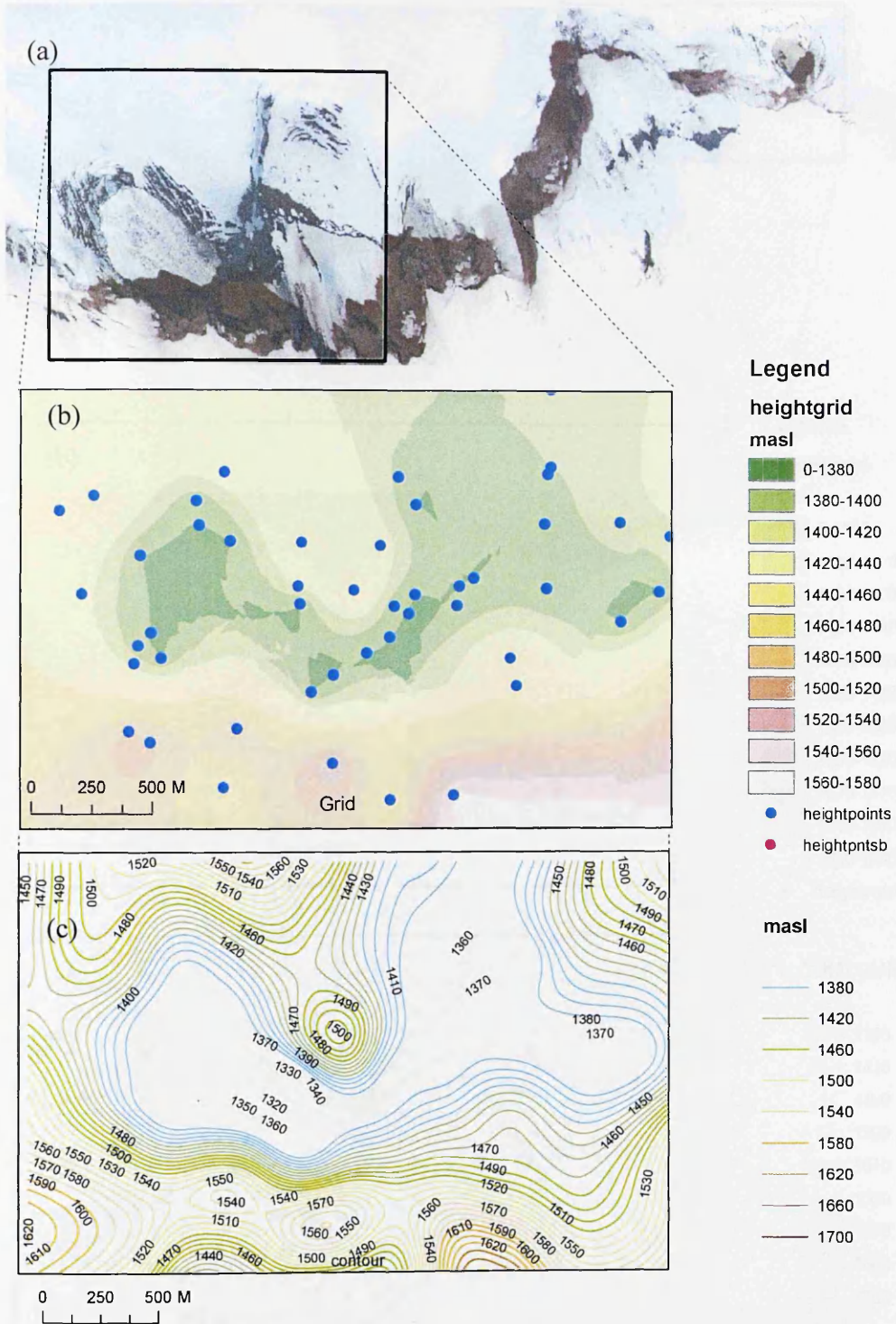
Fig. 7.9(a) The 1998 eruption site including the caldera lake area on a colour composite ATM image. (b) Interpolated TIN grid produced from the height points in the locations shown by the blue points. (c) Contour map derived from the TIN.
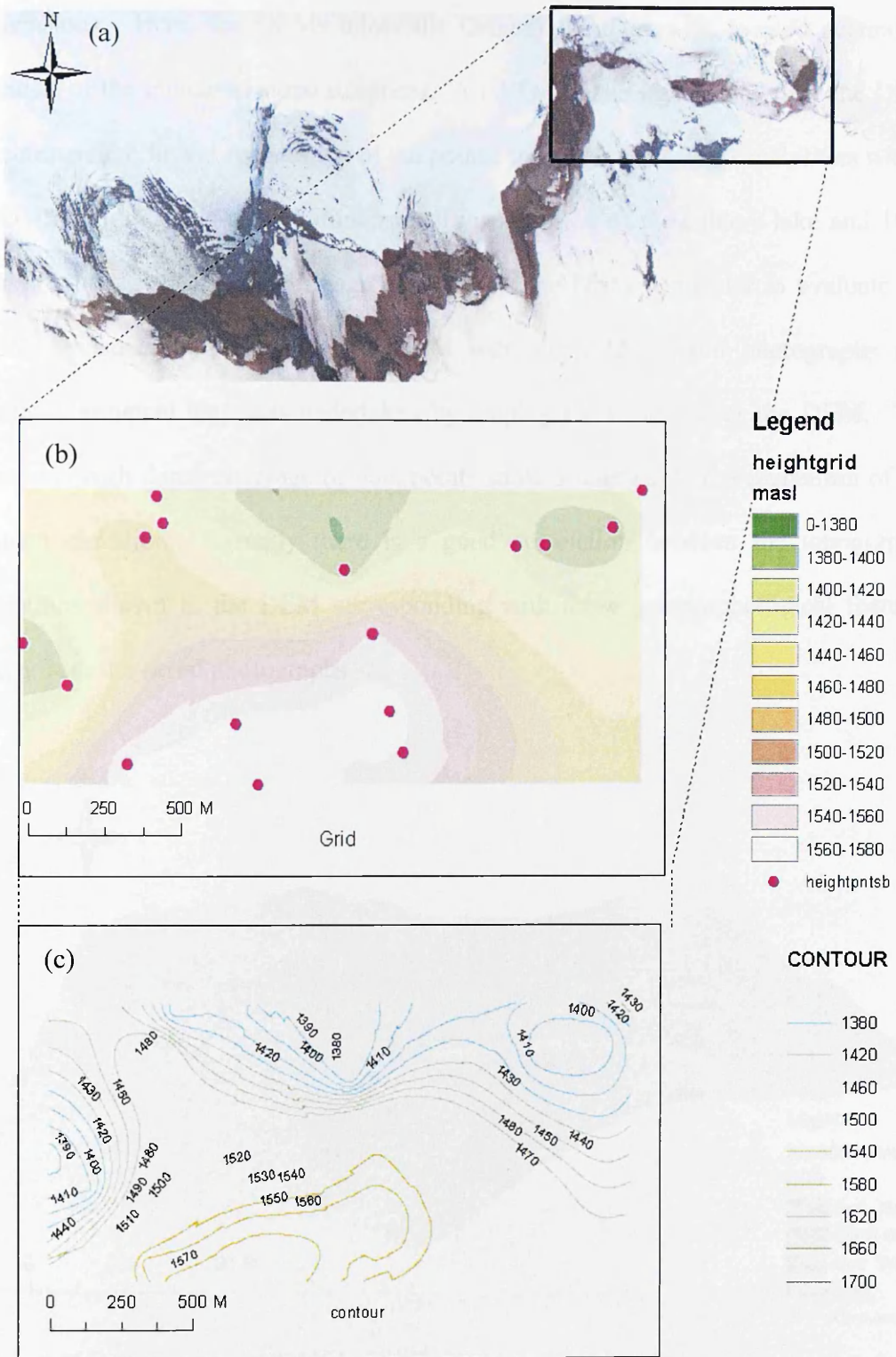
Fig. 7.10(a) A colour composite ATM image, showing the eastern part of the Grímsfjall Ridge. (b) The interpolated TIN grid produced from the height points in the locations shown by the pink points. (c) Contour map produced from the TIN.

DEMs are often used to view the ground surface, in a poorly accessible area, in three dimensions. Here, the DEMs allow the Grímsfjall ridge to be located accurately because of the increased slope steepness. An ATM image was draped over the DEM to compare the fit and registration of the points, using the ArcScene capabilities within ArcGIS. Fig. 7.11 is a three dimensional visualisation of the caldera lake and 1998 eruption site, with an ATM image draped over the DEM. In order to evaluate the DEM a visual comparison of the DEM with the ATM, aerial photographs and geomorphological map was undertaken by draping the images over the DEM. The locations with dense coverage of data points show a reasonable representation of the ground elevation. Visually there is a good correlation between the topographic variations shown in the DEM corresponding with those geomorphological features taken from the aerial photographs.
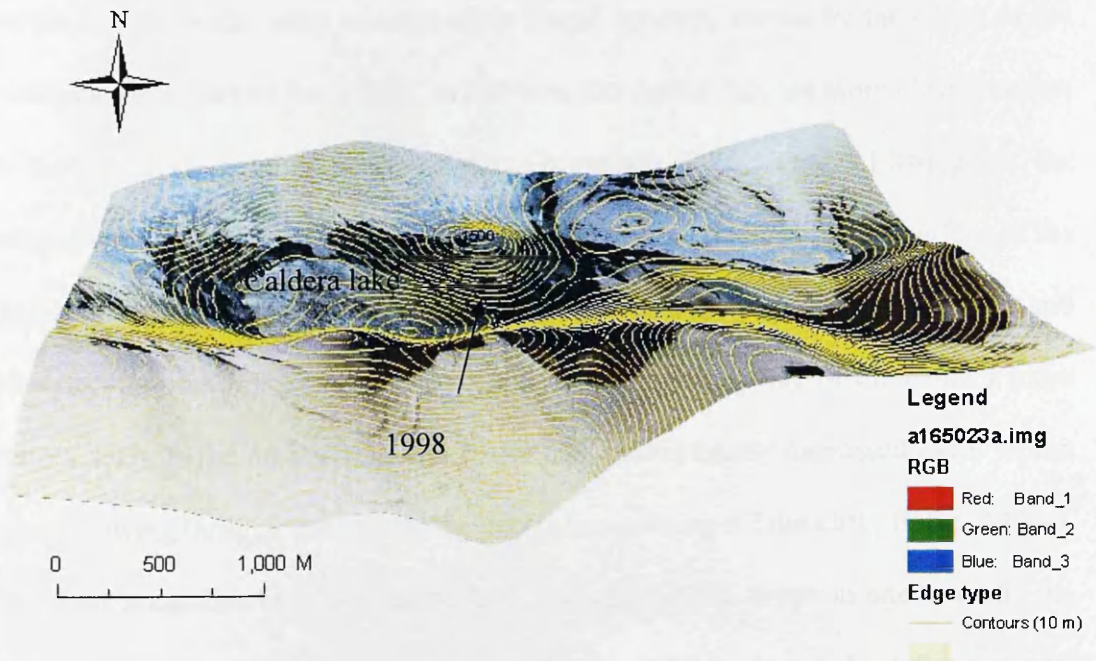
Fig. 7.11 3D visualisation, with colour composite ATM image draped over DEM for the 1998 eruption site and caldera lake.

The 3D visualisation allows an otherwise hazardous area to be viewed more realistically than 2D images. It is possible to see that, to the north of the Grímsfjall ridge, the caldera lake is the lowest point surrounded by ice on two sides, the cliff on the south and open to the east. Taking the visualisation further, the geomorphological map, and thermal image can be draped over the DEM in the same way. Figures 7.12 a, b, and c show the geomorphological map draped over a colour composite ATM image, which in turn is draped over the high resolution DEM. Fig. 7.12(a) looks north eastwards, over the caldera lake, and the 1998 eruption site. In three dimensions the visualisation helps in the orientation and perspective of the geomorphological map, giving a clearer understanding of what the ground surface is like. For the DEM in the 1998 region, height difference points were only collected around the caldera lake, as the lowest elevation was the only elevation known with any confidence. However, there is still some offset with the geomorphological map, due to differences in the warping of the vector map and the raster image beneath, shown by the offset of the crevasses to the fore of the image. In 3D view, the debris fans are more clearly shown in their context, coming down off the Grímsfjall ridge. Fig. 7.12(b) gives the perspective view towards the east along the line of the caldera fault, at the foot of the Grímsfjall ridge. By visualising the geomorphological map in three dimensions and from different angles it is possible to understand some aspects of the caldera more clearly, such as the area around the crater lake that is highly crevassed, with tephra layers showing through the ice and the debris fans coming off the cliff. In fig. 7.12(c), the entire scene has been rotated to look across the 1998 eruption site towards the south and the Grímsfjall ridge. It shows that the cliff face does indeed dominate the region. However more noticeable in this figure is the ice shelf to the north of the 1998 eruption site, around the caldera lake. It stands prominently above the lake.
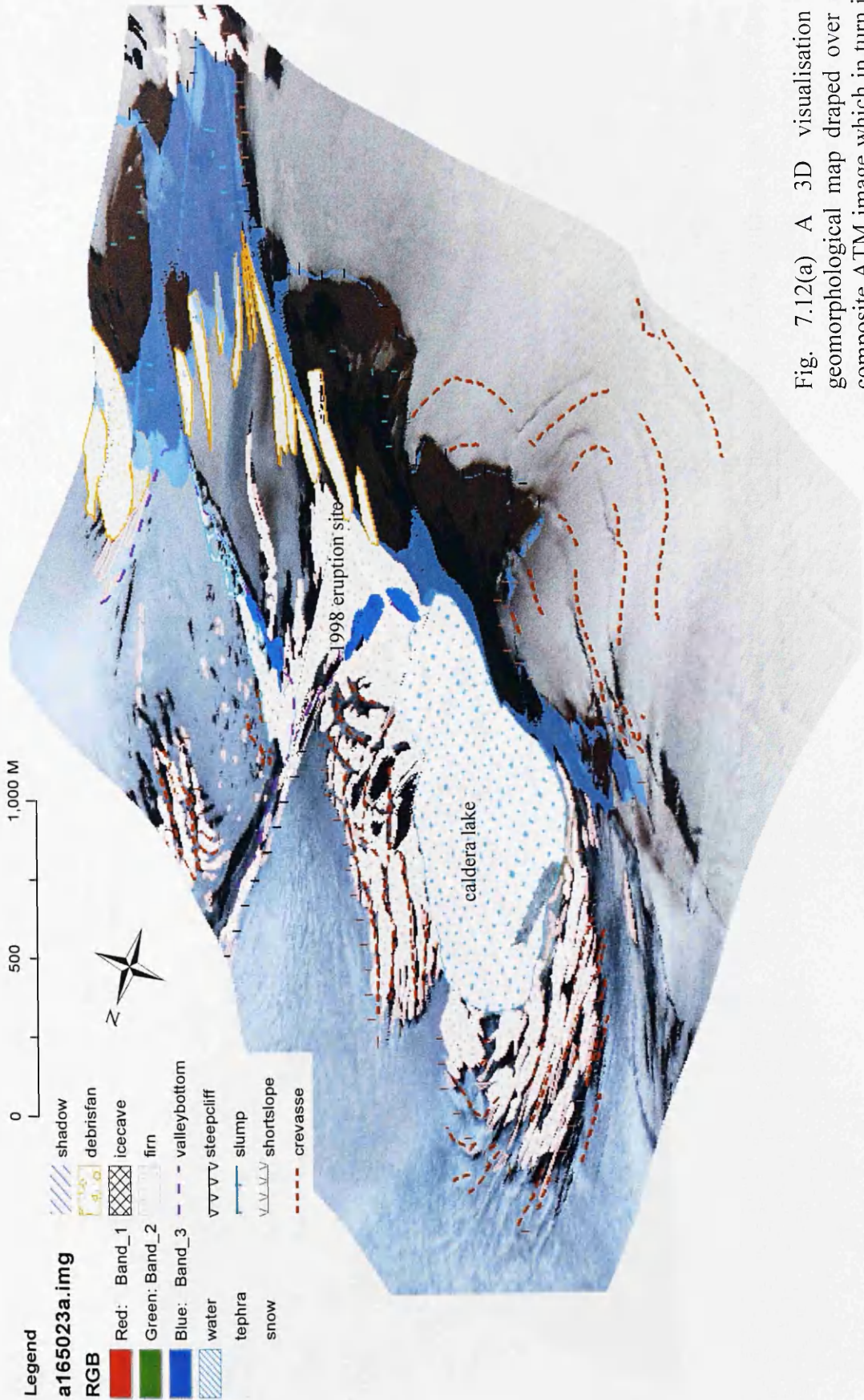
Fig. 7.12(a) A 3D visualisation of the geomorphological map draped over a colour composite ATM image which in turn is draped over the DEM of the 1998 eruption site, and caldera lake areas of the Grímsvötn caldera.
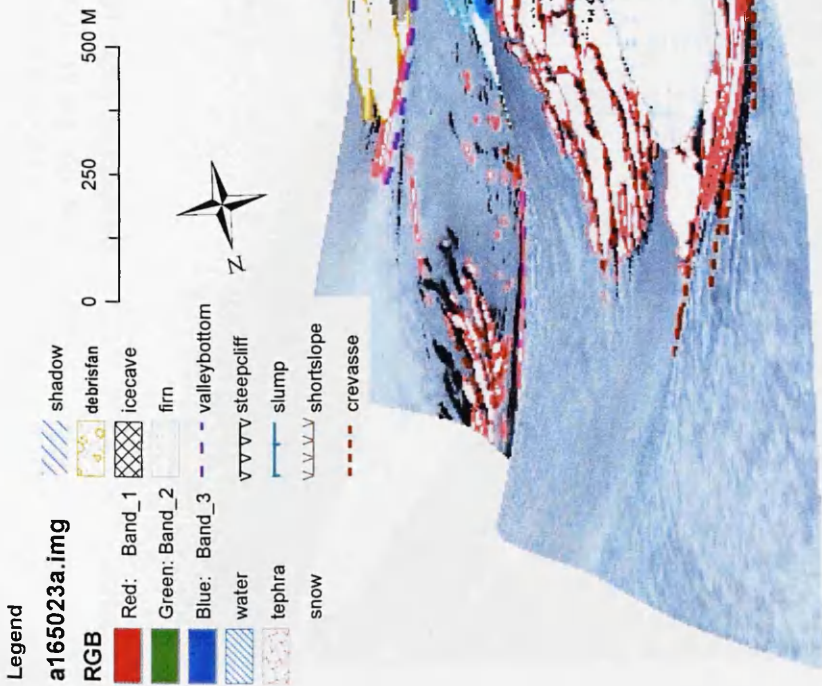
Fig. 7.12(b) Geomorphological map draped over a colour composite ATM image, which in turn is draped over the DEM of the 1998 eruption site, and caldera lake areas of the Grímsvötn caldera. This example shows the perspective views looking eastwards along the line of the caldera fault, at the foot of the Grímsfjall ridge.

Legend

a165023a.img

RGB

Red: Band_1
Green: Band_2
Blue: Band_3

water
tephra
snow

shadow
debrisfan
icecave
firn
valleybottom
steepcliff
slump
shortslope
crevasse

1998 eruption site

caldera lake

0   250   500 M

N

Fig. 7.12(c) Geomorphological map draped over true colour composite ATM, that in turn is draped over the DEM of the 1998 eruption site, and caldera lake. This particular example shows the perspective views to the south across the 1998 eruption site to the Grimsfjall ridge.
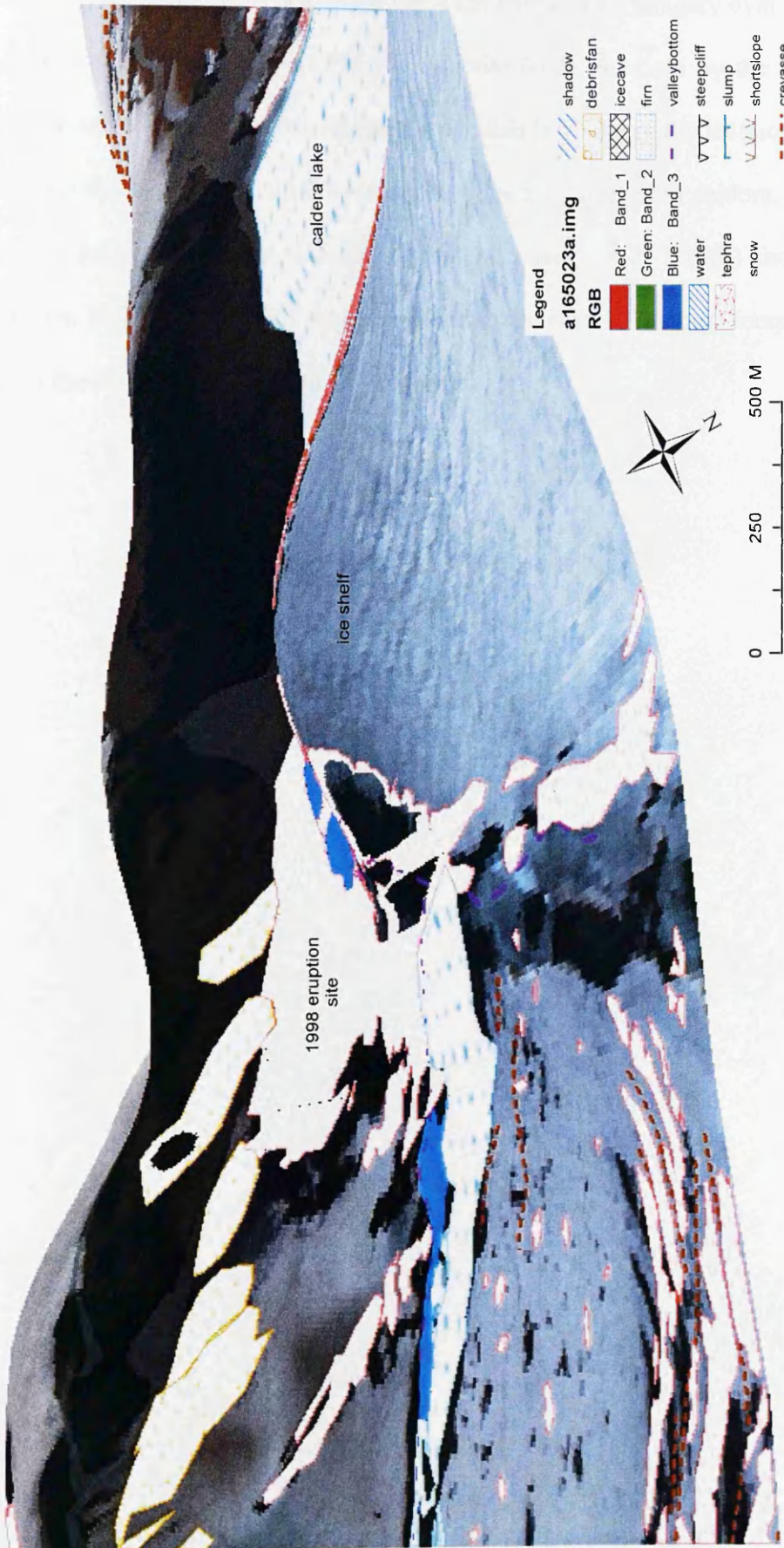
Another way of using the DEM is to drape the ATM temperature imagery over it. Fig.
7.13(a) shows an example of the 1998 eruption site DEM, overlain by the thermal
image for the same area. From this image it is possible to visualise the location of the
1998 eruption site in context with the rest of the ridge and Grímsvötn caldera, as well
as locate the major heat source, i.e. that of the crater lake. Fig. 7.13(b) shows the
rotated image, looking at the 1998 eruption site from the north. The high temperature
anomaly in the centre of the image is the crater lake.

Fig. 7.13(a) Thermal image draped over true colour composite ATM that in turn is draped over DEM of the 1998 eruption site and caldera lake.
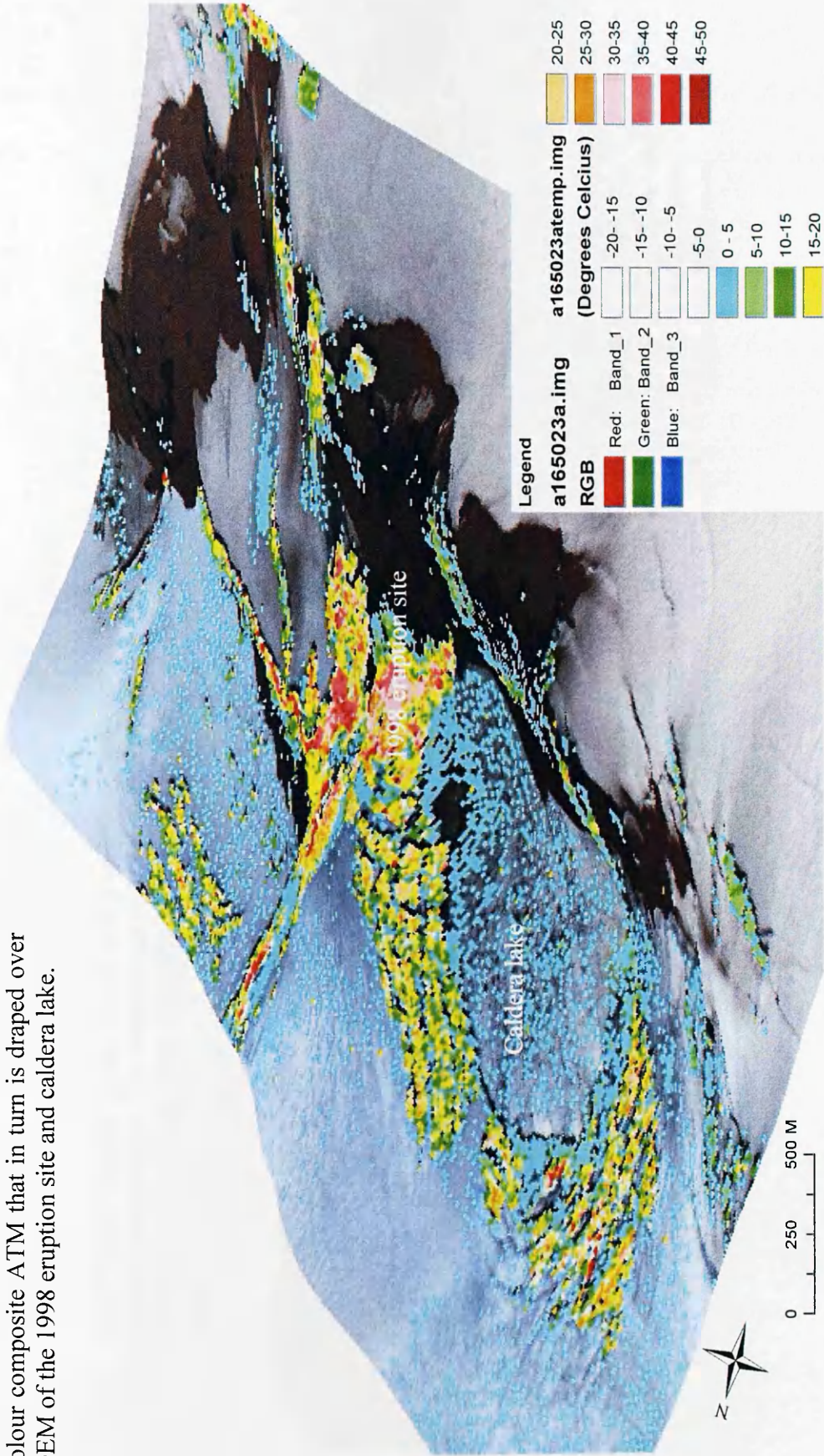
Fig. 7.13(b) Thermal image draped over true colour composite ATM that in turn is draped over DEM of the 1998 eruption site and caldera lake. The entire scene has been rotated to look at the area from a different perspective now looking south towards the Grimsfjall ridge. The central area of the scene, with the high temperature anomalies, marks the site of the 1998 eruption.
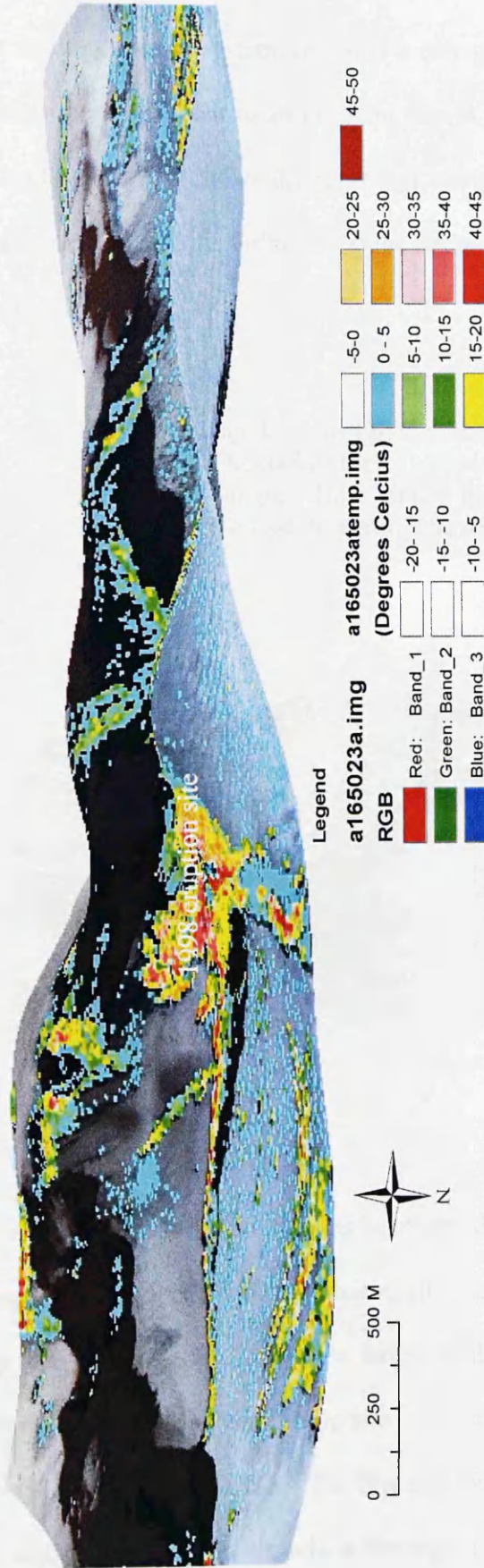
Further to the creation of a DEM, GIS can be used to analyse such things as slope angle. As Grímsvötn is such a dynamic system, not only a change in elevation but also a change is slope might be a precursor to an eruption due to inflation from the intrusion of magma at depth. Fig. 7.14 shows the results of computing slope angle from the DEM. It shows that the area of the Grímsfjall ridge at the side of the caldera lake, has the steepest slope.

Legend
slope
Degrees

	0 - 5
	5-10
	10-15
	15-20
	20-25
	25-30
	30-35
	35-40
	40-45

0   250   500 M

Fig. 7.14 Image to show DEM draped with slope angle data. The darker the coloured contour, the steeper the angle. This image highlights the location of the eastern rim of the 1998 volcanic crater.

eastern rim of crater

1998 eruption site

Grimsfjall Ridge

caldera lake
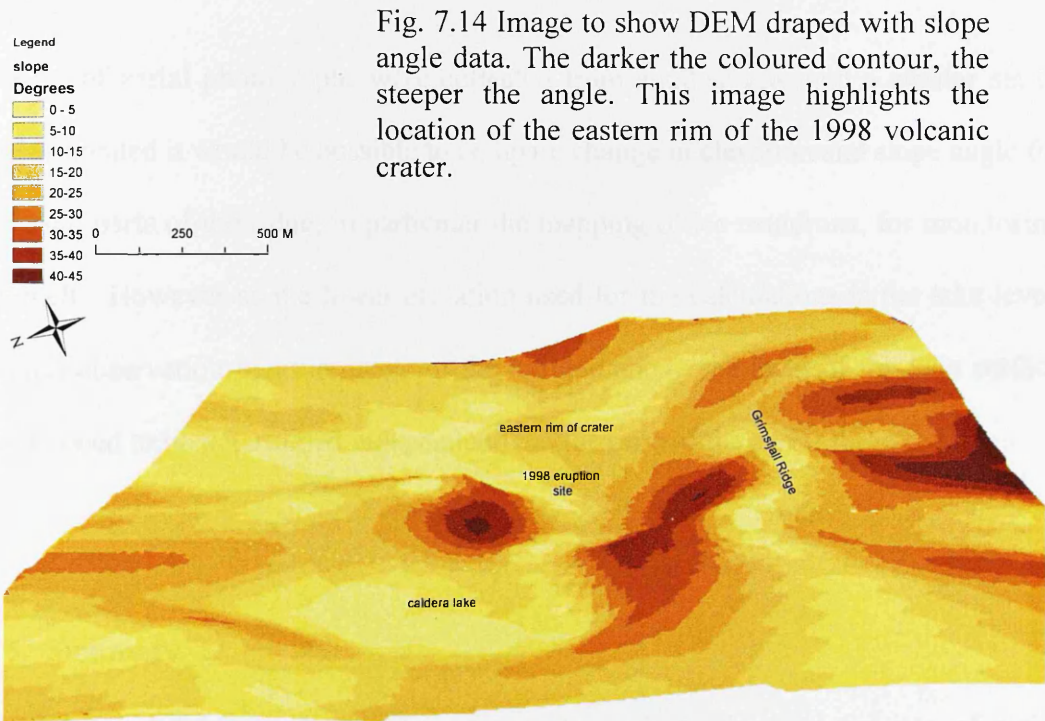
For the purposes of this research, the methodology has been tested to show that it is possible to produce a high resolution DEM of the Grímsfjall ridge using the aerial photographs collected by the ARSF in 2001. However, based on the available data it has only been possible to use that DEM for visual purposes. A number of issues need to be taken into account when studying the DEMs. The first and most important is the assumption that the lake surface is the lowest altitude in the region and is the same as

when the Icelandic DEM was created in June 2001. The second assumption is that the figure taken from the Icelandic DEM is accurate. The height of the cliff varies from the Icelandic DEM by up to 50 m. The low number of elevation data points used for the height difference calculation, 32 in all, can explain this, as well as the fact that the Icelandic DEM is of a much lower resolution, which may average out the heights. By collecting more points around the caldera lake, a more accurate DEM would have been produced.

If a set of aerial photographs were collected from another year and a similar set of DEMs created it would be possible to compare change in elevation and slope angle for different parts of the ridge, in particular the mapping of ice cauldrons, for monitoring ice melt. However as the lower elevation used for the calculations is the lake level, ground observation measurements of the altitude above sea level of the lake surface would need to be determined independently at the time of the aerial survey.

7. 5. Summary

One of the objectives of this research was to evaluate the potential use of aerial photography in creating a geomorphological map and DEM in order to map and more fully understand the Grímsvötn environment. High quality aerial photographs were collected in the 2001 aerial survey, but essential camera orientation information was not available. Therefore the method of digitally creating DEMs from orthophotos (Chandler 1999; Gooch et al. 1999; Lane et al. 2000) was unavailable for use in this case. Instead, the aerial photographs were oriented and analysed manually using a stereoscope and parallax bar, using a methodology adapted from Kerle (2002) and

Lillesand et al. (2004). The photographs were also scanned and co-registered to the georeferenced ATM imagery in order to digitise the geomorphological features. A number of geomorphological features can be distinguished from the photographs including crevasses, ice caves, tephra, water and debris fans. The DEMs created from the height difference calculations show potential. However, to get the most accurate results possible, extensive ground observations are required at the time of the survey, to provide accurate ground control points and the altitude of the lowest available points.

In conclusion, by combining the DEM and the geomorphological map as a 3D model, it is possible to improve understanding of the ground surface without actually having to visit such an inaccessible and hazardous location. Potentially the DEM could be used to map ice cauldron depth, as a means of measuring ice melt over time (Benson & Follett 1986). This would lead to another method of measuring heat flux, along with volcanic inflation prior to eruptions, if regular monitoring was made.

Chapter 8 – Conclusions and Further Work

8.1. Introduction

Vast amounts of data were collected during the 2001 over-flight of Grímsvötn, only some of which has been analysed in the present study. This research intended to test the usefulness of airborne remotely sensed data for monitoring subglacial volcanoes. This chapter discusses the outcome of this study in relation to the wider extent of subglacial research, along with a summary of the main issues found from using the NERC ARSF data. The discussion is followed by a concise summary of the main findings of this research. The chapter concludes with a discussion of additional work and complementary research that would improve future remote sensing studies on subglacial volcanoes.

8.2. Discussion

This research concentrated on establishing whether remote sensing is useful for monitoring Grímsvötn, for improved understanding and better forecasting of eruptions and jökulhlaups. However the wider scope of the project was to show that remote sensing technology could be used for monitoring other subglacial volcanoes that are perhaps more remote, such as those in Antarctica. Although similar subglacial eruption processes occur in Antarctica and Iceland, it must be highlighted that Grímsvötn is an atypical subglacial volcano, having a partially exposed caldera wall, and a number of open water bodies. This has allowed areas of open water to be used to calculate heat flux using meteorology methodologies. In general, subglacial volcanoes often only exhibit a depression in the ice surface as evidence for geothermal activity at depth. Consequently the measurement of heat flux employed in this

research, using meteorology and open water bodies, would be impossible classic subglacial settings.

Topographical variations in the ice surface, shown by geomorphological features such as crevasses; along with digital elevation models (DEMs) have the potential to determine increased heat flow beneath the ice. However regular monitoring would be necessary to detect changes over time, along with ground observations, which would be more difficult in places such as Antarctica. However even in such places as Iceland, where regions of geothermal heat beneath the ice create cauldrons, a lack of clear ground control points would hinder geocorrection and registration of imagery.

Consequently, the ARSF imagery would not be adequate for monitoring volcanoes completely encased in ice, or with greater accessibility issues than Grímsvötn. Likewise ground observations are necessary for accurate geocorrection, registration and analysis of the imagery.

There is a vast amount of information that could be extracted from the ARSF imagery. However time constraints due to issues of geocorrection and co-registration of imagery meant less time was available for image analysis. A number of recommendations for the ARSF have been highlighted through this research [appendix E]. A key point to note is that the ARSF system for geocorrecting imagery using AZGCORR software is not user friendly, for non remote sensing specialists. Therefore, substantial time was spent in finding the correct codes for the most accurate geocorrection possible. The highest accuracy of the imagery can only be

achieved with GPS ground control points. No ground control points were collected specifically for the correction of the imagery. Consequently there was also no way of testing the accuracy to determine the likely errors. At Grímsvötn, there are few locations that would remain unchanged and easily recognisable from the air, due to the intense geothermal activity continuously melting snow and ice. In addition, a further command code was provided by the ARSF at the end of the analysis, with the aim of using Transverse Mercator instead of the UTM, which is used by the Icelanders (section 8.4).

The ARSF now stipulate that a ground based GPS station is necessary before any over flights can take place. In addition to the geocorrection of the imagery, a ground based survey was necessary at the exact time of the aerial survey, using compatible GPS ground points that would aid in the registration of one image to another. The dynamic nature of Grímsvötn has meant that locations that were chosen for ground control points were usually on the boundary between tephra and ice or snow. However, with snow fall or high winds, those locations could have been lost. This would have been reduced with a GPS ground survey.

The comparison of data from the Icelandic ground based temperature survey and the ARSF imagery, was hindered because of a lack of definitive GPS points. This revealed that the geometric correction of the ATM imagery was insufficiently accurate to allow a point within specific pixel comparison. The inadequate geometric correction of the imagery was attributable to the inability to incorporate a DEM of adequate spatial resolution into the geocorrection procedure. This problem could not

be resolved by using ground control points to perform further geocorrection of the imagery as no such ground survey points that were also identifiable in the imagery, were available.

In order to create a DEM for the Grímsfjall ridge area, the calculations of altitude above sea level along with the exterior orientations of the camera were necessary where there is a lack of ground control points, as in the case of the Grímsvötn caldera. The Wild RC-10 camera has no exterior orientation parameters, such as the angular and rotational co-ordinates defining the position and orientation of the camera, making the calculation of elevation impossible using this methodology. However, in order to look at either subsidence or inflation of a volcanic area, only the elevation difference between two points is required. Hence it was possible to use the stereoscope and parallax bar, to produce a high resolution DEM. It was however dependent on knowing the lowest altitude of the region, which was taken as the water level of the Grímsvötn caldera lake. In other circumstances, where an ice cauldron has formed only a depression in the ice, this methodology would unavailable, as no elevation data would be known, without using radar or Lidar scanning equipment (section 8.4).

However, despite the number of unknown errors, and issues of geocorrection, the ARSF data for Grímsvötn has produced some good results, as discussed in section 8.3. For example, water temperatures from inaccessible ice cauldrons have been measured for the first time, and provided us with an idea about the processes at work within and beneath the ice.

8.3. Conclusions

8.3.1   It is possible to extract useful thermal and topographical data from the NERC ARSF data. Thermal anomalies can be mapped and used to calculate heat flux. Topographic data can be used to create slope and 3D models, which have the potential for use in studying instabilities and inflation changes.

8.3.2   Although there were initial issues regarding geocorrection because of the lack of ground control points and easily identifiable locations, the accuracy assessments for classification and parallax bar measurements give confidence in the data. The ARSF now stipulate the need for a GPS receiver to continuously record during aerial surveys. This will decrease the need for ground control points in any future survey and allow remote regions, to be surveyed with a high degree of precision.

8.3.3   Classification of ATM imagery into eight land cover classes, using parallelepiped and maximum likelihood statistical techniques provides a good basis for assigning emissivity values to each land cover for thermal analysis.

8.3.4   Comparison of ground based measurements of surface temperatures with temperature estimates from airborne remotely sensed data is possible, although variations due to pixel integrated temperatures, time of acquisition and topographic variations need to be accounted for. Regions with low interpolation in ground based temperatures, show similarities to remotely sensed temperatures.

8.3.5 Temperatures from inaccessible ice cauldrons can be collected using the ATM temperature imagery. This is fundamental in view of the fact that the 2004 Grímsvötn eruption broke through the ice at two major ice cauldron locations.

8.3.6 Heat energy is lost from the Grímsvötn geothermal system through areas of open water that can be easily identified using ATM temperature images. It is possible to calculate heat flux values for the 1998 eruption crater lake from the ATM temperature imagery when combined with meteorological information. This research has shown that wind speed is the parameter that has the greatest effect on heat flux. The results of heat flux calculations show the potential for using the methodology employed here to calculate a thermal budget for the entire Grímsvötn caldera.

8.3.7 This research has shown that, by using aerial photographs, stereoscopy and GIS, it has been possible to map the main geomorphological features of the Grímsfjall ridge. The photographs show many different features including crevasses, open water, debris fans and ice caves which can be mapped and have the potential to be monitored if more data is collected in the future.

8.3.8 Using a stereoscope and parallax bar, height differences along the Grímsfjall ridge and caldera lake were calculated for a number of easily identified points from the aerial photographs. The points were then interpolated to create a high resolution DEM. From this DEM a slope angle map was produced within a GIS environment that has the potential to be used for detecting elevation changes corresponding to inflation and instabilities along the Grímsfjall ridge. A 3D model of the 1998 eruption

site was created, allowing a visual inspection of the region from different directions. An ATM temperature image and geomorphological map were draped over the 3D model giving good correlation of the key features and further enhancing the environment in terms of topography.

8.3.9   This research has shown the potential for monitoring Grímsvötn remotely. With further surveys, spatiotemporal variations in temperature, geomorphology and slope would allow a greater understanding of the processes at work. Satellites could provide this regular monitoring, especially as aerial surveys are often used as a test bed prior to commissioning satellite reconnaissance. However, for a location such as Grímsvötn, at a high altitude and latitude, cloud cover can present problems with satellite images using passive optical systems. Based on the analysis undertaken during this study, a resolution of 5 metres was used for comparing ground sampling points. However, a higher resolution would have reduced the problems arising from pixel integrated temperatures. Although there are some high resolution optical sensors, satellite thermal imagery is generally of much lower resolution than that attained by aerial surveys. Therefore, this study has shown the benefit of airborne over satellite imagery for the study of thermal anomalies at a location such as Grímsvötn.

8.3.10 Prior to this study, although there had been substantial research into subglacial volcanic processes across the globe, the use of remote sensing to monitor them had not been undertaken. This research has shown that remote sensing can be used effectively to extract information such as heat flux, to calculate the thermal budget of a subglacial system such as Grímsvötn. It has also shown the potential that remote

sensing could have for regular monitoring of morphological changes leading to a greater understanding of subglacial volcanic processes. The use of multidisciplinary monitoring was shown during the 2004 Grímsvötn eruption (Vogfjörd et al. 2005) and this research builds upon that work by adding an extra discipline that could be used for monitoring future eruptions and jökulhlaups.

8.3.11 The ability to use remotely sensed imagery to measure temperatures from otherwise inaccessible areas of open water has shown that the average temperature of the 1998 crater lake is over the critical 20°C temperature necessary for the formation of discharge tunnels (Guðmundsson et al. 1997). The presence of discharge tunnels that have remained open due to high geothermal heat flow could be the reason for the leakage of melt water from the Grímsvötn caldera lake. This research therefore supports and builds upon previous studies of ice melting, discharge tunnels and heat flux.

8.4. Further work

It is evident from this study that a considerable amount of useful information can be obtained from remotely sensed data for inaccessible regions. However, future remote sensing surveys could produce more useful data if the following recommendations are adopted.

8.4.1. Geometric correction

Although the AZGCORR algorithm developed by NASA and modified by Wilson (1997), decreases the need for users to have in-depth knowledge and expertise in geocorrection and computer programming allowing for the geocorrection of the ARSF

imagery, there is still a need for some knowledge of geocorrection techniques. The AZGCORR program requires a limited knowledge of UNIX along with map projections and co-ordinate systems, especially for non-UK based data. All the help files, and user programs are based on UK examples. However internationally acquired imagery requires additional information such as accurate GPS and geodetic datum and projections.

The geocorrection carried out on the ARSF imagery used the UTM spheroid. However the Transverse Mercator WGS84, could be used instead. The command code for use on UNIX workstation is as follows:-

azgcorr –v –be –mTMw –15 –p 5 5 –1 –hs –avhgt –1 inputfile -3 outputfile

where –mTMw is the Transverse Mercator west, -avhgt are the observation heights.

A comparison of the two geometric correction commands, the UTM and TM variations received from the ARSF, would be useful in establishing the best method for correcting data outside of the UK. The imagery could be compared to the Icelandic DEM, though of lower resolution, and the map sheets for Grímsvötn.

8.4.2. Image enhancement techniques

During the present study, only a small amount of image enhancement was carried out. This consisted primarily of Principal Components Analysis (PCA) and different band combinations. However, there are other useful image enhancement techniques available within ERDAS Imagine. For example, areas can be masked out, or the images can be subset. Contrast enhancement techniques can be used to highlight areas of interest. Histogram equalisation and stretching can be used to spread the contrast equally over the full colour display range of 0-255. This can be done on individual

pixels, areas of interest and the image as a whole. Each method would give different results, some of which could lead to more information being extracted from the imagery. These techniques do not alter the data but transformations such as PCA alter the way in which the information is expressed. There are additional techniques that require the image data to be altered. For instance, digital filters can be used to extract particular spatial patterns, such as separating background patterns from higher frequency patterns. These techniques could be used to focus on particular areas, such as ice cauldrons and crater lakes, to look at variations in more detail.

8.4.3. LIDAR

LIDAR (light detection and ranging) systems and digital cameras were in existence at the time of the 2001 survey but they were not present on the NERC ARSF aircraft. The ARSF now have the ability to undertake LIDAR surveys. These can be used to create surface elevation models accurately to a resolution of 50 cm. This would allow the Grímsfjall ridge to be scanned, resulting in a surface elevation model for the entire ridge to be produced at higher resolution. The resulting DEMs could be used to determine when inflation and deflation events take place and to relate that to subglacial volcanic processes.

8.4.4. Lake monitoring

A method for collecting temperature data throughout the water column, as well as water volume and bathymetry from the crater lake and surrounding cauldrons, would be a useful alternative for calculating heat flux, and allow for comparison and further testing of the meteorology method used in this research. For a lake in the English Lake District, a "buoy" regularly collects temperature, and bathymetric data for thermal budget monitoring (Jones et al. 2005). For Grímsvötn, the data collected from

the lakes could be sent either directly back to the university in Reykjavik or the huts on Grímsfjall, to be downloaded during the field visits. This method could complement the remotely sensed data, allowing for a more rigorous calculation of heat flux, and continuous monitoring of the geothermal output.

8.4.5. Geomorphology

The geomorphological map produced in this research showed that a number of features could be distinguished from the aerial photography. However some features within the Grímsfjall ridge area contain small errors in registration. This is especially apparent when draped over the 3D model. Further work to look in detail at regions such as the caldera lake, where topographic shadowing has produced an unnatural line of ice, or the offset of the crevasses, would be useful for making the map more useful for field use.

8.4.6. CASI

Most of the research carried out for this project has concentrated on the thermal imagery in order to understand the heat flow from Grímsvötn, along with using the aerial photography to map and produce a high resolution DEM of the area. Incorporated in this work, is the need to establish the composition of the land surface, for both understanding the processes in terms of geology, but also as a means of applying accurate emissivities to land cover classes for thermal analysis. One method of doing this would be to use the CASI data that were collected at the time of the aerial survey. As the variation between altered and unaltered volcanic material is spectrally clear, CASI data may be adequate. However, further research to establish the usefulness and potential for compositional mapping of the Grímsvötn caldera would be useful. It is necessary to have an idea of the likely composition prior to

analysis so that the correct material spectra can be imported into the analysis workstation, therefore good ground observations would be necessary. Comparisons of hand specimens collected from the Grímsfjall ridge with the CASI imagery could be used to calculate precise emissivities of the different land cover types. A preliminary analysis which outlines the potential usefulness of this approach is contained in appendix F.

8.5. Summary

This research has shown that remotely sensed data can be used successfully in inaccessible and hazardous regions such as Grímsvötn subglacial volcano. Useful information relating to the geothermal system can be extracted, along with topography and morphology. This study has established that remote sensing can be used for atypical subglacial volcanic environments, but there is still much research that can be done to help our understanding, such as regular monitoring of geomorphology, the use of LIDAR and compositional mapping.

References

Ahnert F (1996) Introduction to Geomorphology. Arnold. London.

Allen CC (1980) Icelandic subglacial volcanism: thermal and physical studies. Journal of Geology. 88:108-117.

Allen CC, Jercinovic MJ, Allen JSB (1982) Subglacial volcanism in north-central British Columbia and Iceland. Journal of Geology. 90:699-715.

Anders RJ, Rose WI (1995) Remote sensing spectroscopy of volcanic plumes and clouds. In: McGuire B, Kilburn CRJ, Murray J (!995) Monitoring Active Volcanoes: strategies procedures and techniques. UCL Press. 301-314.

Aries SE, Harris AJL, Rothery DA (2001) Remote infrared detection of the cessation of volcanic eruptions. Geophysical research Letters. Vol.28. No.9:1803-1806.

Azimuth System (2001) AZ-16 Airborne remote sensing control display and data acquisition system.

Bacher U, Bludovsky S, Dorrer E, Munzer U (1999) Precision aerial survey of Vatnajökull, Iceland by digital photogrammetry. 3rd Turkish-German Joint Geodetic Days. Istanbul. June 1999. 1:127-136.

Baldi P, Bonvalot S, Briole P, Marsella m (2000) Digital photogrammetry and kinematic GPS applied to the monitoring of Vulcano Island, Aeolian Arc, Italy. Geophysical Journal International. 142:801-811.

Baltsavias EP, Favey E, Bauder A, Bosch H, Pateraki M (2001) Digital surface modelling by airborne laser scanning and digital photogrammetry for glacier monitoring. Photogrammetric record. 17 (98):243-273.

References

Barducci A, Pippi I (1996) Temperature and Emissivity retrieval from remotely sensed images using the "Grey Body Emissivity" method. IEEE Transactions of Geoscience and Remote Sensing. Vol. 34. No.3:681-695.

Behrendt JC, LeMasurier W, Cooper AK (1992) The West Antarctic rift system propagating rift "captured" by a mantle plume? In: Yoshida Y, Kaminuma K, Shiraishi K (1992) Recent Progress In Antarctic Earth Science. Terra Publishing Tokyo. pp.315-322.

Bennett MR, Glasser NF (1996) Glacial Geology: Ice Sheets and Landforms. John Wiley. Chichester. Pp. 65-82.

Benson CS, Follett AB (1986) Application of Photogrammetry to the study of volcano-glacier interactions on Mount Wrangell, Alaska. Photogrammetric Engineering and Remote Sensing. Vol. 52, No.6 pp.813-827.

Björnsson H (1974) Explanation of jökulhlaups from Grímsvötn, Vatnajökull, Iceland. Jokull.24:1-24.

Björnsson H (1982b) Drainage basins on Vatnajökull mapped by radio echo soundings. Nordic Hydrology. 13(4):213-232.

Björnsson H (1983) A natural calorimeter at Grímsvötn: an indicator of geothermal and volcanic activity. Jökull. 33:13-18.

Björnsson H (1988) Hydrology of ice caps in volcanic regions. Society of Science Iceland. 45:139.

Björnsson H (2002) Subglacial lakes and jökulhlaups in Iceland. Global and Planetary Change 35:255-271.

Björnsson H (2004) Glacial lake outburst floods in mountain environments. In: Owens PN, Slaymaker O (2004) Mountain Geomorphology. Arnold. London. 165-184.

References

Björnsson H, Bjornsson S, Sigurgeirsson Th. (1982) Penetration of water into hot rock boundaries of magma at Grimsvotn. Nature. 295:580-581.

Björnsson H, Gudmundsson MT (1993) Variations in the thermal output of the subglacial Grímsvötn caldera, Iceland. Geophysical Research Letters.Vol.20. No. 19:2127-2130.

Blair CL (1974) The American Landscape: map and aerial photo interpretation. McGraw-Hill. New York.

Bohren CF, Barkstrom BR (1974) Theory of the optical properties of snow. Journal of Geophysical Research. Vol. 79. No.30:4527-4535.

Buongiorno MF, Realmuto VJ, doumaz F (2002) Recovery of spectral emissivity from thermal infrared multispectral scanner imagery acquired over a mountainous terrain: A case study from Mount Etna, Sicily. Remote Sensing of Environment. 79:123-133.

Bourgeois O, Dauteuil O, Van Vleit-Lanöe B (1998) Pleistocene subglacial volcanism in Iceland: Tectonic implications. Earth and Planetary Science Letters. 164:165-178.

Campbell JB (2002) Introduction to Remote Sensing. 3rd Edition. Taylor and Francis. New York.

Cecchi E, van Wyk de Vries B, Lavest JM, Harris A, Davies M (2003) N-view reconstruction: a method for morphological modelling and deformation measurement in volcanology. Journal of volcanology and geothermal research. 123:181-201.

Chandler JH (1999) Effective application of automated digital photogrammetry for geomorphological research. Earth surface processes and landforms. 24:51-63.

References

Congalton RG (1991) A review of assessing the accuracy of classifications of remotely sensed data. Remote Sensing of the Environment. 37;35-46.

Congalton RG, Green K (1999) Assessing the Accuracy of Remotely Sensed Data: Principles and Practices. Lewis Publishers London.

Correig AM, Urqizu M, Vila J, Marti J (1997) Analysis of the temporal occurrence of seismicity at Deception Island (Antarctica). Pure and Applied Geophysics. 149:553-574.

Cracknel AP, Hayes LWB (1991) Introduction to remote Sensing. Taylor and Francis. London.

Crisp J, Bartholomew MJ (1992) Mid-infrared spectroscopy of pahala ash palagonite and implications for remote sensing studies of Mars. Journal of Geophysical research. Vol.97 No.E9:14691-14699.

Cronin SJ, Neall VE, Lecointre JA, Palmer AS (1996) Unusual "snow slurry" lahars from Ruapehu volcano, New Zealand, September 1995. Geology. V.24. No. 12. 1107-1110.

Curran PJ (1992) Principles of Remote Sensing. Longman Scientific and Technical. England.

Decker B, Decker R (1996) Volcanoes. Revised and Updated Edition. WH Freeman & Co. 6th Edition.

Deichmann N, Ansorge J, Scherbaum F, Aschwanden A, Bernardi F, Gudmundsson GH (2000) Evidence for deep ice quakes in an alpine glacier. Annals of Glaciology. International Glaciological Society. 31:85-90.

Donnadieu F, Kelfoun K, van Wyk de Vries B, Cecchi E, Merle O (2003) Digital photogrammetry as a tool in analogue modelling: applications to volcano instability. Journal of volcanology and geothermal research. 123:161-180.

References

Dozier J (1981) A method for satellite identification of surface temperature fields of subpixel resolution. Remote Sensing of Environment 11:221-229.

Drury SA (1993) Image Interpretation in Geology. Chapman & Hall. London.

Edwards BR, Russell JK, Anderson RG (2002) Subglacial phonolitic volcanism at Hoodoo Mountain volcano, northern Canadian Cordillera. Bulletin of Volcanology. 64:254-272.

Edwards BR, Russell JK (2002) Glacial influences on morphology and eruptive products of Hoodoo Mountain volcano, Canada. In: Smellie JL, Chapman MG (Eds) (2002) Volcano-Ice Interaction on Earth and Mars. Geological Society London, Special Publications. 202:179-194.

Einarsson P, Brandsdóttir B, Guðmundsson MT, Björnsson H, Grönvold K, Sigmundsson F (1997) Centre for the Icelandic Hotspot experiences Volcanic Unrest. EOS. Vol. 78. No. 35. p.369,374-375.

Einarsson P (1999) Geology of Iceland: Rocks and Landscape. Mál og Menning.

Einarsson þ, Brandsdóttir B (2000) Earthquakes in the Mýrdalsjökull area, Iceland 1978-1985: Seasonal correlation and connection with volcanoes. Jökull. 49:59-73.

Elachi C (1987) Introduction to the Physics and Techniques of Remote Sensing. Wiley Series in Remote Sensing. New York.

Engman ET, Gurney RJ (1991) Remote Sensing in Hydrology. Chapman and Hall. London.

ERDAS (1999) Erdas Imagine Field Guide. Atlanta. ERDAS Inc.

ESRI (1993) Understanding GIS. The ARC/INFO method. ESRI Inc. Longman Scientific & Technical Group. London.

References

Foody GM (2002) Status of land cover classification accuracy assessment. Remote Sensing of the Environment. 80:185-201

Fountain AG, Walder JS (1998) Water flow through temperate glaciers. Reviews of Geophysics. Vol. 36. No. 3 pp299-328.

Francis PW, Glaze LS, Rothery DA (1989) Lascar volcano set to erupt. Nature. 339:434-434.

Francis P, Rothery D (2000) Remote Sensing of Active Volcanoes. Annual Review of Earth and Planetary Science. 28:81-106.

Fridleifsson IB, Furnes H, Atkins FB (1982) Subglacial volcanics – on the control of magma chemistry on pillow dimensions. Journal of Volcanology and Geothermal Research. 13:103-117.

Garratt JR (1992) The atmospheric boundary layer. Cambridge Atmospheric and Space Science Series. Cambridge University Press.

Gibson PJ (2000) Introductory Remote Sensing: Principles and Components. Routledge. London.

Gill AE (1982) Atmosphere-Ocean Dynamics. International Geophysics Series. Vol.30. Academic Press. London.

Glaze L, Francis PW, Rothery DA (1989) Measuring thermal budgets of active volcanoes by satellite remote sensing. Nature. Vol. 338:144-146.

Goetz AFH, Rowan C (1981) Geologic Remote Sensing. Science. 211:781-791.

Gooch MJ, Chandler JH, Stojic M (1999) Accuracy assessment of digital elevation models generated using the ERDAS Imagine Orthomax digital photogrammetric system.Photogrammetric Record. 16(93):519-531.

References

Gronvold K, Oskarsson N, Johnsen S, Clausen H, Hammer CU, Bond G, Bard E
(1995) Ash layers from Iceland in the Greenland GRIP ice core correlated with
oceanic and land sediments. Earth and Planetary Science Letters. 135:149-
155.

Guðmundsson MT (1989). The Grímsvötn caldera, Vatnajökull: subglacial
topography and structure of caldera infill. Jökull.39:1-9.

Guðmundsson MT (2003) Melting by Magma-Ice-Water interactions during
subglacial eruptions as an indicator of heat transfer in subaqueous eruptions.
Geophysical Monograph 140:61-72.

Guðmundsson MT, Björnsson H (1991) Eruptions in Grímsvötn, Vatnajökull,
Iceland. Jökull. 41:21-45.

Guðmundsson MT, Milsom J (1997) Gravity and magnetic studies of the subglacial
Grímsvötn volcano, Iceland: Implications for crustal and thermal structure.
Journal of Geophysical Research. Vol 102. No. B4: 7691-7704.

Guðmundsson MT, Sigmundsson F, Björnsson H (1997) Ice-volcano interaction of the
1996 Gjálp subglacial eruption, Vatnajökull, Iceland. Nature. 389:954-957.

Guðmundsson MT, Pálsson F, Björnsson H, Högnadóttir þ (2002) The hyaloclastite
ridge formed in the subglacial 1996 eruption in Gjálp, Vatnajökull, Iceland:
present day shape and future preservation. In: Smellie JL, Chapman MG (eds)
2002. Volcano-Ice Interaction on Earth and Mars. Geological Society, London,
Special Publications, 202:319-335.

Guðmundsson MT, Sigmundsson F, Björnsson H, Högnadóttir þ (2004) The 1996
eruption at Gjálp, Vatnajökull ice cap, Iceland: efficiency of heat transfer, ice
deformation and subglacial water pressure. Bulletin of Volcanology. 66:46-65.

References

Guðmundsson S, Björnsson H, Palsson, Haraldsson HH (2003) Physical energy balance and degree-day models of summer ablation on Langjökull ice cap, SW Iceland. Raunvisdastofnun Haskolans. RH-20-2003.

Gwinner K, Hauber E, Jaumann R, Neukum G (2000) High resolution digital photogrammetric mapping: A tool for earth science. EOS. American Geophysical Union. Vol. 81. No. 44. 513, 516-520.

Hall DK, Martinec J (1985) Remote Sensing of Ice and Snow. Chapman and Hall. London.

Harris AJL, Vaughan RA, Rothery DA (1995) Volcano detection and monitoring using AVHRR data: the Krafla eruption 1984. International Journal of Remote Sensing. Vol 16. No. 6:1001-1020.ondon.

Harris AJL, Butterworth AL, Carlton RW, Downey I, Miller P, Navarro P, Rothery DA (1997) Low-cost volcano surveillance from space: case studies from Etna, Krafla, Cerro Negro, Fogo, Lascar and Erebus. Bulletin of Volcanology. 59:49-64.

Harris AJL, Flynn LP, Keszthelyi L, Mouginis-Mark PJ, Rowland SK, Resing JA (1998) Calculation of lava effusion rates from Landsat TM data. Bulletin of Volcanology. 60:52-71.

Harris AJL, Flynn LP, Rothery DA, Oppenheimer C, Sherman SB (1999) Mass flux measurements at active lava lakes: Implications for magma recycling. Journal of Geophysical Research. Vol.104. No. B4:7117-7136.

Harris AJL, Murray JB, Aries SE, Davies MA, Flynn LP, Wooster MJ, Wright R, Rothery DA (2000) Effusion rate trends at Etna and Krafla and their implications for eruptive mechanisms. Journal of Volcanology and Geothermal Research. 102:237-270.

References

Harris AJL, Pilger E, Flynn LP, Garbeil H, Mouginis-Mark PJ, Kauahikaua J,
Thornber C (2001) Automated high temporal resolution thermal analysis of
Kilauea volcano, Hawaii, using GOES satellite data. International journal of
remote Sensing. Vol. 220 No. 6:945-967.

Hicks B,B (1972) Some evaluations of drag and bulk transfer coefficients over water
bodies of different sizes. Boundary Layer Meteorology. 3:201-213.

Hodgkins R (2001) Southern Langjökull outlet glaciers: glaciological and
hydrological application of digital elevation models. In: NERC Airborne
Remote Sensing Facility Project 01/18 Scientific report.

Hoffbeck JP, Landgrebe DA (1994) Effect of radiance to reflectance transformation
and atmosphere removal on maximum likelihood classification accuracy of
high dimensional remote sensing data. IGRASS 1994. International
Geoscience and Remote Sensing Symposium on Surface and Atmospheric
Remote Sensing: technologies, data analysis and interpretation. 2538-2540.

Hoblitt RP, Walder JS, Dreidger CL, Scott KM, Pringle PT, Vallance JW (1998)
Volcano Hazards from Mount Rainier, Washington. Revised 1998. USGS
Open-File Report. 98-428.

Höskuldsson A, Sparks RSJ (1997) Thermodynamics and fluid dynamics of effusive
subglacial eruptions. Bulletin of Volcanology. 59:219-230.

Hurst AW, Bibby HM, Scott BJ, McGuinness MJ (1991) The heat source of Ruapehu
crater lake: Deductions from the energy and mass balances. Journal of
Volcanology and Geothermal Research. 46:1-20.

Jensen JR (1996) Introductory digital image processing: a remote sensing perspective.
2nd edition. Prentice Hall.

Jones I, George G, Reynolds C (2005) Quantifying effects of phytoplankton on the heat budgets of two large limnetic enclosures. Freshwater Biology. 50:1239-1247.

Jones JG (1968) Intraglacial volcanoes of the Laugarvatn region, south west Iceland I. Journal of the Geological Society of London. 124:197-211.

Jones JG (1969) Pillow Lavas as depth indicators. American Journal of Science.267:181-195.

Jones JG (1970) Intraglacial volcanoes of the Laugarvatn region, south west Iceland II. Journal of Geology. 78:127-140.

Jordan R, Kieffer HH (1981) Topographic changes at Mount St. Helens: large scale photogrammetry and digital terrain models. In: Lipman PW, Mullineaux DR (Eds) The 1980 eruptions of Mount St. Helens, Washington. U. S. Geological Survey Professional Paper. 1250:135-141.

Kahle AB, Goetz AFH (1983) Mineralogic information from a new airborne thermal infrared multispectral scanner. Science. 222:24-27.

Kahle AB, Alley RE (1992) Separation of temperature and emittance in remotely sensed radiance measurements. Remote Sensing of Environment. 42: 107-111.

Kavanaugh JL, Clarke GKC (2000) Evidence for extreme pressure pulses in the subglacial water system. Journal of Glaciology. 46 (153):206-212.

Kealy PS, Hook SJ (1993) Separating temperature and emissivity in thermal infrared multispectral scanner data: Implications for recovering land surface temperatures. IEEE Transactions on Geoscience and Remote Sensing. Vol. 13. No. 6:1155-1164.

References

Kerle N (2002) Volume estimation of the 1998 flank collapse at Casita Volcano, Nicaragua: A comparison of photogrammetric and conventional techniques. Earth surface processes and landforms. 27: 759-772.

Kirkland L, Herr K, Keim E, Adams P, Salisbury J, Hackwell J, Treiman A (2002) First use of an airborne thermal infrared hyper spectral scanner for compositional mapping. Remote Sensing of Environment. 80:447-459.

Konstantinou KI, Nolet G, Morgan WJ, Allen RM, Pritchard MJ (2000) Seismic phenomena associated with the 1996 Vatnajökull eruption, central Iceland. Journal of Volcanology and Geothermal research. 102:169-187.

Kristmannsdottir H, Björnsson A, Palsson S, Sveinbjornsdottir AE (1999) The impact of the 1996 subglacial volcanic eruption in Vatnajökull on the river Jökulsá a Fjöllum, North Iceland. Journal of Volcanology and Geothermal Research 92:359–372

Kyle PRK, Meeker K, Finnegan D (1990) Emission rates of sulphur dioxide, trace gases, and metals from Mount Erebus, Antarctica. Geophysical Research Letters. 17:2125-2128.

Lane SN, James TD, Crowell MD (2000) Application of digital photogrammetry to complex topography for geomorphological research. Photogrammetric Record 16(95):793-821.

Larsen G, Gudmundsson MT, Björnsson H (1998) Eight centuries of periodic volcanism at the centre of the Iceland hot spot revealed by glacier tephrostratigraphy. Geology. Vol. 26. No.10:943-946.

Larsen G (2002) A brief overview of eruptions from ice covered and ice capped volcanic systems in Iceland during the past 11 centuries: frequency, periodicity and implications. In: Smellie JL, Chapman MG (Eds) (2002) Volcano-Ice Interaction on Earth and Mars. Geological Society London, Special Publications. 202:81-90.

References

Le Masurier WE (2002) Architecture and Evolution of Hydrovolcanic deltas in Marie Byrd Land, Antarctica. In: Smellie JL, Chapman MG (Eds) (2002) Volcano-Ice Interaction on Earth and Mars. Geological Society London, Special Publications. 202:115-148.

Liang S (2001) An optimisation algorithm for separating land surface temperature and emissivity from multispectral thermal infrared imagery. IEEE Transactions on Geoscience and Remote Sensing. Vol. 39. No.2:264-274.

Lillesand TM, Kiefer RW, Chipman JW (2004) Remote Sensing and Image Interpretation. 5th Edition. Wiley. New York.

Longley PA, Goodchild MF, MaGuire DJ, Rhind DW (2001) Geographic Information Systems and Science. John Wiley & Sons Ltd. Chichester.

Malthe-Sørensson A, Walmann T, Jamtveit B, Feder J, Jossang T (1998) Modelling and characterisation of fracture patterns in the Vatnajökull glacier. Geology. 26:931-934.

Mather PM (1999) Computer Processing of Remotely Sensed Images. An Introduction. 2nd Edition. Wiley. Chichester.

Matson M, Dozier J (1981) Identification of sub-resolution high temperature sources using a thermal infrared sensor. Photogrammetric Engineering and Remote Sensing.47(9):1311-1318.

Motyka R, Mackeith P, Benson C (1978) Increased heating and geothermal heat flow at Mount Wrangell Caldera, Alaska. EOS. Vol. 59. No. 12. p.1201 (Abstract)

Motyka R, Mackeith P, Benson C (1980) Mount Wrangell Caldera. Utilization of glacier ice to measure heat flow and infer thermal regime. EOS. Vol. 61. No. 6. p.69 (Abstract)

Mouginis-Mark PJ, Snell H, Ellisor R (2000) GOES satellite and field observations of the 1998 eruption of Volcano Cerro Azul, Galapagos Islands. Bulletin of Volcanology. 62:188-198.

NERC ARSF User Manuel (2002a) Airborne Thematic Mapper (ATM) and Integrated Data System (IDS). Version 2.

NERC ARSF User Manuel (2002b) Itres Research Compact Airborne Spectrographic Imager (CASI). Version2.

Nichols ARL, Carroll MR, Höskuldsson A (2002) Is the Iceland hot spot also wet? Evidence from the water contents of undegassed submarine and subglacial pillow basalts. Earth and Planetary Science Letters. 202:77-87.

Nolin AW, Dozier J (2000) A hyperspectral method for remotely sensing the grain size of snow. Remote Sensing of Environment. 74:207-216.

Nye JF (1976) Water flow in glaciers: jökulhlaups, tunnels and veins. Journal of Glaciology. Vol. 17. No.76. 181-204

Oke TR (1995) Boundary Layer Climates. 2nd Edition. Routledge. London.

Oliver MA, Webster R (1990) Kriging: a method of interpolation for geographical information systems. International Journal of geographical Information Systems. Vol.4. No. 3. 313-332.

Oppenheimer C (1991) Lava flow cooling estimated from Landsat Thematic Mapper infrared data: the Lonquimay eruption (Chile, 1989). Journal of Geophysical Research. Vol.96. No. B13: 21865-21878.

Oppenheimer C (1996) Crater lake heat losses estimated by remote sensing. Geophysical research letters. Vol. 23. No. 14:1793-1796.

References

Oppenheimer C (1997a) Ramifications of the skin effect for crater lake heat budget analysis. Journal of Volcanology and Geothermal Research. 75:159-165.

Oppenheimer C (1997b) Surveillance and Mapping of Volcanoes and their emissions by satellite remote sensing. Geography. Vol.28(4):317-333.

Oppenheimer C (1997c) Remote sensing of the colour and temperature of volcanic lakes. International Journal of remote Sensing. Vol. 18. No. 1:5-37.

Oppenheimer C, Rothery DA (1991) Infrared monitoring of volcanoes by satellite. Journal of the Geological Society, London, 148:563-569.

Oppenheimer C, Rothery DA, Francis P (1993a) Thermal distributions at fumarole fields: implications for infrared remote sensing of active volcanoes. Journal of Volcanology and Geothermal research. 55:97-115.

Oppenheimer C, Francis PW, Rothery DA, Carlton RWT, Glaze LS (1993b) Infrared Image Analysis of volcanic thermal features: Láscar volcano, Chile, 1984-1992. Journal of Geophysical Research. Vol.98 No. B3:4269-4286.

Oppenheimer C, Francis PW (1997) Remote sensing of heat, lava and fumerole emissions from Erta'Ale volcano, Ethiopia. International Journal of Remote Sensing. Vol. 18. No. 8:1661-1692.

Oppenheimer C, Yirgu G (2002) Thermal imaging of an active lava lake: Erta'Ale volcano, Ethiopia. International Journal of Remote Sensing. Vol. 23. No. 22:4777-4782.

Owens PN, Slaymaker O (2004) Mountain Geomorphology. Arnold. London.

Painter TH, Dozier J, Roberts DA, Davis RE, Green RO (2003) Retrieval of subpixel snow covered area and grain size from imaging spectrometer data. Remote Sensing of Environment. 85:54-77.

References

Pinkerton H, James M, Jones A (2002) Surface temperature measurements of active lava flows on Kilauea volcano, Hawaii. Journal of Volcanology and Geothermal Research. 113:159-176.

Rasemann S, Schmidt J, Schrott L, Dikau R (2004) Geomorphometry in mountain terrain. In: Bishop MP, Shroder JF (2004) Geographic Information Science and mountain Geomorphology. Springer Praxis. Chichester. 101-145.

Realmuto VJR, Sutton AJS, Elias T (1997) Multispectral thermal infrared mapping of sulphur dioxide plumes: A case study from the East Rift Zone of Kilauea Volcano, Hawaii. Journal of geophysical Research Vol.102. No. B7:15057-15072.

Rees WG (1999) The Remote Sensing Data Book. Cambridge University Press. Cambridge.

Rees WG, James SP (1992) Angular variation of the infrared Emissivity of ice and water surfaces. International Journal of remote Sensing. Vol. 13. No.15:2873-2886.

Renz A (1999) Remote Sensing for the Earth Sciences. Manual of Remote Sensing. 3rd Edition.

Richards JA, Jai X (1999) Remote Sensing Digital Image Analysis: An Introduction. 3rd Edition. Springer–Verlag. Berlin.

Roberts MJ, Russell AJ, Tweed FS, Knudsen Ó (2000) Ice fracturing during jökulhlaups: implications for englacial floodwater routing and outlet development. Earth Surface Processes and Landforms. 25:1429-1446.

Rose WI, Bluth GJS, Ernst GGJ (2000) Integrating retrievals of volcanic cloud characteristics from satellite remote sensors: a summary. The Royal Society. London. 358:1585-1606.

Rothery DA, Francis PW, Wood CA (1988) Volcano monitoring using short wavelength infrared data from satellites. Journal of Geophysical Research. Vol. 93. No. B7: 7993-8008.

Rothery DA, Borgia RW, Carlton RW, Oppenheimer C (1992) The 1992 Etna lava flow imaged by Landsat TM. Int. J. of Remote Sensing. Vol.13. No.15:2759-2763.

Rothery DA, Oppenheimer C (1994) Monitoring Mount Erebus by satellite remote sensing. In: Volcanological and environmental studies of Mount Erebus, Antarctica. Antarctic Research studies. 66:51-56.

Rothery DA, Oppenheimer C, Bonneville A (1995) Infrared thermal monitoring. In: McGuire B, Kilburn CRJ, Murray J (1995) Monitoring Active Volcanoes. UCL Press. 184-216.

Rothery DA, Thorne MT, Flynn LP (2003) MODIS thermal alerts in Britain and the North Sea during the first half of 2001. International Journal of Remote Sensing. Vol. 24 No.4:817-826.

Sabine C, Realmuto VJ, Taranik JV (1994) Quantitative estimation of granitoid composition from thermal infrared multispectral scanner (TIMS) data, Desolation Wilderness, Northern Sierra Nevada, California. Journal of Geophysical Research. Vol. 99. No. B3:4261-4271.

Saemundsson K (1979) Outline of the geology of Iceland. Jokull. 29: 7-28.

Schmugge T, Hook SJ, Coll C (1998) Recovering surface temperature and emissivity from thermal infrared multispectral data. Remote Sensing of Environment. 65:121-131.

Schmugge T, French A, Ritchie JC, Rango A, Pelgrum H (2002) Temperature and emissivity separation from multispectral thermal infrared observations. Remote Sensing of Environment. 79:189-198.

Shilling JG, Bergeron MB, Evans R (1980) Halogens in the mantle beneath the North Atlantic. Philosophical Transactions of the Royal Society of London (A). 297:147-178.

Sigmundsson F (1998) 1998 Grímsvötn Eruption. http://www.norvol.hi.is

Sigmundsson F, Gudmundsson MT (2004) Gos í Grímsvötnum 1-6 November 2004. Jokull. 54:139-142 (In Icelandic).

Sigmundsson F, Einarsson P, Gudmundsson MT, Jakobsdottir S, Roberts M, Vogfjord K, Stefansson R (2004) Release of overburden pressure triggers an eruption of Grímsvötn volcano, Iceland, November 1, 2004. Nordic Volcanological Centre, Iceland. Online eruption updates. http://www.norvol.hi.is/index.html

Sigmarsson O, Karlsson HR, Larsen G (2000) The 1996 and 1998 subglacial eruptions beneath the Vatnajökull ice sheet in Iceland: contrasting geochemical and geophysical inferences on magma migration. Bulletin of Volcanology. 61:468-476.

Skilling IP (1994) Evolution of an englacial volcano :Brown Bluff Antarctica. Bulletin of Volcanology. 56:573-591.

Skilling IP (2002) Basaltic pahoehoe lava-fed deltas: large scale characteristics, clast generation, emplacement processes and environmental discrimination. *In*: Smellie JL, Chapman MG (Eds) (2002) Volcano-Ice Interaction on Earth and Mars. Geological Society London, Special Publications. 202:91-113.

Slater L, Jull M, McKenzie D, Grönvold K (1998) Deglaciation effects on mantle melting under Iceland: results from the northern volcanic zone. Earth and Planetary Science letters. 164:151-164.

Smellie JL (1999) Subglacial eruptions. In: Sigurdsson H. (Ed.) Encyclopedia of Volcanoes. Academic Press. pp. 403-418.

References

Smellie JL (2002) The 1969 subglacial eruption on Deception Island (Antarctica): events and processes during an eruption beneath a thin glacier and implications for volcanic hazards. In: Smellie JL, Chapman MG (Eds) (2002) Volcano-Ice Interaction on Earth and Mars. Geological Society London, Special Publications. 202:59-79.

Smellie JL, Hole MJ, Nell PAR (1993) Late Miocene valley confined subglacial volcanism in Northern Alexander Island, Antarctic Peninsula. Bulletin of Volcanology. 55:273-288.

Smellie JL, Skilling IP (1994) Products of subglacial volcanic eruptions under different ice thicknesses: two examples from Antarctica. Sedimentary Geology. 91:115-129.

Smellie JL, Hole MJ (1997) Products and processes in Pliocene-Recent subaqueous to emergent volcanism in the Antarctic Peninsula: examples of englacial Surtseyan volcano construction. Bulletin of Volcanology. 58:628-646.

Smithsonian Institution (1996) Grímsvötn. Bulletin of the Global Volcanism Network. BGVN 21:09.

Smithsonian Institution (1998) Grímsvötn. Bulletin of the Global Volcanism Network. BGVN 23:11.

Smithsonian Institution (2004) Grímsvötn. Bulletin of the Global Volcanism Network. BGVN 29:10.

Sobrino JA, Jimenez-Munoz JC, Labed-Nachbrand J, Nerry F (2002) Surface emissivity retrieval from digital imaging spectrometer data. Journal of Geophysical research. Vol. 107. No. D23:4729

Sparks RSJ, Bursik MI, Carey SN, Gilbert JS, Glaze LS, Sigurdsson H, Woods AW (1997) Remote sensing of volcanic plumes. In: Volcanic Plumes. Wiley. Chichester. 307-345.

References

Steinthorsson S, Hardarson BS, Ellam RM, Larsen G (2000) Petrochemistry of the
Gjálp-1996 subglacial eruption, Vatnajökull, SE Iceland. Journal of
Volcanology and Geothermal Research. 98:79-90

Sturkell E, Einarsson P, Sigmundsson F, Hreinsdóttir S, Geirsson H, (2003)
Deformation of Grímsvötn volcano, Iceland: 1998 eruption and subsequent
inflation. Geophysical Research Letters. Vol. 30, No. 4:1182-1185.

Sturkell E, Einarsson P, Sigmundsson F, Geirsson H, Olafsson H, Pedersen R, de
Zeeuw-van Dalfsen E, Linde AT, Sacks S, Stefansson R (2005) Volcano
geodesy and magma dynamics in Iceland. Journal of Volcanology and
Geothermal Research. In Press.

Teggi S, Bogliolo MP, Buongiorno MF, Pugnaghi S, Sterni A (1999) Evaluation of
SO_2 emission from Mount Etna using diurnal and nocturnal multispectral IR
and visible imaging spectrometer thermal IR remote sensing images and
radiative transfer models. Journal of Geophysical Research. Vol.104.
No.B9:20069-20079.

Thordarson Th, Self S (1993) The Laki (Skafta fires) and Grímsvötn eruptions in
1783-85. Bulletin of Volcanology. 55:233-263.

Thordarson Th, Self S (2003) Atmospheric and environmental effects of the 1783-
1784 Laki eruption: A review and reassessment. Journal of Geophysical
research. Vol. 108. No. 1. p.4011.

Tuffen H, Pinkerton H, McGarvie DW, Gilbert JS (2002a) Melting of the glacier base
during a small-volume subglacial rhyolite eruption: evidence from Bláhnúkur,
Iceland. Sedimentary geology. 149:183-198.

Tuffen H, McGarvie DW, Gilbert JS, Pinkerton H (2002b) Physcial Volcanology of a
subglacial-to-emergent rhyolitic tuya at Rauðufossafjöll, Torfajökull, Iceland.
In:Smellie JL, Chapman MG (Eds) (2002) Volcano-Ice Interaction on Earth
and Mars. Geological Society London, Special Publications. 202:213-236.

References

Van der Meer F (1999) Imaging spectrometry for geological remote sensing. Geologie en Mijnbouw. 77:137-151.

Verstappen H, Th (1977) Remote Sensing in geomorphology. Elsevier. Amsterdam.

Vila J, Marti J, Ortiz R, Garcia A, Correig AM (1992) Volcanic tremors at Deception Island (South Shetland Islands, Antartica). Journal of volcanology and geothermal research. 53:89-102.

Vincent RK (1997) Fundamentals of Geological and Environmental Remote Sensing. Prentice-Hall Inc. London.

Vogfjörd KS, Jakobsdóttir SS, Gudmundsson GB, Roberts MJ, Ágústsson K, Arason T, Geirsson H, Karlsdóttir S, Hjaltadóttir S, Ólafsdóttir U, Thorbjarnardóttir B, Skaftadóttir T, Sturkell E, Jónasdóttir EB, Hafsteinsson G, Sveinbjörnsson H, Stefánsson R, Jonsson TV (2005) Forcasting and monitoring a subglacial eruption in Iceland. EOS, Transactions, American Geophysical Union. Vol. 86, No. 26:246, 247.

Wadge G, Macfarlane DG, Robertson DA, Hale AJ, Pinkerton H, Burrell RV, Norton GE, James MR (2005) AVTIS: A novel millimetre-wave ground based instrument for volcano remote sensing. Journal of Volcanology and Geothermal Research. Vol 146. No. 4:307-318.

Wan Z, Ng D, Dozier J (1994) Spectral emissivity measurements of land surface materials and related radiative transfer simulations. Advance Space Research Vol. 14. No. 3:91-94.

Wilson AK (1997) An Integrated Data System for Airborne Remote Sensing. International Journal of Remote Sensing. Vol. 18. No. 9. 1889 – 1901.

Wilson AK (2003) Personal Communication. Radiance to surface brightness temperature conversion programme.

Wilson L, Head JW (2002) Heat transfer and melting in subglacial basaltic volcanic eruptions: implications for volcanic deposit morphology and melt water volumes. In: Smellie JL, Chapman MG (Eds) (2002) Volcano-Ice Interaction on Earth and Mars. Geological Society London, Special Publications. 202:5-26.

Wilson JP, Gallant JC (2000) Terrain Analysis: Principals and Applications. John Wiley and Sons. New York.

Whitten DGA, Brooks JRV (1972) Dictionary of Geology. Penguin London.

Wolf PR (1983) Elements of Photogrammetry. 2nd Edition. McGraw-Hill. New York.

Wolf PR, Dewitt BA (2000) Elements in Photogrammetry with applications in GIS. 3rd Edition. McGraw-Hill.

Wood and Kienle, 1990, Volcanoes of North America: United States and Canada: Cambridge University Press, 354p, p.158-160.

Wooster MJ, Rothery DA (1997) Thermal monitoring of Lascar Volcano, Chile, using infrared data from the along track scanning radiometer: a 1992-1995 time series. Bulletin of Volcanology. 58:566-579.

Wright R, Rothery DA, Blake S, Pieri DC (2000a) Visualizing active volcanism with high spatial resolution satellite data: the 1991-1993 eruption of Mount Etna. Bulletin of Volcanology. 62:256-265.

Wright R, Rothery DA, Blake S, Pieri DC (2000b) Improved remote sensing estimates of lava cooling: A case study of the 1991-1993 Mount Etna eruption. Journal of geophysical Research. Vol. 15. No. B10:23681-23694.

References

Wright R, Flynn L, Garbeil H, Harris AJL, Pilger E (2002) Automated volcanic eruption detection using MODIS. Remote Sensing of Environment. 82:135-155.

Wright R, Blake S, Harris AJL, Rothery DA (2001) A simple explanation for the space based calculation of lava eruption rates. Earth and Planetary Science Letters. 192:223-233.

Zobin M (1999) The fault nature of the Ms 5.4 volcanic earthquake preceding the 1996 subglacial eruption of Grímsvötn volcano, Iceland. Journal of Volcanology and geothermal Research. 92:349-358.

Zuidam RA van (1986) Aerial photo interpretation in terrain analysis and geomorphological mapping. International Institute for Aerospace Survey and Earth Sciences. The Hague. Smits.

Appendices

Appendix A:

Mathematical and Physical symbols

Equations

Abbreviations

Glossary

HDF header files

Appendix B:

ATM imagery – prior to image enhancement

Principal components analysis

Classification accuracy assessment

Appendix C:

Temperature conversion algorithm

Radiance to temperature conversion

Heat flux

Meteorological station data

Appendix D:

Mean square error calculation (for the parallax bar)

Aerial photographs used in the generation of geomorphological map and DEM

Appendix E:

Recommendations to the NERC ARSF

Appendix F:

CASI compositional mapping

Appendix G:

Conferences attended

Selected conference abstracts

Appendix H:

Publications derived from thesis

Appendix A

A1. Mathematical and Physical Symbols

M_λ	Planck Function
C_1	Radiation constant
λ	Wavelength
C_2	Radiation constant
T	Temperature
ε	Emissivity
L_λ	Spectral radiance
π	pi
M_g	Radiance of greybody
M_b	Radiance of blackbody
Q_T	Total Heat Flux
Q_{Lo}	Outgoing long wave radiation
Q_{Sh}	Sensible heat flux
Q_{LE}	Latent heat flux
Q_{Si}	Solar incoming radiation
σ	Sigma
ρ	Air Density
C_p	Specific heat capacity of air
C_e	Transfer coefficient for sensible and latent heat
U_a	Wind speed
T_s	Surface temperature
T_a	Air temperature
L	Latent heat of evaporation
$q*s$	Saturated specific humidity at water surface
q_a	Specific humidity at reference height
n_c	Cloud cover
$e*s$	Saturated vapour pressure at the surface
e_a	Vapour pressure of water in the air
P_o	Air pressure
f	Focal length
H	Mean altitude above sea level
h	Mean height of terrain above sea level
Δh	Height Difference
Δp	Differential parallax
Pa	Stereoscopic parallax
Za	Average flying height
Zo	Average aircraft altitude
hm	Relative terrain elevation
Ma	Floating mark top of object
Mb	Floating mark bottom of object

A2. Equations

3.1   Planck Function: $M_\lambda = C_1 \lambda^{-5} \left[\exp(C_2 \div \lambda T) - 1 \right]^{-1}$

3.2   Emissivity: $\varepsilon(\lambda) = M_\lambda \left(material^\circ K \right) \div M_\lambda \left(blackbody^\circ K \right)$

5.1   Percentage of total variance of each component $\%_p = (\lambda_i \times 100) \div \sum_{i=1}^{n} \lambda_i$

5.2   Factor Loadings for Principal components $R_{kp} = a_{kp} \times \sqrt{\lambda_p} \div \sqrt{(Var_k)}$

5.3   KHAT statistic (kappa) $\hat{k} = \dfrac{N \sum_{i=1}^{r} x_{ii} - \sum_{i=1}^{r} (x_i + \bullet x +_i)}{N^2 - \sum_{i=1}^{r} (x_i + \bullet x +_i)}$

6.1   Spectral exitance $L_\lambda = M_\lambda \div \pi$

6.2   Radiance of a graybody $M_g = M_b \varepsilon$

6.3   Radiance of a blackbody $M_b = M_g \div \varepsilon$

6.4   Planck's formula with sensor response $M_\lambda = \dfrac{C_1 \lambda^{-5} resp}{\exp(C_2 \div \lambda T) - 1}$

6.5   Total heat flux $Q_T = Q_{Lo} + Q_{Sh} + Q_{LE} - Q_{Si}$

6.6   Net upward longwave $Q_{Lo} = \varepsilon_s \sigma T_s^4$

6.7   Sensible heat flux $Q_{Sh} = \rho C_p U_a (T_s - T_a)$

6.8   Latent Heat flux $Q_{LE} = \rho C_e U_a (q^*_s - q_a)$

6.9   Net upward longwave corrected for cloud cover
$Q_{Lo} = \varepsilon_s \sigma T_s^4 (0.39 - 0.05 e_a^{1/2})(1 - 0.6 n_c^2)$

6.10   (a) specific saturated humidity at the surface $q^*_s = \dfrac{\lambda e^*_s}{P_o + (\lambda - 1) e^*_s}$

(b) specific humidity of the air $\quad q_a = \dfrac{\lambda e_a}{P_o + (\lambda - 1) e_a}$

6.11   saturated vapour pressure at the surface

$$e^*_s = 6.112 \exp\left[\frac{[17.67(T_s - 273.15)]}{(T_s - 29.65)}\right]$$

6.12   vapour pressure of the air

$$e^*_a = 6.112 \exp\left[\frac{[17.67(T_a - 273.15)]}{(T_a - 29.65)}\right]$$

6.13   vapour pressure of the air, corrected for humidity $\quad e_a = relative humidity \times e^*_a$

7.1   Scale: $\qquad\qquad$ Scale $= \dfrac{f}{H - h}$

7.2   Mean sq. error: $\qquad m.sq.e = \dfrac{\sum V^2}{n - 1}$

7.3   Parallax equation: $\qquad \Delta h = \dfrac{\Delta p}{Pa + \Delta p} \times Za$

7.4   Differential parallax: $\Delta p = Ma - Mb$

7.5   Stereoscopic parallax: $Pa = (h2 - h1) \div 2$

7.6   Flying height: $\qquad Za = Zo - hm$

A3. Abbreviations

AOI - Area of Interest

ARSF - Airborne Remote Sensing Facility (since Jan 2005 this has been Airborne Research and Survey Facility)

ATM - Airborne Thematic Mapper

ATSR – Along – Track Scanning Radiometer

AVHRR – Advanced Very High Resolution Radiometer

AVIRIS – Airborne Visible Infrared Imaging Spectrometer

AVTIS – All-Weather Volcano Topography Imaging Sensor

Bil - band interleaved file format

CASI - Compact Airborne Spectrographic Imager

CCD – Charge Coupled Device

DEM – Digital Elevation Model

DTM – Digital Terrain Model

EM – Electromagnetic

EMR – Electromagnetic radiation

ENVI – The Environment for Visualising Images

ERDAS - Earth Resources Data Analysis Systems

GIS - Geographical Information System

GPS - Global Positioning System

Hdf - hierarchical data file

IDS - Integrated Data System

Img – image file format

MSS – Multispectral Scanner

NERC - Natural Environmental Research Council

NIR – Near Infrared

PCA - Principal Components Analysis

RGB – Red, Green and Blue

SWIR – Short wave infrared

TIMS – Thermal Infrared Multispectral Scanner

TIN – Triangulated Irregular Network

TM – Thematic Mapper

UTM – Universal Transverse Mercator

WGS - World Geodetic System

A4. Glossary

atmospheric correction the correction of satellite and / or aircraft received data to allow for the effects on the radiation as it passes through the atmosphere

blackbody a body that absorbs all the radiation incident upon it, reflecting none

caldera a basin-shaped volcanic depression; by definition, at least a mile in diameter. Such large depressions are typically formed by the subsidence of volcanoes

calorimetry the science of measuring the heat of chemical reactions or physical changes

classificiation an aspect of image processing in which quantitative decisions are made on the basis of the data present in an image, grouping pixels or regions of an image into classes of different land cover types

clustering process of identifying groups of pixels in an image that have similar properties

change detection image processing tool used to discriminate land cover changes between different times of aquisition

digital elevation model a representation of the surface topography of a region of the
(DEM) Earth's surface

digitial number the value associated with a pixel in a digital image, corresponding to the value of some physical quantity such as the radiance in a particular band.

debris flow deposit general term for poorly sorted clastic rock deposited by dense, often fluidised flow of debris

electromagnetic system of oscillating electrical and magnetic fields that carry
radiation (EMR) energy from one point to another

EM spectrum range of frequencies over which EMR can be propagated

emmissivity ratio of thermally generated power, flux density and radiance emitted by a body

en-echelon Set of geologic features that are in an overlapping or a staggered arrangement (e.g., faults). Each is relatively short, but collectively they form a linear zone in which the strike of the individual features is oblique to that of the zone as a whole.

englacial	entirely surround by ice
firn	intermediate between snow and ice – typically comprises the upper 40-60 m of temperate glaciers
fumerole	a vent or opening through which issue steam, hydrogen sulphide, or other gases
geometric correction	the process of mapping a remotely sensed image onto a chosen projection such as latitude/longitude or a co-ordinate grid
geomorphology	study of landforms and landscapes
geothermal	Energy derived from the internal heat of the earth
ground control point (GCP)	a feature recognisable both in an image and on the ground used for geometric correction for an image
hyaloclastite	a fragmental volcanic rock composed of glassy angular fragments formed by magma-water interaction
hyperspectral sensors	instruments that acquire images in many narrow spectral bands throughout the visible, NIR and thermal infrared portions of the EM spectrum
ice cauldron	depression in the glacier surface above a region of melting (also known as a subsidence bowl)
ice sheet	a large body of ice, typically >20 Km across and >400 m thick
image processing	manipulation of data contained in an image to extract quantitative information or to emphasise features of interest
jökulhlaups	a catastrophic glacial melt water flood often triggered by melting due to geothermal activity.
lahar	a rapidly flowing mixture of rock debris and water that originates on the slopes of a volcano. Lahars are also referred to as volcanic mudflows or debris flows
Lambertian reflection	an ideally rough surface scatters radiation according to Lamberts law according to which the reflected radiance is isotropic for any illumination that is uniform across the surface
map projection	geometric transformation between the geographical co-ordinates of a point on the Earth and co-ordinates on a map or image
multispectral imager	a type of sensor operating in the visible and infrared part of the electromagnetic spectrum and providing radiance data for

	a few spectral bands for each pixel of the image
nadir	vertically downwards i.e. towards the centre of the earth
phreatomagmatic	an explosive volcanic eruption that results from the interaction of surface or subsurface water and magma
pillow lava	lava, usually basaltic occurring in pillow shaped masses, formed in a subaqueous environment
radiance	total energy radiated over a unit of area and a solid angle of measurement
spectral exitance	total energy radiated in all directions by a unit area in a unit time
stapi	Icelandic term for a table mountain
subaerial	formed within air; of volcanic deposits or eruptions, formed once the ice surface has been pierced.
subaqueous	an environment beneath water. In a subglacial setting often a subglacial lake
subglacial	occurring at the base of a glacier
table mountain	geomorphological term for any steep sided flat topped mountain including tuyas
temperate glacier	a glacier with a non frozen bed, found in Iceland and other mid to low latitude regions today
tephra	a general term for fragments of volcanic rock and lava regardless of size that are blasted into the air by explosions or carried upward by hot gases in eruption columns or lava fountains.
tuya	flat toped landforms formed by flat lying subaerial lavas overlying fragmental subglacial deposits
valley glacier	an elongate tongue like glacier confined by steep valley sides.
variogram	a measure of variance between data as a function of distance

Definitions from Whitten & Brooks (1972), Rees (1999), Smellie (1999), Lillesand et al. (2004).

A5. HDF file header information for the imagery used in this research

For further information the AZGCORR User Guide can be found on the ARSF website.
http://www.nerc.ac.uk/arsf/pages/data/manuals/usrguide.pdf

```
*******************
HDF file:a161133a.hdf
*******************
```

VGroup: Processing

PRdesc	Latest processing level of file
PRlevel	3A
PRcdate	Thur Mar 7 17:18:30 2002
PRhostn	nidsa
PRhostid	80fe0757
PRsoftware	Release 2.xx ©Azimuth Systems UK 1996,1999

`====================`

VGroup: Description

DEdesc	Data items description

`====================`

VGroup: Mission

MIdesc	Mission and site details from flight logs
MIprog1	azsite 2.0.1 Nov 16 2001
MIprog2	
MIcopyw	Data: © UK Natural Environmental Research Council, 2001.
MIairc	D-CALM
MIpilot	C. Joseph
MInavig	Tracker
MIoper	G. Osborn
MIbase	Kidlington
MIdate	10/06/01
MIfltno	019
MIprojco	00/19
MIpiaff	Prof. Harry Pinkerton, Dept. of Env. Science, Univ of Lancaster
MItarget	Grimsvotn
MIscene	Iceland
MIfline	2
MIaspeed	130kts
MItrack	NE
MIalt	8980ft
MIweath	Generally clear, a little cloud and shadow
MIcloud	10%
MIland	100%
MIcomm	None
MIfnum	0
MIalper	0
MIscanner	AZ16
MIslimit	2
MIsday	161
MIstime	164900
MIetime	165300
MIsscan	32448
MIescen	40573
MIlimits	64.3799N 17.4031 W, 64.4164 N 17.1711 W

VGroup: Mapping

Appendix A

```
----------------------
MPdesc          Mapping parameters for level 3
MPprog1
MPsphc          0
MPdatm          3
MPproj          1
MPlng0          28.00
MPlat1          0.00e+00
MPlat2          0.00e+00
MPglat          0.00e+00
MPglng          28.00
MPgx0           500000.00
MPgy0           0.00e+00
MPscf           0.9996000
MPdshc          0
MPdsVG
MPdsvec         [7] 73.00-> -8.300e+00
MPimx0          0.00e+00
MPimy0          0.00e+00
MPtiles         0
= = = = = = = = = = = = = = = = = = =
```

VGroup: ATM2

```
----------------------
ATdesc          AZ16 version ATM scanner details, calibration and data
ATprog1         azatm 2.0.8 Mar 6 2002
ATprog2
ATprog3
ATprog4
ATsbend         0
ATrgyro         0
ATrmedia        MO disc
ATtype          AZ16
ATid            NERC
ATfov           90.00
ATpixfov        2.500
ATpixrec        938
ATpixred        938
ATpixsav        938
ATsscan         32448
ATescan         40573
ATchan          11
ATbpix          16
ATwavu          [11] 448.00 -> 11500.00
ATwavl          [11] 424.00 -> 8400.00
ATscps          50.00
ATbbtf          1
ATbb1           0.00
ATbb2           0.00
ATbbscan        0
ATsbb1          [8126] 0.15000 -> 0.18000
ATsbb2          [8126] 15.14000 -> 15.14000
ATvbb1          [8126] 24785.00 -> 23745.00
ATvbb2          [8126] 27773.00 -> 26919.00
ATsync          [8126] 1753987470 -> 2659061843
ATcal           calibrated
ATcalver        az260301C.cal
ATcalfmt        band pairs
ATcalfile       az260301C.cal
ATcaltab        [20] 51.47222 -> 24338.00
```

```
ATradsc        [11] 1000.00 -> 1000.00
ATrunits       uW.cm-2.sr-1.nm-1
ATimgmin       [11] 3037.00 -> 5229.00
ATimgmax       [11] 52090.00 -> 12538.00
ATimgzer       [11] 0 -> 0
ATimgovr       [11] 0 -> 0
SCimtype       resampled 0 fill
SCorder        BIL
SClindir       left -> right
SCtiles        not tiled
SCbands        11
SCpixels       938
SClines        8126
SCpixfmt       uint16
SCHDFfmt       23
SCpixbytes     2
SCimover       0.00
SCimunder      0.00
SCposn         per image
SCaxes         north up
SCxypix        pixel centre
SCpixwid       5.00
SCpixhgt       5.00
SCviewty       nav height to MSL
SCvplane       0
SCposimag      [8] 3011.00 -> 5.00
SCbedit        [8126] 0000 -> 0000
SCsused        [2] 32448 -> 40573
SCpxyn         0
SCpxy_sc       0.100
====================
Vgroup: ATM2 SDS : Atsata dims:3011 1952 11
====================
```

****

Appendix A

HDF file:a165023a.hdf
****
VGroup: Processing

PRdesc	Latest processing level of file
PRlevel	3A
PRcdate	Wed Feb 27 09:21:39 2002
PRhostn	nidsc
PRhostid	80fe70fe
PRsoftware	Release 2.xx ©Azimuth Systems UK 1996,1999

= = = = = = = = = = = = = = = = = = = =

VGroup: Description

DEdesc	Data items description

= = = = = = = = = = = = = = = = = = = =

VGroup: Mission

MIdesc	Mission and site details from flight logs
MIprog1	azsite 2.0.1 Nov 16 2001
MIprog2	
MIcopyw	Data: © Uk Natural Environmental Research Council, 2001.
MIairc	D-CALM
MIpilot	C. Joseph
MInavig	Tracker
MIoper	G. Osborn
MIbase	Kidlington
MIdate	14/06/01
MIfltno	01/025
MIprojco	01/19
MIpiaff	Prof. Harry Pinkerton, Dept. of Env. Science, Univ of Lancaster
MItarget	Grimsvotn
MIscene	Iceland
MIfline	2
MIaspeed	125kts
MItrack	W
MIalt	8190ft
MIweath	Clear
MIcloud	0%
MIland	100%
MIcomm	
MIfnum	0
MIalper	0
MIscanner	AZ16
MIslimit	2
MIsday	165
MIstime	101300
MIetime	101900
MIsscan	24753
MIescen	30881
MIlimits	64.4178N 17.1298 W, 64.3856 N 17.4442 W

= = = = = = = = = = = = = = = = = = = =

VGroup: Mapping

MPdesc	Mapping parameters for level 3
MPprog1	
MPsphc	0
MPdatm	3

Appendix A

MPproj	1
MPlng0	28.00
MPlat1	0.00e+00
MPlat2	0.00e+00
MPglat	0.00e+00
MPglng	28.00
MPgx0	500000.00
MPgy0	0.00e+00
MPscf	0.9996000
MPdshc	0
MPdsVG	
MPdsvec	[7] 73.00-> -8.300e+00
MPimx0	0.00e+00
MPimy0	0.00e+00
MPtiles	0

= = = = = = = = = = = = = = = = = = = =

VGroup: ATM2

ATdesc	AZ16 version ATM scanner details, calibration and data
ATprog1	azatm 2.0.8 Feb 24 2002
ATprog2	
ATprog3	
ATprog4	
ATsbend	0
ATrgyro	0
ATrmedia	MO disc
ATtype	AZ16
ATid	NERC
ATfov	90.00
ATpixfov	2.500
ATpixrec	938
ATpixred	938
ATpixsav	938
ATsscan	24753
ATescan	30881
ATchan	11
ATbpix	16
ATwavu	[11] 448.00 -> 11500.00
ATwavl	[11] 424.00 -> 8400.00
ATscps	25.00
ATbbtf	1
ATbb1	0.00
ATbb2	0.00
ATbbscan	0
ATsbb1	[6129] –9.97000 -> -9.97000
ATsbb2	[6129] 15.00000 -> 15.00000
ATvbb1	[6129] 22626.00 -> 22883.00
ATvbb2	[6129] 27644.00 -> 27841.00
ATsync	[6129] 2521363713 -> 1775379574
ATcal	calibrated
ATcalver	az260301B.cal
ATcalfmt	band pairs
ATcalfile	az260301B.cal
ATcaltab	[20] 57.90625-> 24338.00
ATradsc	[11] 1000.00 -> 1000.00
ATrunits	uW.cm-2.sr-1.nm-1
ATimgmin	[11] 2085.00 -> 4185.00
ATimgmax	[11] 53042.00 -> 11759.00
ATimgzer	[11] 0 -> 0

Appendix A

```
ATimgovr        [11] 0 -> 0
SCimtype        resampled 0 fill
SCorder         BIL
SClindir        left -> right
SCtiles         not tiled
SCbands         11
SCpixels        938
SClines         6129
SCpixfmt        uint16
SCHDFfmt        23
SCpixbytes      2
SCimover        0.00
SCimunder       0.00
SCposn          per image
SCaxes          north up
SCxypix         pixel centre
SCpixwid        5.00
SCpixhgt        5.00
SCviewty        nav height to MSL
SCvplane        0
SCposimag       [8] 3082.00 -> 5.00
SCbedit         [6129] 0000 -> 0000
SCsused         [2] 24753 -> 30881
SCpxyn          0
SCpxy_sc        0.100
===================
Vgroup: ATM2 SDS : Atsata dims:3011 1952 11
===================
```

****

233

HDF file:c165023a.hdf
****
VGroup: Processing

PRdesc	Latest processing level of file
PRlevel	3A
PRcdate	Wed Feb 13 13:13:182002
PRhostn	nidsc
PRhostid	80fe70fe
PRsoftware	Release 2.xx ©Azimuth Systems UK 1996,1999

= = = = = = = = = = = = = = = = = = = =

VGroup: Description

DEdesc	Data items description

= = = = = = = = = = = = = = = = = = = =

VGroup: Mission

MIdesc	Mission and site details from flight logs
MIprog1	azsite 2.0.1 Nov 16 2001
MIprog2	caschk2 0.0.1 Nov 16 2001
MIcopyw	Data: © Uk Natural Environmental Research Council, 2001.
MIairc	D-CALM
MIpilot	C. Joseph
MInavig	Tracker
MIoper	G. Osborn
MIbase	Kidlington
MIdate	14/06/01
MIfltmo	01/025
MIprojco	01/19
MIpiaff	Prof. Harry Pinkerton, Dept. of Env. Science, Univ of Lancaster
MItarget	Grimsvotn
MIscene	Iceland
MIfline	2
MIaspeed	125kts
MItrack	W
MIalt	8190ft
MIweath	Clear
MIcloud	0%
MIland	100%
MIcomm	
MIfnum	3
MIalper	3
MIscanner	CASI
MIslimit	3
MIsday	165
MIstime	101300
MIetime	101900
MIsscan	600
MIescen	16000
MIlimits	64.4172N 17.1376 W, 64.3871 N 17.4339 W

= = = = = = = = = = = = = = = = = = = =

VGroup: Mapping

MPdesc	Mapping parameters for level 3
MPprog1	
MPsphc	0
MPdatm	3

Appendix A

```
MPproj          1
MPlng0          28.00
MPlat1          0.00e+00
MPlat2          0.00e+00
MPglat          0.00e+00
MPglng          28.00
MPgx0           500000.00
MPgy0           0.00e+00
MPscf           0.9996000
MPdshc          0
MPdsVG
MPdsvec         [7] 73.00-> -8.300e+00
MPimx0          0.00e+00
MPimy0          0.00e+00
MPtiles         0
= = = = = = = = = = = = = = = = = = =

VGroup: CASI
----------------------
CAdesc          CASI scanner details and data
CAprog1         cas_2 1.0.1 Nov 26 2001
CAprog2
CAprog3         azgcorr 4.3.3 DEC 20 2002
CAprog4
CAserial        2007
CAswver         5.03oAlphaR$
CAexa           unknown
CAfnum          0
CAconfig        VEG
CAsday          14
CAstime         101347
CAmode          0
CAg             [4] 950.04 -> 3.26168e-07
CAinteg         15.00
CAapert         3.00
CAfapert        1.00
CAoaxis         253.50
CAfov           53.20
CAfovport       0.00
CAfovpix        512
CApsfov         [512] 26.28600 -> -26.82400
CApside         0
CAsscan         600
CAescan         16001
CAlooks         23
CAlooksp        4
CAlookc         256
CAsumdch        1
CAsrcpres       0
CAsrcbands      1
CAsrcchan       170
CAsrcpix        0
CAilspres       1
CAilsbands      13
CAilspix        1
CAbstart        [13] 259 -> 4
CAbend          [13] 268 -> 8
CAwavc          [13] 449.93 -> 940.41
CAwavh          [13] 9.47570 -> 4.95339
CAcalfile       in22a3.rad
```

```
CAradsc        1000.00
CArunits       uW.cm-2.sr-1.nm-1
CAiunits       uW.cm-2.nm-1
CAimgmin       [13] 1130.61 ->0.50027
CAimgmax       [13] 64275.92 -> 14597.26
CAimgzer       [13] 0 -> 57
CAimgobr       [13] 1 -> 0
CAilsmin       [13] 10816.17 -> 2205.29
CAilsmax       [13] 12929.17 -> 3814.63
CAilszer       [13] 0 -> 0
CAilsovr       [13] 0 -> 0
SCimtype       1
SCorder        0
SClindir       0
SCtiles        0
SCbands        13
SCpixels       512
SClines        15401
SCpixfmt       1
SCHDFfmt       23
SCpixbytes     2
SCimover       65536.00
SCimunder      0.00
SCposn         0
SCaxes         1
SCxypix        0
SCpixwid       5.00
SCpixhgt       5.00
SCviewty       1
SCvplane       0
SCposimag      [8] 2793.00 -> 5.00
SCposscan      0
SCsused        [2] 600 -> 16000
SCpxyn         0
SCpxy_sc       0.100
= = = = = = = = = = = = = = = = = = =
Vgroup: CASI SDS : CAimage dims:2793 2068 13
= = = = = = = = = = = = = = = = = = =
```

B1. ATM Imagery – colour composite image prior to image enhancement

Legend

ATM image (14th June 2001)

RGB

Red: Band_1
Green: Band_2
Blue: Band_3

0   1,000   2,000 m

Legend

ATM image (10th June 2001)

RGB

Red: Band_1
Green: Band_2
Blue: Band_3

0   1,000   2,000 m
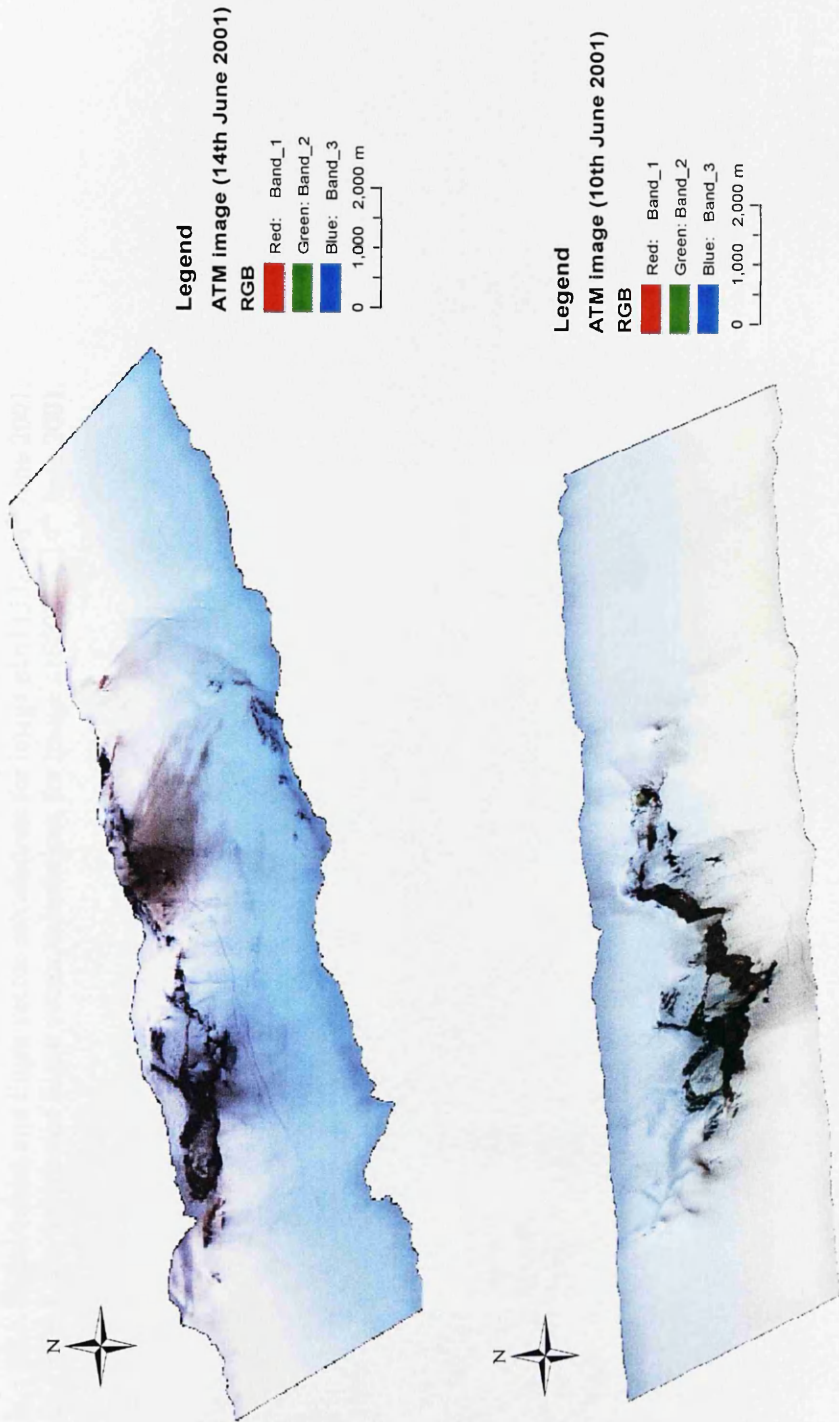
B2. Principal Components Analysis.

a. Principal Component analysis equations of Excell spreadsheet

b. PCA Eigen values and Eigen vector calculations for image a161133a, 10th June 2001.

c. PCA Eigen values and Eigen vector calculations for image a165023a, 14th June 2001.

Eigenvalues

Band	Vark	PC	Eigenvalues	Eigenvalue * 100	% Variance (E/sum)
1		1	Produced during PCA	(D2*100)	(E2/$D$13)
2		2		(D3*100)	(E3/$D$13)
3		3		(D4*100)	(E4/$D$13)
4		4		(D5*100)	(E5/$D$13)
5		5		(D6*100)	(E6/$D$13)
6		6		(D7*100)	(E7/$D$13)
7		7		(D8*100)	(E8/$D$13)
8		8		(D9*100)	(E9/$D$13)
9		9		(D10*100)	(E10/$D$13)
10		10		(D11*100)	(E11/$D$13)
11		11		(D12*100)	(E12/$D$13)
		Total	SUM(D2:D12)		SUM(F2:F12)

Vark: From Variance –covariance matrix produced using model maker. Vark is the diagonal number.

VarCovar Matrix: From Variance –covariance matrix produced using model maker. Vark is the diagonal number.

Eigenvector: Produced during PCA

Factor Loadings

	PC 1	PC 2	PC 3	PC 4	PC 5	PC 6	PC 7	PC 8	PC 9	PC 10	PC 11
Band 1	(B28*SQRT(D2))/SQRT(B2)	(C28*SQRT(D2))/SQRT(B2)	(D28*SQRT(D2))/SQRT(B2)	(E28*SQRT(D2))/SQRT(B2)	(F28*SQRT(D2))/SQRT(B2)	(G28*SQRT(D2))/SQRT(B2)	(H28*SQRT(D2))/SQRT(B2)	(I28*SQRT(D2))/SQRT(B2)	(J28*SQRT(D2))/SQRT(B2)	(K28*SQRT(D2))/SQRT(B2)	(L28*SQRT(D2))/SQRT(B2)
Band 2	(B29*SQRT(D3))/SQRT(B3)	(C29*SQRT(D3))/SQRT(B3)	(D29*SQRT(D3))/SQRT(B3)	(E29*SQRT(D3))/SQRT(B3)	(F29*SQRT(D3))/SQRT(B3)	(G29*SQRT(D3))/SQRT(B3)	(H29*SQRT(D3))/SQRT(B3)	(I29*SQRT(D3))/SQRT(B3)	(J29*SQRT(D3))/SQRT(B3)	(K29*SQRT(D3))/SQRT(B3)	(L29*SQRT(D3))/SQRT(B3)
Band 3	(B30*SQRT(D4))/SQRT(B4)	(C30*SQRT(D4))/SQRT(B4)	(D30*SQRT(D4))/SQRT(B4)	(E30*SQRT(D4))/SQRT(B4)	(F30*SQRT(D4))/SQRT(B4)	(G30*SQRT(D4))/SQRT(B4)	(H30*SQRT(D4))/SQRT(B4)	(I30*SQRT(D4))/SQRT(B4)	(J30*SQRT(D4))/SQRT(B4)	(K30*SQRT(D4))/SQRT(B4)	(L30*SQRT(D4))/SQRT(B4)
Band 4	(B31*SQRT(D5))/SQRT(B5)	(C31*SQRT(D5))/SQRT(B5)	(D31*SQRT(D5))/SQRT(B5)	(E31*SQRT(D5))/SQRT(B5)	(F31*SQRT(D5))/SQRT(B5)	(G31*SQRT(D5))/SQRT(B5)	(H31*SQRT(D5))/SQRT(B5)	(I31*SQRT(D5))/SQRT(B5)	(J31*SQRT(D5))/SQRT(B5)	(K31*SQRT(D5))/SQRT(B5)	(L31*SQRT(D5))/SQRT(B5)
Band 5	(B32*SQRT(D6))/SQRT(B6)	(C32*SQRT(D6))/SQRT(B6)	(D32*SQRT(D6))/SQRT(B6)	(E32*SQRT(D6))/SQRT(B6)	(F32*SQRT(D6))/SQRT(B6)	(G32*SQRT(D6))/SQRT(B6)	(H32*SQRT(D6))/SQRT(B6)	(I32*SQRT(D6))/SQRT(B6)	(J32*SQRT(D6))/SQRT(B6)	(K32*SQRT(D6))/SQRT(B6)	(L32*SQRT(D6))/SQRT(B6)
Band 6	(B33*SQRT(D7))/SQRT(B7)	(C33*SQRT(D7))/SQRT(B7)	(D33*SQRT(D7))/SQRT(B7)	(E33*SQRT(D7))/SQRT(B7)	(F33*SQRT(D7))/SQRT(B7)	(G33*SQRT(D7))/SQRT(B7)	(H33*SQRT(D7))/SQRT(B7)	(I33*SQRT(D7))/SQRT(B7)	(J33*SQRT(D7))/SQRT(B7)	(K33*SQRT(D7))/SQRT(B7)	(L33*SQRT(D7))/SQRT(B7)
Band 7	(B34*SQRT(D8))/SQRT(B8)	(C34*SQRT(D8))/SQRT(B8)	(D34*SQRT(D8))/SQRT(B8)	(E34*SQRT(D8))/SQRT(B8)	(F34*SQRT(D8))/SQRT(B8)	(G34*SQRT(D8))/SQRT(B8)	(H34*SQRT(D8))/SQRT(B8)	(I34*SQRT(D8))/SQRT(B8)	(J34*SQRT(D8))/SQRT(B8)	(K34*SQRT(D8))/SQRT(B8)	(L34*SQRT(D8))/SQRT(B8)
Band 8	(B35*SQRT(D9))/SQRT(B9)	(C35*SQRT(D9))/SQRT(B9)	(D35*SQRT(D9))/SQRT(B9)	(E35*SQRT(D9))/SQRT(B9)	(F35*SQRT(D9))/SQRT(B9)	(G35*SQRT(D9))/SQRT(B9)	(H35*SQRT(D9))/SQRT(B9)	(I35*SQRT(D9))/SQRT(B9)	(J35*SQRT(D9))/SQRT(B9)	(K35*SQRT(D9))/SQRT(B9)	(L35*SQRT(D9))/SQRT(B9)
Band 9	(B36*SQRT(D10))/SQRT(B10)	(C36*SQRT(D10))/SQRT(B10)	(D36*SQRT(D10))/SQRT(B10)	(E36*SQRT(D10))/SQRT(B10)	(F36*SQRT(D10))/SQRT(B10)	(G36*SQRT(D10))/SQRT(B10)	(H36*SQRT(D10))/SQRT(B10)	(I36*SQRT(D10))/SQRT(B10)	(J36*SQRT(D10))/SQRT(B10)	(K36*SQRT(D10))/SQRT(B10)	(L36*SQRT(D10))/SQRT(B10)
Band 10	(B37*SQRT(D11))/SQRT(B11)	(C37*SQRT(D11))/SQRT(B11)	(D37*SQRT(D11))/SQRT(B11)	(E37*SQRT(D11))/SQRT(B11)	(F37*SQRT(D11))/SQRT(B11)	(G37*SQRT(D11))/SQRT(B11)	(H37*SQRT(D11))/SQRT(B11)	(I37*SQRT(D11))/SQRT(B11)	(J37*SQRT(D11))/SQRT(B11)	(K37*SQRT(D11))/SQRT(B11)	(L37*SQRT(D11))/SQRT(B11)
Band 11	(B38*SQRT(D12))/SQRT(B12)	(C38*SQRT(D12))/SQRT(B12)	(D38*SQRT(D12))/SQRT(B12)	(E38*SQRT(D12))/SQRT(B12)	(F38*SQRT(D12))/SQRT(B12)	(G38*SQRT(D12))/SQRT(B12)	(H38*SQRT(D12))/SQRT(B12)	(I38*SQRT(D12))/SQRT(B12)	(J38*SQRT(D12))/SQRT(B12)	(K38*SQRT(D12))/SQRT(B12)	(L38*SQRT(D12))/SQRT(B12)

PCAa161133a

Band	Vark	PC	Eigenvalues	Eigenvalue * 100	% Variance (E/sum)
1	119305158.06	1	574801590.2	57480159015	98.0215
2	127423169.51	2	9190359.905	919035990.5	1.5672416
3	96431857.03	3	1644027.484	164402748.4	0.2803577
4	85983565.28	4	458904.2369	45890423.69	0.0782574
5	69465101.99	5	147789.8861	14778988.61	0.0252028
6	48343036.77	6	89704.76751	8970476.751	0.0152974
7	241147224.24	7	38531.00288	3853100.288	0.0065707
8	8088056.61	8	11842.08154	1184208.154	0.0020194
9	27017.39	9	11687.22661	1168722.661	0.001993
10	1092.20	10	8894.021114	889402.1114	0.0015167
11	7220744.22	11	192.5191586	19251.91586	3.283E-05
		Total	586403523		100

VarCovar Matrix	PC 1	PC 2	PC 3	PC 4	PC 5	PC 6	PC 7	PC 8	PC 9	PC 10	PC 11
Band 1	119305158.06	121922311.26	103715345.48	98502949.03	86689885.70	71556649.99	49704443.06	25674685.35	1218885.66	282944.55	254927603.5
Band 2	121922311.26	127423169.51	109841106.13	104168471.52	92565285.54	76877616.88	53738097.62	28767211.36	1278231.13	297205.86	265471691.2
Band 3	103715345.48	109841106.13	96431857.03	90699860.75	81639885.85	67754595.93	47616166.78	26079246.49	1129584.62	263030.13	236072495.7
Band 4	98502949.03	104168471.52	90699860.75	85983565.28	76872246.03	64060106.58	44950889.29	24481297.41	1058450.02	246301.83	219649087.4
Band 5	86689885.70	92565285.54	81639885.85	76872246.03	69465101.99	57790375.24	40719093.16	22571504.45	958429.82	223427.75	199829668.3
Band 6	71556649.99	76877616.88	67754595.93	64060106.58	57790375.24	48343036.77	34094430.39	19045561.48	795741.60	185705.29	164890029.3
Band 7	49704443.06	53738097.62	47616166.78	44950889.29	40719093.16	34094430.39	24114724.24	13602277.58	561383.62	131216.96	116206386.4
Band 8	25674685.35	28767211.36	26079246.49	24481297.41	22571504.45	19045561.48	13602277.58	8088056.61	312858.16	73775.26	64366772.9
Band 9	1218885.66	1278231.13	1129584.62	1058450.02	958429.82	795741.60	561383.62	312858.16	27017.39	4087.76	330902.10
Band 10	282944.55	297205.86	263030.13	246301.83	223427.75	185705.29	131216.96	73775.26	4087.76	1092.20	79335.55
Band 11	254927603.5	265471691.2	236072495.7	219649087.4	199829668.3	164890029.3	116206386.4	64366772.9	330902.10	79335.55	7220744.22

Eigenvector	PC 1	PC 2	PC 3	PC 4	PC 5	PC 6	PC 7	PC 8	PC 9	PC 10	PC 11
Band 1	0.446718795	-0.704050712	0.105209803	0.037825344	-0.080617739	-0.502504675	0.159606265	0.07769271	-0.038349067	-0.01624535	8.32E-05
Band 2	0.469773277	-0.210349357	-0.226696627	0.197210122	0.517995709	0.452354658	-0.332767269	-0.224336241	0.079270878	-0.067026139	0.001247011
Band 3	0.408397956	0.177732728	0.115005968	-0.713911532	0.148595363	0.210107644	0.460141511	0.023128883	-0.004115556	0.014687824	-0.001584378
Band 4	0.386240599	0.099806445	-0.177707306	0.286626964	-0.51806215	0.34991884	0.082420758	0.376220246	-0.090152837	0.424279413	0.00368623
Band 5	0.345251663	0.305831438	0.056534323	-0.324192355	-0.211691103	-0.324657039	-0.726046232	0.032913835	-0.004061551	-0.022542626	-0.002274791
Band 6	0.286873349	0.324822418	-0.08907167	0.307944522	-0.178932019	-0.065811103	0.233597135	-0.03457644	-0.091104178	-0.780351034	-0.008476269
Band 7	0.201094769	0.300283598	-0.038919807	0.21613807	-0.044289672	-0.294266129	0.223199238	-0.666704176	0.300225941	0.384870611	0.005723958
Band 8	0.108918756	0.356981864	0.01181495	0.252079695	0.596486831	-0.367364105	0.096759175	0.472611575	-0.172589094	0.209076926	0.006307029
Band 9	0.004791952	0.002747547	0.034418297	0.020469096	0.009488837	-0.000677696	0.009136431	0.359276313	0.924267206	-0.116540249	0.035509628
Band 10	0.001115765	0.000801116	0.009273935	0.006336827	0.004377178	0.000714412	0.000450682	0.012794718	0.033831485	0.007593958	-0.999242778
Band 11	0.09981511	0.045355866	0.93737848	0.23917197	0.003892261	0.212114816	-0.065526536	-0.046715321	-0.021153821	0.009003561	0.009257547

Factor Loadings	PC 1	PC 2	PC 3	PC 4	PC 5	PC 6	PC 7	PC 8	PC 9	PC 10	PC 11
Band 1	0.980536119	-1.545372971	0.230932777	0.083025645	-0.176953837	-1.102984672	0.350331594	0.170533475	-0.084175204	-0.035658121	0.00018263
Band 2	0.126162523	-0.056491518	-0.060881749	0.052962839	0.139113161	0.121484571	-0.089368128	-0.060247842	0.021289023	-0.01800057	0.000334898
Band 3	0.053324628	0.023206609	0.015016359	-0.093215615	0.019402135	0.02743381	0.060080797	0.003010944	-0.000537369	0.001917793	-0.000206873
Band 4	0.028217026	0.007218361	-0.012982508	0.020939695	-0.037847324	0.025563519	0.006021295	0.027484983	-0.006586167	0.030995973	0.0002693
Band 5	0.01592483	0.014106561	0.002607661	-0.014953463	-0.009764311	-0.014974897	-0.033489086	0.00151816	-0.00018734	-0.001039785	-0.000104925
Band 6	0.012357511	0.013992225	-0.0003836899	0.013265184	-0.007707772	-0.002834915	0.010062556	-0.001489433	-0.003924453	-0.033614821	-0.000365128
Band 7	0.008038311	0.012003161	-0.001555732	0.008639633	-0.00177038	-0.011762626	0.008921887	-0.026649998	0.012000856	0.015384336	0.000228802
Band 8	0.004167682	0.013659603	0.000452089	0.009645612	0.022824054	-0.014056871	0.003702406	0.018084074	-0.006603973	0.008000148	0.000241333
Band 9	0.00315712	0.001807087	0.022637236	0.013462717	0.006240897	-0.000445727	0.006009116	0.236299401	0.60789921	-0.076649615	0.023355016
Band 10	0.003183986	0.002286091	0.026464418	0.018082986	0.012490863	0.00203671	0.001286081	0.036511443	0.096542679	0.021670379	-2.851473227
Band 11	0.000515397	0.000234196	0.004840174	0.00123497	2.00978E-05	0.001095259	-0.000338348	-0.000241216	-0.000109228	4.64901E-05	4.78015E-05

PCAa165023a

Band	Vark	PC	Eigenvalues	Eigenvalue * 100	% Variance (E/sum)
1	202151058.3	1	797660730.15	79766073015	97.038461
2	178878380.9	2	21067061.2	2106706120	2.5628449
3	105703830.7	3	2105701.422	210570142.2	0.2561666
4	123619894.2	4	824334.7743	82433477.43	0.1002835
5	76328693.59	5	116827.2939	11682729.39	0.0142125
6	75192274.97	6	116544.6877	11654468.77	0.0141781
7	33124177.18	7	60010.24256	6001024.256	0.0073005
8	21397252.41	8	25481.19324	2548119.324	0.0030999
9	65289.33358	9	23828.90931	2382890.931	0.0028989
10	4109.063203	10	4380.723624	438072.3624	0.0005329
11	5539761.44	11	176.6026458	17660.26458	2.148E-05
		Total	822004722		100

VarCovar Matrix	PC 1	PC 2	PC 3	PC 4	PC 5	PC 6	PC 7	PC 8	PC 9	PC 10	PC 11
Band 1	202151058.3	187692999.9	137186344.7	153213864.8	114936346.1	115055518.6	74719645.34	51030149.46	3377681.231	865755.2793	27415857.64
Band 2	187692999.9	178878380.9	134378306.5	148089873.1	113245838.5	113416468.9	73977877.8	53563237.51	3269638.252	829012.9532	27036847.3
Band 3	137186344.7	134378306.5	105703830.7	112910894.9	89691290.58	88591676.31	58930492.92	44217867.46	2503695.096	626680.3924	21821091.13
Band 4	153213864.8	148089873.1	112910894.9	123619894.2	95472315.66	95626654.41	62534610.02	46517656.78	2732809.155	689088.0183	22729809.02
Band 5	114936346.1	113245838.5	89691290.58	95472315.66	76328693.59	75245579.84	50221070.84	37973427.01	2120674.356	529732.6766	18571376.66
Band 6	115055518.6	113416468.9	88591676.31	95626654.41	75245579.84	75192274.97	49483965.25	38026253.59	2119283.195	529829.4378	17996048.61
Band 7	74719645.34	73977877.8	58930492.92	62534610.02	50221070.84	49483965.25	33124177.18	25197275.11	1391125.152	346926.1001	12197140.73
Band 8	51030149.46	53563237.51	44217867.46	46517656.78	37973427.01	38026253.59	25197275.11	21397252.41	1038864.957	253550.3228	9181224.079
Band 9	3377681.231	3269638.252	2503695.096	2732809.155	2120674.356	2119283.195	1391125.152	1038864.957	65289.33358	15764.95801	521516.6072
Band 10	865755.2793	829012.9532	626680.3924	689088.0183	529732.6766	529829.4378	346926.1001	253550.3228	15764.95801	4109.063203	130830.4608
Band 11	27415857.64	27036847.3	21821091.13	22729809.02	18571376.66	17996048.61	12197140.73	9181224.079	521516.6072	130830.4608	5539761.44

242

Appendix B

Eigenvector

	PC 1	PC 2	PC 3	PC 4	PC 5	PC 6	PC 7	PC 8	PC 9	PC 10	PC 11
Band 1	0.491312739	-0.672848583	0.147178087	0.014998005	0.310710619	0.238506307	-0.127560071	0.335534111	-0.026925295	0.031556617	0.003313432
Band 2	0.472368313	-0.187538485	-0.233712878	-0.137894999	-0.163592011	0.068821715	0.316389682	-0.730273045	0.009103706	-0.055154524	-0.005994013
Band 3	0.36023148	0.289553716	0.392025755	0.230523289	-0.587700271	0.392814667	-0.127197853	0.106939863	0.228295626	-0.011072704	-0.003853546
Band 4	0.393045127	0.048077049	-0.364934806	-0.0778139	-0.308707326	-0.588611747	0.17608423	0.461157857	0.126752466	0.049028722	0.00809206
Band 5	0.304389455	0.315100275	0.349300151	0.243321252	0.220295201	-0.188640277	0.289272417	0.00888481	-0.677369719	-0.011582171	-0.002549244
Band 6	0.303482525	0.268030611	-0.282170701	-0.02764567	0.138051346	-0.087195264	-0.81748852	-0.171814105	-0.176402791	-0.0092871	-0.000641007
Band 7	0.199274525	0.24401966	0.225339494	0.211762924	0.528012394	-0.242155628	0.072125558	-0.149531411	0.662847421	0.02663876	0.006938591
Band 8	0.146067328	0.431134039	-0.407103733	-0.26922133	0.297946084	0.563340362	0.274447748	0.268351813	0.019832306	0.026875043	0.000345559
Band 9	0.008695896	0.002125786	-0.002759148	-0.017490987	0.027831814	-0.019518722	0.001036188	0.076080632	0.029704559	-0.991207784	0.096364742
Band 10	0.002195758	-0.000369919	-0.000237586	-0.005065925	0.00759556	-0.009315065	-0.0001177357	0.015337409	0.009428631	-0.094792553	-0.995246228
Band 11	0.073128339	0.096932669	0.46765948	-0.86251914	-0.003915987	-0.134028096	-0.06285115	-0.004528609	0.018113685	0.017819813	0.004044329

Factor Loadings

	PC 1	PC 2	PC 3	PC 4	PC 5	PC 6	PC 7	PC 8	PC 9	PC 10	PC 11
Band 1	0.97595349	-1.336559936	0.292157507	0.029792338	0.617201812	0.473773717	-0.253387886	0.666511695	-0.053484946	0.062287414	0.006581868
Band 2	0.162106395	-0.064359075	-0.080205109	-0.047322525	-0.056141173	0.023618096	0.108577966	-0.250613615	0.003124191	-0.018927817	-0.002057013
Band 3	0.050843413	0.040867886	0.055330887	0.032536276	-0.082948574	0.055442235	-0.017952826	0.015093594	0.032221861	-0.001562812	-0.000543893
Band 4	0.032095936	0.003925956	-0.029800456	-0.006354258	-0.025208939	-0.048065842	0.01437898	0.037657999	0.010350565	0.004003669	0.000660795
Band 5	0.011908522	0.012327557	0.013665547	0.009519372	0.008618532	-0.007380107	0.011317103	0.000347741	-0.026500497	-0.000453125	-9.97332E-05
Band 6	0.011947948	0.010552225	-0.011108912	-0.001088396	0.005435009	-0.003432832	-0.032184094	-0.006764231	-0.006944885	-0.000365628	-2.52361E-05
Band 7	0.008481876	0.010386398	0.0095913	0.009013429	0.022474201	-0.010307058	0.003069936	-0.006364621	0.028213289	0.001133846	0.000295333
Band 8	0.00504062	0.014877953	-0.014048694	-0.009290527	0.010281786	0.019440245	0.009470885	0.009260521	0.000684391	0.000927428	1.19248E-05
Band 9	0.005253458	0.001284253	-0.001666886	-0.010566844	0.016814055	-0.011791861	0.000625993	0.045962652	0.017945438	-0.598819133	0.058216907
Band 10	0.00226718	-0.000381951	-0.000245314	-0.005230706	0.007842623	-0.009618058	-0.000183126	0.015836293	0.009735318	-0.097875893	-1.027618838
Band 11	0.000412894	0.000547297	0.00264048	-0.00486992	-2.21103E-05	-0.000756744	-0.000354868	-2.55692E-05	0.000102273	0.000100613	2.28349E-05

243

B3 Classification Accuracy Assessment Report

Error Matrix   Image file:- S:/supa161133a

Classified Data	Unclassified	Snow1	Snow2	Snow3	Snow4
				Reference Data	
Unclassified	0	0	0	0	0
Snow	0	6	27	78	2
Ice	0	0	0	0	0
Firn	0	0	3	3	0
Tephra	0	0	0	0	0
Shadow	0	0	0	0	0
Debrisfan	0	0	0	1	0
Water	0	0	0	0	0
DirtySnow	0	0	6	11	0
Column Total	**0**	**6**	**33**	**96**	**2**

Classified Data	Ice1	Ice2	Ice3	Ice4
			Reference Data	
Unclassified	0	0	0	0
Snow	0	0	0	0
Ice	0	0	2	0
Firn	0	0	0	0
Tephra	0	0	0	0
Shadow	0	0	0	0
Debrisfan	0	0	0	0
Water	0	0	0	0
DirtySnow	0	0	0	0
Column Total	**0**	**0**	**2**	**0**

Classified Data	Firn1	Firn2	Firn3	Firn4
			Reference Data	
Unclassified	0	0	0	0
Snow	0	0	0	0
Ice	0	0	1	0
Firn	0	0	0	0
Tephra	0	0	0	0
Shadow	0	0	0	0
Debrisfan	0	0	0	0
Water	0	0	0	0
DirtySnow	0	0	0	0
Column Total	**0**	**0**	**1**	**0**

Classified Data	Tephra1	Tephra2	Tephra3	Tephra4
			Reference Data	
Unclassified	0	0	0	0
Snow	0	0	0	0
Ice	0	0	0	0
Firn	1	0	0	0
Tephra	0	0	1	0
Shadow	0	0	0	0
Debrisfan	0	0	0	1
Water	0	0	0	0
DirtySnow	0	0	0	0
Column Total	**1**	**0**	**1**	**1**

Classified Data	Shadow1	Shadow2	Reference Data Shadow3	Shadow4
Unclassified	0	0	0	0
Snow	0	0	0	0
Ice	0	0	0	0
Firn	0	0	0	0
Tephra	0	0	0	0
Shadow	0	· 0	0	0
Debrisfan	0	0	0	0
Water	0	0	0	0
DirtySnow	0	0	0	0
Column Total	**0**	**0**	**0**	**0**

Classified Data	Debrisfan1	Debrisfan2	Reference Data Debrisfan3	Debrisfan4
Unclassified	0	0	0	0
Snow	0	0	0	0
Ice	0	0	0	0
Firn	0	0	0	0
Tephra	1	0	0	0
Shadow	0	0	0	0
Debrisfan	0	0	0	2
Water	0	0	0	0
DirtySnow	0	0	0	0
Column Total	**1**	**0**	**0**	**2**

Classified Data	Water1	Water2	Reference Data Water3	Water4
Unclassified	0	0	0	0
Snow	0	0	0	0
Ice	0	0	0	0
Firn	0	0	0	0
Tephra	0	0	0	0
Shadow	0	0	0	0
Debrisfan	0	0	0	0
Water	0	0	0	0
DirtySnow	0	0	0	0
Column Total	**0**	**0**	**0**	**0**

Classified Data	DirtySnow1	DirtySnow2	Reference data DirtySnow3	DirtySnow4
Unclassified	0	0	0	0
Snow	2	0	0	0
Ice	0	0	0	0
Firn	0	0	0	0
Tephra	0	0	0	0
Shadow	0	0	0	0
Debrisfan	1	0	0	0
Water	0	0	0	0
DirtySnow	1	0	0	0
Column Total	**4**	**0**	**0**	**0**

Classified Data	Row Total
Unclassified	0
Snow	115
Ice	3
Firn	7
Tephra	2
Shadow	0
Debrisfan	5
Water	0
DirtySnow	18
Column Total	**150**

-- End of Error Matrix --

Accuracy Totals

Class Name	Reference Totals	Classified Totals	Number Correct	Producers Accuracy	Users Accuracy
Unclassified	0	0	0	--	--
Snow1	6	6	6	100%	100%
Snow2	33	27	27	81.82%	100%
Snow3	96	80	78	81.25%	97.50%
Snow4	2	2	2	100%	100%
Ice1	0	1	0	--	--
Ice2	0	0	0	--	--
Ice3	2	2	2	100%	100%
Ice4	0	0	0	--	--
Firn1	0	1	0	--	--
Firn2	0	3	0	--	--
Firn3	1	3	0	0%	0%
Firn4	0	0	0	--	--
Tephra1	1	0	0	--	--
Tephra2	0	0	0	--	--
Tephra3	1	2	1	100%	50%
Tephra4	1	0	0	--	--
Shadow1	0	0	0	--	--
Shadow2	0	0	0	--	--
Shadow3	0	0	0	--	--
Shadow4	0	0	0	--	--
Debrisfan1	1	0	0	--	--
Debrisfan2	0	0	0	--	--
Debrisfan3	0	2	0	--	--
Debrisfan4	2	3	2	100%	66.67%
Water1	0	0	0	--	--
Water2	0	0	0	--	--
Water3	0	0	0	--	--
Water4	0	0	0	--	--
DirtySnow1	4	17	1	25%	5.88%
DirtySnow2	0	1	0	--	--
DirtySnow3	0	0	0	--	--
DirtySnow4	0	0	0	--	--
Totals	**150**	**150**	**119**		

Overall Classification Accuracy = 79.33%

Appendix B

<u>Kappa (K^) Statistics</u>

Overall Kappa Statistics = 0.6632

Conditional Kappa for each category

Class Name	Kappa
Unclassified	0
Snow1	1
Snow2	1
Snow3	0.9306
Snow4	1
Ice1	0
Ice2	0
Ice3	1
Ice4	0
Firn1	0
Firn2	0
Firn3	-0.0067
Firn4	0
Tephra1	0
Tephra2	0
Tephra3	0.4966
Tephra4	0
Shadow1	0
Shadow2	0
Shadow3	0
Shadow4	0
Debrisfan1	0
Debrisfan2	0
Debrisfan3	0
Debrisfan4	0.6622
Water1	0
Water2	0
Water3	0
Water4	0
DirtySnow1	0.033
DirtySnow2	0
DirtySnow3	0
DirtySnow4	0

-- End of Kappa Statistics --

Error Matrix

Image file:- S:/supa165023a

Classified Data	Unclassified	Snow1	Snow2	Reference Data Snow3	Snow4
Unclassified	0	0	0	0	0
Snow	0	42	29	1	26
Ice	0	0	0	0	0
Firn	0	0	0	1	0
Tephra	0	0	0	0	0
Shadow	0	0	0	0	0
Debrisfan	0	0	0	1	0
Water	0	0	0	0	0
DirtySnow	0	6	6	19	0
Column Total	**0**	**48**	**35**	**21**	**26**

Classified Data	Ice1	Ice2	Reference Data Ice3	Ice4
Unclassified	0	0	0	0
Snow	0	0	0	0
Ice	0	0	0	0
Firn	0	0	0	0
Tephra	0	0	0	0
Shadow	0	0	0	0
Debrisfan	0	0	0	0
Water	0	0	0	0
DirtySnow	0	0	0	0
Column Total	**0**	**0**	**0**	**0**

Classified Data	Firn1	Firn2	Reference Data Firn3	Firn4
Unclassified	0	0	0	0
Snow	0	0	0	0
Ice	0	0	0	0
Firn	0	0	1	0
Tephra	0	0	0	0
Shadow	0	0	0	0
Debrisfan	0	0	0	0
Water	0	0	0	0
DirtySnow	0	0	0	1
Column Total	**0**	**0**	**1**	**1**

Classified Data	Tephra1	Tephra2	Reference Data Tephra3	Tephra4
Unclassified	0	0	0	0
Snow	0	0	0	0
Ice	0	0	0	0
Firn	0	0	1	0
Tephra	0	0	0	0
Shadow	0	0	0	0
Debrisfan	0	0	0	0
Water	0	0	0	0
DirtySnow	0	0	0	0
Column Total	**0**	**0**	**1**	**0**

Classified Data	Shadow1	Shadow2	Reference Data Shadow3	Shadow4
Unclassified	0	0	0	0
Snow	0	0	0	0
Ice	0	0	0	0
Firn	0	0	0	0
Tephra	0	0	0	0
Shadow	1	0	3	0
Debrisfan	0	0	0	0
Water	0	0	0	0
DirtySnow	0	0	0	0
Column Total	**1**	**0**	**3**	**0**

Classified Data	Debrisfan1	Debrisfan2	Reference Data Debrisfan3	Debrisfan4
Unclassified	0	0	0	0
Snow	0	0	0	0
Ice	0	0	0	0
Firn	0	1	0	0
Tephra	0	0	0	0
Shadow	0	1	0	0
Debrisfan	0	0	0	0
Water	0	0	0	0
DirtySnow	0	0	0	0
Column Total	**0**	**2**	**0**	**0**

Classified Data	Water1	Water2	Reference Data Water3	Water4
Unclassified	0	0	0	0
Snow	0	0	0	0
Ice	0	0	0	0
Firn	0	0	0	0
Tephra	0	1	0	0
Shadow	0	0	0	0
Debrisfan	0	0	0	0
Water	0	0	0	0
DirtySnow	0	0	0	0
Column Total	**0**	**1**	**0**	**0**

Classified Data	DirtySnow1	DirtySnow2	Reference data DirtySnow3	DirtySnow4
Unclassified	0	0	0	0
Snow	2	0	0	0
Ice	0	0	0	0
Firn	0	1	0	0
Tephra	0	0	0	0
Shadow	0	0	0	0
Debrisfan	0	0	0	0
Water	0	0	0	0
DirtySnow	0	3	5	0
Column Total	**0**	**4**	**5**	**0**

Classified Data	Row Total
Unclassified	0
Snow	98
Ice	0
Firn	5
Tephra	1
Shadow	5
Debrisfan	0
Water	0
DirtySnow	41
Column Total	**150**

-- End of Error Matrix --

Accuracy Totals

Class Name	Reference Totals	Classified Totals	Number Correct	Producers Accuracy	Users Accuracy
Unclassified	0	0	0	--	--
Snow1	48	43	42	87.50%	97.67%
Snow2	35	29	29	82.86%	100%
Snow3	21	1	1	4.76%	100%
Snow4	26	25	25	96.15%	100%
Ice1	0	0	0	--	--
Ice2	0	0	0	--	--
Ice3	0	0	0	--	--
Ice4	0	0	0	--	--
Firn1	0	0	0	--	--
Firn2	0	3	0	--	--
Firn3	1	2	1	100%	50%
Firn4	1	0	0	--	--
Tephra1	0	0	0	--	--
Tephra2	0	0	0	--	--
Tephra3	1	0	0	--	--
Tephra4	0	1	0	--	--
Shadow1	1	1	1	100%	100%
Shadow2	0	0	0	--	--
Shadow3	3	4	3	100%	75%
Shadow4	0	0	0	--	--
Debrisfan1	0	0	0	--	--
Debrisfan2	2	0	0	--	--
Debrisfan3	0	0	0	--	--
Debrisfan4	0	0	0	--	--
Water1	0	0	0	--	--
Water2	1	0	0	--	--
Water3	0	0	0	--	--
Water4	0	0	0	--	--
DirtySnow1	4	5	3	75%	60%
DirtySnow2	5	27	5	100%	18.52%
DirtySnow3	1	9	1	100%	11.11%
DirtySnow4	0	0	0	--	--
Totals	**150**	**150**	**111**		

Overall Classification Accuracy = 74.00%

Kappa (K^) Statistics

Overall Kappa Statistics = 0.6850

Conditional Kappa for each category

Class Name	Kappa
Unclassified	0
Snow1	0.9658
Snow2	1
Snow3	1
Snow4	1
Ice1	0
Ice2	0
Ice3	0
Ice4	0
Firn1	0
Firn2	0
Firn3	0.4966
Firn4	0
Tephra1	0
Tephra2	0
Tephra3	0
Tephra4	0
Shadow1	1
Shadow2	0
Shadow3	0.7449
Shadow4	0
Debrisfan1	0
Debrisfan2	0
Debrisfan3	0
Debrisfan4	0
Water1	0
Water2	0
Water3	0
Water4	0
DirtySnow1	0.589
DirtySnow2	0.1571
DirtySnow3	0.1051
DirtySnow4	0

-- End of Kappa Statistics --

C1. Wilson (2003) Temperature conversion algorithm

This program calibrates thermal channel data from the IDS AZ-16 ATM to surface brightness temperatures - A.K. Wilson, CEH Monks Wood ((c)1987, 2000, 2003). To create executable: cc -lm -o xtempcal tempcal.c in directory with C compiler setup

At command line prompt type   xtempcal <cr>

You will be prompted for input of a 1 band Level 1b BIL format calibrated Thermal Infrared (ATM channel 11) radiance band, an output file name of scaled (x1000) surface brightness temperature (in degrees Celcius),and the number of scanlines (ROWS) in the 1 band input radiance BIL file. ATM data is expected to be 938 samples (COLUMNS) wide.

It is hardwired for surface emissivity of 1.00, but can be edited.
eg example inputs and <carriage return>
xtempcal <cr>
a12301ch11.bil <cr>   (File names)
a12301temp.bil <cr>
2358 <cr>
Use example azexhdf command
azexhdf -h Level1bATMfile.hdf -BIL Channel11ATMfile.bil -bl 11 -1
to create the required input file (ie. a12301ch11.bil).
azgcorr the 1 band surface brightness channel using example azgcorr command

azgcorr -v -1 Level1bATMfile.hdf -3 Level3ach11map.hdf -Bi a12301temp.bil
-B 2358 1 0 0 1 0 -p 2.5 2.5 -eh DEM_file   (plus any non-UK projection options)

type   azgcorr -help   for full details of options

```
*******************************************************************************/
main()
{int       n,i, ii, ROWS,COLUMNS, k, j, size, repeatno;
float      value;
unsigned short int      *image, newval;
char       inname[35];
char       innameplus[35];
char       outname[35];
char       outnameplus[35];
float      temperature,rad1,C1,C2,MaxTemp,MinTemp,TargetEmis,DeltaTemp,sum,R1;
float      DRESP[141],lamda[141],resp[141],*arrad;
float      slope;
float      intercept,tplo,tphi,fnewval;
int        NumTable;
int        ihi,imid,ilo;
```

```
FILE        *infile;
FILE        *outfile;

printf("\n input *.bil filename? (max char: 35 incl. directory path):\n ");
            scanf("%s", inname);
            sprintf(innameplus,"%s",inname);
            infile = fopen(innameplus,"r");
            if(infile == NULL){
             printf("\n error opening input file");
             exit(1);}
printf("\n output filename for new *.bil file ? (max char: 60 incl. directory path):\n ");
            scanf("%s", outname);
            sprintf(outnameplus,"%s",outname);
            outfile = fopen(outnameplus,"w+");
            if(outfile == NULL) {
            printf("error creating bil-output-file \n");
            exit(1);}
printf("number of rows ? (int) :\n ");
            scanf("%i", &ROWS);
/* printf("number of columns ? (int):\n ");
            scanf("%i", &COLUMNS); */
            COLUMNS = 938;
printf("\n starting the temperature calibration of imagery\n");
/* Definition of spectral response */
            DRESP[0] = 0.355;
            DRESP[1] = 0.601;
            DRESP[2] = 1.516;
            DRESP[3] = 3.861;
            DRESP[4] = 9.228;
            DRESP[5] = 18.909;
            DRESP[6] = 32.217;
            DRESP[7] = 49.088;
            DRESP[8] = 66.147;
            DRESP[9] = 74.362;
            DRESP[10] = 73.921;
            DRESP[11] = 74.650;
            DRESP[12] = 79.395;
            DRESP[13] = 85.655;
            DRESP[14] = 89.796;
            DRESP[15] = 89.961;
            DRESP[16] = 86.917;
            DRESP[17] = 83.729;
            DRESP[18] = 81.554;
            DRESP[19] = 81.689;
            DRESP[20] = 82.382;
            DRESP[21] = 83.753;
            DRESP[22] = 85.398;
            DRESP[23] = 87.673;
            DRESP[24] = 90.818;
            DRESP[25] = 93.771;
            DRESP[26] = 97.239;
            DRESP[27] = 99.093;
            DRESP[28] = 99.788;
            DRESP[29] = 99.303;
            DRESP[30] = 97.256;
            DRESP[31] = 94.367;
            DRESP[32] = 91.656;
            DRESP[33] = 89.055;
            DRESP[34] = 89.012;
```

DRESP[35] = 89.984;
DRESP[36] = 91.436;
DRESP[37] = 93.076;
DRESP[38] = 96.083;
DRESP[39] = 97.547;
DRESP[40] = 97.839;
DRESP[41] = 96.276;
DRESP[42] = 95.595;
DRESP[43] = 93.101;
DRESP[44] = 90.414;
DRESP[45] = 89.376;
DRESP[46] = 88.846;
DRESP[47] = 88.937;
DRESP[48] = 89.450;
DRESP[49] = 89.090;
DRESP[50] = 88.989;
DRESP[51] = 89.273;
DRESP[52] = 89.493;
DRESP[53] = 91.365;
DRESP[54] = 91.361;
DRESP[55] = 90.564;
DRESP[56] = 93.651;
DRESP[57] = 96.481;
DRESP[58] = 94.359;
DRESP[59] = 89.362;
DRESP[60] = 83.905;
DRESP[61] = 79.661;
DRESP[62] = 77.323;
DRESP[63] = 73.960;
DRESP[64] = 71.288;
DRESP[65] = 68.293;
DRESP[66] = 63.318;
DRESP[67] = 59.337;
DRESP[68] = 56.775;
DRESP[69] = 54.588;
DRESP[70] = 52.397;
DRESP[71] = 50.389;
DRESP[72] = 48.655;
DRESP[73] = 46.431;
DRESP[74] = 44.638;
DRESP[75] = 42.024;
DRESP[76] = 41.344;
DRESP[77] = 39.604;
DRESP[78] = 39.065;
DRESP[79] = 38.557;
DRESP[80] = 38.788;
DRESP[81] = 38.903;
DRESP[82] = 39.965;
DRESP[83] = 40.435;
DRESP[84] = 41.115;
DRESP[85] = 41.589;
DRESP[86] = 40.722;
DRESP[87] = 40.448;
DRESP[88] = 39.724;
DRESP[89] = 39.700;
DRESP[90] = 40.509;
DRESP[91] = 39.513;
DRESP[92] = 39.043;
DRESP[93] = 38.721;
DRESP[94] = 38.377;

```
            DRESP[95] = 37.527;
            DRESP[96] = 36.191;
            DRESP[97] = 35.059;
            DRESP[98] = 35.889;
            DRESP[99] = 32.060;
            DRESP[100] = 30.039;
            DRESP[101] = 27.925;
            DRESP[102] = 25.090;
            DRESP[103] = 23.672;
            DRESP[104] = 20.754;
            DRESP[105] = 18.254;
            DRESP[106] = 16.791;
            DRESP[107] = 15.736;
            DRESP[108] = 12.703;
            DRESP[109] = 10.610;
            DRESP[110] = 8.807;
            DRESP[111] = 8.775;
            DRESP[112] = 7.364;
            DRESP[113] = 6.668;
            DRESP[114] = 6.233;
            DRESP[115] = 4.960;
            DRESP[116] = 3.874;
            DRESP[117] = 3.444;
            DRESP[118] = 3.832;
            DRESP[119] = 4.096;
            DRESP[120] = 3.517;
            DRESP[121] = 3.584;
            DRESP[122] = 1.962;
            DRESP[123] = 2.043;
            DRESP[124] = 2.200;
            DRESP[125] = 2.027;
            DRESP[126] = 2.063;
            DRESP[127] = 1.373;
            DRESP[128] = 2.123;
            DRESP[129] = 1.357;
            DRESP[130] = 1.182;
            DRESP[131] = 1.296;
            DRESP[132] = 0.652;
            DRESP[133] = 1.234;
            DRESP[134] = 0.645;
            DRESP[135] = 0.676;
            DRESP[136] = 0.695;
            DRESP[137] = 0.687;
            DRESP[138] = 0.577;
            DRESP[139] = 0.686;
            DRESP[140] = 0.757;

/* calculate wavelength for each digitized point */
sum=0.0;
for(i=0;i<141;i++)
            {sum+=DRESP[i];
            lamda[i]=8.000+(i*0.05);}
for(i=0;i<141;i++)
            {resp[i]=DRESP[i]/sum;}
C1=119095879.96;
/*C1=374151000.0;*/
C2=14387.9;
MaxTemp=50.0;
MinTemp=0.0;
DeltaTemp=0.01;
```

```
/* Default surface emissivity is set to equal 1.00. You could set it to other
value eg. 0.97,if you know the exact value */
TargetEmis=1.00;

NumTable=(int) (((MaxTemp-MinTemp)/DeltaTemp)+1.0);
/* assign memory for arrad */
if ((arrad=(float *) calloc(NumTable,sizeof(float))) == 0)
     {fprintf(stderr,"thermcal : frame core allocation failed\n");exit(1);}
for(i=0;i<NumTable;i++)
             {rad1=0.0;
             temperature=(MinTemp+i*DeltaTemp)+273.16;
             for(j=0;j<141;j++)
                      {R1=(resp[j]*C1)/(pow(lamda[j],5)*exp(C2/(lamda[j]*temperature))-1.0);
                      rad1+=R1;}
             arrad[i]=rad1*TargetEmis*1000.0;

/* printf("%9.4f %9.4f\n",(temperature-273.16), arrad[i]);*/}
repeatno=BANDS*COLUMNS*ROWS;
image = (unsigned short int*) malloc(sizeof(unsigned short int)*repeatno);
fread(image,sizeof(unsigned short int), repeatno, infile);

for(i=0; i<ROWS; i++){
             if ((i/100)== ((float)(i))/100.0) printf("row: %i \n", i);
for(k=0; k<BANDS; k++){
for(j=0; j<COLUMNS; j++){
value = (float) *(image+j +(k*COLUMNS)+(i*BANDS*COLUMNS));

                              {ilo=0; ihi=NumTable-1;
                              while(ihi > (ilo+1))
                                        {imid=(ilo+ihi)/2.0;
                                        if(imid<0) imid=0;
                                        if(value<arrad[imid])
                                                  ihi=imid;
                                        else ilo=imid;}
                              tplo=MinTemp+(ilo*DeltaTemp);
                              tphi=MinTemp+(ihi*DeltaTemp);
                              slope = (tphi-tplo)/(arrad[ihi]-arrad[ilo]);
                              intercept = tplo - (slope*arrad[ilo]);
                              fnewval = (slope*value) + intercept;
if (i == 0) printf("%9.4f %9.4f %9.4f\n",value, arrad[ilo], fnewval);
             if(fnewval<MinTemp) fnewval=MinTemp;
                              if(fnewval>MaxTemp) fnewval=MaxTemp;}
                    newval = (unsigned short int) (fnewval*1000.0);
                    fwrite(&newval, sizeof(unsigned short int), 1, outfile)}

fclose(outfile);
fclose(infile);}
```

C2. Radiance to Temperature conversion

```
compile_opt STRICTARR

;selects input image – image must be open                    →    data to image
envi_select, title='Input filename', fid=fid, pos=pos
if (fid eq –1) then return
ENVI_FILE_QUERY, fid, ns=ns, n1=n1
dims = [-1, 0, ns-1, 0, n1-1]
data = ENVI_GET_DATA (fid=fid, dims=dims, pos=0)            →    gets data from image file

xdim=0
ydim=0
xdim1=dims[2]                                                →    giving co-ordinate input to
ydim1=dims[4]                                                     xdim, ydim, xdim1, ydim1

envi_select, title='Classified Filename', fid=fid, pos=pos
if (fid eq –1) then return
ENVI_FILE_QUERY, fid, ns=ns, n1=n1
dims = [-1, 0, ns-1, 0, n1-1]
data2 = ENVI_GET_DATA (fid=fid, dims=dims, pos=0)          →    Data 2 = classified

envi_select, title='Classified Emmissivities', fid=fid, pos=pos
if (fid eq –1) then return
ENVI_FILE_QUERY, fid, ns=ns, n1=n1
dims = [-1, 0, ns-1, 0, n1-1]
data3 = ENVI_GET_DATA (fid=fid, dims=dims, pos=0)          →    Data 3 = emissivity

envi_select, title='Response', fid=fid, pos=pos
if (fid eq –1) then return
ENVI_FILE_QUERY, fid, ns=ns, n1=n1
dims = [-1, 0, ns-1, 0, n1-1]
dresp = ENVI_GET_DATA (fid=fid, dims=dims, pos=0)          →    Dresp = sensor response
drespsum=total (dresp)      →  Sum of all response
resp=fltarr(141)
resp=dresp/drespsum         →
                               Each response / sum of all responses

base = widget_auto_base (title='Output File')     ;Give option for file output
wo = widget_outff(base, uvalue='outf',/auto)               →    Asks for name of output files
result = auto_wid_mng(base)                                      (prefix)
if (result.accept eq 0) then return


CALCULATING EMISSIVITIES

Emisarr=fltarr (xdim1+1, ydim1+1)                          →    Fltarr = makes array full of
For x=0, xdim1 do begin                                          zeros
For y=0, ydim1 do begin

if (data2[x,y] eq 0) then emis=1
if (data2[x,y] ge 1) AND (data2[x,y] le 3) then emis=data3[0]
if (data2[x,y] ge 4) AND (data2[x,y] le 6) then emis=data3[1]
if (data2[x,y] ge 7) AND (data2[x,y] le 9) then emis=data3[2]
if (data2[x,y] ge 10) AND (data2[x,y] le 12) then emis=data3[3]      Creating array
if (data2[x,y] ge 13) AND (data2[x,y] le 15) then emis=data3[4]      of
if (data2[x,y] ge 16) AND (data2[x,y] le 18) then emis=data3[5]   →  emmissivities
if (data2[x,y] ge 19) AND (data2[x,y] le 21) then emis=data3[6]
if (data2[x,y] ge 22) AND (data2[x,y] le 24) then emis=data3[7]
```

```
if (data2[x,y] ge 25) AND (data2[x,y] le 27) then emis=data3[8]

emisarr[x,y]=emis
endfor
endfor


temp_name = ''                        ──────────▶   Temp_name = character string, i.e written
temp_name=result.outf                               letters and numbers.
temp_nam2=''
temp_nam2=temp_name+'.emis'
temp_nam3=''
temp_nam3='C:\Documents and Settings\stewarts\Ajusted\'+temp_nam2; print, temp_nam3
wid=(xdim1+1)*15
close, 104                            ──────────▶   Writing out emissivities
openw,104, temp_nam3, width=wid
printf, 104 emisarr
close, 104


wavlow=8.0
wavhigh=15.05
wavdiv=(wavhigh-wavlow)/141
wavhalf =(wavhigh-wavlow)/2           ──────────▶   ½ difference between max and min
wavmid2=wavlow+(wavhalf)              ──────────▶   midpoint between mid and max wavelength


rads = fltarr(xdim1+1, ydim1+1)
for x=0, xdim1 do begin               ──────────▶   creates array of new (blackbody) radiances
for y=0, ydim1 do begin


rads[x,y]=data[x,y]/emisarr[x,y]
end for
endfor

                                                    Writes out new radiances
temp_name = ''                        ──────────▶
temp_name=result.outf
temp_nam2=''
temp_nam2=temp_name+'.newrads'
temp_nam3=''
temp_nam3='C:\Documents and Settings\stewarts\Ajusted\'+temp_nam2; print, temp_nam3
wid=(xdim1+1)*15
close, 100
openw,100, temp_nam3, width=wid
printf, 100, rads
close, 100



CALCULATING TEMPERATURES



C1=119095879.96;        {c1}
C2=14387.9;             {c2}

newtemp=fltarr(xdim1+1, ydim1+1)
arrl=fltarr(141)

clarr=fltarr(141)



wav=wavlow+(wavdiv/2)
```

```
for i=0, 140 do begin
arrl[i]=wav
wav=wav+(wavdiv)
endfor
```
⟶ Writing array with mid points of divisions

```
clarr=c1*(arr1^(-5))
;print,resp,clarr,arr1
```
⟶ $Clarr = C_1 \lambda^{-5}$

```
for x=0, xdim1 do begin
for y=0, ydim1 do begin
tempguess=273
radarr=fltarr(141)
radarr=resp*clarr*(1/(exp(c2/(arr1*tempguess)))-1)
radtotal=total (radarr)
rad2=radtotal*1000
rad=rads[x,y]
radfix=fix(rad)
;print, radfix, rad2
```
⟶ Radiances in each division
(2nd part of Planck formula)
⟶ Area under graph
⟶ New radiance
⟶ New radiance fixed to integer

```
if rad eq 0 then begin
newtemp[x,y]=0
endif else begin
if rad2 ge rad then begin
```
⟶ If outside image set temp to zero

```
a=10.0000
repeat begin

radarr2=fltarr(1000)
radarr2=resp*clarr*(1/(exp(c2/(arr1*tempguess)))-1)
radtotal2=total (radarr2)
rad3=radtotal2*1000
rad3=fix(rad3)
```
⟶ Area under graph

⟶ New radiance fixed to integer

```
if rad3 lt rad then begin
tempguess=tempguess+(2*a)
a=a/10
endif
tempguess=tempguess-a

endrep until (rad3 eq radfix)

endif else begin

a=10.0000
repeat begin
radarr3=fltarr(1000)
aradtemp3=fltarr(1000)
radarr3=resp*clarr*(1/(exp(c2/(arr1*tempguess)))-1)
radtotal3=total (radarr3)
rad3=radtotal3*1000
rad3=fix(rad3)

;print, 'lower', rad3, radfix
if rad3 gt rad then begib
tempguess=tempguess-(2*a)
a=a/10
n=1
endif
tempguess=tempguess+a
```

```
endrep until (rad3 eq radfix)
endelse

newpixtemp=tempguess-273;
newtemp[x,y]=newpixtemp

newsumpix=0.;{**reset output values ready for next sweep, otherwise they keep adding up!**}
newpixtemp=0.;{**this sets this value as a real number}
pixvsum=0
endelse
endfor;
endfor;




temp_name = ' '
temp_name = result.outf
temp_nam2 = ' '
temp_nam2=temp_name+'.newtemp'
temp_nam3='' '
temp_nam3='C:\Documents and Settings\stewarts\Ajusted\'+temp_nam2; print, temp_nam3
wid=(xdim1+1)*15
close, 102
openw,102, temp_nam3, width=wid
printf, 102, newtemp
close, 102

Print, 'FINISHED'
End.
```

C3. Heat Flux Spreadsheet

1\A	B	C	D	E
2	Surface Temperature	Air Temperature	Saturated vapour pressure of surface	Specific Saturated Humidity at Surface
3	T_s	T_a	e^*_s	q^*_s
4	305.44	274.15	=6.112*EXP(17.67*(B4-273.15)/(B4-29.65))	=(0.622*D4)/(823+((0.622-1)*D4))
5				
6	Saturated vapour Pressure for the Air			
7	e^*_a	Relative Humidty	Vapour Pressure of the Air	Specific Humidity of the Air
8			e_a	q_a
9	=6.112*EXP(17.67*(C4-273.15)/(C4-29.65))	0.7895	=C9*B9	=(0.622*D9)/(823+((0.622-1)*D9))
10				
11	Saturated surface humidity minus			
12	Specific humidity of the air	Wind Speed	air density	Latent Heat of Evaporation
13	$q^*\_s-q\_a$	u_a	rho_a	L
14	=E4-E9	6.78	1	2500000
15				
16	Heat Transfer Coefficient	**Latent Heat Flux**	Surface Temp minus Air Temp	Specific Heat Capacity of Air
17	C_e	Q_e	T_s-T_a	C_p
18				
19	0.0014	=D14*E19*C14*B14	=B4-C4	1005
20				
21	**Sensible Heat Flux**	Stefan Boltzman Constant	Emmisivity of Water	Outgoing Long wave radiation
22	Q_h	sigma	eps	Q_lo
23		0.0000000567	0.985	
24	=D14*E19*B19*C14*D19			=D24*C24*POWER(B4,4)
25				
26	Outgoing long wave with no cloud cover	Cloud Cover	**Outgoing Longwave with cloud cover**	Incoming short wave solar radiation
27	$Q\_l(no\ cc)$	n_c	$Q\_l\ (cc)$	Q_si
28				
29	=E24*(0.39-(0.05*SQRT(D9)))	0.575	=B29*(1-0.6*(C29*C29))	-280
30				
31	Solar Reflectance	**Net Short Wave Radiation**	**Total Heat Flux**	
32	Q_sr	Q_s	Q_T	
33	=-0.07*E29	=E29+B33	=C19+B24+D29+C33	

C4. Meterological Stations used for weather data for heat flux calculations

<u>Fagurhólsmýri, Skaftafell</u> – used for cloud cover and wind speed

Synoptic observations at Fagurhólsmýri 1 to 15 June 2001

Location: 63°52.647'N, 16°38.830'V, (63.877, 16.647)
Height above sea level: 46 m
Height of wind speed gauge over ground: 10.09 m
Start of weather observations: 1903

n = total cloud cover in oktas,
nh=total low cloud cover in oktas
wind dir in deg N=360   E=90   variable=990
wind speed (force) in m/s
precipitation in mm
= no measurement OR no precipitation,
precipitation measured at 9 and 18utc

id	yr	month	day	hour	temp.	n	nh	wind dir	force	precip
745	2001	6	10	6	8.8	6	3	90	6.7	#
745	2001	6	10	9	9.5	3	1	110	10.3	#
745	2001	6	10	12	9.8	6	1	110	8.2	#
745	2001	6	10	18	9.6	3	1	130	4.1	#
745	2001	6	10	21	8.9	5	2	270	4.6	#
745	2001	6	14	6	7.7	5	4	90	4.1	#
745	2001	6	14	9	9.5	4	1	130	6.7	0.5
745	2001	6	14	12	9.1	7	5	130	7.7	#
745	2001	6	14	18	6.5	8	7	90	7.2	2.3
745	2001	6	14	21	6.2	8	5	90	7.7	#

10th June 01	Average cloud cover =	**4.6**
	Average wind speed =	**6.78**
14th June 01	Average cloud cover =	**6.4**
	Average wind speed =	**6.68**

Six of the nearest meteorological weather stations were looked at for relative humidity.

Hjarðarnes.	No relative humidity data
Höfn	no relative humidity data
Akurnes	79.1 %
Vagnsstaðir	No relative humidity data
Fagurhólsmýri	No relative humidity data
Kirkjubaejarklaustur 78.8%	

Therefore an average of the two stations with readings was taken = **78.95%**

C5. Grímsvötn Meteorological station

Average air temperature 10th June 2001 = **274.15 K**
                          14th June 2001 = **268.65 K**

Average air pressure 10th June 2001 = **823 hPa**
                       14th June 2001 = **825 hPa**

Shortwave radiation incoming (Gudmundsson et al 2003) = **280 Wm^{-2}**

D1. Mean Square Error Calculation.

Point A

Reading No.	Value	V	V2
1	33.89	-0.035	0.001225
2	33.8	0.055	0.003025
3	33.83	0.025	0.000625
4	33.81	0.045	0.002025
5	33.87	-0.015	0.000225
6	33.87	-0.015	0.000225
7	33.9	-0.045	0.002025
8	33.91	-0.055	0.003025
9	33.84	0.015	0.000225
10	33.83	0.025	0.000625
Sum	338.55		0.01325
Mean	33.855		
M.sq.e	**0.001472**		

Point C

Reading No.	Value	V	V2
1	26.8	0.021	0.000441
2	26.78	0.041	0.001681
3	26.79	0.031	0.000961
4	26.82	0.001	1E-06
5	26.8	0.021	0.000441
6	26.81	0.011	0.000121
7	26.97	-0.149	0.022201
8	26.81	0.011	0.000121
9	26.83	-0.009	8.1E-05
10	26.8	0.021	0.000441
Sum	268.21		0.02649
Mean	26.821		
M.sq.e	**0.002943**		

Point B

Reading No.	Value	V	V2
1	22.21	0.007	4.9E-05
2	22.25	-0.033	0.001089
3	22.26	-0.043	0.001849
4	22.18	0.037	0.001369
5	22.22	-0.003	9E-06
6	22.21	0.007	4.9E-05
7	22.24	-0.023	0.000529
8	22.2	0.017	0.000289
9	22.21	0.007	4.9E-05
10	22.19	0.027	0.000729
Sum	222.17		0.00601
Mean	22.217		
M.sq.e	**0.000668**		

Appendix D2

Aerial photographs used to create the geomorphological map of the Saltarinn geothermal area, and the 1998 eruption site.

Appendix D

266
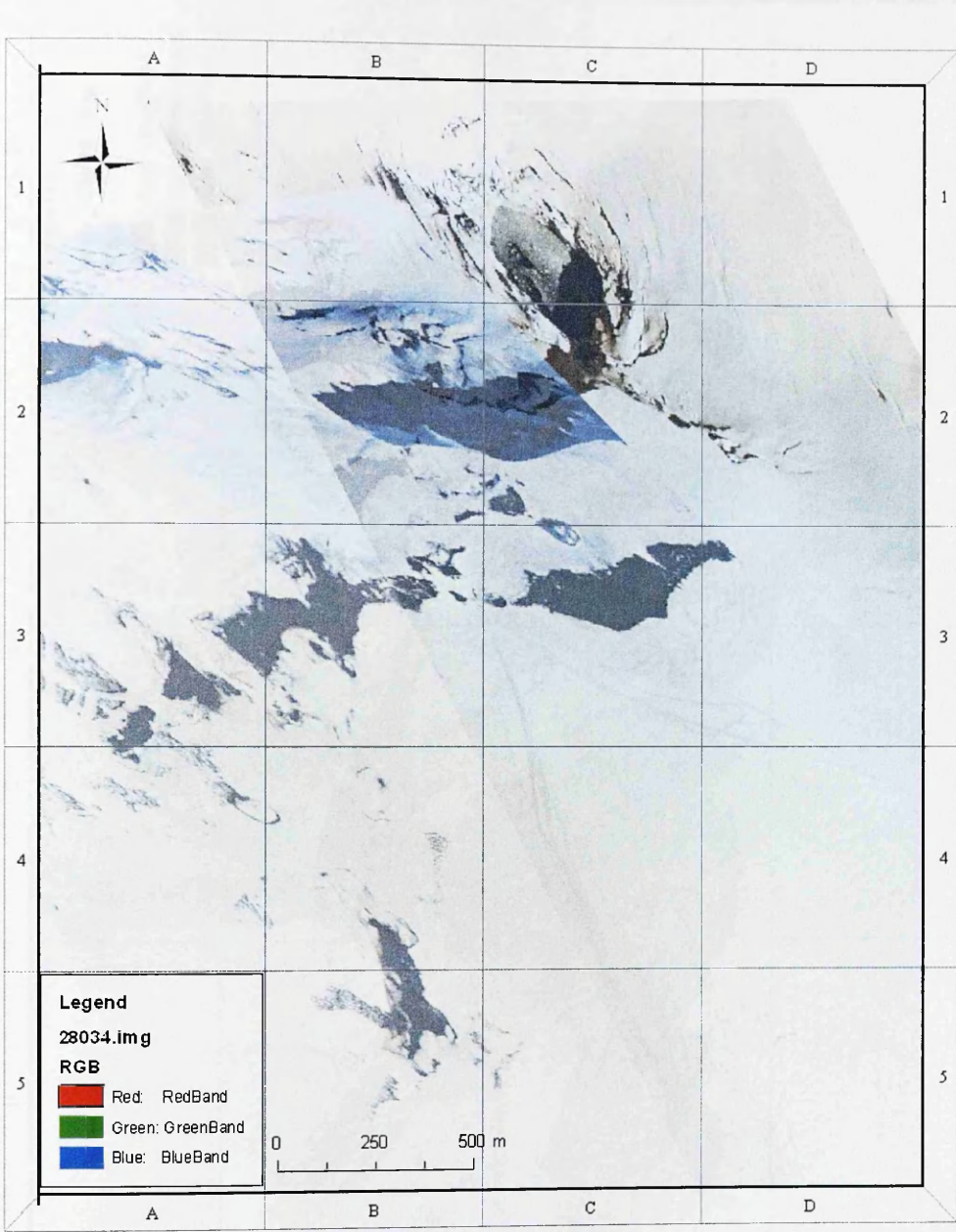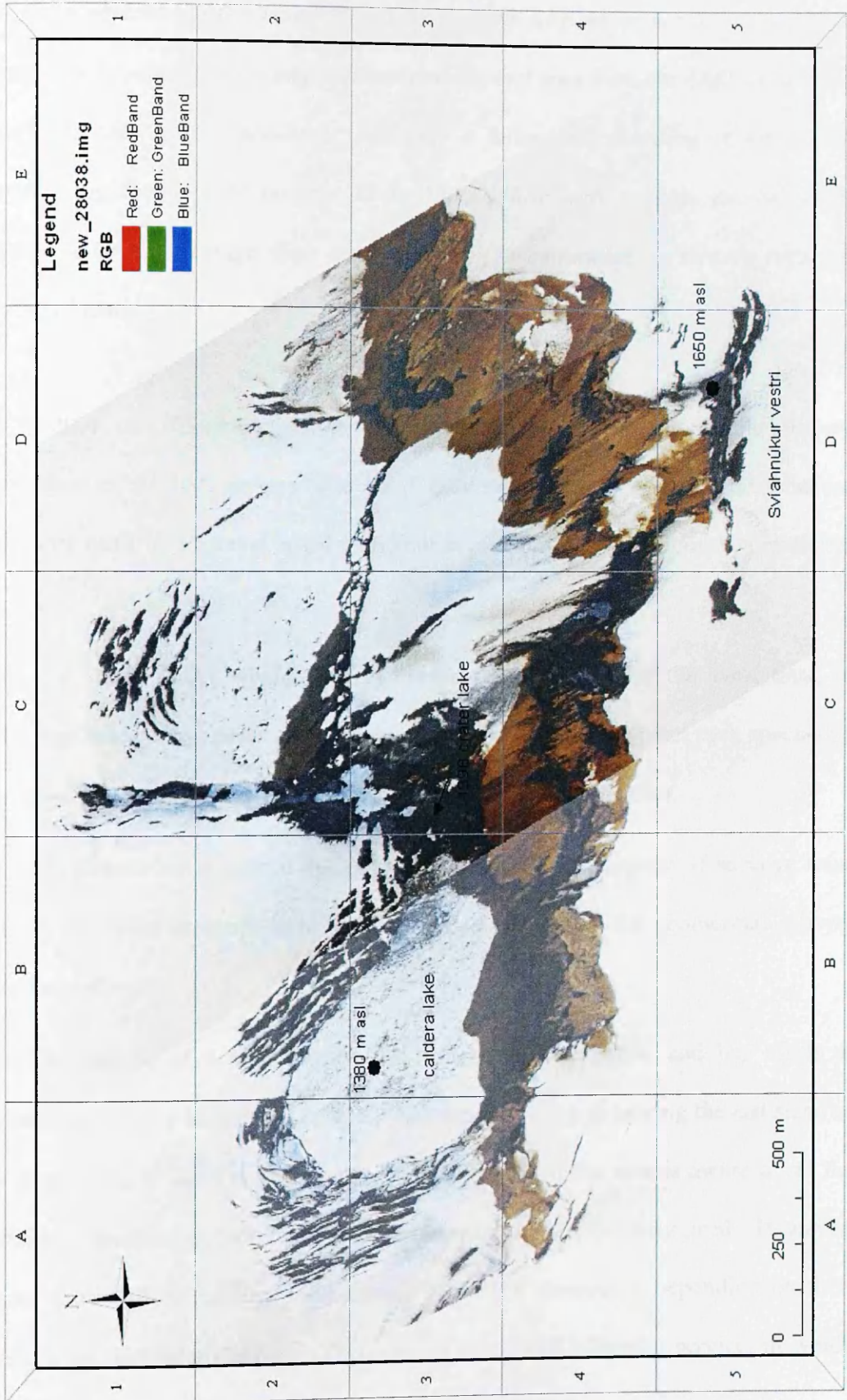
Appendix E. Recommendations to the NERC ARSF

The main objective of this research was to establish whether or not it is possible to extract useful topographic, compositional and thermal data from the ARSF data. It is clear that this can be achieved. However a fuller understanding of Grimsvötn requires regular airborne surveys. If the NERC ARSF were to make another flight across the Grímsfjall ridge, there are a number of recommendations that the research has highlighted.

E1. In 2001, no GPS ground station was established for the correction of the imagery at the time of the 2001 survey. The ARSF now stipulate in their survey information, that there must be a ground based GPS station measuring at one-second intervals set up.

E2. Any future survey would need to have a field excursion at the same time, to collect ground control points, temperature data from tephra and water, rock specimens and good meteorological data, in order to accurately analyse the data.

E3. As Grímsvötn is such a dynamic environment, consequently, if surveys were carried out either annually or bi-annually, small changes in the geothermal activity may be observed.

E4. The data is of a high quality, has considerable potential, and has much to recommend it for a large range of uses. The current policy of leaving the last stage of the processing to the user has much to recommend it, if the user is aware of all the different aspects of geocorrection and knows what they particularly need. However, some users will be satisfied with default geometric correction, depending on their reasons for analysing the data. Therefore, if the ARSF offered a service, in which

they geocorrect the data and perform atmospheric corrections, this may be welcomed by the user community. The assistance that was received from the ARSF was very useful in reducing the issues regarding geocorrection of the Grímsvötn imagery.

E5. The addition of a "help line", or clearly defined support network, that could use lay terminology to help none remote sensing specialists. This would benefit the user community, reducing the time needed to correct the data, whilst also being beneficial to the ARSF by alleviating pressure on ARSF processing staff, ultimately leading to more useful results for the scientific community at large.

Appendix F. CASI Compositional Mapping

For inaccessible regions the composition of the land surface can be difficult to determine without hand specimens. However, one method of doing this is to use the visible wavelengths from the CASI data that was collected at the time of the aerial survey. Some preliminary analysis has been carried out on the CASI data to establish the usefulness and potential for compositional mapping of the Grímsvötn caldera.

Using the Spectral Analysis Workstation capability within ERDAS Imagine, a CASI image was mapped for materials such as basalt and altered or unaltered volcanic tuff. It is known that Grímsvötn is composed of tholeiitic basalt (Sigmarsson et al. 2000, Steinthorsson et al. 2000), but in order to test the accuracy of the workstation, rhyolite was included to the material list. The material list of spectra was taken from the ASTER (Advanced Spaceborne Thermal Emission and Reflection Radiometer), spectral library within ERDAS Imagine. A number of points within the 1998 eruption site and Saltarinn geothermal areas were chosen (fig. F1) and spectral curves were drawn (fig. F2), before the workstation carried out a material identification, using spectral angle mapping (Van der Meer, 1999), based on those spectra.
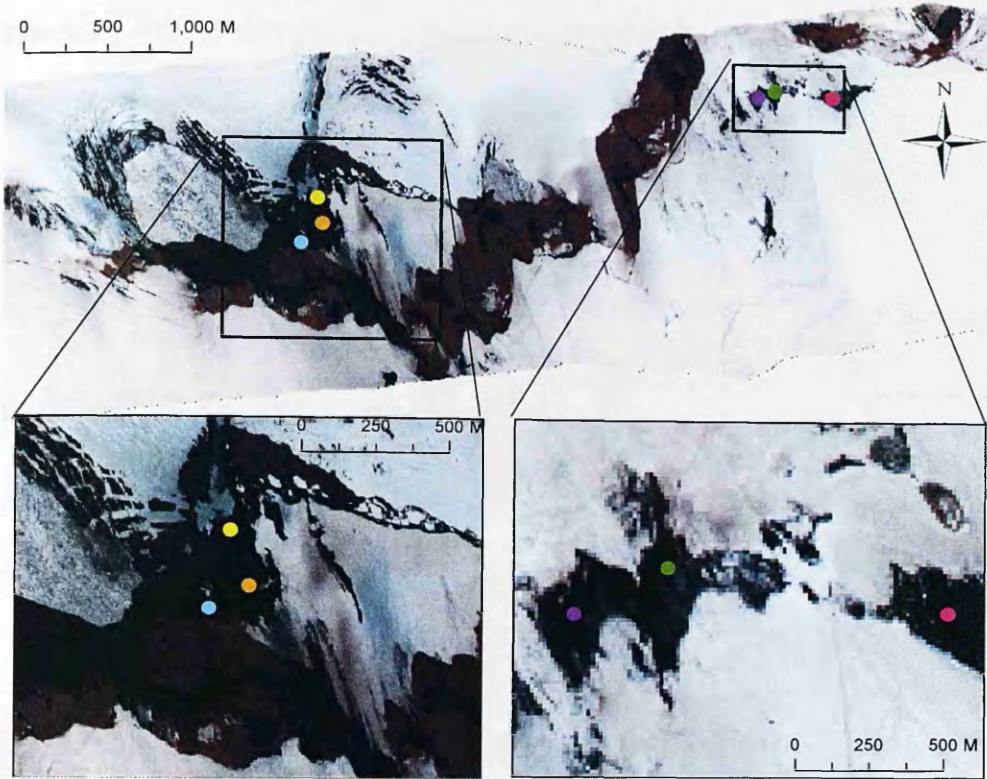
Fig. F1 Compact Airborne Spectrographic Imager (CASI) image (True colour RGB with bands 123) of the Grímsfjall ridge, showing 6 locations where reflectance spectra were collected from the imagery.
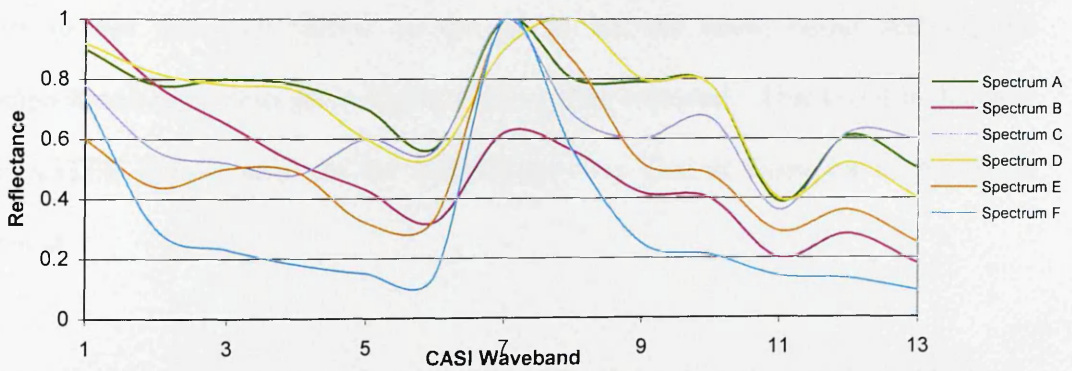

Fig F2 Graph to show the reflectance spectra of 6 points from the Saltarinn geothermal area (A, B, C) and the 1998 eruption site (D, E, F).

The results were in the form of a likelihood value, and were then ranked. The higher the value the more likely the spectra relate to a certain material. Fig. F3 shows the results in the form of a bar chart. The first three spectrum results are from the

Spectrum A and B shown the ground surface is likely to be composed of tholeiitic

basalt and altered volcanic tuff. Spectrum C, D, E, F, also show that tholeiitic basalt is

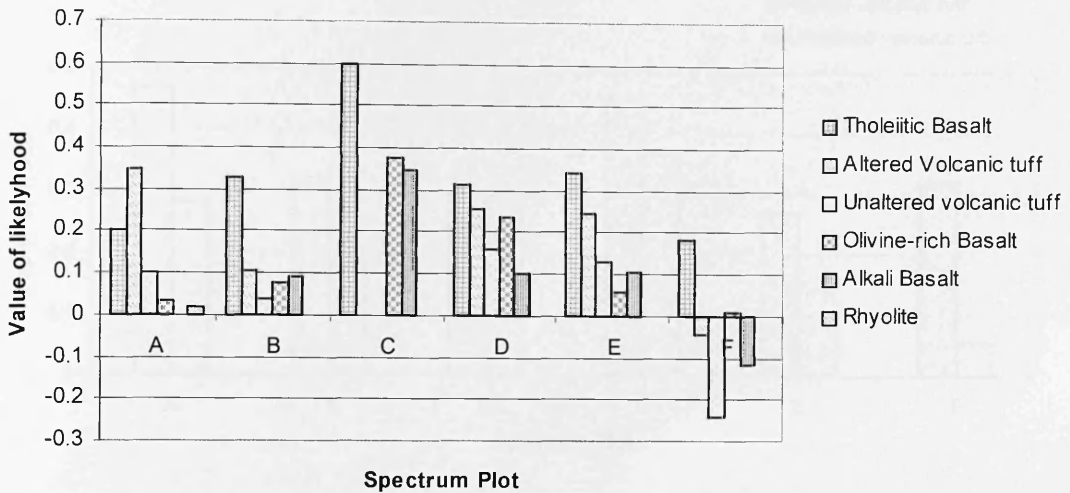the main composition, followed by altered and unaltered volcanic tuff.

Fig. F3 Graph to show the likely composition of the Grímsvötn area, along six lines of
spectra.

However, spectrum C is anomalous. The greatest likelihood is tholeiitic basalt which

correlates with the other results, but the altered and unaltered volcanic tuff is around

zero so has not been shown on the graph, but the alkali basalt and rhyolite

compositions have been given higher ranking than expected. This could be because

the ASTER spectra used for the analysis are very distinct examples from outside

Iceland.

Overall these results are as expected. From the field excursion in June 2004, the

Saltarinn area was visited and was covered in poorly consolidated tephra, which had

been altered in places by the large number of steam vents and fumaroles. Instead of

being dark grey in colour the tephra was a range of colours from reds through to

oranges, yellow and white, in some areas. Because both case study sites were covered

by tephra, the analysis was repeated using only the altered and unaltered volcanic tuff spectra, to see whether mineral alteration could be distinguished using the CASI data. Fig. F4 shows the results of that analysis.
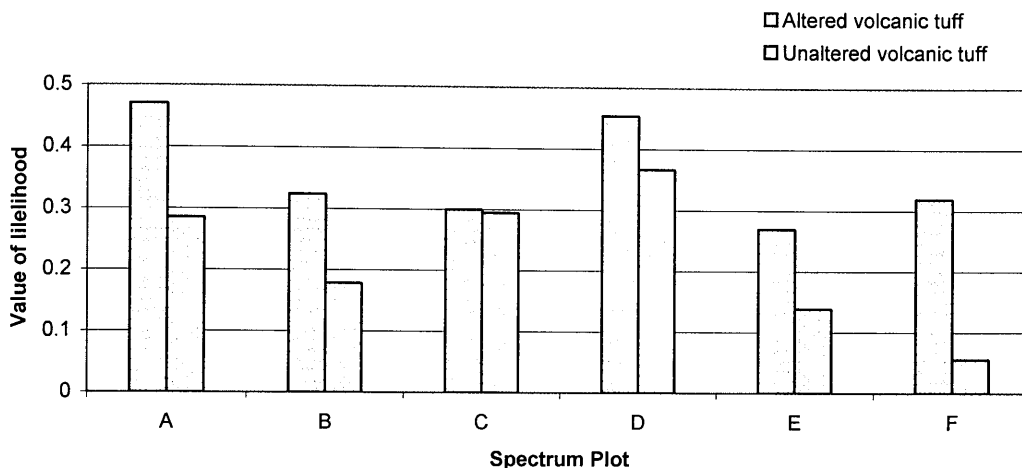

Fig. F4 Graph to show the likely composition of the Grímsvötn area, along six lines of spectra, using only two source materials, altered and unaltered volcanic tuff, taken from the ASTER spectral library.

The results from the analysis showed that the majority of spectra taken show that the likely composition of the land surface is altered volcanic tuff. The result is even for spectrum C, between altered and unaltered compositions. These results fit with the observations made in the field that showed that there was a combination of altered and unaltered tephra, because of the large number of steam vents and fumaroles through out the two case study sites.

These results show there is potential to use the CASI data for looking at the composition of the exposed rock surfaces. For this research an emissivity value taken from known literature, will be used for the exposed rock areas, as more research is needed in terms of composition.

Appendix G. List of conferences attended

*NERC ARSF Workshop, RAL, December 2002.

†Volcanic and Magmatic Studies Group (VMSG) Annual conference, Bath, January 2004.

*RSPSoc Workshop, British Antarctic Survey (BAS), April 2004.

*RSPSoc and The Geological Society Remote Sensing Group, Mapping hazardous terrain using remote sensing, London, December 2004.

*Oral presentation

†Poster presentation

Selection of Abstracts

NERC ARSF Workshop, December 2002.

Airborne Remote Sensing of the Thermal Activity of Grímsvötn, Iceland: Introduction to the research. Sukina Stewart[1], Harry Pinkerton[1], Alan Blackburn[2], Magnus T. Guðmundsson[3], [1]Environmental Science Department, Lancaster University, Lancaster, LA1 4QY, [2] Geography Department, Lancaster University, [3]Science Institute, University of Iceland, Reykjavik, Iceland.

A combined thermal infrared and photogrammetric study of partly ice-covered Grímsvötn volcano in Iceland was carried out in June 2001, in an attempt to gain information on heat flow from one of Iceland's most active volcanoes. Grímsvötn which last erupted in 1998 has a partially exposed geothermal system that has until now been used for simple calorimetry, to make estimates connecting the close links between volcanic eruption rate and heat flux.

Increased melting at Grímsvötn in the aftermath of the 1998 eruption has changed the ice conditions considerably. Increase melting at the ice dam that used to seal Grímsvötn in the periods between drainage in glacier floods (jökulhlaups) has resulted in major leakage of the dam. This makes calorimetric estimates of melting more difficult.

Thermal images of the Grímsvötn caldera show distinct areas of geothermal activity. Along with ground survey studies of the same area carried out by the Science Institute, University of Iceland, analysis of the data has begun to show that areas of protruding ground above the ice, nunataks, have high geothermal heat flux all year round. The component of heat flow lost to the atmosphere cannot be measured using calorimetric techniques based on ice melting. This research will provide an alternative methodology for calculating heat flux.

The aerial photographs collected from Grímsvötn have begun to be used to map new exposed regions of the caldera walls, crevasses and ice cauldrons that cannot be accurately mapped from the ground because of safety issues. The combined data sets will be analysed both visually and quantitatively using a combinations of ERDAS Imagine and ARCGIS environments. Together these surveys will provide a reliable estimate of the present heat output and record the changes occurring in Grímsvötn, one of the most powerful geothermal systems in the world.

RSPSoc Workshop, Remote sensing and Photogrammetry of challenging environments. BAS, April 2004.

Airborne Remote Sensing of the Thermal Activity of Grímsvötn, Iceland: Problems and Solutions Sukina Stewart[1], Harry Pinkerton[1], Alan Blackburn[2], Magnus T. Guðmundsson[3], [1]Environmental Science Department, Lancaster University, Lancaster, LA1 4QY, [2] Geography Department, Lancaster University, [3]Science Institute, University of Iceland, Reykjavik, Iceland.

Grímsvötn is Iceland's most active volcano. This sub-glacial volcano, which erupted in 1996 and again in 1998, has a partially exposed geothermal system, and ground-based measurements have been used to make calorimetric estimates of the relationship between volcanic eruption rate and heat flux. However, increased melting in Grímsvötn during and after the 1998 eruption has resulted in major leakage of a sub-glacial dam. This has significantly increased the problems of calculating heat flux calorimetrically. To overcome this the NERC ARSF carried out a combined infrared and photogrammetric aerial survey of Grímsvötn Volcano, Iceland in 2001.

The aims of the project are to learn more about the processes in operation within this particular subglacial volcano, its usefulness in understanding other full or partial subglacial edifices and to evaluate the value of this technology. The aerial photographs will be used to produce geomorphological maps of the instabilities on the caldera wall, together with deep geothermal cauldrons that cannot be safely mapped from the ground. The photographs will be scanned and the resultant images are orthorectified and mosaiced using ERDAS Imagine. The combined data sets will be analysed both visually and quantitatively using a combination of ERDAS Imagine and ArcGIS environments.

The June 2001 thermal images of the Grímsvötn subglacial caldera show distinct areas of geothermal activity. The hope is that the remotely sensed images will detect previously unknown fumarolic activity and anomalies, for further ground based study in the future.

Appendix H.

Abstracts of papers derived from work presented in this thesis.

Stewart SF, Pinkerton H, Blackburn GA, Gudmundsson MT (In Review) Mapping thermal anomalies using Airborne Thematic Mapper imagery: Grímsvötn caldera, Vatnajökull, Iceland. Geological Society of London Special Publication.

Abstract

Grímsvötn, Iceland's most active volcano, is also one of the most powerful geothermal areas in Iceland. This sub-glacial volcano is located in the centre of Vatnajökull, Europe's largest temperate ice cap, and it erupted most recently in 1998 and 2004. As part of ongoing research on heat flux, morphological changes and volcanic processes at Grímsvötn, thermal anomalies were mapped using remote sensing NERC ARSF data. The 2001 thermal images of the Grímsvötn subglacial caldera reveal distinct areas of geothermal activity as well as providing an overall view of the thermal anomalies associated with water and rock exposures. A crater lake located on the 1998 eruption site is shown to have a surface temperature of 30°-35°C. There is a good correlation between the ARSF data and ground-based temperature measurements. The thermal images also revealed previously undetected areas of high heat flow. Factors that complicate the interpretation and comparison of different data sets from an ice-covered area include recent cornice collapses and variations in atmospheric humidity. To reduce uncertainty in future missions temperature measurements should be made at points whose position is well constrained using differential GPS. In addition, humidity and temperature measurements should be made at the time of flight.

Stewart SF, Pinkerton H, Blackburn GA (In Review) Monitoring active subglacial volcanoes: a case study using airborne remote sensing images of Grímsvötn, Iceland. Bulletin of Volcanology.

Abstract

Grímsvötn, Iceland's most active volcano, is also one of the most powerful geothermal areas in Iceland. This sub-glacial volcano is located in the centre of Vatnajökull, Europe's largest temperate ice cap, and it erupted most recently in 1998 and again in 2004. As part of ongoing research on heat flux, morphological changes and volcanic processes at Grímsvötn, thermal

anomalies were calculated using remote sensing NERC ARSF data. The 2001 thermal images of the Grímsvötn subglacial caldera reveal distinct areas of geothermal activity and provided an overall view of the thermal anomalies associated with water and rock exposures. A crater lake located on the 1998 eruption site has an average surface temperature above 20°C. The thermal images also revealed previously undetected areas of high heat flow. Ground-based measurements of Grímsvötn's partially exposed geothermal system have previously been used to make calorimetric estimates of the relationship between volcanic eruption rate and heat flux. However, increased melting in Grímsvötn during and after the 1998 eruption has resulted in major leakage from a sub-glacial dam. This has significantly increased the problems of calculating heat flux calorimetrically. This research has shown that the ATM imagery can be used to calculate heat flux from the crater lake when combined with meteorological data. Aerial photographs collected during the survey have been used to produce geomorphological maps of the caldera wall, together with areas that cannot be safely mapped from the ground. A high resolution DEM of the 1998 eruption site has been produced, allowing slope angle analysis, and 3D models of the Grímsfjall ridge to be produced. This, in combination with the temperature data, has the potential to monitor future volcanic changes of Grímsvötn.